



IntechOpen

Solar Cells

*Edited by Majid Nayeripour,
Mahdi Mansouri and Eberhard Waffenschmidt*



Solar Cells

*Edited by Majid Nayeripour, Mahdi Mansouri
and Eberhard Waffenschmidt*

Published in London, United Kingdom



IntechOpen





Supporting open minds since 2005



Solar Cells

<http://dx.doi.org/10.5772/intechopen.77422>

Edited by Majid Nayeripour, Mahdi Mansouri and Eberhard Waffenschmidt

Assistant to the Editor(s): Farnaz Orooji

Contributors

Jejiron Maheswari Maheswari Baruah, Jyoti Narayan, Muhammad Y. Bashouti, Riam Abu Much, Prakash Natarajan, Sumesh Sadhujan, Awad Shalabny, Sherina Harilal, Pedro Pablo Zamora, Klaus Bieger, Samy K. K. Shaat, Hussam Musleh, Jihad Asad, Nabil Shurrab, Ahmed Issa, Amal AlKahlout, Naji Al Dahoudi, Mehul C. Raval, Sukumar Madugula Reddy, S. Saravanan, Nagarajan Balaji, Shafiqh Mehraeen, Daniel Christiansen

© The Editor(s) and the Author(s) 2020

The rights of the editor(s) and the author(s) have been asserted in accordance with the Copyright, Designs and Patents Act 1988. All rights to the book as a whole are reserved by INTECHOPEN LIMITED. The book as a whole (compilation) cannot be reproduced, distributed or used for commercial or non-commercial purposes without INTECHOPEN LIMITED's written permission. Enquiries concerning the use of the book should be directed to INTECHOPEN LIMITED rights and permissions department (permissions@intechopen.com).

Violations are liable to prosecution under the governing Copyright Law.



Individual chapters of this publication are distributed under the terms of the Creative Commons Attribution 3.0 Unported License which permits commercial use, distribution and reproduction of the individual chapters, provided the original author(s) and source publication are appropriately acknowledged. If so indicated, certain images may not be included under the Creative Commons license. In such cases users will need to obtain permission from the license holder to reproduce the material. More details and guidelines concerning content reuse and adaptation can be found at <http://www.intechopen.com/copyright-policy.html>.

Notice

Statements and opinions expressed in the chapters are these of the individual contributors and not necessarily those of the editors or publisher. No responsibility is accepted for the accuracy of information contained in the published chapters. The publisher assumes no responsibility for any damage or injury to persons or property arising out of the use of any materials, instructions, methods or ideas contained in the book.

First published in London, United Kingdom, 2020 by IntechOpen

IntechOpen is the global imprint of INTECHOPEN LIMITED, registered in England and Wales, registration number: 11086078, 7th floor, 10 Lower Thames Street, London, EC3R 6AF, United Kingdom

Printed in Croatia

British Library Cataloguing-in-Publication Data

A catalogue record for this book is available from the British Library

Additional hard and PDF copies can be obtained from orders@intechopen.com

Solar Cells

Edited by Majid Nayeripour, Mahdi Mansouri and Eberhard Waffenschmidt

p. cm.

Print ISBN 978-1-78984-125-1

Online ISBN 978-1-78984-126-8

eBook (PDF) ISBN 978-1-78923-899-0

We are IntechOpen, the world's leading publisher of Open Access books Built by scientists, for scientists

4,700+

Open access books available

121,000+

International authors and editors

135M+

Downloads

151

Countries delivered to

Our authors are among the
Top 1%

most cited scientists

12.2%

Contributors from top 500 universities



WEB OF SCIENCE™

Selection of our books indexed in the Book Citation Index
in Web of Science™ Core Collection (BKCI)

Interested in publishing with us?
Contact book.department@intechopen.com

Numbers displayed above are based on latest data collected.
For more information visit www.intechopen.com



Meet the editors



After 8 years of industrial experience and academic work in the electrical engineering and renewable energy fields, Prof. Majid Nayeripour was promoted to full professor in the field of microgrids in 2016. He was given a sabbatical from Shiraz University of Technology, Iran, and was invited to Cologne University of Applied Sciences, Germany, in January 2016. During his research there, he gained new experiences about problems relating to high penetration levels of distributed generations and towards 100% renewable energy in Germany, and as a result he was awarded a fellowship program for an experienced researcher from the Alexander von Humboldt (AvH) Foundation in 2017. Currently, he is at the Cologne University of Applied Science and is involved in research on the control and dynamic investigation of interconnected microgrids. He has published more than 120 journal and conference papers, four books, and supervised more than 10 research projects.



Mohammad Mahdi Mansouri was born in Yazd, Iran, in 1975. He received his BS degree in Electronic Engineering and MS degree in Electronic Power both from Sharif University of Technology at Power Electronics-STATCOM, as well as his PhD degree in Renewable Energy Systems from Doubly-Fed Induction Generator-Based Wind Turbines from Shiraz University of Technology. He has 20 years experience in high-voltage transmission substations and lines as a technical engineer, consultant, and executive project manager. His research interests include flexible alternating current transmission system devices, power quality, and power system protection. He currently conducts power electronics, power relay protection, and power quality projects as a consultant and project manager.



Eberhard Waffenschmidt (Prof. Dr. Ing.) received his degree in Electronic Engineering and his PhD degree from RWTH Technical University, Aachen, Germany. From 1995 to 2011, he was employed at Philips Research, Aachen, Germany, finally as a senior scientist. Since 2011, he has been Professor of Electrical Power Grids at TH Köln University of Applied Sciences, Cologne, Germany. There, he participates with the Cologne Institute for Renewable Energy (CIRE). He has been an IEEE member since 2005, meanwhile he became senior member of the same. He is currently Chairman of the Solarenergie-Förderverein Deutschland e.V. (SFV, Society to Promote Solar Energy Germany), Aachen, Germany. His current research interests include identifying and removing obstacles to achieve 100% use of renewable energy.

Contents

Preface	XIII
Chapter 1 Industrial Silicon Solar Cells <i>by Mehul C. Raval and Sukumar Madugula Reddy</i>	1
Chapter 2 Review on Metallization in Crystalline Silicon Solar Cells <i>by Nagarajan Balaji, Mehul C. Raval and S. Saravanan</i>	25
Chapter 3 Polymers in Solar Cells <i>by Pedro Pablo Zamora and Klaus Bieger</i>	45
Chapter 4 Impact of Active Layer Morphology, Density of States, Charge Carrier Concentration, and Local Charge Density Fluctuations on Bimolecular Recombination of Bulk Heterojunction Solar Cells: A Theoretical Perspective <i>by Daniel Christiansen and Shafiqh Mehraeen</i>	67
Chapter 5 Nanoplasmonic for Solar Energy Conversion Devices <i>by Samy K.K. Shaat, Hussam Musleh, Jihad Asad, Nabil Shurrah, Ahmed Issa, Amal AlKahlout and Naji Al Dahoudi</i>	93
Chapter 6 Heterojunction-Based Hybrid Silicon Nanowires Solar Cell <i>by Riam Abu Much, Prakash Natarajan, Awad Shalabny, Sumesh Sadhujan, Sherina Harilal and Muhammad Y. Bashouti</i>	119
Chapter 7 Aqueous-Mediated Synthesis of Group IIB-VIA Semiconductor Quantum Dots: Challenges and Developments <i>by Jeyron Maheswari Baruah and Jyoti Narayan</i>	139

Preface

This edited volume is a collection of reviewed and relevant research chapters concerning developments within the solar cells field of study. The book includes scholarly contributions by various authors and is edited by a group of experts pertinent to physical sciences, engineering, and technology. Each contribution comes as a separate chapter complete in itself but is directly related to the book's topics and objectives.

The book contains the following chapters: "Industrial Silicon Solar Cells", "Review on Metallization in Crystalline Silicon Solar Cells", "Polymers in Solar Cells", "Impact of Active Layer Morphology, Density of States, Charge Carrier Concentration, and Local Charge Density Fluctuations on Bimolecular Recombination of Bulk Heterojunction Solar Cells: A Theoretical Perspective", "Nanoplasmonic for Solar Energy Conversion Devices," "Heterojunction-Based Hybrid Silicon Nanowires Solar Cell", and "Aqueous-Mediated Synthesis of Group IIB-VIA Semiconductor Quantum Dots: Challenges and Developments".

The target audience comprises scholars and specialists in the field.

Majid Nayeripour

Cologne University of Applied Sciences,
Germany

Alexander von Humboldt Foundation,
Bonn, Germany

Mahdi Mansouri

Yazd University,
Iran

Eberhard Waffenschmidt

Cologne University of Applied Sciences,
Germany

Industrial Silicon Solar Cells

Mehul C. Raval and Sukumar Madugula Reddy

Abstract

The chapter will introduce industrial silicon solar cell manufacturing technologies with its current status. Commercial p-type and high efficiency n-type solar cell structures will be discussed and compared so that the reader can get a head-start in industrial solar cells. A brief over-view of various process steps from texturing to screen-printed metallization is presented. Texturing processes for mono-crystalline and multi-crystalline silicon wafers have been reviewed with the latest processes. An over-view of the thermal processes of diffusion and anti-reflective coating deposition has been presented. The well-established screen-printing process for solar cell metallization is introduced with the fast-firing step for sintering of the contacts. I-V testing of solar cells with various parameters for solar cell characterization is introduced. Latest developments in various processes and equipment manufacturing are also discussed along with the expected future trends.

Keywords: silicon, solar cells, manufacturing, multi-crystalline, mono-crystalline, texturing

1. Introduction

Photovoltaics are an important renewable energy source which has grown rapidly from 8 GW in 2007 to 400 GW in 2017 [1]. Along with the increasing demand, the PV system costing has also dropped significantly from 35.7 \$/W_p in 1980 to 0.34 \$/W_p in 2017 accelerating its adoption [2]. Silicon (Si) which is an important material of the microelectronics industry has also been the widely used bulk material of solar cells since the 1950s with a market share of >90% [2]. The chapter will introduce the typical steps for manufacturing commercial silicon solar cells. A brief history of solar cells and over-view of the type of silicon substrates along with the different solar cell architecture will be introduced in Sections 2 and 3. Subsequently, the wet-chemistry and high temperature steps used in fabrication will be described in Sections 4 and 5. Section 6 will discuss about the metallization process along with typical characterization parameters for commercial solar cells. Finally, future roadmap and expected trends will be discussed in the concluding section.

2. Evolution of solar cells

The 'photovoltaic effect' literally means generation of a voltage upon exposure to light. The phenomenon was first observed by the French physicist Edmund Becquerel on an electrochemical cell in 1839, while it was observed by British scientists W.G. Adams and R.E. Day on a solid-state device made of selenium in 1876 [3]. From the 1950s onwards, there was rapid progress in the performance of commercial

solar cells from <1% to >23% [2] and silicon has been the ‘work-horse’ of the photovoltaic industry since then. The evolution of silicon solar cells is shown in **Figure 1**.

The first silicon solar cells demonstrated by Russell Ohl of Bell Laboratories during 1940s were based on natural junctions formed from impurity segregation during the recrystallization process [3]. The cells had an efficiency of <1% due to lack of control over the junction location and the quality of the silicon material. The nomenclature for naming the regions (p-type: side which is illumination and n-type: other side) given by Ohl are since then being used for the solar cell naming conventions.

During the 1950s, there was rapid development in the high-temperature diffusion process for dopants in silicon. Person, Fuller and Chaplin of Bell Laboratories demonstrated a 4.5% efficient solar cell with lithium-based doping, which improved to 6% with boron diffusion. The solar cell had a ‘wrap-up’ around structure (**Figure 1(b)**) with both contacts on back side to avoid shading losses, but led to higher resistive losses due to the wrap-around structure. By 1960, the cell structure evolved to as shown in **Figure 1(c)**. Since the application was for space explorations, high resistivity substrate of 10 Ω cm was used to have maximum radiation resistance. Vacuum evaporated contacts were used on both sides, while a silicon monoxide coating was used as an anti-reflective coating (ARC) on the front-side (FS) [3].

In early 1970s it was found that having sintered aluminum on the rear-side improved the cell performance by forming a heavily doped interface known as the ‘back-surface field (Al-BSF)’ and gettering of the impurities [3]. The Al-BSF reduces recombination of the carriers on the rear-side and hence improves the voltage and the long-wavelength spectral response. Implementation of finer and closely

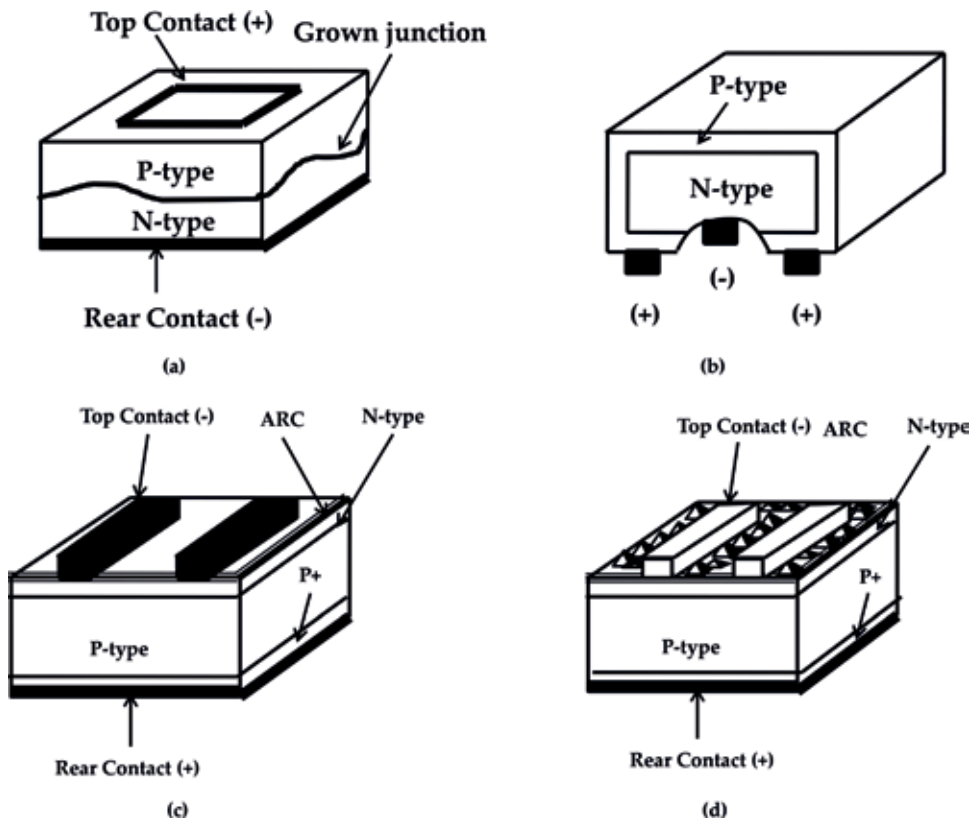


Figure 1. Evolution of silicon solar cells. (a) 1941: Solar cell reported with grown-in junction, (b) 1954: Solar cell p-n junction formed with dopant diffusion, (c) 1970: Violet cell with Aluminum back-surface field, (d) 1974: Black cell with chemically textured surface [3].

spaced fingers reduced the requirement on the junction doping and eliminated the dead layer. An ARC of titanium dioxide (TiO_x) was used and its thickness was selected to reduce the reflection for shorter wavelengths and gave a violet appearance to the solar cells. Further improvement was made by texturing the wafers using anisotropic etching of (100) wafers to expose the (111) surfaces. The texturing led to improved light-trapping and gave the cells a dark velvet appearance. The improved cell architecture is shown in **Figure 1(d)**. In 1976, Rittner and Arndt demonstrated terrestrial solar cells with efficiencies approaching 17% [3].

The passivated emitter solar cell (PESC) achieved a milestone of 20% efficiency in 1984–1986. The metal/silicon contact area was only 0.3% in PESC cells, while a double layer ARC of ZnS/MgF_2 was used in both cell structures. In 1994, passivated emitter rear locally diffused (PERL) cell with an efficiency of 24% were demonstrated [3]. As compared to the PESC cell, the PERL cell had inverted pyramids on FS for better light-trapping and oxide-based passivation on both sides. Oxide passivation layer on the rear-side also improved the internal reflectance of the long wavelength and hence the spectrum response.

In addition to the evolving solar cell architectures, there has also been continuous development in the manufacturing domain in terms of increased throughput, improved process-steps and reduced costs. A brief over-view of the manufacturing of Si substrates and various types of solar cells is given in the next section.

3. Commercial silicon solar cell technologies

Si is the second most abundant material on earth after oxygen and has been widely used in the semiconductor industry. Metallurgical grade silicon (Mg-Si) of 98% purity is obtained by heating quartz (SiO_2) with carbon at high temperatures of 1,500–2,000 [4]. Mg-Si is further purified to obtain solar grade silicon chunks of 99.99% purity. The refined solar grade Si chunks are then processed further to obtain mono-crystalline and multi-crystalline forms of Si ingots, which are a large mass of silicon. In mono-crystalline Si, the atoms are arranged in the same crystal orientation throughout the material. For solar cells, (100) orientation is preferred as it can be easily textured to reduce the surface reflection [5]. Multi-crystalline Si, as the name suggest has multiple grains of Si material with different orientations, unlike the mono-crystalline substrates. Mono-crystalline material have higher minority carrier lifetime compared to multi-crystalline Si and hence higher solar cell efficiencies for a given solar cell technology.

The Czochralski (Cz) method for making mono-crystalline Si ingots is illustrated in **Figure 2(a)**. High purity molten silicon with dopant is maintained above the melting point and then a seed crystal is pulled at a very slow rate to obtain an ingot of as large as 300 mm in diameter and 2 m in length [6]. The molten silicon can be doped with either p-type or n-type dopants to obtain the specific type of mono-crystalline Si ingot of up to 200 kg [2]. Wafers sawn from the ingots have circular edges and hence the shape is called a 'pseudo square'. Multi-crystalline silicon ingots are made by melting high purity Si and crystallizing them in a large crucible by directional solidification process [7] as demonstrated in **Figure 2(b)**. The process does not have a reference crystal orientation like the Cz process and hence forms silicon material of different orientations. Currently the multi-crystalline Si ingots weigh >800 kg [2] which are then cut into bricks and wafers are sawn further. Current size of mono-crystalline and multi-crystalline wafers for solar cell fabrication is 6 inch \times 6 inch. The area of the mono-crystalline wafers will be little less due to the pseudo-square shape. The most widely used base material for making solar cells is boron doped p-type Si substrates. N-type Si substrates for also used

for making high efficiency solar cells, but have additional technical challenges like obtaining uniform doping along the ingot compared to p-type substrates.

A broad classification of different types of solar cells along with efficiency ranges is shown in **Figure 3**. The standard aluminum back-surface field (Al-BSF) technology is one of the most common solar cell technology given its relatively simple manufacturing process. It is based on full rear-side (RS) Al deposition by screen-printing process and formation of a p^+ BSF which helps repel the electrons from the rear-side of p-type substrate and improve the cell performance. The manufacturing flow for Al-BSF solar cells is shown in **Figure 4**. The standard design of commercial solar cells is with grid-pattern FS and full area RS contacts.

The passivated emitter rear contact (PERC) solar cell improves on the Al-BSF architecture by addition of rear-side passivation layer to improve rear-side passivation and internal reflection. Aluminum-oxide is a suitable material for RS passivation with average solar cell efficiencies nearing 21% obtained in production [8]. An existing

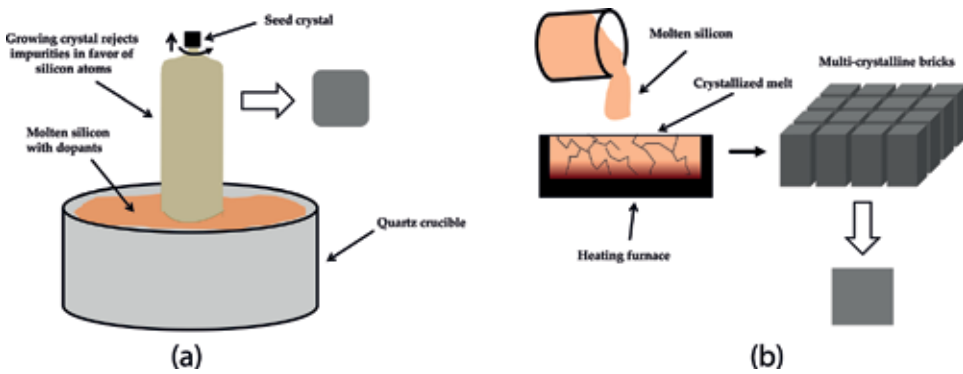


Figure 2. Illustration of (a) Cz process for mono-crystalline ingots and (b) directional solidification process for multi-crystalline ingots.

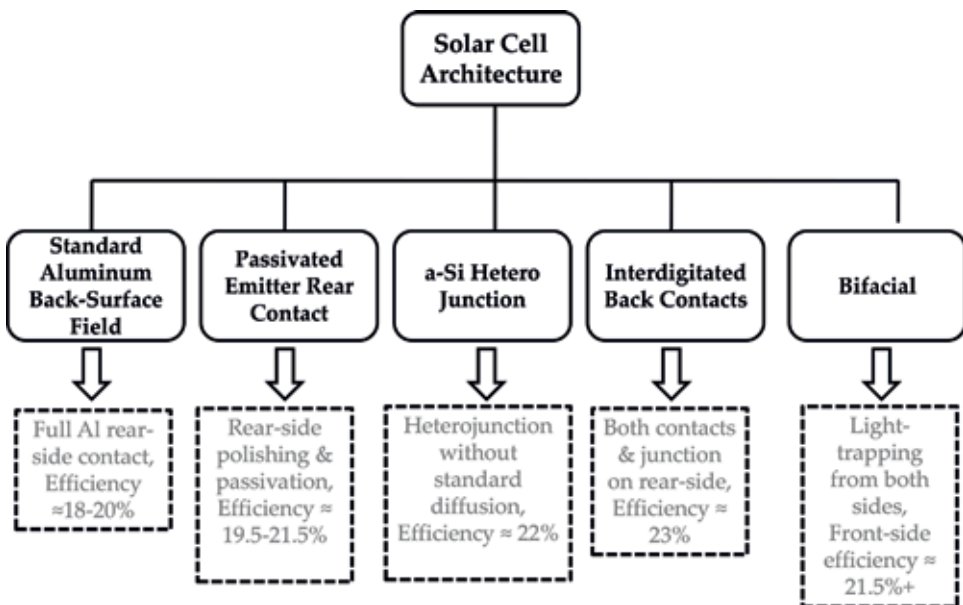


Figure 3. Broad classification of different types of solar cell.

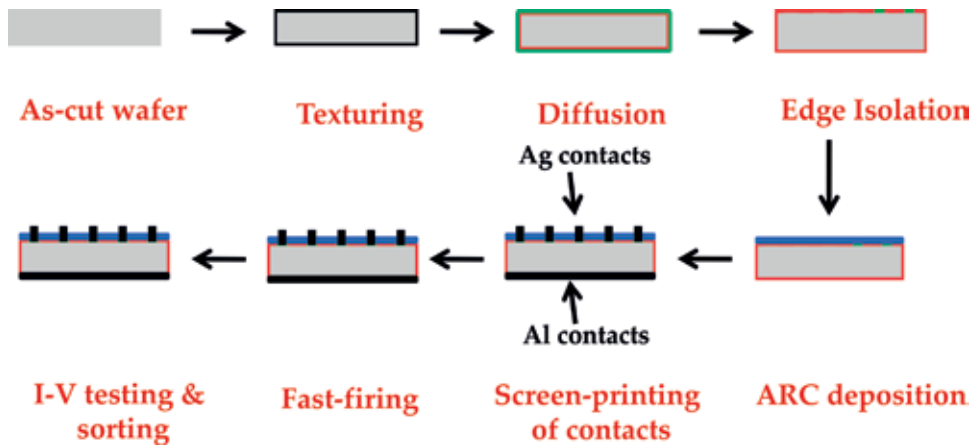


Figure 4.
 Manufacturing flow of Al-BSF solar cells.

Al-BSF solar cell line can be upgraded to PERC process by two additional tools (RS passivation layer deposition and laser for localized contact opening on the RS).

The remaining three cell architectures are mainly higher efficiency technologies based on n-type Si substrates. The a-Si heterojunction solar cell has a-Si layers on the FS and RS of n-type Si substrate to form ‘heterojunctions’ unlike the conventional high temperature diffusion-based p-n junction. Such technology allows processing at lower temperatures, but is very sensitive to the quality of the surface interfaces. a-Si-based heterojunction solar cell was commercially manufactured by Sanyo Electric, which is now taken over by Panasonic [9]. In the interdigitated back contact (IBC) solar cell design, both contacts are present on the rear-side eliminating the FS contact shading losses. Typically for IBC solar cells, the junction will also be located on the rear-side. One of the early manufacturers of the high efficiency n-type IBC solar cell is SunPower Corporation [10]. Bifacial cells, as the name suggests can capture light from both sides of the solar cells. This entails that the rear-side also has a grid-pattern contacts to enable light collection. An example of the bifacial technology is the BiSON solar cell developed and commercialized by ISC, Konstanz [11]. It should be noted that the indicated classification is not an exhaustive list of various other types of solar cell architectures which are in R&D phase, close to commercialization or already being manufactured. The subsequent sections will give an over-view of the process steps for manufacturing of Al-BSF solar cells.

4. Wet-chemistry processes for solar cell fabrication

Wet-chemistry-based treatment is an important step in solar cell processing for saw damage removal (SDR) for the as-cut wafers, texturing of the surface to increase the absorption of incoming solar radiation and edge isolation after the diffusion process. As discussed in the previous section, there are mainly mono-crystalline and multi-crystalline silicon wafers used for fabrication of solar cells. The wet-chemistry-based processing for the respective types of wafers will be discussed ahead.

4.1 Texturing of mono-crystalline silicon wafers

As indicated in Section 2, the development of solar cells started primarily with mono-crystalline wafers and hence employed well-established methods from the domain of microelectronics. Alkaline anisotropic etching based on KOH/NaOH

is used for pyramidal texturing of mono-crystalline wafers. An as-cut mono-crystalline wafer has a weighted average reflectance of >30% (over wavelength of 300–1,200 nm) which reduces to 11–12% after the texturing process. Typical morphology of an alkaline textured surface is shown in **Figure 5**. The anisotropic etching solution etches the (100) surface of the wafers to expose the (111) faces which have a higher density of silicon atoms and hence a slower etch rate compared to the (100) faces. This results in formation of random pyramid structures which form an angle of 54.7° with respect to the wafer surface.

Typical parameters for the alkaline texturing process are shown in **Table 1**. It should be noted that the values of various parameters are indicative and are not to be taken as absolute as there are a variety of additive manufacturers in the market. Isopropyl alcohol (IPA) was initially used as an additive in the texturing solution, which is not involved in the etching reaction, but acts as a wetting agent to improve the homogeneity of texturing process by preventing the H_2 bubbles (generated during the reaction) adhering to the silicon surface [12]. However by 2010, IPA was gradually replaced with alternative additives due to drawbacks like unstable concentration as the bath temperature is close to the boiling point of IPA (82.4°C), high costs, high consumption, health hazards and explosiveness [12]. Many groups have published development work to replace IPA with alternate additives to overcome the disadvantages of IPA, increase the process window and reduce the surface reflectance [12–16]. Additives also reduce the processing time to <10 minutes and increases the bath life to >100 runs.

The texturing process of the mono-crystalline wafers is typically performed in a ‘batch’ which implies that the wafers are loaded in a carrier with slots to hold the wafers (100 slots in a carrier) and then the batch is processed sequentially in baths for texturing, cleaning, treatment steps to remove the organic residue and metal contamination and drying the processed wafers. The carriers are typically coated with PVDF which has very good resistance to various chemicals, abrasion and mechanical wear and tear. Typical carrier for mono-crystalline wafers handling is shown in **Figure 6**. The batch texturing tool has dedicated baths for each step with dosing tanks for chemicals used in the bath. The tool processes many carriers simultaneously and can reach a throughput of >6,000 wafers/h with processing of four carriers at the same time.

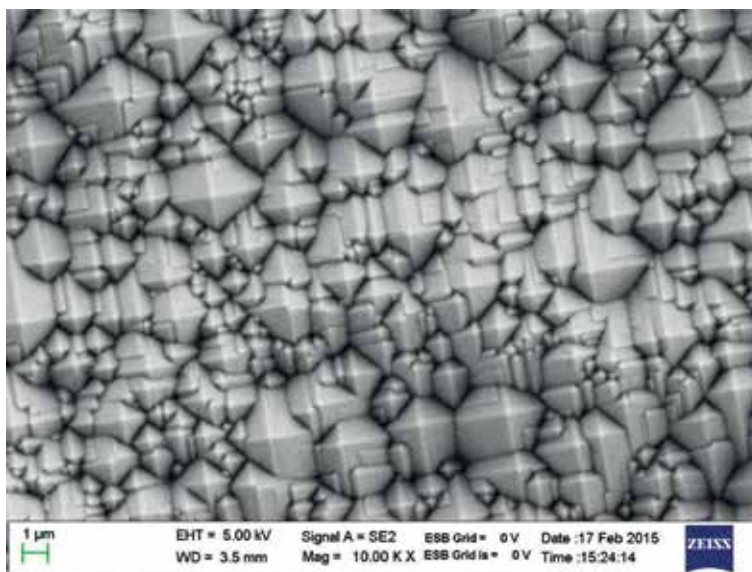


Figure 5.
Typical surface morphology of an alkaline textured mono-crystalline wafer.

Process	KOH/IPA	KOH/additive
KOH (%)	3	<3
IPA (%)	6	—
Additive (%)	—	<2
Process temperature [°C]	>80	70–100
Pyramid size [μm]	5–12	2–7
Process time [min]	30–40	5–10
Organic content [wt%]	4–10	<1.0
Boiling point [°C]	83	>100
Bath lifetimes	<15	>100

Table 1.
Process parameters for IPA-based and additive-based alkaline texturing of mono-crystalline wafers.

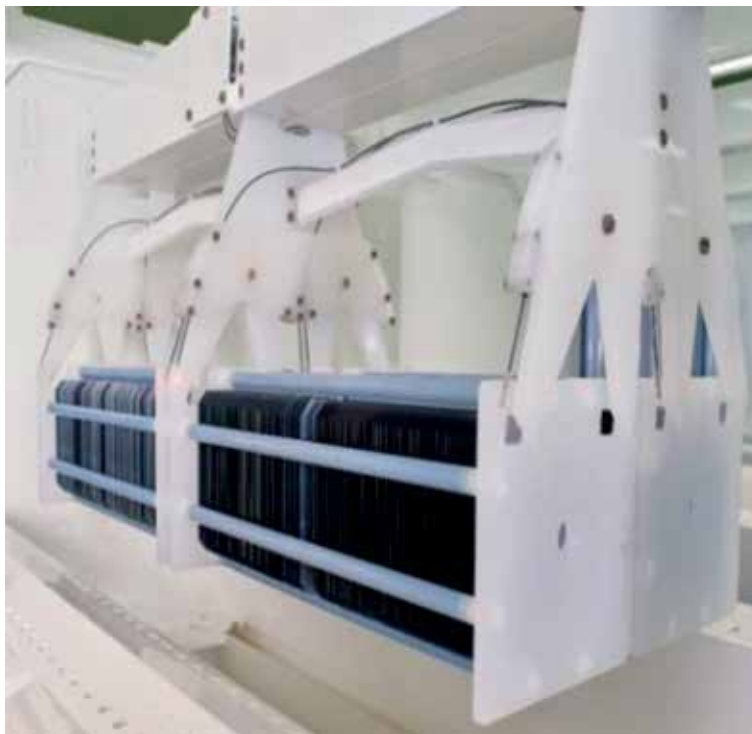


Figure 6.
Carriers for loading wafers in the batch tool. Source: RCT solutions GmbH.

4.2 Texturing of multi-crystalline silicon wafers

Multi-crystalline wafers offer a cost advantage compared to the mono-crystalline wafers and hence have been more widely adopted. However, the alkaline chemistry used for texturing mono-crystalline wafers does not work well for multi-crystalline wafers due to the presence of different grain orientations. An alternative acidic chemistry based on HF and HNO₃ was developed to remove the saw damage and texture the multi-crystalline wafers simultaneously [17, 18]. The acidic solution-based texturing operates at temperatures below room temperature and hence leads to

reduced reaction gas emission, little heat generation, higher stability of the etching solution and better control of the etch rate [18]. A comparison of alkaline texturing and acidic texturing process for multi-crystalline wafers is shown in **Figure 7**.

The acidic texturing process of multi-crystalline wafer can be done in significantly reduced time compared to the alkaline texturing process and hence can be implemented in an 'inline' configuration where the wafers are passed through rollers immersed in the etching bath. A representative image of an inline process along with the typical acidic texturing process is shown in **Figure 8**. For a five lane configuration, the inline tool can have a throughput of up to 4,000 wafers/h. It is important to note that the wafer surface facing down in the etching solution is textured better than the top-side and is the 'sunny-side' for further processing. The acidic texturing process leads to formation of porous silicon on the textured surface which absorbs light and also increases the surface recombination [18]. Hence the porous silicon is removed using a dilute alkaline solution. Subsequently, an acidic clean ($\text{HF} + \text{HCl}$) is performed to remove oxides and metal contamination from the wafer surfaces.

It is important to note that the acidic texturing process discussed above is suitable for the slurry-wire sawn (SWS) multi-crystalline wafers. In the past few years, diamond-wire sawing (DWS) process has replaced the slurry-wire-based cutting due to process and economic advantages [19]. The saw damage of the SWS multi-crystalline wafers is more than the DWS wafers, which have deep straight grooves and a much more smoother surface than the slurry-wire sawn wafers [19]. The saw damage for the SWS wafers plays an important role for initiating the texturing process, which does not occur for the DWS wafers.

Various methods have been proposed to texture DWS multi-crystalline wafers and are summarized in **Table 2** [20]. By tuning the various methods, reflectance of close to 0% can be obtained and hence the term 'black silicon' has been used for the texturing process of DWS multi-crystalline wafers. RIE was the first method for making black silicon and uses sulfur hexafluoride (SF_6) to react with Si and gases like Cl_2 and O_2 for passivating and limiting the reaction [20]. Recently, commercial multi PERC solar cells with average efficiency of 21.3% have been demonstrated with RIE-based

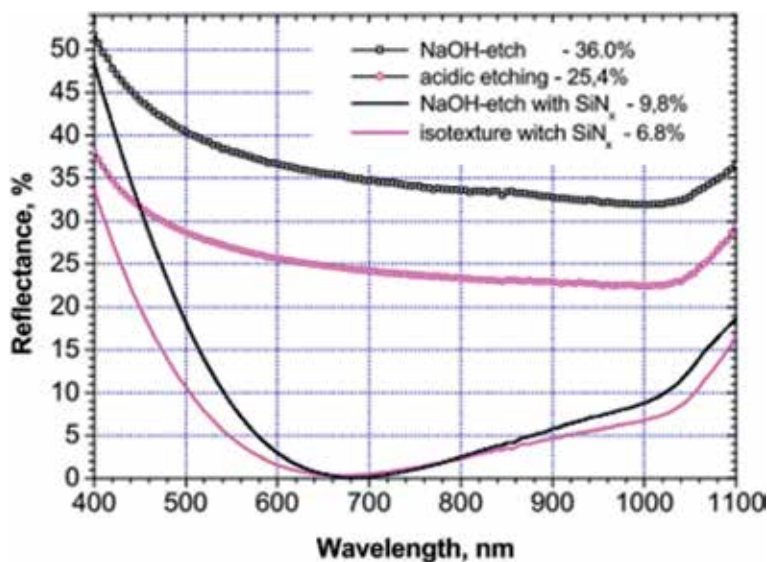


Figure 7.

Comparison of alkaline and acidic texturing for multi-crystalline wafers. Reflectance curves after deposition of $\text{SiN}_x\text{:H}$ are also showed for comparison [17].

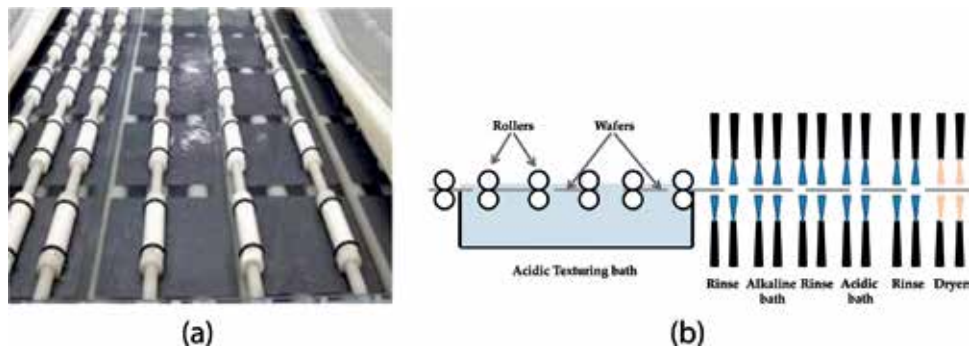


Figure 8.
 (a) Representative inline process with five lanes and (b) acidic texturing process flow for multi-crystalline wafers.

Method	Reagents	Mask	Catalyst	Minimum reflectance (%)
Reactive ion etching (RIE)	SF ₆ /O ₂ , SF ₆ /Cl ₂ /O ₂ , SF ₆ /O ₂ /CH ₄	None	None	4.0
Plasma immersion ion implantation (PIII)	SF ₆ /O ₂	None	None	1.8
Laser irradiation	CCL ₄ , C ₂ Cl ₃ F ₃ , SF ₆ , Cl ₂ , N ₂ , air	None	None	2.5
Plasma etching	SF ₆	Ag nano particles	None	4.2
Metal-assisted chemical etching (MACE)	AgNO ₃ /HF/HNO ₃	None	Ag, Au	0.3
Electrochemical etching	HF, EtOH, H ₂ O	None	None	<5.0

Table 2.
 Various methods for texturing diamond-wire sawn multi-crystalline wafers [20].

texturing process [21]. However, since RIE is a vacuum-based process the throughput is low as compared to a typical inline process and also additional pre-processing and post-processing is required to remove the saw damage and damage due to ion-bombardment, respectively. A variant of the RIE method which does not require vacuum or plasma has been implemented in a commercial tool [22].

One of the approaches for texturing DWS multi-crystalline wafers is to upgrade the existing acidic texturing-based chemistry with additives [23–25]. Such an approach can potentially have a lower CoO compared to the MACE-based approach [23]. Reflectance of such an additive-based approach has been demonstrated to be similar to the conventional isotexturing solution with solar cell efficiency of 18.7% for the Al-BSF-based structure [24].

MACE-based texturing is similar to the conventional acidic etching method with an additional step of catalytic metal deposition. The process flow consists of SDR, catalyst metal deposition, chemical etching and post-treatment. Efficiencies of 19.2% have been obtained for commercial multi Al-BSF cells using batch-type MACE texturing process [26]. Inline-type MACE-based commercial tool has been demonstrated with the possibility to tune the reflectance in the range of 12–23% and obtain average efficiency for Al-BSF and PERC structure of 18.8 and 20.2%, respectively [27]. Representative images of textured surface based on MACE process are shown in **Figure 9**. The cost of ownership (CoO) of the inline MACE process is potentially lower compared to the batch-based MACE process with scope to reduce it further by recycling Ag from the texturing bath [27].

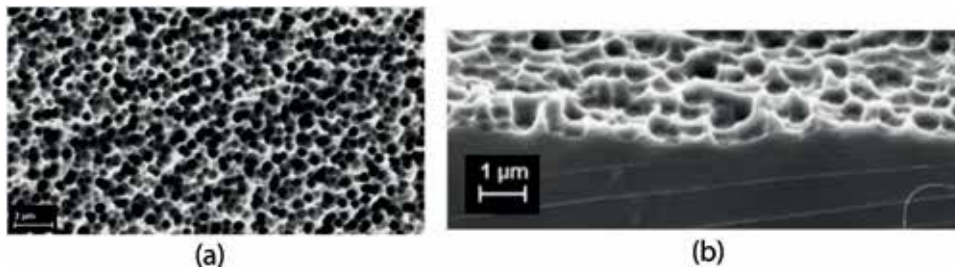


Figure 9. MACE textured DWS multi wafers, (a) surface with $R_{avg} = 12\%$ and (b) surface with $R_{avg} = 22\%$ [27].

4.3 Wet-chemistry-based edge isolation

The emitter region in a solar cell is fabricated by a high temperature diffusion process (to be discussed in sections ahead). During the diffusion process, phosphor silicate glass (PSG) is deposited on the wafer which should be removed before deposition of the ARC layer. As depicted in **Figure 10**, after the diffusion step, the n-type region is also present on the edges and the rear-side of the wafer. The n-type layer on edges and the rear-side will short-circuit the emitter with the base substrate and hence it is important to etch these regions and isolate the emitter on the FS from the base substrate as depicted in **Figure 10(c)**.

The edge isolation process can be performed in an inline manner similar to the texturing process discussed in the previous section. The exception in this case is that the chemical should etch only the rear-side and edges without interacting with the FS. A representative image of the edge isolation process is shown in **Figure 11**. It is important to note that the rollers are present only on the bottom-side to avoid any contact of the etching solution with the front-side. The subsequent steps after the RS etching are similar to those in the inline texturing machine.

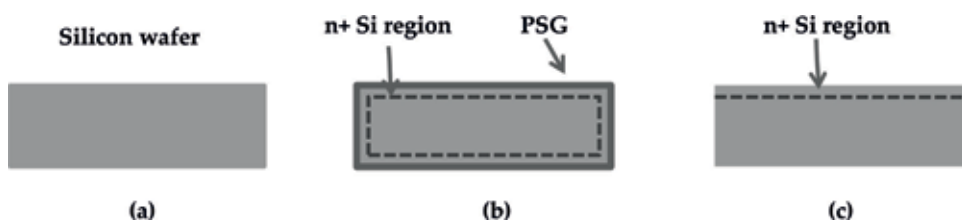


Figure 10. Processing of silicon wafer after diffusion and edge isolation (a) Textured silicon wafer, (b) Diffused silicon wafer, (c) Diffused silicon wafer after edge-isolation.

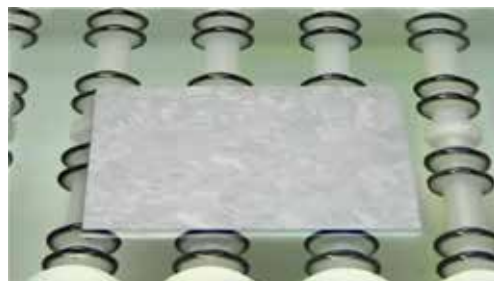


Figure 11. Representative image of solar cell in an inline edge-isolation bath.

5. Thermal processes for solar cell fabrication

High temperature processes form a vital part of solar cell fabrication. Examples of such processes are forming the p-n junction by diffusion, firing of screen-printed contacts, activating surface passivation layers or annealing process induced defects. The section glimpses the basic physics of emitter diffusion process and plasma enhanced chemical vapor deposition (PECVD).

5.1 Emitter diffusion

Emitter diffusion is one of the crucial thermal steps in the industrial solar cell fabrication. The n-type emitter of the crystalline p-type silicon solar cells is formed by phosphorus (P) diffusion. In the diffusion process, the Si wafers are sent in a furnace and exposed at 800–900°C to phosphoryl chloride (POCl_3) and O_2 which results in PSG deposition on the Si wafer surfaces. This step is called as pre-deposition, where the PSG [28] acts as a source of phosphorus (P) dopants to diffuse into the Si wafer. The next step is drive-in, where the supply of dopant gases is disconnected and P from the PSG layer diffuses further into the Si wafer. Hannes et al. [29] illustrates the optimum process feasibility for photovoltaic applications, three different effects have to be considered. Firstly, the in-diffusion of P from the PSG and its presence in electrically active and inactive states in the Si wafer, which increases Shockley-Read-Hall (SRH) recombination. Secondly, the gettering of impurities into the Si layer towards the PSG layer. Finally, the metal contact formation with the P-doped Si emitter draws out the generated power.

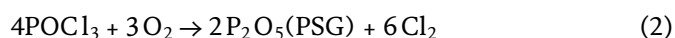
The diffusion process is quantified by sheet resistance which depends on the depth of p-n junction process and P concentration profile. The sheet resistance has units of Ω/cm (commonly measured as Ω/\square) and is measured using a four-point probe system. The definition of sheet resistance is illustrated in Eq. (1).

$$R = \frac{\rho l}{A} = \frac{\rho l}{W * D} = \frac{\rho}{D} = \rho_{sheet} \quad (1)$$

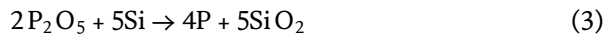
where R = resistance of a rectangular section (Ω); ρ = resistivity ($\Omega \text{ cm}$); l = length of the rectangular section (cm); A = area of the rectangular section (cm^2); W = width of the rectangular section (cm); D = depth of the rectangular section (cm) and ρ_{sheet} = resistance for given depth (D) when $l = W$ (Ω/\square).

The earlier values of emitter sheet resistance were 30–60 Ω/\square with p-n junction depths of >400 nm and high P surface concentration. With improvements in the front-side silver (Ag) contacting paste, the emitter sheet resistance is now in the range of 90–110 Ω/\square with junction depth of around 300 nm and lower P surface concentration. Shifting to larger sheet-resistance allows to capture more light in the UV and blue spectrum, while also reducing the surface recombination to improve the V_{oc} . It should be noted that the diffusion process occurs on the FS (directly exposed to the gases) and also on the edges and RS. If the edge isolation process is not carried out (as discussed in Section 4.3), the emitter will be short-circuited with the substrate.

Figure 12 shows the POCl_3 diffusion process in a closed quartz-tube system. POCl_3 is a liquid source supplied to the process tube by bubbling it with a carrier gas N_2 . By mixing O_2 with the POCl_3 , there will be an epitaxial growth of PSG layer as indicated in Eq. (2) [30].



At the Si surface, $2P_2O_5$ is reduced to elemental phosphorus during the drive-in step as shown in Eq. (3) [30].



Chlorine which is a by-product during the pre-deposition cleans the wafers and quartz-tube by forming complexes with metals. PSG is used as source for driving in the P atoms into Si surface. During the drive-in process, $POCl_3$ is switched off and only O_2 is added to build up a thin oxide layer beneath the PSG to enhance the diffusion of P atoms into Si surface.

Inside the diffusion tube there are five heating zones as illustrated in **Figure 13**. The zones are:

- Loading zone (LZ)—area from where the wafers are loaded into the tube.
- Center loading zone (CLZ)—area between the loading zone and centre zone.
- Center zone (CZ)—center area of the tube.
- Center gas zone (CGZ)—area between the centre zone and gas zone.
- Gas zone (GZ)—area from where the gases move out through the exhaust.

Typically the temperatures of each heating zone are adjusted to obtain equal emitter sheet resistance for all wafers across the boat.

Environment of diffusion process should be very clean and hence quartz material is used for the tubes. Cleanliness of the tubes and loading-area maintenance also affects the process results. Since in gas-phase diffusion there is no residue in the tube, it results in a cleaner process. By half pitch loading in the low pressure (LP) conditions [31], the throughput can be increased. Commonly 1,000 wafers are loaded in a single tube and with five diffusion tubes in a batch-type diffusion system, a throughput of up to 3,800 wafers/h can be achieved for solar cell manufacturing.

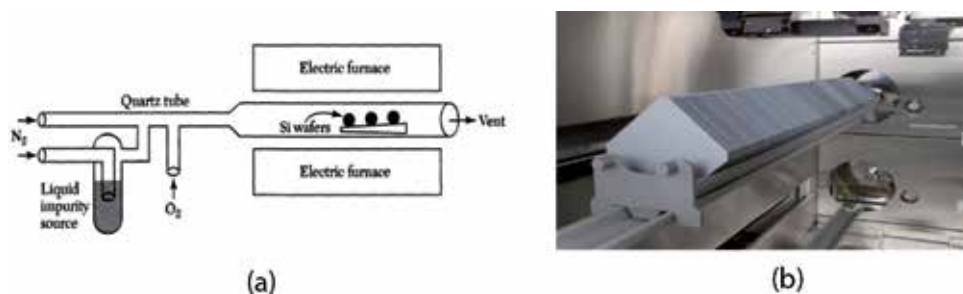


Figure 12. (a) Schematic representation of the batch-type diffusion process and (b) representative image of a batch-type diffusion equipment. Source: centrotherm GmbH.

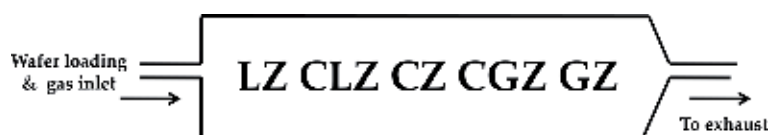


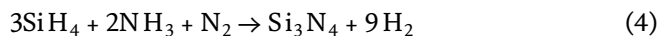
Figure 13. Heating zones inside the diffusion tube.

An inline diffusion system where the wafers are transported on a belt with phosphoric acid as the source of P dopants was also used in commercial production [32]. However, compared to the inline process, the batch process is more clean, effective and efficient. For n-type solar cells or advanced solar cells concepts like PERT, the p-type batch diffusion is based on boron (B) dopant sources like boron tribromide (BBr₃) [33, 34].

5.2 Anti-reflective coating (ARC) deposition

A bare Si surface reflects >30% of the light incident. As discussed in Section 4, the texturing process improves the light-capturing. It is desirable to reduce the reflectance further which is obtained by depositing an ARC layer. TiO_x was one of the earliest material to be used as an ARC layer for solar cells, however since it could not provide adequate surface passivation it was eventually replaced by SiN_x:H [37]. Thermally grown silicon oxide (SiO₂) was also employed as the passivating material in the record breaking passivated emitter rear locally diffused (PERL) cells [37]. High thermal budget and long process time made SiO₂-based passivation unsuitable for mass-production of solar cells [37]. A comprehensive review of various ARC and passivating material for solar cell applications is discussed in [37].

The plasma enhanced chemical vapour deposition (PECVD) process is suitable for depositing an ARC layer of SiN_x:H which not only reduces the reflection but also passivates the front-side n-type emitter and the bulk thus improving the solar cell efficiency [36, 37]. A schematic of a batch-type PECVD system is shown in **Figure 14**. The wafers are loaded in a graphite boat with the front-sides facing each other. An RF plasma based on process gases ammonia (NH₃) and silane (SiH₄) operating at a temperature of 400–450°C deposit the hydrogenated SiN_x:H layer as per Eq. (4) [35]. The hydrogen incorporated in the SiN_x:H film diffuses into the bulk during the firing step (discussed in next section) and passivates the dangling bonds to improve the solar cell performance [36, 37].



The refractive index (RI) of the SiN_x:H film is controlled by the ratio of SiH₄/NH₃ gas, while the thickness depends on the deposition duration. The SiN_x:H-based ARC can minimize the reflection for a single wavelength and the wavelength-thickness is given by [38],

$$t = \frac{\lambda_0}{4n_1} \quad (5)$$

where t = thickness of the SiN_x:H ARC layer, λ_0 = wavelength of incoming light and n_1 = refractive index of the SiN_x:H layer.

Based on the relationship, the ARC is also called as a ‘quarter wavelength ARC’. For solar cells, the RI and thickness are selected to minimize the reflection at a wavelength of 600 nm as it is the peak of the solar spectrum. The thickness and RI of the ARC is selected to be the geometric mean of materials on either side, i.e., glass/air and Si. The typical thickness of the SiN_x:H ARC is 80–85 nm with RI of 2.0–2.1 giving the solar cell a color of blue to violet blue. A representative image of textured multi-crystalline solar cell deposited with SiN_x:H is shown in **Figure 15(a)**, while the variation of SiN_x:H color based on its thickness is shown in **Figure 15(b)**. It is important to note that there is a dependence on the surface texture and ARC color for given deposition parameters. There is a variety of solar modules where the color of the solar cells is darker unlike the typical blue color. A typical ARC

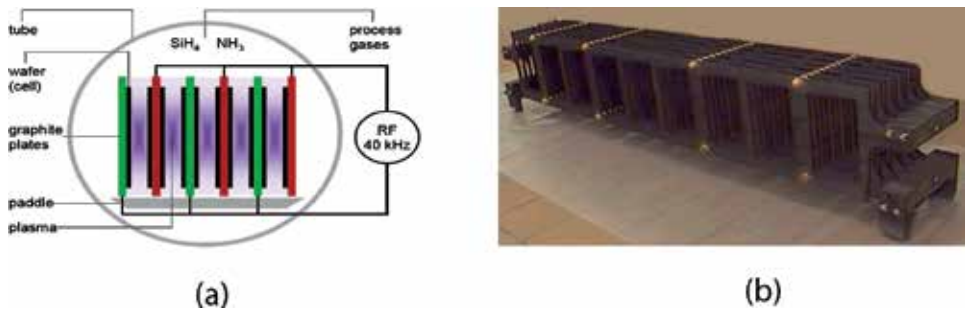


Figure 14. (a) Schematic diagram of batch-type PECVD process for $\text{SiN}_x\text{:H}$ deposition and (b) graphite boat for loading Si wafers in the PECVD furnace.

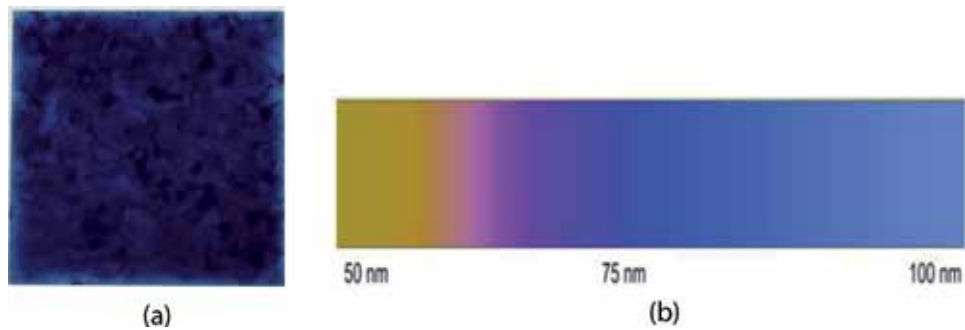


Figure 15. (a) Representative image of $\text{SiN}_x\text{:H}$ coated multi-crystalline solar cell, (b) variation of $\text{SiN}_x\text{:H}$ layer based on its thickness.

deposition stage in a solar cell manufacturing line consists of two PECVD systems, each with four tubes and a throughput of up to 3,500 wafers/h.

$\text{SiN}_x\text{:H}$ is not suitable for passivating p-type Si and hence dielectrics like Al_2O_3 are used for RS passivation for cell architecture like PERC cells [8] or for p-type emitters in n-type solar cells. For PERC solar cells, the Al_2O_3 passivating layer is capped by a $\text{SiN}_x\text{:H}$ to protect it from the Al-paste during the firing process and also serve as an internal reflector for the long wavelength light. Commercial PECVD and atomic layer deposition (ALD)-based systems are available for depositing Al_2O_3 with throughput of up to 4,800 wafers/h [39].

6. Metallization and solar cell characterization

6.1 Screen-printing-based metallization

The last processing step for solar cell fabrication is the FS and RS metallization to draw out the power with minimum resistive losses. Ag is a good contact material for the n-type emitter, while Al makes a very good contact with the p-type substrate. A combination of Ag/Al paste is used to print pads on the RS to facilitate interconnection of solar cells in a module. Screen-printing is a simple, fast and continuously evolving process for solar cell metallization.

A schematic representation of the screen-printing process is shown in **Figure 16**. The screens have an emulsion coated stainless steel mesh with openings as per the desired metallization pattern as illustrated in **Figure 17(a)**.

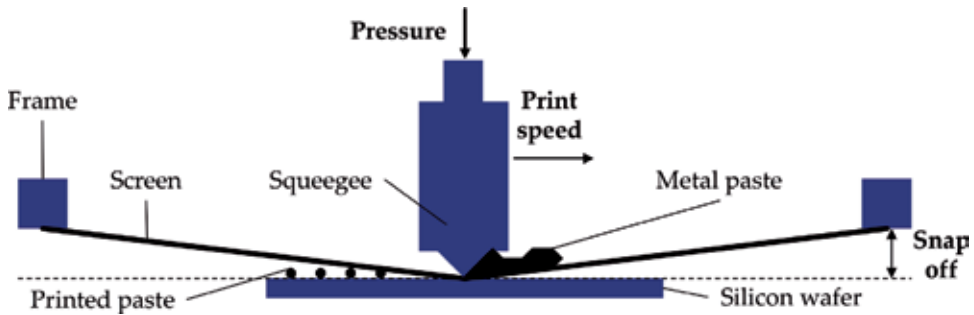


Figure 16.
Illustration of the screen-printing process for solar cell metallization.

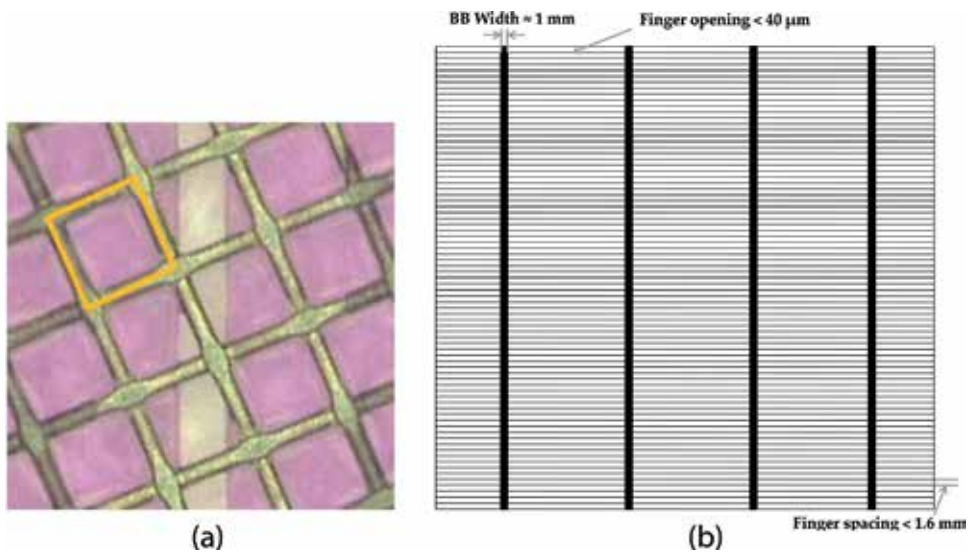


Figure 17.
(a) Mesh-emulsion screen with finger opening for FS Ag printing [40] and (b) representative FS metallization pattern.

The metal paste is spread over the screen via the flood and the squeegee movement that deposits the paste on the solar cell based on the screen-pattern. Snap-off is the distance the screen and the solar cell. The squeegee pressure and the snap-off distance are the critical parameters that determine the paste lay down and geometry of the Ag FS fingers.

Typical paste lay down for Ag/Al RS pads, RS Al and FS Ag are 35–45 mg, 1.1–1.4 g and 100–120 mg, respectively for a 6 inch Al-BSF multi-crystalline solar cell. An illustrative Ag FS metallization pattern is shown in **Figure 17(b)**. The Ag finger opening has reduced to below $30 \mu\text{m}$, while application of 5 bus-bar is being increasingly adopted now. With such screen parameter and good paste lay down, consistent FF of $>80\%$ should be obtained for the Al-BSF solar cells with an optical shading loss of $<6\%$.

6.2 Drying and fast firing of metallization pastes

The metallization pastes consist of metal powder, solvents and organic binders. In case of FS Ag paste, the paste also contains glass-frit while etches the $\text{SiN}_x\text{:H}$ layer and makes contact with the n-type emitter [41]. The metal pastes

are dried after printing and finally they are sent through a fast-firing furnace for sintering and form the RS Al-BSF and FS Ag contact. An example of such a fast-firing furnace with the temperature profile is shown in **Figure 18**. The FS Ag finger sintering process is illustrated in **Figure 19**. When the solar cell passes through the fast-firing furnace, the organic binders are burnt, followed by melting of the glass frit and finally formation of Ag crystallites contacting the n-type emitter. The firing profile needs to be tuned based on the specific types of metallization pastes and emitter diffusion profile. As an example, the firing peak temperature could be low to not form a good ohmic contact on the FS, while a too high temperature can lead to diffusion of Ag through the junction and shunting of the p-n junction. Image of a complete multi-crystalline Al-BSF solar cell is shown in **Figure 20**.

6.3 Plating-based front-side metallization

The costing of various factors in solar cell processing have decreased over the years, while the contribution of front Ag is still the most significant [42]. Significant amount of work has been done to replace Ag by alternate metal like copper (Cu) which has a conductivity value of very close to that of Ag and also offers a potential significant cost advantage [43, 44]. Cu has high diffusivity and solubility in Si and hence a barrier-layer like nickel (Ni) is deposited on Si prior to Cu plating [42]. Light-induced plating (LIP) which is derived from conventional plating utilizes the photovoltaic effect of light to plate the desired metal and has many advantages compared to conventional plating [43, 44].

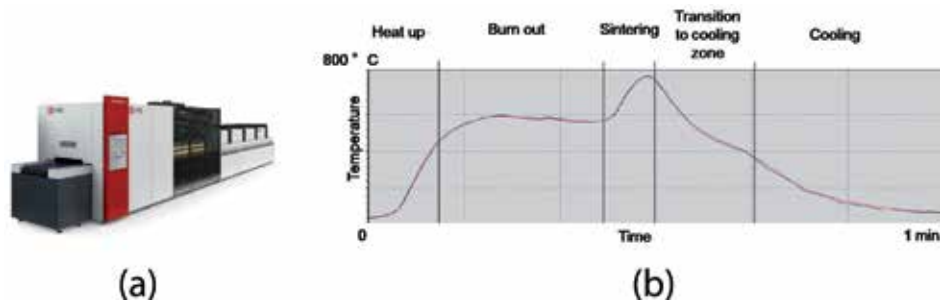


Figure 18. (a) Example of a firing furnace for sintering metal contacts and (b) illustrative temperature profile of a firing furnace. Source: centrotherm GmbH.

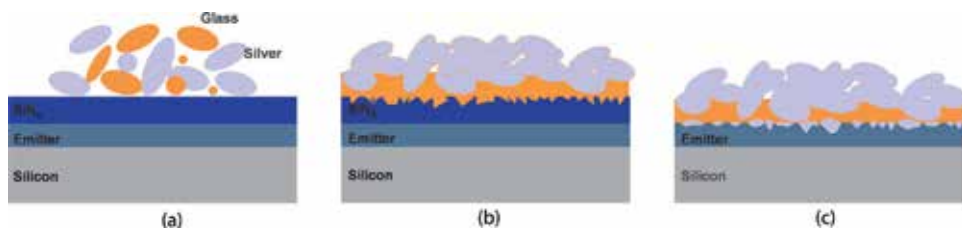


Figure 19. Illustration of the firing process. (a) Burning out of the organic binders, (b) melting of glass frit which etches the $\text{SiN}_x\text{:H}$ and (c) Ag crystallite formation at the emitter interface.

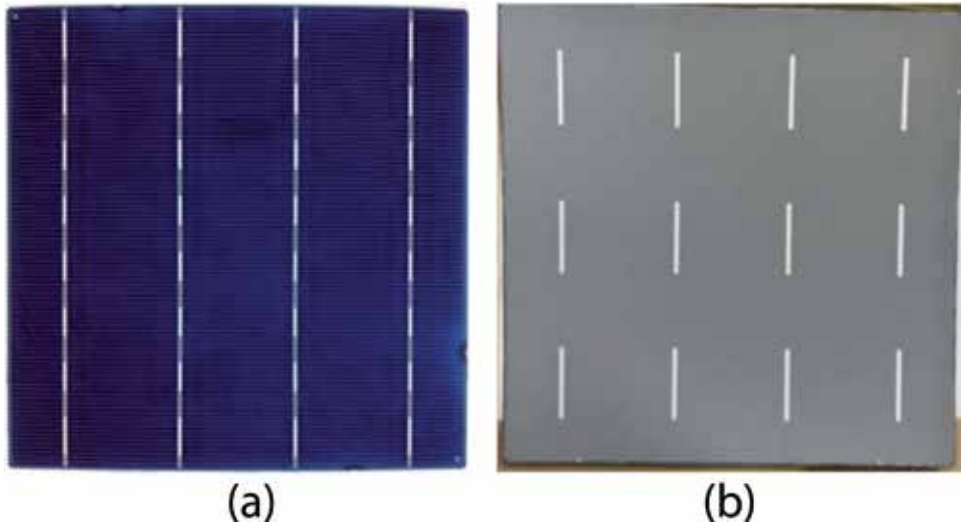


Figure 20.
(a) FS of a complete solar cell and (b) RS of a complete solar cell.

Ni-Cu-based front-side metallization requires an additional front-side ARC patterning step unlike the Ag paste-based metallization and in most cases also an additional Ni sintering step to reduce the contact resistance and have good adhesion of the metal stack [42]. Commercial DWS cut mc-Si solar cells based on Ni-Cu-Ag plated stack have been demonstrated with finger width of 22 μm , aspect-ratio of close to 0.5 and similar efficiency as that of reference screen-printed Ag-based solar cells [45].

Continuous improvement in the Ag FS pastes along with simplicity, reliability and high throughput of the screen-printing process has made it difficult for Ni-Cu-based metallization to compete with Ag-based FS metallization. However, high solar cell efficiency concepts like bifacial heterojunction solar cells, where Cu can be directly plated onto the transparent conducting oxide, the plating process is simplified and requires only a single tool [39]. Similarly, high efficiency concepts which require reduced amount of metal can achieve the same using plating-based metallization [42, 46].

6.4 I-V testing and characterization of solar cells

The final step is I-V testing of the complete solar-cells as per the standard test conditions (STC), i.e., AM 1.5G, 1000 W/m^2 with a Class AAA solar simulator. An example of FS probing of solar cell is shown in **Figure 21**. The typical parameters obtained from the I-V tester are indicated in **Table 3**. I-V testers have many characterization parameters which can be helpful for diagnosis of solar cell defects. Representative electroluminescence (EL) and thermal IR image of a solar cell with some defects are shown in **Figures 22(a)–(c)**. An EL image of a good solar cell with uniform intensity is shown in **Figure 22(a)**, while for a solar cell in which the FS fingers are not printed uniformly, a darker contrast can be seen in **Figure 22(b)**. **Figure 22(c)** shows a thermal IR image of a solar cell with a localized shunt which has been formed during one of the processing steps. In the end, the solar cells are sorted in different efficiency bins based on the selected classification.

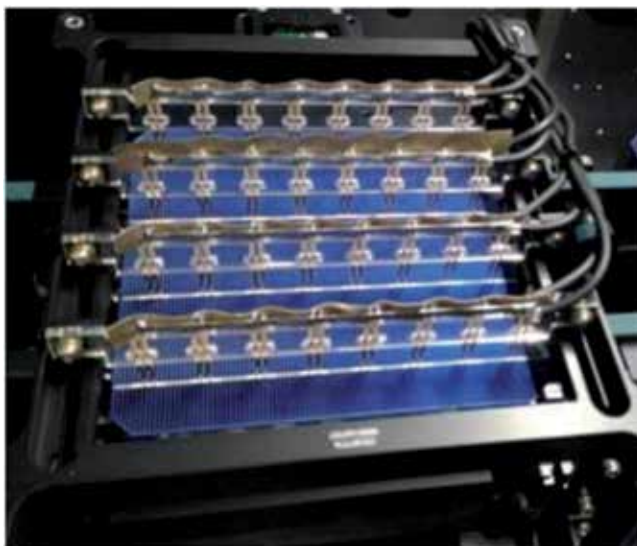


Figure 21.
I-V measurement FS probing for solar cell characterization.

Parameter	Comments
V_{oc} (V)	Good mc-Si Al-BSF solar cells have a value of >0.635 V
I_{sc} (A)	Good mc-Si Al-BSF solar cells have a value of >9.0 A
FF (%)	Good mc-Si Al-BSF solar cells have a value of $>80\%$
Efficiency (%)	Good mc-Si Al-BSF solar cells have a value of $>18.6\%$
V_{mpp} (V)	Corresponding voltage at the maximum power point
I_{mpp} (A)	Corresponding current at the maximum power point
R_s (Ω)	Good mc-Si Al-BSF solar cells have a value of <1.5 m Ω
R_{sh} (Ω)	Good mc-Si Al-BSF solar cells have a value of >100 Ω
I_{rev} (A)	Reverse current at a voltage of -12 V should be <0.5 A for good solar cells
FS BB-BB resistance (Ω)	Resistance measured between the BB's on the FS
RS BB-BB resistance (Ω)	Resistance measured between the BB's on the RS

Table 3.
Parameters for characterization of a solar cell obtained from I-V measurement.

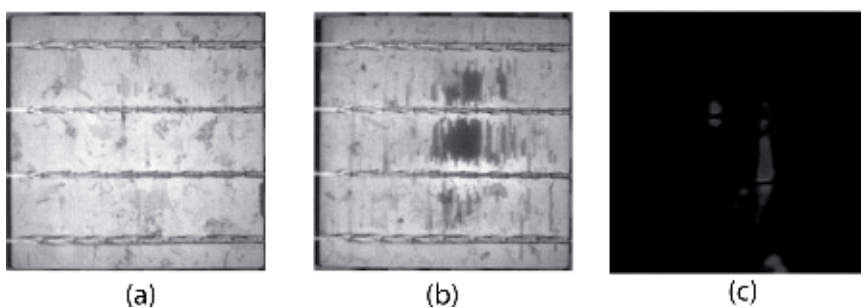


Figure 22.
(a) EL image of a good solar cell, (b) EL image of a solar cell with non-uniformity in Ag finger printing and (c) thermal IR image of a solar cell indicating presence of localized shunts.

7. Future trends

DWS has become the standard for mono-crystalline wafers, while it is expected to have a market share of >80% by 2022 for multi-crystalline wafers [2]. SWS for multi-crystalline wafers is expected to phase-out by that time. With DWS, the kerf loss would also become <80 μm by 2022, which would in turn reduce the poly-Si consumption per wafer below 15 g. 3BB design for front-contacts are expected to phase-out by 2020 with 50% share for 5BB design. With continuous improvements in Ag pastes and screens, the FS finger width is projected to reduce to 30 μm by 2022. Wet-chemical processing tools have crossed throughput of 8,000 wafers/h in 2018 and would touch 9,000 wafers/h by 2020. Thermal processing equipments have reached throughput of 5000 wafers/h in 2018 and expected to cross 7,000 wafers/h by 2020. The metallization and I-V testing/sorting section is expected to have a throughput of >7,000 wafers/h by 2022.

Al-BSF-based cell technology which has a market share of >60% in 2018 is expected to reduce to <20% by 2025. With more emphasis on high efficiency solar cells concepts, share of PERC technology is expected to be >50% by 2022. Production efficiency of Mono PERC is expected to be >22% by 2022, while for multi PERC it should touch 21% by the same time. An important aspect related to multi-PERC is the mitigation of LeTID-based problem to minimize the loss of efficiency after installations of the modules in the field. Si HJ cells with efficiencies of >22% in 2018 after expected to reach stable efficiency of 23% by 2020, with a market share of around 10% by 2022. High efficiency bifacial cells with an additional advantage of tapping the solar radiation from the rear-side is expected to have a market share of 20% by 2022. N-type back contact solar cells are expected to cross 24% efficiency by 2020.

8. Conclusions

Si solar cells have become an important part of the renewable energy domain over past decades with matured manufacturing technologies. P-type multi-crystalline wafers have become the main-stay for solar cell production. However, with higher efficiency and decreasing production costs, mono-crystalline solar cells have also gained a significant share and are expected to compete closely with multi-crystalline wafers in the near future. For standard Al-BSF technology, 19 and 20% has become the bench-mark for multi-crystalline and mono-crystalline solar cells, respectively. Mono-PERC and multi-PERC cells have reached stabilized efficiencies of 21.5 and 20%, respectively. In addition, PERC also provides a simpler approach for bifacial solar cells by having a grid pattern on the RS instead of the full area contact. High efficiency n-type and bifacial solar cells have a market-share of <10% which is expected to increase in the future. The manufacturing technologies have matured considerably over the past few years with further improvements to increase the throughput.

Acknowledgements


The authors would like to thank the colleagues from RCT Solutions GmbH from whom some of the contents for the chapter have been taken. Mehul C. Raval would like to thank colleague Jim Zhou for the discussions regarding black silicon texturing.

Author details

Mehul C. Raval* and Sukumar Madugula Reddy
RCT Solutions GmbH, Konstanz, Germany

*Address all correspondence to: mehul.c.raval@iitb.ac.in

IntechOpen

© 2019 The Author(s). Licensee IntechOpen. This chapter is distributed under the terms of the Creative Commons Attribution License (<http://creativecommons.org/licenses/by/3.0>), which permits unrestricted use, distribution, and reproduction in any medium, provided the original work is properly cited. 

References

- [1] Renewables 2018 Global Status Report. REN21. 2018
- [2] International Technology Roadmap for Photovoltaic (2017) including maturity report 2018. 9th ed. 2018
- [3] Wenham SR, Green MA. Silicon solar cells. *Progress in Photovoltaics: Research and Applications*. 1996;**4**: 3-33. DOI: 10.1002/(SICI)1099-159X(199601/02)4:1%3C3::AID-PIP117%3E3.0.CO;2-S
- [4] PVEDUCATION.ORG. Available from: <https://www.pveducation.org/pvcdrom/manufacturing/refining-silicon> [Accessed: 10 December 2018]
- [5] PVEDUCATION.ORG. 2018. Available from: <https://www.pveducation.org/pvcdrom/manufacturing/single-crystalline-silicon> [Accessed: 10 December 2018]
- [6] PVEDUCATION.ORG. 2018. Available from: <https://www.pveducation.org/pvcdrom/manufacturing-si-cells/czochralski-silicon> [Accessed: 10 December 2018]
- [7] Kim JM, Kim YK. Growth and characterization of 240 kg multicrystalline silicon ingot by directional solidification. *Solar Energy Materials and Solar Cells*. 2004;**81**: 217-224. DOI: 10.1016/j.solmat.2003.11.020
- [8] Huang H, Lv J, Bao Y, Xuan R, Sun S, Sneck S, et al. 20.8% industrial PERC solar cell: ALD Al₂O₃ rear surface passivation, efficiency loss mechanisms analysis and roadmap to 24%. *Solar Energy Materials and Solar Cells*. 2017;**161**:14-30. DOI: 10.1016/j.solmat.2016.11.018
- [9] Panasonic. Available from: <https://www.panasonic.com/global/corporate/technology-design/technology/hit.html> [Accessed: 16 December 2018]
- [10] Sun Power Corporation. Available from: <https://us.sunpower.com/why-sunpower/maxeon-solar-cells/> [Accessed: 16 December 2018]
- [11] Lossen J, Buchholz F, Comparotto C, Eisert S, Libal J, Mihailetchi VD, et al. From lab to fab: Bifacial n-type cells entering industrial production. In: *Proceedings of 31st EU PVSEC*; Hamburg. 2015. pp. 965-968
- [12] Chen G, Kashkoush I, Nemeth D, Rieker J, Danel A. Development of IPA-free texturing processes in advanced solar cell fabrication. In: *Proceedings of 29th EU PVSEC*; Amsterdam. 2014. pp. 1096-1099
- [13] Strinitz F, Schoerg F, Fuerst M, El Jaouhari A, Kuehnlein H. Fast alkaline texturing process for high throughput PERC solar cell manufacturing. In: *Proceedings of 33rd EU PVSEC*; Brussels. 2017. pp. 955-959
- [14] Moynihan M, O'Connor C, Barr B, Tiffany S, Braun W, Allardyce G, et al. IPA free texturing of mono-crystalline solar cells. In: *Proceedings of 25th EU PVSEC*; Valencia. 2010. pp. 1332-1336
- [15] Wefringhaus E, Helfricht A. KOH/surfactant as an alternative to KOH/IPA for texturisation of monocrystalline silicon. In: *Proceedings of 24th EUPVSEC*; Hamburg. 2009. pp. 1860-1862
- [16] George M, Bohling D, Treichel H, Goldstein A, Kern W, Potter BG Jr. Investigation of biodegradable texturing chemistries for crystalline Si. In: *Proceedings of 27th EU PVSEC*; Frankfurt. 2012. pp. 1105-1108
- [17] Hauser A, Melnyk I, Wefringhaus E, Delahaye F, Vilsmeier G, Fath P. Acidic texturisation of MC-SI using a high throughput in-line prototype system with no organic chemistry. In:

Proceedings of 19th EU PVSEC; Paris. 2004. pp. 1094-1097

[18] Hauser A, Melnyk I, Fath P, Narayanan S, Roberts S, Bruton TM. A simplified process for isotropic texturing of MC-Si. In: Proceedings of WCPEC-3; Osaka. 2003. pp. 1447-1450

[19] Cao F, Chen K, Zhang J, Ye X, Li J, Zou S, et al. Next-generation multi-crystalline silicon solar cells: Diamond-wire sawing, nano-texture and high efficiency. *Solar Energy Materials & Solar Cells*. 2015;**141**:132-138. DOI: 10.1016/j.solmat.2015.05.030

[20] Hsu C-H, Wu J-R, Lu Y-T, Flood DJ, Barron AR, Chen L-C. Fabrication and characteristics of black silicon for solar cell applications: An overview. *Materials Science in Semiconductor Processing*. 2014;**25**:2-17. DOI: 10.1016/j.mssp.2014.02.005

[21] Ye Q, Wang W, Dong J, Wei W, Yang Y, Cai W, et al. Industrially feasible PERC cells on diamond wire sawing multi-crystalline silicon wafers textured by RIE towards 21.62% efficiency. In: Proceedings of 35th EU PVSEC; Brussels; 2018. pp. 401-405

[22] Nines Photovoltaics. 2018. Available from: <http://nines-pv.com/ade-technology/> [Accessed: 03 December 2019]

[23] Richter M, Straub B, Plettig M, Pedititakis A, Sander B, Queisser S, et al. Metal-free inline texturing for effective light trapping on DW mc-Si. In: Proceedings of 11th SNEC. Shanghai; 2017

[24] Schmitt C, Zhou B, Straub B, Burgenmeister B, Pedititakis A, Sander B-U, et al. Metal-free texturing for diamond-wire-sawn multi-crystalline silicon (DWS-mc). In: Proceedings of 35th EU PVSEC; Brussels. 2018

[25] Black Silicon 4th Generation-Nanjing Nascien New Material Co.,

Ltd. In: Proceedings of 3rd Black Silicon Forum; 2018

[26] Status and application of black silicon technology-Canadian Solar Inc. In: Proceedings of 3rd Black Silicon Forum; 2018

[27] Jooss W, Melnyk I, Jung-König J, Teppe A, Werling T, Voigt O, et al. Development and optimization of a novel inline black silicon texturing process for increased solar cell performance. In: Proceedings of 33rd EU PVSEC; Amsterdam. 2017. pp. 368-372

[28] Wolf SWA, Kimmerle A. Status and perspective of emitter formation by POCl₃-diffusion. In: Proceedings of 31st EU PVSEC; Munich. 2015. pp. 414-419

[29] Wagner H, Dastgheib-Shirazi A, Min B, Morishige AE, Steyer M, Hahn G, et al. Optimizing phosphorus diffusion for photovoltaic applications: Peak doping, inactive phosphorus, gettering, and contact formation. *Journal of Applied Physics*. 2016;**119**:185704. DOI: 10.1063/1.4949326

[30] Air Products and Chemical, Inc. Process guidelines for using phosphorous oxychloride as an N-type silicon dopant. 2016

[31] Dastgheib-Shirazi A, Steyer M, Micard G, Wagner H, Altermatt PP, Hahn G. Relationships between diffusion parameters and phosphorus precipitation during the POCl₃ diffusion process. *Energy Proedia*. 2013;**38**:254-262. DOI: 10.1016/j.egypro.2013.07.275

[32] Voyer C, Buettner T, Bock R, Biro D, Preu R. Microscopic homogeneity of emitters formed on textured silicon using in-line diffusion and phosphoric acid as the dopant source. *Solar Energy Materials & Solar Cells*. 2009;**93**:932-935. DOI: 10.1016/j.solmat.2008.11.061

- [33] Mihailetchi VD, Coletti G, Komatsu Y, Geerligs LJ, Kvande R, Arnberg L, et al. Large area and screen printed N-type silicon solar cells with efficiency exceeding 18%. In: Proceedings of 23rd EU PVSEC; Valencia. 2008. pp. 1036-1039
- [34] Richter A, Horteis M, Benick J, Henneck S, Hemle M, Glunz SW. Towards industrially feasible high-efficiency n-type Si solar cells with boron diffused front side emitter-combining firing stable Al₂O₃ passivation and fine line printing. In: Proceedings of 35th PVSC; Honolulu, Hawaii. 2010
- [35] PVEDUCATION.ORG. 2019. Available from: <https://www.pveducation.org/pvcdrom/manufacturing-si-cells/anti-reflection-coatings>
- [36] Bonilla RS, Hoex B, Hamer P, Wilshaw PR. Dielectric surface passivation for silicon solar cells: A review. *Physica Status Solidi A: Applications and Materials Science*. 2017;214(7):1700293. DOI: 10.1002/pssa.201700293
- [37] Soppe W, Rieffe H, Weeber A. Bulk and surface passivation of silicon solar cells accomplished by silicon nitride deposited on industrial scale by microwave PECVD. *Progress in Photovoltaics: Research and Applications*. 2005;13:551-569. DOI: 10.1002/pip.611
- [38] PVEDUCATION.ORG. 2019. Available from: <https://www.pveducation.org/pvcdrom/design-of-silicon-cells/anti-reflection-coatings> [Accessed: 29 January 2019]
- [39] Chunduri SK, Schmela M. PERC solar cell technology report. *Taiyang news*. 2017
- [40] Zhang Y, Zhang L, Jiang L, Song L, Guo C, Dua V, et al. Knotless screen printing for crystalline silicon solar cells. In: Proceedings of 7th Workshop on Metallization; Konstanz. 2017
- [41] Lin C-H, Tsai S-Y, Hsu S-P, Hsieh M-H. Investigation of Ag-bulk/glassy-phase/Si heterostructures of printed Ag contacts on crystalline Si solar cells. *Solar Energy Materials & Solar Cells*. 2008;92:1011-1015. DOI: 10.1016/j.solmat.2008.02.032
- [42] Lennon A, Flynn S, Young T, Nampalli N, Edwards M, Evans R, et al. Addressing perceived barriers to the adoption of plated metallisation for silicon photovoltaic manufacturing. In: Proceedings of 52nd Annual Conference of the Australian Solar Council; Melbourne. 2014
- [43] Raval MC, Solanki CS. Review of Ni-Cu based front side metallization for c-Si solar cells. *Journal of Solar Energy*. 2013;2013:Article ID 183812. DOI: 10.1155/2013/183812
- [44] Lennon A, Yao Y, Wenham S. Evolution of metal plating for silicon solar cell metallisation. *Progress in Photovoltaics: Research and Applications*. 2013;21:1454-1468. DOI: 10.1002/pip.2221
- [45] Fox S, Jie X, Wu H, Burschik J, Bay N, Crouse K, et al. Pilot production of high efficient metal catalyzed textured diamond wire sawn mc-Si solar cells combined with nickel-copper plated front contact processing. In: Proceedings of 33rd EU PVSEC; Amsterdam. 2017. pp. 362-367
- [46] Cornagliotti E, Russell R, Tous L, Uruena A, Duerinckx F, Aleman M, et al. Bifacial n-PERT cells (Bi-PERT) with plated contacts for multi-wire interconnection. In: Proceedings of 32nd EU PVSEC; Munich. 2016. pp. 420-425

Review on Metallization in Crystalline Silicon Solar Cells

Nagarajan Balaji, Mehul C. Raval and S. Saravanan

Abstract

Solar cell market is led by silicon photovoltaics and holds around 92% of the total market. Silicon solar cell fabrication process involves several critical steps which affects cell efficiency to large extent. This includes surface texturization, diffusion, antireflective coatings, and contact metallization. Among the critical processes, metallization is more significant. By optimizing contact metallization, electrical and optical losses of the solar cells can be reduced or controlled. Conventional and advanced silicon solar cell processes are discussed briefly. Subsequently, different metallization technologies used for front contacts in conventional silicon solar cells such as screen printing and nickel/copper plating are reviewed in detail. Rear metallization is important to improve efficiency in passivated emitter rear contact cells and interdigitated back contact cells. Current models on local Al contact formation in passivated emitter rear contact (PERC) cells are reviewed, and the influence of process parameters on the formation of local Al contacts is discussed. Also, the contact mechanism and the influence of metal contacts in interdigitated back contact (IBC) cells are reviewed briefly. The research highlights on metallization of conventional screen printed solar cells are compared with PERC and IBC cells.

Keywords: silicon solar cells, process flows, metallization, passivated emitter rear contact cells, interdigitated back contact cells

1. Introduction

The photovoltaic industry plays a critical part in the global energy scenario [1] to compete with the other renewable and conventional energy sources. Crystalline silicon (c-Si) wafer-based technologies [2, 3] dominate the photovoltaic market for terrestrial application due to its high efficiency, stability, and benefits arising out of microelectronic industry. Due to high production cost (i.e., high \$/watt), researchers are continuously putting their efforts to improve low cost Si solar cell technology. Silicon solar cell fabrication process involves various vital steps [4, 5] which includes texturing [6], n+ and p+ diffusion [7, 8], antireflection coatings [9], and contact metallization [7–15]. Electrical parameters of the solar cell, namely open circuit voltage (V_{oc}), short circuit current (I_{sc}), and fill factor (FF) vary with processing conditions. Though the conventional Si processing technology is mature, it is important to modify fabrication process and device structure to improve electrical performance. Approaches such as nickel/copper metallization in conventional solar cell structure [16–18], passivated emitter rear contact (PERC) cells [19] and interdigitated back contacts (IBC) cells [20], etc. are being used in lab scale and production. In this chapter, contact mechanism in conventional structure and novel structures is reviewed.

2. Process flow and current status

Conventional silicon solar cell process and its current status in PV industry are discussed in detail. Subsequently, the process steps of advanced process techniques such as Ni/Cu plating-based silicon solar cell, PERC, and IBC are also discussed.

2.1 Conventional Si solar cell

Currently, most of the PV industries use boron-doped p-type wafers as the starting material for c-Si solar cell fabrication. The schematic diagram of conventional fabrication process is shown in **Figure 1**. As reported in [2, 21], every processing step contributes to losses in conventional screen printing solar cell. Screen printing metallization is cost-competitive and robust technology used in production. Screen printing technology has attracted considerable attention due to significant improvement in printing medium and simplicity of the process. Also, this technology increases the throughput and decreases the production cost. For metallization, several alternatives to screen printing are available to improve cell efficiency [22, 23]. However, the existing screen printing technology is the matured and cost effective technology [24, 25] compared to recently developed technologies such as PERC, IBC, and HIT. Hence, around 85% of Si solar cells are manufactured using screen printing of thick film pastes. In a typical solar cell process, screen printing has the potential to improve efficiency and lower the cost, since metallization pastes are continuously evolving and new generation of pastes are available.

In addition to the new generation pastes, the right choice of front grid design and screen pattern results in better efficiency with reduced cost. The new generation paste provided a better aspect ratio (the ratio of line height to line width). The improvement in the aspect ratio improves the current carrying capacity of the contacts, as the shadow loss is decreased as well as the series resistance also decreases. In addition to the paste rheology, enhancement of the aspect ratio relies on choosing the right screen parameters such as mesh count, wire dimension, and emulsion thickness. Along with the paste material, optimized screen parameters are also the important factors for making the front contact with high aspect ratio and reduced shadow loss, which are desired for getting high efficiency solar cells. The silicon solar cell researchers or industries have achieved a maximum efficiency of 19% on multicrystalline silicon and around 20% on mono crystalline silicon-based solar cells by using the conventional process as shown in **Figure 1** and are still working to enhance the efficiency using advanced materials.

Screen printing-based metallization technology occupies the significant role in solar cell manufacturing due to high throughput in cell production with better efficiencies. Though it is a mature technology, the finger aspects of the cells were limited by screen specifications and paste rheology.

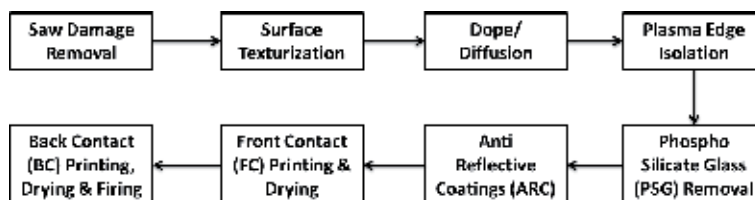


Figure 1.
Si solar cell process flow.

2.2 Ni/Cu metallization-based solar cell

The limitations of screen printing and chance of considering alternate materials for front contact led many researchers [26] to look for the Ni/Cu metallization-based cell process. It is observed that it is important to optimize the Ni/Cu metallization to compete with screen printing technology in terms of reliability, cost competitiveness, and high throughput production. Ni plating on solar cells started in 1959, and the process has been developed in subsequent years and came into the present process flow in early 1980s. Interdigitated back contact solar cells by Sun Power Corporation integrated metallization scheme of patterned Al followed by plated Ni—Cu—Ag which was further annealed to realize the contact [27] and its world record efficiency is 24% [28].

Table 1 shows the cost and properties comparison of copper (Cu), silver (Ag), and nickel (Ni). It can be seen that the resistivity of copper is only more by 3.7% as compared to Ag, while the cost being less by around a 100 times, which process to be an important factor for cost reduction. Moreover, Cu is widely used as interconnects in ultra-large-scale integrated circuits owing to its low resistivity and good resistance to electro migration and has a proven track record in the microelectronics industry. Hence, Cu is a possible choice for metallization of solar cells. The main drawback of Cu is its high mobility and being a highly reactive recombination center in silicon. This necessitates a diffusion barrier like Ni to prevent its diffusion in Si. The nickel silicide formed at the interface reduces the contact resistance, which will ensure minimum power loss due to series resistance (R_s) in a solar cell. Many groups have demonstrated cells based on Ni—Cu front side metallization with improved fill factor (FF) and higher efficiency (η) compared to Ag-based cells. The laser grooved buried contact (LGBC) technology utilizes Ni-Cu-based front-side metallization and has been successfully commercialized by BP Solar. The process flow of silicon solar cells with Ni/Cu front contact is shown in **Figure 2**.

One of the crucial steps in Ni/Cu metallization is opening of ARC to make selective contact with an emitter. Literatures reported for patterning ARC and subsequent metal deposition to make the front contact; however, it is important to choose the process which can compete with screen printing technology both in cost and performance. It has been found that one such a technique is Ni/Cu metallization which can be commercialized with few additional process steps. But in Ni/Cu metallization, it is

Parameters	Ag	Cu	Ni
Conductivity (10^6 S/m)	61.4	59.1	13.9
Density (gm/cm ³)	10.5	8.9	8.9
Typical cost (\$/kg)	431.0	4.5	14.2

Table 1.
 Cost and properties comparison of copper (Cu), silver (Ag), and nickel (Ni).

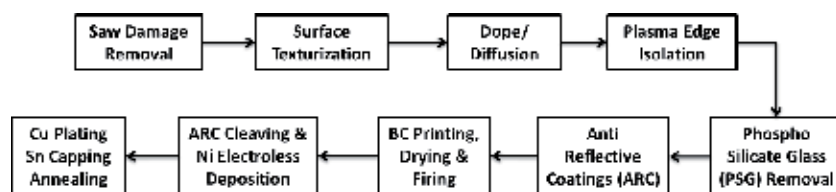


Figure 2.
 Ni-Cu process flow.

Result type	Process difference	Substrate type	VOC (mV)	JSC (mA/cm ²)	FF (%)	η (%)
Best	Before LIP	mc-Si	612.1	34.6	74.9	15.9
Best	After LIP	mc-Si	613.4	34.1	79.2	16.6
Average	Before LIP	mc-Si	610.0 \pm 2	34.5 \pm 0.1	74.3 \pm 0.6	15.6 \pm 0.2
Average	After LIP	mc-Si	611.0 \pm 2	34.1 \pm 0.1	77.9 \pm 0.9	16.3 \pm 0.2
Best	Ni—Ni—Cu—Sn	Cz	619.0	35.7	72.7	16.4
Best	Ni—Cu—Sn	Cz	624.0	35.4	69.5	15.4
Best	Ni—Cu—Sn	Cz	623.0	37.3	74.2	17.2
Best	Background plating present	Cz	639.0	38.7	74.2	18.3
Best	No background plating	Cz	634.3	38.7	78.3	19.2
Best	—	Cz	638.3 \pm 2	38.4 \pm 0.7	78.8 \pm 0.5	19.3 \pm 0.4

Table 2.

Solar cell performance data for front contacts with electroplated metal layer(s).

important to standardize and optimize few critical parameters such as Ni thickness, annealing temperature for silicide formation, and Ni/Cu deposition parameters. The 80- μ m thick stencil printed grid lines were thickened by electroplating of Ni—Cu—Sn stack with a commercial plating tool, improving the efficiency of the solar cells by 0.4% abs [29]. The platform had single side wafer processing and hence no chemical attack on the back side Al. Complete solar cell metallization based on electrochemical deposition of Ni and Cu has also been demonstrated [30]. Pulsed plating was used as compared to direct plating in the work to ensure homogeneous and well adhered contacts. LIP-based thickening of screen-printed contacts was first reported by Mette et al. [31]. An absolute η gain of 0.4% was obtained for large area cells based on standard production process, while an improvement of more than 1% absolute was possible for fine line 70- μ m printed contacts. For an optimized grid design, an absolute η gain of 0.7% was achieved for large area cells as shown in **Table 2**. With an optimized SiN_x:H, η of 19.2% has been demonstrated on industrial grade Si with Ni and Cu layers deposited by LIP on LDSE cells [32]. pFF nearing 80% were possible with Ni—Cu—Sn-based contacts deposited by LIP, with no observable degradation in the pFF after a stress test at 200°C for 1000 hours.

After plating the conducting Cu layer, an Ag or Sn capping layer is deposited to protect the Cu conducting lines from oxidation and facilitate soldering of the interconnection tabs. Another important function of the capping layer is to prevent interaction of Cu with the EVA encapsulant. An impulse voltage test failure indicated by development of discharge sites was observed due to the presence of Cu particles at the Al/EVA interface on the back side [33]. Though the Ni—Cu contact-based LGBC cells were commercialized, low throughput rates and increased processing costs led to screen printed contacts becoming the standard for solar cell metallization [34]. Other major concern is regarding the chemical waste due to the metal baths which can lead to serious environment contamination issues [35]. Steady research and advances in plating techniques have enabled transition of solar cell with Ni—Cu-based metallization from labs to commercial scale production. Economic factors play vital role when considering an alternative technology with the introduction of new equipment in the fabrication line. As per the ITRPV roadmap, direct plating and plating on the seed layer are expected to have a share of around 15% in 2028 for the front-side metallization [36].

The Pluto series from Suntech Power is based on Ni—Cu metallization with stabilized efficiencies of 19.0% on large area mono-Si solar cells. There was an improvement of over 6% as compared to the screen printed contacts due to reduced shading and improvement in V_{OC} . IMEC has demonstrated conversion efficiencies of 20.3% on large area i-PERC cells with plated contacts. Using a PERC structure, Schott Solar along with Schmid Group demonstrated 20.9% efficient 6" cells. Schott Solar has also demonstrated a median η of 20.8% with a best η of 21.3% on an industrial production line with electroplated contacts. Rena has recently demonstrated solar cells based on PERC technology reaching 20.8% with Ni—Cu metallization. Modules made with these cells successfully passed IEC 61215 test three times and adhesion of >1 N/mm. The technology can lead to a reduction in the cell production cost by \$ 0.06.

Ni—Cu metallization yields the better efficiency compared to the conventional screen printing solar cells; however, due to the low throughput rates and increased processing costs, standard solar cell metallization dominates the PV industry. Also the chemical wastes of the metal baths in Ni—Cu metallization lead to environment disputes.

2.3 Passivated emitter rear contact solar cell

The conventional screen-printed Al-BSF cells suffer from the optical losses (front reflectance), transmission losses, and the recombination (rear side). The major limitation arises from the rear surface recombination which is due to the low solubility of Al in Si (doping concentration $7 \times 10^{18} \text{ cm}^{-3}$) during the very short firing process employed for alloying of screen printed Al paste. Though the boron co-doping with Al-BSF improves the doping concentration of Al-BSF [37, 38] owing to the higher solubility of boron, only 65% of the internally reflected longer wavelength light reaches the rear side, and hence the rear surface recombination is still being high [39]. One way to overcome the drawback of Al-BSF is the introduction of a dielectric rear side passivation with local contact points, which improves the optical properties with less surface recombination. One such cell architecture is the passivated emitter and rear cell [40]. With this structure, low rear surface recombination velocity of $60\text{--}200 \text{ cm}^{-1}$ and internal reflectance over 95% have been realized so far. The dielectric passivation layer is locally opened for contact formation [40–47] by laser [48–50] or by printing etching pastes [51]. About 1% of the total rear surface is covered by the local point contacts. The local point contact is realized by photolithography in the laboratory level, and in mass production, the contacts are formed either by screen printed Al [38, 46, 47, 51–60] or by physical vapor deposition (PVD) of Al [40, 47]. The process flow for the PERC cell is shown in **Figure 3**. The key challenge in the local aluminum contact formation is that the Al should not be penetrated into the dielectric passivation layer [45]. The local Al-BSFs produced during the alloying process create voids below the Al contacts. These voids result in incomplete BSF formation and hence the rear surface recombination and contact resistances

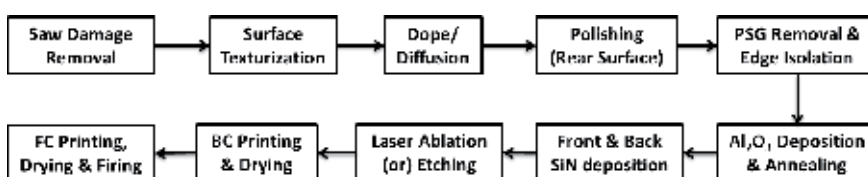


Figure 3.
PERC process flow.

are increased [38, 46, 47, 51–60]. An effective local Al-BSF is formed [61, 62] in the laser-fired contact process [63]. In this process, the deposition of the passivation layer followed by rear metallization (screen printed or evaporated contact) is carried out and finally with laser local contacts were formed. As a novel route, the rear Al electrode is formed by using commercial Al foil, thus complicated equipment such as evaporation or screen printing systems are avoided [64].

The best commercial PERC cell with 20–21% (mc-Si) and 21–22% (mono c-Si) has been achieved in the commercial scale [36]. A detailed investigation on the various factors involved in the formation of local Al contact formation and the influences of process steps have been studied by various authors and are described in the following sections. Meemongkolkiat et al. [52] observed that voids are created beneath the local Al contacts during the alloying process. Rauer et al. [38] avoided these voids by adding Si powder to the Al paste. The various factors that influence the contact formation are: (a) dielectric opening method, (b) rear-side contact geometry, (c) the amount of Al in the metallization paste, and (d) firing process.

2.3.1 Influence of process parameters on local-BSF formation

To form a high-quality localized contact, a deep Al-BSF is required for Al—Si contact interface to minimize the rear surface combination along with shunt free rear surface passivation. Urrejola [58] reported a shallow BSF or the presence of Kirkendall voids at the Al—Si interface as shown in **Figure 4**. **Figure 4(a)** shows the uniform BSF with a thickness of (4 μm). Void formation is due to sub-optimal conditions (**Figure 4(b)**) or inadequate BSF depth (**Figure 4(c and d)**). These voids reduce the FF as well as act as high recombination centers which affects J_{sc} and V_{oc} . Though the electrical contact is not affected with inadequate BSF depth, a very high contact recombination is expected. To minimize R_s with low contact resistivity, a very narrow local opening is required, hence high recombination beneath the metal contact is reduced. Urejola [56] obtained a lowest contact resistivity of 8 $\text{m}\Omega \text{cm}^2$ for a shallow dielectric opening which lead to the FF loss minimization. However, narrow Al—Si alloy formation increases the dielectric passivated area under the contact, thus reducing J_{sc} and V_{oc} . The influence of contact size and finger spacing was investigated by Urejola [58]. The decrease in contact spacing reduced the overlap of Al on each side of the local opening leading to high quality BSF, thus lowering the presence of voids. For a contact spacing of 100 μm , the BSF thickness around 6–7 μm with less void (8%) was obtained. Similarly, Rauer et al. [38] concluded that the thickness of the local BSF depends on the contact spacing and obtained a BSF thickness up to 4 μm for a contact spacing of 400 μm . Further to increase the local BSF thickness and to avoid the void formation, the authors added more Si powder to the Al paste. This prevents the contact penetration into the Si bulk with enhanced Al-BSF thickness. Moreover, this increase in Si powder diminishes the emitter saturation current density (J_{0e}).

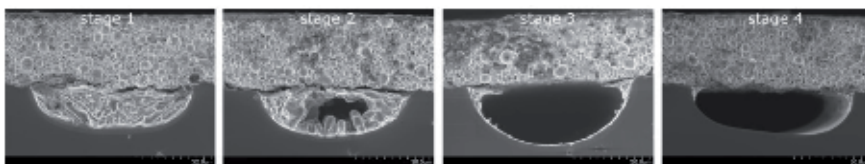


Figure 4. The Al-Si interface showing (a) a well formed contact with deep BSF and no void formation, (b) a Kirkendall void, and (c) & (d) contact with shallow BSF [58].

2.3.2 Impact of dielectric opening method

A detailed investigation on the influence of formation of BSF using industrially screen printable local BSF Al paste and laser processing for removing the dielectric barrier was carried by Fang et al. and Bahr et al. [51, 53]. The laser ablation was carried out using nanosecond [wavelength (λ) = 1064 nm, pulse duration = 300ns, and pulse energy = <1.6 mJ] and femtosecond [wavelength (λ) = 1025 nm, pulse duration = 300fs and pulse energy = <36 μ J] laser. The ns laser has a strong influence on the local removing of the dielectric stack $\text{AlO}_x/\text{SiN}_x\text{:H}$, whereas fs showed a moderate influence. The strong and moderate influence is attributed to the interaction time between the laser pulse and the silicon substrate. With ns laser, few ten micrometer etching depth is achieved depending on the laser power, whereas in fs laser with very short interaction, few-micrometer depth is obtained. With screen printable local BSF Al etching paste, the passivation stack with 105 nm thick is etched off. After firing in an IR furnace with optimum belt speed, the local BSF formed with etching paste was more thicker (around 5 μm) and homogeneous with less voids. In the case of ns and fs, laser showed more voids with inhomogeneous thinner BSF (1–2 μm) due to the increased surface roughness.

2.3.3 Impact of contact resistivity

In recent days, the aluminum pastes are improved in such a way that even for thin laser contact opening (LCO), very low surface recombination is achievable. In future, decrease in the fraction of metallized area at the rear might be expected, hence R_s plays a vital role in the contact resistance of the Al—Si interface which is given by

$$R_{c, \text{rear}} = \rho_c / f_{\text{rear}} \quad (1)$$

where f_{rear} is the rear metallization fraction and ρ_c is the specific contact resistivity. However, ρ_c is independent of the contact size [65]. Similarly, Rohatgi et al. [66], on 2.3 Ω -cm wafers, obtained a $\rho_c = 10 \text{ m}\Omega \text{ cm}^2$. Urrejola et al. [56] carried out the contact measurements with a PERC structure. The Al paste is printed on the top of the locally opened dielectric, and the transmission line model revealed the dependence of the ρ_c on the contact area. They obtained the ρ_c of 9–17 $\text{m}\Omega \text{ cm}^2$ for the dielectric opening width of 80–170 μm . Gatz et al. [67], to determine ρ_c , varied the rear contact pitch of PERC solar cells and obtained a ρ_c of 40–55 $\text{m}\Omega \text{ cm}^2$. The contribution of the bulk to the series resistance R_b is acquired either by calculation or numerical simulation. Kranz et al. [68] processed PERC-like TLM samples and measured the ρ_c of 3 $\text{m}\Omega \text{ cm}^2$, whereas the fit to the solar cell data resulted in ρ_c of 0.2–2 $\text{m}\Omega \text{ cm}^2$ and is shown in **Figure 5**.

2.3.4 PVD metallization

In most of the high efficiency solar cell concepts, the metallization is carried out using three different physical vapor deposition (PVD) techniques: sputtering, electron gun, and thermal evaporation. During the deposition of aluminum layer (2 μm), the substrate temperature increases to $\sim 350^\circ\text{C}$, which mainly arises from the recrystallization heat of the aluminum. Comparing with the screen printing process, the mechanical and thermal impact on the wafer is substantially reduced. After the deposition of PVD aluminum layers, the contacts can be formed using laser pulses with different laser parameters which results in a much shallower profile. Hoffmann et al., on a 0.5 $\Omega \text{ cm}$ p-type silicon, demonstrated a solar cell efficiencies up to 21.7% [69]. Reinwand et al. [70] investigated PERC cells with

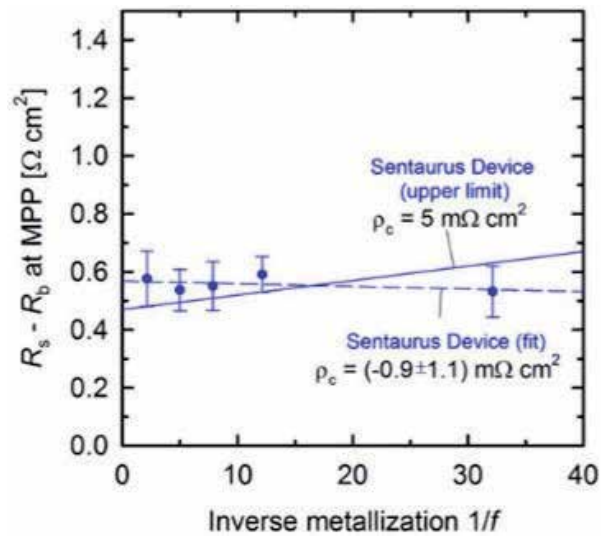


Figure 5. $R_s - R_b$ vs. inverse metallization fraction $1/f$. Reproduced with permission from [68].

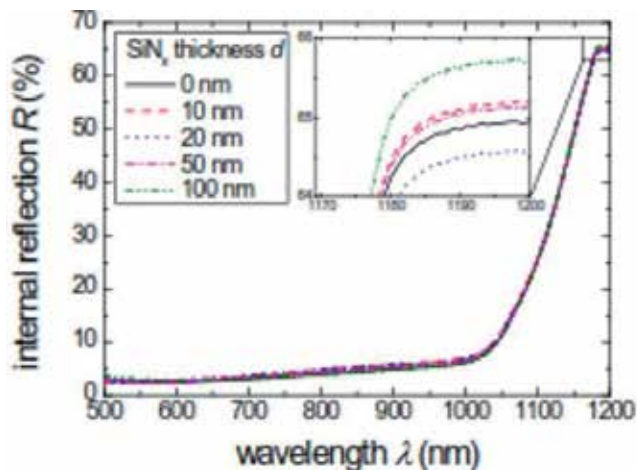


Figure 6. Measurement of the internal reflection R at the rear side, after foil attachment and laser fired contacts dependent on the SiN_x capping layer thickness. The reflection varies by $< 0.5\%$ in the IR regime [74].

sputtered aluminum on the rear side and a Ti—Ag (50/100 nm) seed layer on top prior to the silver plating. With the optimized annealing temperature, the highest efficiency $\eta = 21.1$ and 19.4% for FZ and CZ wafers, respectively, was determined with the lowest contact resistivity $\rho_c = 0.36 \text{ m}\Omega \text{ cm}^2$.

2.3.5 Foil metallization

In 2007, researchers from F-ISE introduced the laser-based foil metallization technology called “FolMet.” With this technology, the conventional aluminum foil is attached to the silicon wafer [71], and thus the laser fired contact process forms both the electrical contact at the rear side of PERC cell as well as the mechanical contact by locally melting the aluminum through the passivation layer into the bulk silicon [72]. The key advantages of this process is its enhanced internal optical

Issues	PVD	Screen print	Foil
Efficiency-potential	High	High	High
Flexibility	Medium	Low	High
Maturity	High	High	Low
Process temperature	300 °C	800–900°C	—
Cost	Medium	High	Low

Table 3.
Advantages and disadvantages of different printing mechanisms [75].

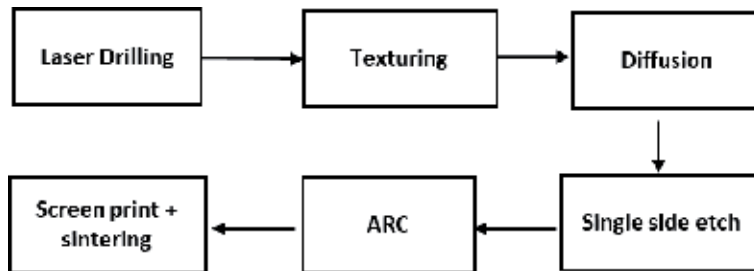


Figure 7.
Process flow of MWT PERC solar cells.

properties obtained due to the air gap between foil and passivation layer [73], cost reduction potential by decreasing the capping layer thickness, and ease of cell production process [74].

Figure 6 shows the internal reflection R at the rear side, after foil attachment and laser fired contacts. Nekarda et al., [73] by using the thick passivation layer optimized for the screen printed Al-paste, obtained an efficiency of 20.5%. In order to further reduce the cost, Graf et al. [74] adapted the rear side passivation layer with thinner capping layer and demonstrated an efficiency of 21.3% with a high J_{sc} due to the improved internal reflectance. Moreover, a low series resistance of $9 \text{ m}\Omega \text{ cm}^2$ of Al foil improved the FF to 80%. Pros and cons of various metallization schemes such as screen printing (SP), physical vapor deposition (PVD), and foil are tabulated in **Table 3**.

2.3.6 Metal wrap through PERC

MWT cell (**Figure 7**) is similar to the conventional solar cell design, and the external front contact busbars for interconnection are located at the rear side which increases J_{sc} due to the reduced shading loss. Lohmüller et al. [76], from FhG-ISE, combined the MWT concept (J_{sc} improvement) and passivated emitter rear contact (PERC) concept (reduced rear SRV) and reported a conversion efficiency of 18.7% with J_{sc} of 39.9 mA/cm^2 , V_{oc} of 638 mV, and FF of 80.9% on a boron-doped p-type Cz grown silicon. The higher FF is due to the successful implementation of seed and plate technology [76]. Thaidigsmann from the same group introduced a simplified MWT-PERC cell called HIP-MWT (high performance metal wrap) to improve the efficiency by reducing the process complexity. In HIP-MWT structure, the formation of rear emitter is neglected hence no need of structuring steps. On a p-type FZ wafer with $0.5 \Omega \text{ cm}$, a substrate thickness of $160 \mu\text{m}$, on a cell area of 149 cm^2 resulted in an efficiency of 20.1% with J_{sc} of 39.1 mA/cm^2 , V_{oc} of 659 mV, and FF of 77.8%, was obtained. The HIP-MWT cell demonstrated an efficiency of 19.6%

with J_{sc} of 40.2 mA/cm², V_{oc} of 649 mV, and FF of 75.1% on Cz grown wafer with 2.6 Ω cm for the same substrate thickness and cell area [77].

Passivated emitter rear contact solar cell with dielectric layer at the rear side and locally rear aluminum contacts reduces the recombination losses which increases the open circuit voltage. Also the rear dielectric layer increases the internal reflection and thus increases the current of the solar cell. Though the performance of PERC cell is better, the efficiency of PERC cell decreases after light-induced degradation which is around 0.5–1.0% absolute.

2.4 Interdigitated back contact solar cell

In IBC solar cells, optical shading loss is eliminated as both polarities of the metal contact are placed on the rear surface. In addition, the resistive power loss is reduced largely as the rear surface furnishes an opportunity for best design of metal contact formation. The other key advantages of IBC cell are (a) module manufacturing cost is reduced as the interconnection between the cells is simplified and (b) higher cell packing density increases the module power. The process flow of the IBC cell is shown in **Figure 8**. The major challenges present in the metallization of IBC cell includes: (i) shunting between the two polarities of metal contacts must be prevented and (ii) the metal conductors must be thick enough to ascertain the low resistive power loss. To isolate both the contacts, different cell-based metallization techniques can be used. One such method is patterning metal seed layer [78, 79], with electroplating to reduce resistance [80]. However, this plating up process needs electrical contact to the seed metal lines, which may lead to be problem with thinner wafers.

IBC solar cells with a record high efficiency of 25.6% were obtained by Sanyo/Panasonic [81], and the pioneer SunPower Corporation achieved 25% efficiency [82]. For IBC cells, the front surface field (FSF) reduces the surface recombination at the front as it acts as an electrical field which pushes back the minority carriers at the front surface [83]. The high expensive photolithography process is replaced with laser processing or screen printing which leads to a significant reduction in position accuracy which increases the pitch. This makes the majority carriers to travel from vertical to lateral direction. Depending on the pitch and base resistivity, series resistance over 90% contributing to the lateral majority carrier transport reduces the cell efficiency. Moreover the lateral majority carrier's current transport as well as the front surface passivation has been enhanced by FSF and finally the series resistance also significantly reduced to 0.1 and 1.3 Ω cm² for the base resistivity of 1 and 8 Ω cm, respectively, for the pitch of 3.5 mm [84].

The rear metallization of IBC cells is usually done with silver (Ag) and aluminum (Al) pastes [85], and Si/Ti/Pd/Ag or Si/Al/Ti/Pd/Ag metal stack and Al-deposited by PVD form a good ohmic contact with both n- and p-type silicon [86]. In Si/Ti/Pd/Ag or Si/Al/Ti/Pd/Ag metal stack, the Ag layer is used as a conductive layer because of its low resistivity. To avoid the reaction between Ti and Ag, the Pd layer is deposited between Ti and Ag layer. The work function of Ti or Al makes it suitable to contact with low contact resistivity [87] on both p- and n-doped

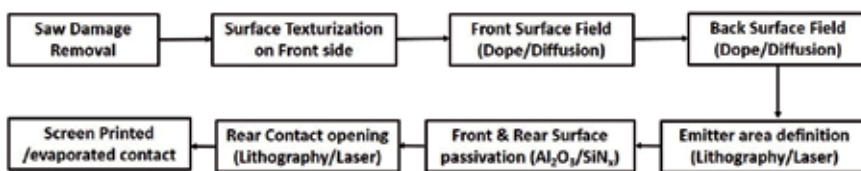


Figure 8.
IBC process flow.

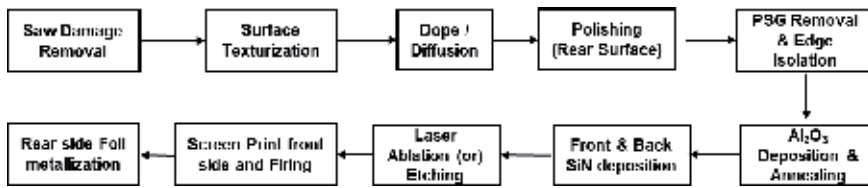


Figure 9.
 Process flow of AMELI interconnection process.

regions. As Ti is a poor reflector, the Si/Al/Ti/Pd/Ag structure is adopted owing to the higher reflectance obtained with an Al layer which increases the light trapping. Couderca et al. [20] used Si/Ti/Ag stack with a thin Ti layer which has a low contact resistivity on both n- and p- doped regions. For n-doped surfaces, the specific resistivity is very low, and hence, the resistive losses are negligible. As the p-doped surfaces are lowly doped, the specific resistivity is higher though it stays under the crucial limit of $0.01 \Omega \text{ cm}^2$. As a low-cost approach, Chena et al. [88] applied the aluminum electrodes deposited by e-beam evaporation using Al contact for high performance IBC cells. The specific contact resistivity of the Al contact cell resulted in 0.7 and $0.05 \text{ m}\Omega \text{ cm}^2$ on an n-doped and p-doped surface, respectively, and the final Al-contacted IBC cell resulted in an efficiency of 22.72%.

Recently, carrier selective contacts [TOPcon] using tunnel oxide and amorphous (a-Si) layer resulted in V_{oc} values around 720 mV and contact resistivities less than $10 \text{ m}\Omega \text{ cm}^2$ [89]. With poly-Si/SiO_x approach, similar values for their passivated contact have been achieved by various researchers [90–92]. Young et al. used the similar contact for the IBC solar cell patterned with ion implantation. The metallization layer consisting of thin Ti/Pd adhesion layer with 1- μm thick Ag layer and a Pd capping layer resulted in the contact resistivities less than $0.1 \text{ m}\Omega \text{ cm}^2$ [93].

Electrical shading loss plays a detrimental role as it reduces the collection efficiency of the minority carriers over the BSF regions [94], which compromises J_{sc} . By decreasing the width of the BSF region, this detrimental effect can be resolved. In the active cell area, by decreasing the finger pitch and BSF finger width, the electrical shading loss is minimized. Nevertheless, the base busbar still enforces electrical shading. In addition, as the majority carriers generated over the emitter busbar have to traverse over the entire wafer area, result in transport losses. The electrical shading loss and the transport loss contribute to the resistive losses and FF losses in the busbar metallization. Hence for further efficiency improvement, research group from ISFH developed a busbar less metallization which omits the busbar and eliminates the resistive losses in metallization with aluminum-based mechanical and electrical laser interconnection (AMELI) process for contacting aluminum-metallized IBC cells [95] and obtained a conversion efficiency of 22.1% with a V_{oc} of 683 mV, J_{sc} of 41.4 mA/cm^2 , and FF of 78.1% on a cell area of 132 cm^2 . AMELI process interconnects the solar cell with highly flexible interconnection geometry performed by a laser as structuring of the metallization. In addition, this AMELI process can interconnect that are as wide as the whole cell edge with a lower electrical resistance between the cells [96, 97]. **Figure 9** depicts the AMELI interconnection scheme for busbar-free solar cells. Woehl et al. introduced a point-shaped metallized IBC cells interconnected to a printed circuit board. The presence of only point-shaped metal contacts, increases the V_{oc} as the recombination area, is significantly reduced [98].

The main advantage of interdigitated back contact solar cells over other type of solar cells is zero shadow loss due to the absence of complete front contact. Although IBC is the high efficiency single junction cells among all other type of silicon solar cells, the carrier collection efficiency in front of the back surface field is low.

3. Conclusions

Process flows of conventional silicon solar cell, Ni/Cu plating for silicon solar cells, passivated emitter rear contact solar cells, and interdigitated back contact solar cells were discussed. Influences of process parameters in electrical parameters were analyzed. Though the contact formed by lithography, sputtering, etc. is reliable and resulting in good energy conversion efficiency, however, it is expensive due to the vacuum evaporation and single wafer type process. In this context, screen printed contacts are consistent in reliable and providing the best approach in production industry. Screen printing-based metallization is one of the key and crucial processes in silicon solar cell fabrication process which was discussed by interpreting the paste rheology, screen, and printing parameters. The screen printing paste used for contacting the solar cells is the other expensive element after the silicon wafer, and thus it is important to find an alternate technique for silver paste-based printing mechanism. Researchers arrived at a Ni/Cu plating technique for contact mechanism, and the technique has proved its capability in manufacturing industry as well. However, advanced structures such as PERC and IBC are using either screen printing or evaporation technique for making contacts. By seeing current scenario of metallization in different types of solar cells, it has been concluded that screen printing will continue to be an important and reliable metallization technique. The current efficiency status of different silicon solar cell technologies is depicted in **Table 4**.

S/N	Technology	Efficiency in %
1	Al BSF multi Si cell	19.0
2	Al BSF mono Si cell	20.0
3	Ni/Cu plating Si cell	21.3
4	PERC multi Si cell	22.0
5	PERC mono Si cell	25.0
6	MWT PERC Si cell	19.6
7	IBC Si cell	26.7

Table 4.
Current efficiency trend of different technology solar cells [36, 77, 99].

Acknowledgements

SS thanks the Management, RenewSys India Pvt. Ltd. and Faculties, National Centre for Photovoltaic Research and education, Indian Institute of Bombay, Mumbai for their support.

Disclaimer

The technical content in this article is the literature review of authors and do not necessarily reflect the official policy or position of RenewSys India Pvt. Ltd. Further, the authors hereby undertake to protect the proprietary technical and confidential information of RenewSys India Pvt. Ltd, including but not limited to the process parameters, recipes, formulations, sequences, methods, data, information etc. if any, referred in the above article, and have taken sufficient and appropriate measures and precaution to avoid the same from being inferred directly or indirectly in any manner whatsoever.

Definitions

V_{oc}	open circuit voltage
I_{sc}	short circuit current
J_{sc}	short circuit current density
J_{0e}	emitter saturation current density
FF	fill factor
R_s	series resistance
η	efficiency
ARC	anti-reflective coating
SP	screen printing
FSF	front surface field
AIBSF	aluminum back surface field
PERC	passivated emitter rear contact
IBC	interdigitated back contact
HIT	heterojunction with intrinsic thin layer
LGBC	laser grooved buried contacts
LIP	light induced plating
LDSE	laser-doped selective emitter
EVA	ethylene vinyl acetate
ITRPV	international technology roadmap for photovoltaic
i-PERL	passivated emitter with rear locally diffused
PVD	physical vapor deposition
LCO	laser contact opening
MWT	metal wrap through
HIP MWT	high performance metal wrap through
CZ	czochralski
FZ	float zone
SRV	surface recombination velocity
AMELI	aluminum based mechanical and electrical laser interconnection

Author details

Nagarajan Balaji¹, Mehul C. Raval² and S. Saravanan^{3*}

1 Solar Energy Research Institute of Singapore (SERIS), Singapore

2 RCT Solutions GmbH Line - Eid, Konstanz, Germany

3 RenewSys India Pvt. Ltd, Hyderabad, India

*Address all correspondence to: shrisharavanan@yahoo.co.uk

IntechOpen

© 2019 The Author(s). Licensee IntechOpen. This chapter is distributed under the terms of the Creative Commons Attribution License (<http://creativecommons.org/licenses/by/3.0>), which permits unrestricted use, distribution, and reproduction in any medium, provided the original work is properly cited. 

References

- [1] Bolton JR. Solar cells—A technology assessment. *Sol Energy*. 1983;**31**: 483-502
- [2] Koch W, Endros AL, Franke D, et al. Bulk crystal growth and wafering for PV. In: Luque A, Hegedus S, editors. *Handbook of Photovoltaic Science and Engineering*. 2nd ed. Chichester: John Wiley and Sons/Wiley; 2003. pp. 205-254
- [3] Tobias I, del Canizo C, Alonso J. Crystalline silicon solar cells and modules. In: Luque A, Hegedus S, editors. *Handbook of Photovoltaic Science and Engineering*. 2nd ed. Chichester: John Wiley and Sons/Wiley; 2003. pp. 255-306
- [4] Saravanan S, Meera M, Suratkar P, Gijo EV. Efficiency improvement on the multicrystalline silicon wafer through six sigma methodology. *International Journal of Sustainable Energy*. 2012;**31**:143-153
- [5] Saravanan S, Suresh ChSR, Subraveti VV, Kumar KC, Jayaram UK. Effects of texture additive in large-area diamond wire cut multicrystalline silicon solar cells. *Photovoltaics International*. 2019;**42**:46-49
- [6] Sankarasubramanian S, Saud GK, Shashikala M, Suratkar P, Saravanan S. Impact of surface texturization on overall performance of mono crystalline silicon solar cells. *ECS Transactions*. 2015;**66**:9-17
- [7] Kumar D, Saravanan S, Suratkar P. Effect of oxygen ambient during phosphorous diffusion on silicon solar cell. *Journal of Renewable and Sustainable Energy*. 2012;**4**:33105-33113
- [8] Guru Prasad A, Saravanan S, Gijo EV, et al. Six sigma approach on throughput improvement in the diffusion process of crystalline silicon solar cell manufacturing Int. *International Journal of Sustainable Energy*. 2016;**35**:190-204
- [9] Guru Prasad A, Sreenivasa MD, Prakash S, Saravanan S. Effect of gas flow rates in optimizing silicon nitride films for large area multicrystalline silicon solar cells. *International Journal of Electronics Letters*. 2015;**3**:87-93
- [10] Aakella PS, Saravanan S, Joshi SS, Solanki CS. Pre-metallization processes for c-Si solar cells. *Solar Energy*. 2013;**97**:388-397
- [11] Coates K, Morrison S, Narayanan S, Madan A. Deposition of silicon nitride to improve the conversion efficiency of multicrystalline silicon solar cells. In: *Proceedings of 16th EU PVSEC*; Glasgow. 2000. pp. 1279-1281
- [12] Hilali MM, Nakayashiki K, Khadilkar C, et al. Effect of Ag particle size in thick-film Ag paste on the electrical and physical properties of screen printed contacts and silicon solar cell. *Journal of the Electrochemical Society*. 2006;**153**:A5-A11
- [13] Papet P, Nichiporuk O, Kaminski A, et al. Pyramidal texturing of silicon solar cell with TMAH chemical anisotropic etching. *Solar Energy Materials & Solar Cells*. 2006;**90**:2319-2328
- [14] Park H, Kwon S, Lee JS, et al. Improvement on surface texturing of single crystalline silicon for solar cells by saw-damage etching using an acidic solution. *Solar Energy Materials & Solar Cells*. 2009;**93**:1773-1778
- [15] Schultz O, Glunz SW, Riepe S, Willeke GP. High efficiency solar cells on phosphorus gettered multicrystalline silicon substrate. *Progress in Photovoltaics: Research and Applications*. 2006;**14**:711-719

- [16] Mehul CR, Amruta PJ, Sandeep SS, Suckow S, Saravanan S, Solanki CS, et al. Study of nickel silicide formation and associated fill-factor loss analysis for silicon solar cells with plated Ni-Cu based metallization. *IEEE Journal of Photovoltaics*. 2015;5:1554-1562
- [17] Mehul CR, Sandeep SS, Stephan S, Saravanan S, Solanki CS, Kottantharayil A. N₂O plasma treatment for minimization of background plating in silicon solar cells with Ni-Cu front side metallization. *Solar Energy Materials & Solar Cells*. 2016;144:671-677
- [18] Jörg TH, Yuan S, Norbert B, et al. Industrial Si solar cells with Cu-based plated contacts. *IEEE Journal of Photovoltaics*. 2016;5:1595-1600
- [19] Philipp RL, Gerd F, Lamine S, et al. Progress in fine-line metallization by co-extrusion printing on cast monosilicon PERC solar cells. *Solar Energy Materials & Solar Cells*. 2016;142:18-23
- [20] Romain C, Mohamed A, Mustapha L. Improvement of back surface metallization in a silicon interdigitated back contacts solar cell. *Energy Procedia*. 2013;38:684-690
- [21] Green MA. *Silicon Solar Cells: Advanced Principles and Practice*. 2nd ed. Chichester: Wiley/Centre for Photovoltaic Devices and Systems; 1995
- [22] Wenham SR, Green MA. Laser grooved solar cell. US Patent 4,626,613. 1986
- [23] Ehling C, Schubert MB, Merz R, et al. 0.4% absolute efficiency gain by novel back contact. *Solar Energy Materials & Solar Cells*. 2009;93:707-709
- [24] Denis E, Aleksander F, Marc R, et al. Advanced screen printing technique for high definition front side metallization of crystalline silicon solar cells. *Solar Energy Materials & Solar Cells*. 2010;94:57-61
- [25] Dziejdzic D, Nijs J, Szlufcik J. Thick-film fine-line fabrication techniques-application to front metallisation of solar cells. *Microelectronics International*. 1993;10(1):18-26
- [26] Mehul CR, Chetan SS. Review of Ni-Cu based front side metallization for c-Si solar cells. *Journal of Solar Energy*. 2013. Article ID 183812. 20 pages
- [27] Neuhaus DH, Munzer A. Industrial silicon wafer solar cells. *Advances in Opto Electronics*. 2007. Article ID 24521. 15 pages
- [28] Content. 2013. Available from: <http://us.sunpowercorp.com/>
- [29] Kuehnlein MBHH, Koesterke N, Cimiotti G, et al. >0.4% absolute efficiency gain by fast Ni-Cu-Sn electroplating of solar cells with fine line printed contacts by a single side wet treatment technology. In: *Proceedings of 24th EU PVSEC*. 2009. pp. 282-284
- [30] Kroner F, Kroner Z, Reichmann K. All electrochemical layer deposition for crystalline silicon solar cell manufacturing: Experiments and interpretation. *Solar Energy*. 2012;86:548-557
- [31] Mette AGWA, Schetter C, Wissen D, et al. Increasing the efficiency of screen-printed silicon solar cells by light-induced silver plating. In: *Proceedings of IEEE 4th World Conference on Photovoltaic Energy Conference*. 2006. pp. 1056-1059
- [32] Lee E, Lee H, Choi J, et al. Improved LDSE processing for the avoidance of overplating yielding 19.2% efficiency on commercial grade crystalline Si solar cell. *Solar Energy Materials & Solar Cells*. 2011;95:3592-3595

- [33] Gambogi WJ, McCord EF, Rosenfeld HD, et al. Failure analysis methods applied to PV module reliability. In: Proceedings of 24th EU PVSEC. 2009. pp. 3530-3534
- [34] Hilali MM. Understanding and development of manufacturable screen-printed contacts on high sheet resistance emitters for low-cost solar cells [thesis]. Georgia Institute of Technology; 2005
- [35] Ghannam M, Sivoththaman S, Poortmans J. Trends in industrial silicon solar cell processes. *Sol Energy*. 1997;59:101-110
- [36] Fischer M. ITRPV 9th edition 2018 report release and key findings. In: PV Cell Tech conference. 2018
- [37] Lolgen P, Sinke WC, Leguijt C, et al. Boron doping of silicon using coalloying with aluminium. *Applied Physics Letters*. 1994;65:2792
- [38] Rauer M, Schmiga C, Woehl R, et al. Investigation of aluminum-alloyed local contacts for rear surface-passivated silicon solar cells. *IEEE Journal of Photovoltaics*. 2011;1:22-28
- [39] Dong L, Malcolm A, Doris L, et al. Process optimization of localized BSF formation for solar cells with over 20% energy conversion efficiency. In: Proceedings of 40th IEEE PVSC. Denver; 2014. pp. 2503-2506
- [40] Blakers AW, Wang A, Milne AM, et al. 22.8% efficient silicon solar cell. *Applied Physics Letters*. 1989;55:1363-1365
- [41] Dullweber T, Gatz S, Hannebauer H, et al. 19.4%-efficient large area rear-passivated screen printed silicon solar cells. In: Proceedings of 26th EU PVSEC. Hamburg; 2011. pp. 811-816
- [42] Zielke D, Petermann JH, Werner F, et al. 21.7% efficient PERC solar cells with AlO_x tunneling layer. In: Proceedings of 26th EU PVSEC. Hamburg; 2011. pp. 1115-1119
- [43] Urrejola E, Petres R, Glatz-Reichenbach J, et al. High efficiency industrial PERC solar cells with all PECVD-based rear surface passivation. In: Proceedings of 26th EU PVSEC. Hamburg; 2011. pp. 2233-2235
- [44] Choulat P, Agostinelli G, Ma Y, et al. Above 17% industrial type PERC solar cell on thin multicrystalline silicon substrate. In: Proceedings of 22nd EU PVSEC. Milan; 2007. pp. 1011-1014
- [45] Agostinelli G, Szlufcick J, Choulat P, Beaucarne G. Local contact structures for industrial PERC-type solar cells. In: Proceedings of 20th EU PVSEC. Barcelona; 2005. pp. 942-945
- [46] Lauermann T, Lüder T, Scholz S, et al. Enabling dielectric rear side passivation for industrial mass production by developing lean printing-based solar cell processes. In: Proceedings of 35th IEEE PVSC. Honolulu; 2010. pp. 28-33
- [47] Uruena A, John J, Beaucarne G, et al. Local Al-alloyed contacts for next generation Si solar cells. In: Proceedings of 24th EU PVSEC. Hamburg; 2009. pp. 1483-1486
- [48] Metz A, Adler D, Bagus S, et al. Industrial high performance crystalline silicon solar cells and modules based on rear surface passivation technology. *Solar Energy Materials & Solar Cells*. 2014;120:417-425
- [49] Münzer KA, Schöne J, Teppe A, et al. Towards 19.5% industrial crystalline silicon solar cells. In: Proceedings of 26th EUPVSEC. Hamburg; 2011. pp. 843-848
- [50] Glunz SW, Preu R, Schaefer S, et al. New simplified methods for patterning the rear contact of RP-PERC high-efficiency solar cells. In: Proceedings

of 28th IEEE PVSC. Anchorage, Alaska; 2000. pp. 168-171

[51] Bahr M, Heinrich G, Doll O, et al. Differences of rear-contact formation between laser ablation and etching paste for PERC solar cells. In: Proceedings of 26th EU PVSEC. Hamburg; 2011. pp. 1203-1209

[52] Meemongkolkiat V, Nakayashiki K, Kim DS, et al. Investigation of modified screen-printing Al pastes for local back surface field formation. In: Proceedings of 4th WCPEC. Hawaii; 2006. pp. 1338-1341

[53] Fang T, Lin CM, Wang LT, Tang WC. Metallization of rear-side passivated solar cells: Reducing cavities on local contacts. In: Proceedings of 26th EU PVSEC. Hamburg; 2011. pp. 2220-2222

[54] Lauer mann T, Zuschlag A, Scholz S, et al. Influence of the contact geometry and sub-contact passivation on the performance of screen printed Al₂O₃ passivated solar cells. In: Proceedings of 26th EU PVSEC. Hamburg; 2011. pp. 1137-1143

[55] Urrejola E, Peter K, Glatz-Reichenbach J, et al. Al-Si alloy formation in narrow p-Si contact areas. In: Proceedings of 2nd Metallization Workshop. Konstanz; 2010. pp. 11-14

[56] Urrejola E, Peter K, Plagwitz H, Schubert G. Al-Si alloy formation in narrow p-type Si contact areas for rear passivated solar cells. *Journal of Applied Physics*. 2010;**107**:124519

[57] Urrejola E, Peter K, Plagwitz H, Schubert G. Silicon diffusion in Aluminum for rear Passivated solar cells. *Applied Physics Letters*. 2011;**98**:153508

[58] Urrejola E, Peter K, Plagwitz H, Schubert G. Distribution of silicon in the aluminum matrix for rear passivated solar cells. *Energy Procedia*. 2011;**8**:331-336

[59] Urrejola E, Peter K, Plagwitz H, Schubert G. Effect of gravity on the microstructure of Al-Si alloy for rear-passivated solar cells. *Journal of Applied Physics*. 2011;**110**:056104

[60] Grasso FS, Gautero L, Rentsch J, Preu R, Lanzafame R. Characterisation of local Al-BSF formation for PERC solar cell structures. In: Proceedings of 25th EUPVSEC. Valencia; 2010. pp. 371-374

[61] Glunz SW, Schneiderlöchner E, Kray D, et al. Laser-fired contact solar cells on p- and n-type substrates. In: Proceedings of 19th EUPVSEC. Paris, France; 2004. pp. 408-411

[62] Kray D, Hermle M, Glunz SW. Theory and experiments on the back side reflectance of silicon wafer solar cells. *Progress in Photovoltaics: Research and Applications*. 2006;**14**:195

[63] Schneiderloch ner E, Preu R, Ludemann R, Glunz SW. Laser-fired rear contacts for crystalline silicon solar cells. *Progress in Photovoltaics: Research and Applications*. 2002;**10**:29-34

[64] Nekarda JF, Lottspeich F, Wolf A, Preu R. Silicon solar cells using aluminum foil as rear side metallization reaching 21.0% efficiency. In: Proceedings of 25th EUPVSEC. Valencia; 2010. p. 2211

[65] Melczarsky M, Gallego GG, Posthuma N, et al. Contact resistance measurement techniques for Ag thick-film screen-printed contacts to solar cells. In: Proceedings of 34th IEEE Photovoltaic Spec. Conf. Philadelphia, PA; 2009. pp. 960-963

[66] Rohatgi A, Narasimha S, Ruby DS. Effective passivation of the low resistivity silicon surface by a rapid thermal oxide/PECVD silicon nitride stack and its application to passivated rear and bifacial Si solar cells. In: Proceedings of 2nd World Conference.

Photovoltaic Energy Conversion.
Vienna, Austria; 1998. pp. 1566-1569

[67] Gatz S, Dullweber T, Brendel R. Evaluation of series resistance losses in screen-printed solar cells with local rear contacts. *IEEE Journal of Photovoltaics*. 2011;1:37-42

[68] Kranz C, Lim B, Baumann U, Dullweber T. Determination of the contact resistivity of screen-printed Al contacts formed by laser contact opening. *Energy Procedia*. 2015;67:64-69

[69] Hofmann M, Glunz SW, Preu R, Willeke G. 21%-efficient silicon solar cells using amorphous silicon rear side passivation. In: *Proceedings of 21st EUPVSEC*. Dresden, Germany; 2006. pp. 609-613

[70] Reinwand D, Specht J, Stüwe D, et al. 21.1% efficient PERC silicon solar cells on large scale by using inline sputtering for metallization. In: *Proceedings of 35th IEEE Photovoltaic Specialists Conference (PVSC)*. Honolulu; 2010. pp. 3582-3586

[71] Nekarda J, Grohe A, Schultz O, Preu R. Aluminum foil as back side metallization for LFC cells. In: *Proceedings of 22nd EUPVSEC*. 2007. pp. 1499-1501

[72] Schneiderlöchner E, Preu R, Lüdemann R, Glunz SW, Willeke G. Laser-fired contacts (LFC). In: *Proceedings of 17th EUPVSEC*. 2001. pp. 1303-1306

[73] Nekarda J, Graf M, Rodofili A, Preu R, Böhme R, Sontag D. Laser-based foil-metallization for industrial PERC solar cells. In: *Proceedings of 28th EUPVSEC*. 2013. pp. 797-799

[74] Graf M, Nekarda J, Eberlein D, Wöhrle N, Preu R, Böhme R, et al. Progress in laser-based foil metallization for industrial PERC solar cells. In:

Proceedings of 29th EUPVSEC. 2014. pp. 532-535

[75] Nekarda J, Hörteis M, Lottspeich F, et al. Comparison of three different metallization concepts for LFC cells. In: *Proceedings of 25th EUPVSEC*. 2010. pp. 2245-2249

[76] Lohmüller E, Thaidigsmann B, Bartsch J, et al. Advanced metallization of rear surface passivated metal wrap through silicon solar cells. *Energy Procedia*. 2011;8:546-551

[77] Thaidigsmann B, Lohmüller E, Jäger U, et al. Large-area p-type HIP-MWT silicon solar cells with screen printed contacts exceeding 20% efficiency. *Physica Status Solidi RRL: Rapid Research Letters*. 2011;5:286-288

[78] Li Z, Cordiner D, Borojevic N, et al. Lift-off contact separation method for Interdigitated rear-contact solar cells. In: *Proceedings of 21th International Photovoltaic Science and Engineering Conference*. Fukuoka, Japan; 2011

[79] Mulligan WP, Cudzinovic MJ, Pass T, et al. Solar cell and method of manufacture. US Patent, US 7339,110 B. 2008

[80] Mir I, Kumar D. Recent advances in isotropic conductive adhesives for electronics packaging applications. *International Journal of Adhesion and Adhesives*. 2008;28:362-371

[81] Contents. Available from: <http://news.panasonic.com/global/press/data/2014/04/en140410-4/en140410-4.html>

[82] Smith DD, Cousins PJ, Masad A. SunPower's Maxeon gen III solar cell: High efficiency and energy yield. In: *Proceedings of 39th IEEE PVSC*. Tampa, FL; 2013

[83] Engelhart P, Harder NP, Grischke R, et al. Laser structuring for back

junction silicon solar cells. *Progress in Photovoltaics: Research and Applications*. 2007;**15**:237-243

[84] Granek F, Hermle M, Huljic DM, et al. Enhanced lateral current transport via the front N+ diffused layer of N-type high-efficiency back-junction back-contact silicon solar cells. *Progress in Photovoltaics: Research and Applications*. 2009;**17**:47-56

[85] Galbiati G, Mihailetchi VD, Roescu R, et al. Large-area back-contact back-junction solar cell with efficiency exceeding 21%. *IEEE Journal of Photovoltaics*. 2013;**3**:560-565

[86] Fong KC, Teng K, McIntosh KR, et al. Optimisation of n+ diffusion and contact size of IBC solar cells. In: *Proceedings of 28th EU PVSEC*. Paris; 2013

[87] Schroder D, Meier D. Solar cell contact resistance a review. *IEEE Transactions on Electron Devices*. 1984;**31**:637-646

[88] Chena Y, Yang Y, Zhang X, et al. Forming aluminum electrodes by screen printing and electron-beam evaporation for high performance interdigitated back contact solar cells. *Solar Energy Materials & Solar Cells*. 2015;**143**:205-211

[89] Feldmann F, Bivour M, Reichel C, Hermle M, Glunz SW. Passivated rear contacts for high-efficiency n-type Si solar cells providing high interface passivation quality and excellent transport characteristics. *Solar Energy Materials & Solar Cells*. 2014;**120**(A):270-274

[90] Romer U, Peibst R, Ohrdes T, et al. Recombination behavior and contact resistance of n+ and p+ poly-crystalline Si/mono-crystalline Si junctions. *Solar Energy Materials & Solar Cells*. 2014;**131**(A):85-91

[91] Upadhyaya A, Ok YW, Chang E, et al. Ion implanted screen printed N-type solar cell with tunnel oxide passivated back

contact. In: *Proceedings of 42nd IEEE Photovoltaic Specialists Conference*. New Orleans, Louisiana; 2015

[92] Cuevas A, Allen T, Bullock J, et al. Skin care for healthy silicon solar cells. In: *Proceedings of 42nd IEEE Photovoltaic Specialists Conference*. New Orleans, Louisiana; 2015

[93] Young DL, Nemeth W, LaSalvia V, et al. Interdigitated back passivated contact (IBPC) solar cells formed by ion implantation. *IEEE Journal of Photovoltaics*. 2016;**8**:41-47

[94] Herme M, Granek F, Schultz-Wittmann O, Glunz SW. Shading effects in back junction back contacted silicon solar cells. In: *Proceedings of 33rd IEEE PVSC*. St. Diego, CA; 2008

[95] Schulte-Huxel H, Blankemeyer S, Merkle A, et al. Interconnection of busbar-free back contacted solar cells by laser welding. *Progress in Photovoltaics: Research and Applications*. 2015;**23**:1057-1065

[96] Schulte-Huxel H, Bock R, Blankemeyer S, et al. Aluminum-based mechanical and electrical laser interconnection process for module integration of silicon solar cells. *IEEE Journal of Photovoltaics*. 2012;**2**(1):16-21

[97] Schulte-Huxel H, Blankemeyer S, Bock R, et al. Aging behavior of laser welded Al-interconnections in crystalline silicon modules. *Solar Energy Materials & Solar Cells*. 2012;**106**:22-26

[98] Woehl R, Krause J, Granek F, Birot D. 19.7% efficient all-screen-printed back-contact back-junction silicon solar cell with aluminum-alloyed emitter. *IEEE Electron Device Letters*. 2011;**32**:345-347

[99] Green MA, Hishikawa Y, Dunlop ED, et al. Solar cell efficiency tables (version 53). *Progress in Photovoltaics: Research and Applications*. 2019;**27**:3-12

Polymers in Solar Cells

Pedro Pablo Zamora and Klaus Bieger

Abstract

Due to the promising properties of semiconducting polymers they have attracted wide spread interest. During the last decade we have worked on a smart chemistry approach to these substrates and organometallic compounds with special focus on design, synthesis and characterization of materials that could be used in photovoltaic devices. In these materials, one of the most important aspects is high absorbance in the UV-Vis spectrum as a necessary characteristic for high conversion rates of light to electric energy. We were able to show that this can be achieved introducing certain functional groups as, e.g., NO₂-moieties. Another important aspect is the interaction with the buffer layers that also form part of the whole photovoltaic device. Here we show that a double layer of CuI/MoO₃ increased the energy yield for a large variety of organic substrates along with related results from other leading groups reported in literature.

Keywords: polymers, photovoltaics, buffer layer

1. Introduction

Organic photovoltaic devices are often seen as the future of solar cells [1] as they permit energy conversion with much less consumption of material resources than the conventional silicon based semiconductor cells [2]. Additionally they permit the development of flexible devices while the traditional cells are rigid and fragile [3].

Even though since the discovery of the photoelectrical effect in organic substrates large progresses have been achieved [4] to increase yield and stability the organic devices still are much less efficient and present lower lifetimes than the traditional solar cell form [5]. There have also been progresses in developing different cell types. For practical reasons here we center on heterojunction bulk cells as they provide high reproducibility and easy experimental access to poly-layer devices [6].

The construction of heterojunction cells requires several basic elements apart of the proper semiconducting polymer. The polymer has to be linked to a layer—normally fullerene—that accepts the electrons from it. It is also important to count with a “buffer layer” that inhibits the recombination of electrons with the “holes” formed in the same process. Buffer layers are often made of copper-(I)-iodide and molybdenum-(VI) oxide. An appropriate design of this layer can increase the electrical yield in up to 10 times in some cases.

As limits for commercialization 10% of efficiency and 10 years of life expectancy are considered for organic cells. The yield limit already has been reached in some cases due to improvements in the chemical design of donor and acceptor materials [7]. Lifetime is still problematic as degradation of the organic substrate can take place for several reasons as photochemical reactions, interaction with traces of water, encapsulation of the device, thermal instability, etc. Same problems have been found also in other applications and strategies to overcome them are developed [8].

2. Charge transport in polymers

One of the most important aspects in the conversion of light to electrical energy is the electron transport in the semiconductor. It permits the separation of positive and negative charge and prevents the recombination of the exciton known as “quenching” [9]. Therefore a high conductivity in the organic phase as well intra- as intermolecular is desirable and the contact surface among chains in the same layers as well as between layers should be as large as possible to facilitate electron movement. Here homojunction cells have a clear advantage due to the large transition zone between substrates. Anyhow, as mentioned before, it is very difficult to produce this gradient transition in a reproducible manner resulting in larger experimental errors and poorer comparability of results for different materials. Some of the most important aspects are detailed in the following sections:

2.1 Aspects of the material

The backbone of conducting polymers is generally formed by aromatic ring systems with delocalized π -electrons that occupy completely the bonding molecule orbitals. Due to the large amount of orbitals with similar energies they form a completely occupied valence band similar to the situation in classical inorganic semiconductors. The conduction band is made up by the antibonding π^* -orbitals and is generally empty. As in the inorganic counterpart the organic polymers as well can be doped with electron abstracting or electron donating agents leading to p- or n-semiconductors. P-dotation withdraws electrons from the valence band while n-dotation adds electrons to the conduction band increasing the conductivity of the material.

The band gap is defined as the energy gap between valence and conduction band. Generally electrons can be promoted by light energy causing π - π^* -transitions. The electron loss results on the site in a mesomerically stabilized radical cation called “polaron” that can be delocalized in the polymer generally over several monomeric units.

With another bond theoretical focus the band gap corresponds to the difference between HOMO and LUMO as they correspond to the highest occupied bonding and the lowest antibonding orbitals (see **Figure 1**). The electrical conductivity in these terms is due to the excitation of an electron from the HOMO passing to the LUMO and its increased mobility in the delocalized antibonding orbital.

As molecules have a finite extension electrons can only occupy a finite number of discrete energies and normally all bonding orbitals are occupied. Electron

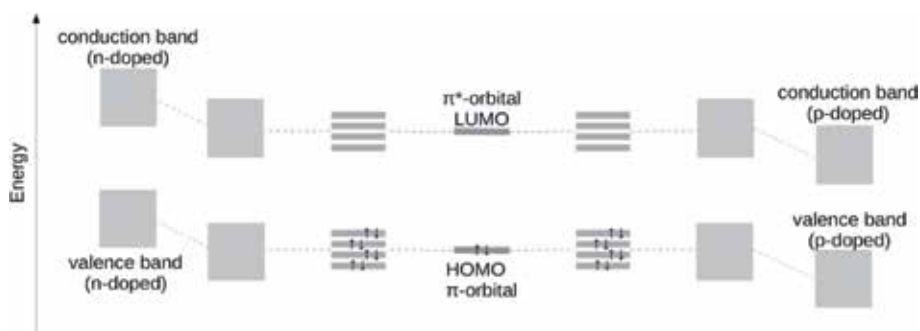


Figure 1. Energy of a simple double bond (center), in a conjugated oligomer (aside) band formation in a polymer and the influence of doping.

mobility is only possible in partly occupied orbitals that can be achieved either by doping the material adding or abstracting electrons with chemical or electrochemical methods. Physically thermal or optical excitation of electrons can be used.

Doping also changes the energies of HOMO and LUMO (or valence-band and conduction band respectively), as these energies are no fixed terms. N-doping—this is adding electrons to the LUMO-orbitals or reduction of the material—will increase the energy level as the electrons will repulse each other while p-doping has the opposite effect and decreases the orbital energy. Additionally doping also alters to a small but significant amount the positions of the atoms as the introduced charges interact with the counter-ions of the doping agent. When the concentration of the doping agent is low it results in the formation of small doped “islands of charge” that can be classified in three types: solitons, polarons and bipolarons. While solitons are wave packets, polaron and bipolaron make reference to quasiparticles.

Polarons and bipolarons can be seen as the polarization of a material due to the presence of charges moving through it. A moving electron, for example, will attract positive charges of the nuclei and push back the negative charges of the electrons in its environment. The polaron is the result of a quantum mechanical treatment of this phenomenon. Bipolarons result from the fact that close polarons may lower their respective energies similar to what happens in Cooper-pairs in superconductors. As the polarization of the surroundings stabilizes the electron lowering the energy of its fundamental state the presence of polarons will result in the formation of new energy bands in the material known as “polaron bands” and new electron transitions may be observed corresponding to this new state could be observed, too. The effect could also be interpreted as a band gap reduction in the semiconducting material [10]. Normally in organic semiconductors polarons and bipolarons are formed due to positive charges found in the polymers. A polaron will correspond to a radical cation while a bipolaron would be formed by a bi-cation. The corresponding energy scheme can be found in **Figure 2**. In organic conducting polymers the presence of various bipolarons at the same time can even lead to the formation of bipolaron bands [11].

The polaron/bipolaron effect has been widely studied on organic semiconducting polymers of different types [12–14]. The effect on bond length has even been confirmed by X-ray diffraction on model substrates with a thiophene backbone similar to the motive found in polythiophenes described later on [15].

While charges are bound to islands where linear parts of molecular chains located in parallel the electron mobility is still relatively low. Anyhow when increasing the doping concentration the charge islands start to overlap giving rise to partly

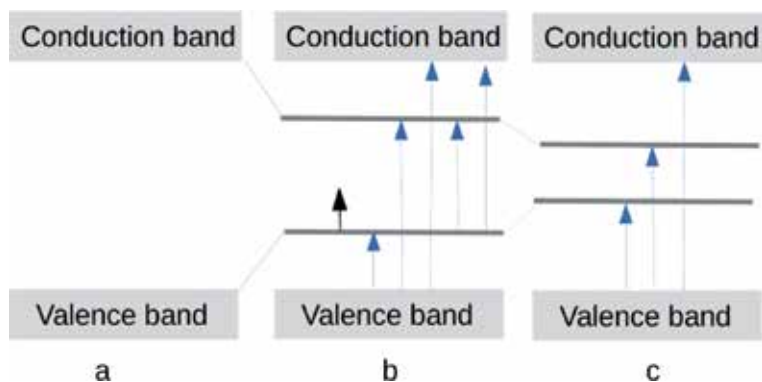


Figure 2. Energy scheme without polarons (a), in presence of polarons (b) (the black arrow represents the radical electron) and in presence of a bipolaron (c). Blue arrows represent possible electron transitions.

occupied bands. In these bands charge mobility increases drastically as electrons can move freely along the whole macromolecule and it becomes an electrical conductor. The overall conductivity depends on the electron mobility in an electrical field within the macromolecular chains as well in their “charge islands” as in the intermolecular charge transport. The step that represents the mayor resistance will limit the overall charge mobility and therewith the conductivity.

The electron transport between polymer chains is linked directly to the degree of order that present molecules. The larger the order the more likely it is that polymer chains are located in parallel and with little distance between each other and this favors the electron transfer. When chains enclose an angle or are even located in perpendicular the jump of an electron from one molecule to the other is much more difficult. In long chain polymers it is not even necessary that a charge is transported along the whole molecule but can jump in part to another nearby unity. The shorter the polymer chain the more important is ordered chain morphology as here inter-chain transport has to occur more often. Unfortunately the general tendency of this type of polymers is to present more disorder or have the chains disposed in a perpendicular manner (see **Figure 3**).

For these reasons long chain per-conjugated polymers are desirable targets for highly conducting materials. The larger the polymer backbone is the larger is the probability to find some ordered region with easy inter-chain electron transport. This is the case even when the crystalline parts are interrupted by amorphous regions. Anyhow chain defects that interrupt the electron delocalization through the chain can make it more appropriate to treat this type of material as an accumulation of several short chain structures. These structures form island-like regions with high conductivity while electron transport between islands is more difficult.

Reasons for the loss of per-conjugation could be torsion between substructures or the formation of neighbored single bonds that do not allow the π -system to extend across the affected site.

2.2 Morphology

Morphology describes the form of the material employed in the construction of a photovoltaic device. It can make reference to the form in which the molecules are present in the substrate or on the physical form of the substrates surface.

Polymer can be present as unordered glass-like phases with the polymer chains in random orientations or as crystalline regions where the chains are ordered in

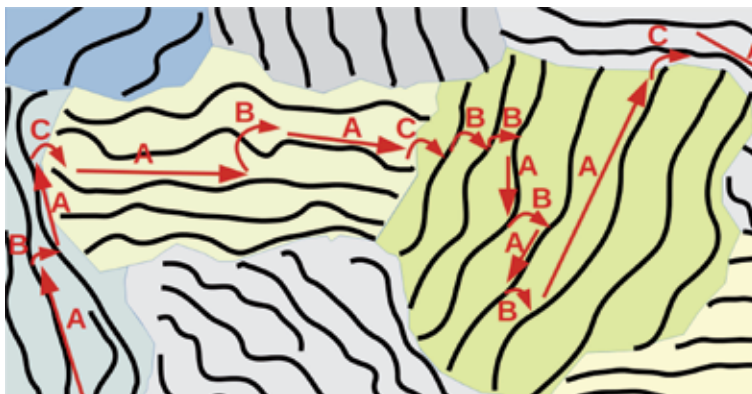


Figure 3. Schematic electron transport in polymers with conductivity islands within the same chain (A), between chains (B) and between islands (C).



Figure 4. Gradual transition in heterojunction cells (left) and hard interphase in heterojunctions (right). Larger contact reduces the electrical resistance.

parallel. This order or the lack of it will also be related to electronic properties of the substrate as polyconjugation is related to co-planar stretched structures that are lead more easily to crystalline regions while disorder requires generally more flexible structures. These are obtained when the π -system is interrupted due to larger torsion angles and the lack of overlap. Conjugation on the other hand is crucial for electron mobility and transport. Thus crystalline ordered regions will exhibit lower electrical resistance than the glass like zones and are the preferred form for high overall yields.

Morphology reflects to some extent the chemical properties of the molecules. Rigid annulated aromatic ring systems are more likely to form rigid rod-like structures than other open chain backbones. On the other hand, it can be controlled to a certain extent by the conditions used in the deposition of the layers. When deposited by sublimation slow deposition rates at relatively high temperatures favor that the polymer reaches the thermally most stable perconjugated form while fast deposition at relatively low temperatures fixes the higher disorder.

In homojunction devices various substrates have to be deposited at the same time forming a determined gradient. This adds several new parameters and complications to the manufacturing process as diffusion rates, inter-material interactions with the possibility of phase separation, differences in vapor pressure and different requirements for the formation of crystalline phases have to be controlled at the same time over the whole substrate surface. For these reasons results obtained are very difficult to reproduce.

While in homojunction cells charges can pass from one “layer” to the next along the whole gradient that exists between both, in heterojunction cells charges have to pass through the layer-layer-interface. This interface acts as an electrical resistance. Therefore increasing the contact surface with rough surfaces will help to increase the electrical yield. On the other hand, if grooves are too large in comparison with the layer thickness, there exists the risk of hole-formation and direct contact formation of layers that should be separated by the intermedium layer (see **Figure 4**). Surface morphology also depends on substrate and on deposition conditions. A review on morphology of thin film transistors that can be applied in large extend to solar cells can be found in [16].

3. Operational principles of organic photovoltaic cells (OPVCs)

OPVCs use the internal photoelectrical effect that liberates electrons and is used to transform light into electrical energy. The energy generation depends on the

absorbed light. The higher the absorption rate the more electrical energy is produced [17] in form of excitons. This makes it clear that the conversion rate is linked to the absorption coefficient of the substrate in the UV-Vis spectrum. The maximum is also indicative for the band gap. The higher the wavelength of the absorption maximum the lower is the band gap and the higher can be the theoretical photovoltaics yield. On the other hand too low band gaps favor the recombination of the electrical charges as the substrate becomes a conductor and inhibit the proper work of the cell. Therefore values of 1–2 eV are desirable what would correspond to an absorption maximum at about 1200–600 nm [18]. Absorbed energy is used to promote an electron from the HOMO to the LUMO. In a first moment the electron stays close to the positive charge produced in the same process (see **Figure 5**). The electron-hole pair is known as “exciton.” It has to be taken to the polymer—electron acceptor interface where it is separated and the electron is guided to the electrode. An exciton blocker layer (EBL) between the acceptor layer and the electrode inhibits that positive charges migrate to the electrode as this would result in direct charge recombination and no electrical current could be obtained from the device.

The distance an exciton could migrate in a layer is of the order of several 100 nm [19, 20]. The polymer donor layer should therefore have a thickness that is inferior to the migration distance to avoid that excitons recombine on their way to the acceptor-layer. Better conductivity of the polymer allows building thicker layers as it increases the maximum migration distance. Thicker polymer layers are desirable as they lead to higher absorption rates. The same accounts for the acceptor layer.

Typical dimensions found in cells using phtalocyanine-copper as donor and fullerene as acceptor, are some 20 nm for the fullerene and some 40 nm for the phtalocyanine layer for larges possible negative charge transfer.

For charge transfer also a high contact surface is desirable. Double layer and interpenetrated layer devices have been developed. Interpenetrated devices present at least theoretically higher conversion rates due to the large contact surface. Anyhow their construction is difficult and often cannot be reproduced easily.

Double layer devices on the other hand are easily obtained and their structure can be controlled with little effort but have small contact surfaces and herewith lower yields. At least for comparison reasons, the benefits of the high reproducibility compensate the lower yields as they permit detecting promising materials with more accuracy. For real world applications the thus found substrate can later still be used to produce interpenetrated devices.

The construction of a double layer device starts with a transparent and conducting substrate. Normally this is glass or poly ethylene terephthalate (PET) with an

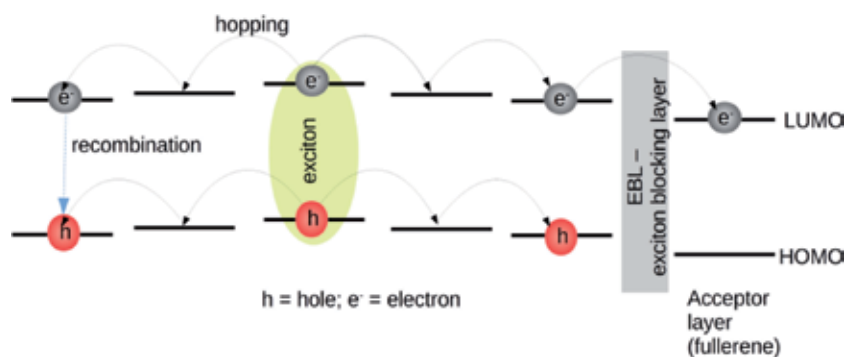


Figure 5. Excitons can travel along the organic semiconducting material and are separated to electrons and holes on the exciton blocking layer. Long diffusion length favors recombination and efficiency loss [23].

indium-tin-oxide (ITO) layer as transparent conductor. On this generally commercially available substrate an anode buffer layer (ABL) of some 20 nm is deposited. In our work we use molybdenum-(VI)-oxide and copper-(I)-iodide. In spite of their high band gap (>3 eV) characteristic for electrical insulators they help to extract cations as ITO has a high barrier to hole collection. The ABL reduces the barrier matching the energies of the involved bands. In some cases and depending on the ABL substrate it also induces higher crystallinity and improved morphology in the following polymer layer [21]. In our work with polyaniline and polyaminothiophene we observed an increase of the photoelectrical yield of some 10 times due to the proper design of the ABL using MoO₃/CuI. An explication could be the interaction of copper ions with the nitrogen atoms present in the polymer. Optimization of these interactions forces the polymer chains in a parallel direction to the polymer-ABL-interface and herewith leads to an increased order close to the interface. A prove for higher degree of orientation is given by X-ray diffraction where polymer deposits on CuI layers show more and sharper peaks than polymers grown on other substrates. The higher crystalline degree lowers the electrical resistance and this leads to the observed yield improvements. Further investigation shall show if other elements known to show high tendency to form interactions with nitrogen as cobalt, nickel or zinc have similar or even better effects on the polymer growth. After the polymer is deposited as electron donor it follows an electron acceptor layer, normally 40 nm of fullerene for best electron mobility [22].

It follows a thin layer of bathocuproine (BCP). As in the case of the ABL it is a substrate with a relatively high band gap (about 3.5 eV). Its purpose is to avoid the pass of the positive holes to the cathode and herewith recombination of holes with electrons. Therefore the layer is also known as exciton blocking layer (EBL). On the other hand the insulating properties of the material that are necessary for the exciton blocking will decrease the yield of the solar cell. Thus it is necessary to find a balance that optimizes both effects looking for an improved layer thickness. In most applications this is about 4–5 nm.

Finally on the EBL follows aluminum as cathode and selenium as protecting material that prevents oxidation of the organic molecules involved in the sandwich structure.

As shown above buffer—and blocking layers play an important role in the optimization strategy of organic photovoltaic devices and have to be treated along with the organic substrate used as electron donor. The combined tuning of all parameters has allowed designing photovoltaic cells that reach already 13% [24].

When looking for improved electron donor materials at least two important features should be taken into account:

- A high absorption coefficient in the UV-Vis and the near IR spectrum is essential. Only the absorbed light can be transformed into electrical energy and this is the most intense part of the solar spectrum that permits to reach usable electrical tensions by exciton formation.
- For long term stability the material has to be resistant to photochemical degradation as well as to high temperatures as in real world applications it will be exposed to high UV-light densities and temperatures above 100°C.

Additional optimization can be done in all other involved layers. Thus molecules with higher electron acceptor capacities and better stability than fullerene are investigated [25].

Apart of this more chemical part also the electrical behavior of the solar cell is important. Generally it can be seen as a serial circuit. All layers act in this case as

serial resistors (R_S). The electrical resistance especially of the donor—and acceptor layers will diminish the current density (J_{sc}) in the solar cell. Additionally due to the cell construction and its electrical contacts some parallel resistances (R_{sh}) can be observed. The resistances increment also when quenching (coQ) occurs as it lowers the quantity of charges present in the valence- and conduction band.

There also exists a phenomenon known as “dark current.” It consists in the flow of electrons that have already passed to the fullerenes as electron acceptors back to the HOMO of the electron donor. This effect is increased by the polarization observed in the working solar cell as here the negative charge produced in the cathode attracts the positive charges still present in the donor material and increases its density close to the electrode. The dark current could be seen as an “indirect quenching” and also lowers the obtained electrical current. To diminish the dark current, an electron blocking layer (EBL) is applied with an E_g sufficiently high as to prevent the migration of positive charges to the cathode.

As one can deduct from the previous chapters after the exciton formation charge separation is a key step of the whole photo-electrical process. Whatever substrate is used as donor- and acceptor, ionization potential (HOMO) and electron affinity (LUMO) have to match in the way that it permits the exciton dissociation. The electron affinity of the donor has to be less than that of the acceptor and the ionization potential of the acceptor has to be considerably higher than that of the donor molecule. Otherwise no exciton separation corresponding to the crossing of electrons from the LUMO of the donor to the LUMO of the acceptor will occur [26]. The whole construct can be seen in **Figure 6**.

The already mentioned need for high absorption rates makes it clear that the design of solar cell materials and the design of dyes have to be intimately related. In fact a part of the here mentioned bulk layer solar cells there exist other designs as the “dye-sensitized solar cell” (or Grätzel-cell) where the relation becomes even more evident [27]. One of the best known dye-precursor is aniline. Already its discoverer Wöhler mentioned that wood treated by aniline turned to several colors of a while. Anyhow it was Perkin some years later who patented the first synthetic dye also based on aniline—the mauveine [28]. Since then a whole family of colored compounds known as “aniline dyes” has been synthesized. It is also known that aniline can be polymerized under oxidating conditions forming a green semi-conductive polymer known as “emeraldine” due to its intense green color. Further oxidation would lead to blue-violet pernigraniline. The difference is the presence of varying quantities of hydrogen on the nitrogen atoms. Higher hydrogen-content is related to a reduced leuco-form with only amino groups while oxidation and hydrogen abstraction leads to a large proportion of quinoid structures that allow better perconjugation and herewith lowers the energy of the LUMO-orbitals. The result is a semiconducting organic material with low band gap and high absorption coefficient—perfect for applications in organic solar cells.

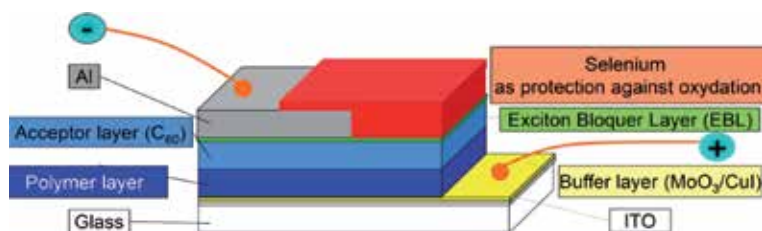


Figure 6. Typical disposition of the elements that belong to a bulk heterojunction solar cell made of organic polymers as electron donor material.

Another substructure known to lead to good properties as organic semiconducting material is thiophene. The thienyl-system is in many aspects equivalent to a benzene moiety but has an even higher “aromatic” character. Additionally due to the presence of the sulfur heteroatom it undergoes easier oxidation reactions. For this reason we became interested in aniline-analog polymers based on thiophene systems. The natural precursors in this case are 2- and 3-aminothiophenes. Unlike aniline in an amino substituted thienyl system all carbons are different leading to a larger amount of possible isomers formed in the polymerization reaction that is formally an additional substitution.

3.1 Photoelectrical parameters important for the yield of an organic photovoltaic devices

In **Figure 7** a classical J/V-diagram is shown. The characteristics of an OPVD depend mainly on four factors:

- V_{OC} or open circuit voltage
- J_{SC} or short circuit current density
- ff or form factor/fill factor
- η or photovoltaic yield

Here we explain briefly the meaning of these concepts and how they are related to the photoelectrical behavior of the solar cell.

3.1.1 The open circuit voltage V_{OC}

The open circuit voltage is the electrical potential between anode and cathode of an OPVD when illuminated and the circuit is left open. This means that no electrical current passes between the electrodes. Chemically the V_{OC} is related to the energetic difference between the LUMO of the acceptor and the HOMO of the

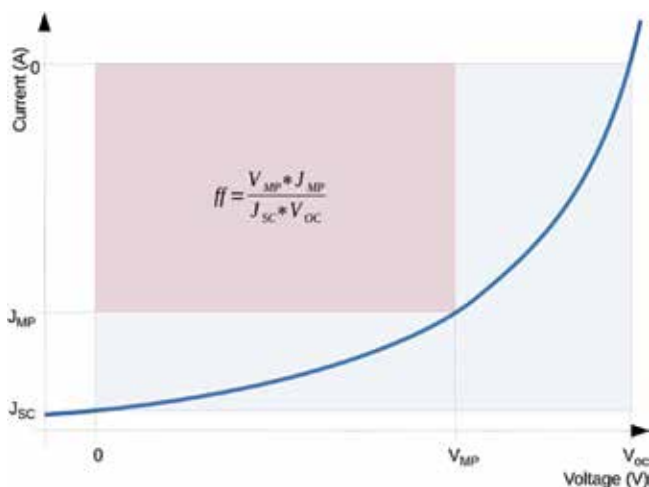


Figure 7. J/V-diagram with the graphical representation of the form factor ff as relation between the light blue and violet areas.

donor material. The larger the difference between both orbitals the higher is the voltage that can be achieved in the solar cell. In **Figure 7** you can see that V_{OC} can be determined graphically as the point where the curve passes through the x-axis of the diagram as here the current displayed on the y-axis is zero.

3.1.2 Short circuit current density J_{SC}

The short circuit current density is the photoelectrical current that can be observed when the OPVD is irradiated with light and a direct contact between both contacts forces the potential difference to be 0 V. Practically you produce a short circuit of the photoelectrical cell.

It has been demonstrated that the current density observed in these conditions is related to the interaction between the electron donor and the ABL as well as the light absorption by the donor material. In this sense a molecule with a large absorption rate over large parts of the electromagnetic spectrum contributes to increase the photoelectrical yield. Anyhow you also need a large efficiency for passing positive charges to the anode through the buffer layer. Increase in efficiency will lead directly to higher short circuit currents and as consequence to higher photoelectrical yields. As a third factor also the electrical resistance of the organic substrate is important here as resistance and electrical current in a DC device are directly related by ohms law.

3.1.3 Form factor (or fill factor) ff

The form factor of a solar cell is defined as the relation of the measured maximum electrical power that is provided by the cell and the product of J_{SC} and V_{OC} . Thus you can use the form factor as an indicator of how close the electrical behavior of the cell is to an ideal device.

In the figure you can see J_{mp} and V_{mp} as current and voltage delivered by the cell at maximum power. The product of both will give directly the maximum power that can be obtained from the device.

3.1.4 Photovoltaic yield η

$$\eta(\%) = \frac{J_{SC}[mAcm^{-2}]v_{OC}[V]ff}{I_0[mWcm^{-2}]} \quad (1)$$

The photoelectrical yield η is defined as the relation between the maximum electrical power delivered from the photoelectrical device calculated as the product of short circuit current J_{SC} , open circuit voltage V_{OC} and form factor ff divided by the power it receives in form of light energy I_0 by the formula:

As one can see from an electrical point of view J_{SC} , V_{OC} and I_0 have to be optimized together in order to obtain high yields. As we have seen before they are related to the chemical nature of the substrates that are used to build up the cell. This explains why until now improvements of the cell yields always implied the design of optimized molecules. The improvement has to imply the donor and acceptor molecules as well as the material employed in the ABL as only an optimized hole extraction work will lead to a high short circuit current. Thus an intelligent cell design will take into account that:

- The electron donor interacts with the anode in that way that allows to extract the highest possible percentage of positive charges possible.

- The donor material has a high absorption coefficient in the part of the spectrum important for electrical energy generation (near IR to UV).
- The interaction between donor and acceptor is as large as possible and an EBL has to be applied to avoid the recombination of holes with the already separated charges (dark current).

On a molecular level these needed photophysical and electrochemical properties can be achieved designing molecules with a high degree of order and preferably π -stacking interactions that bear functional groups able to optimize the interaction with the anode material and herewith the energy transference. The functional group design has to take into account the affinities that exist towards the elements involved in the ABLs. When copper is used in ABL—construction good candidates will be thio- and nitrogen(-III) containing groups as copper is known for his high affinity towards this kind of moieties. For molybdenum-(VI) also oxygen groups could be important as the small size of the element in this oxidation state fits well to the small orbitals of oxygen.

3.2 Conducting polymers in solar cells

There is a large number of monomers that lead to a variety of conducting polymers. Modifications can lead to an even increased amount of derivatives that could be employed in solar cells. Some of them have been used in our investigation group as derivatives of aniline, pyrrole, thiophene or furane.

3.2.1 Polypyrroles

Polypyrroles (**Figure 8**) can be obtained via electrochemical deposition using cyclovoltic techniques [29]. During the synthesis different solvents could be employed as THF, acetonitrile chloroform, etc. The solvent is important for the morphology of the deposited polymer. Using acetonitrile a product is obtained than from chloroform. The solvent is therefore selected according to the needs of the desired application and in function of the employed oxidating agent.

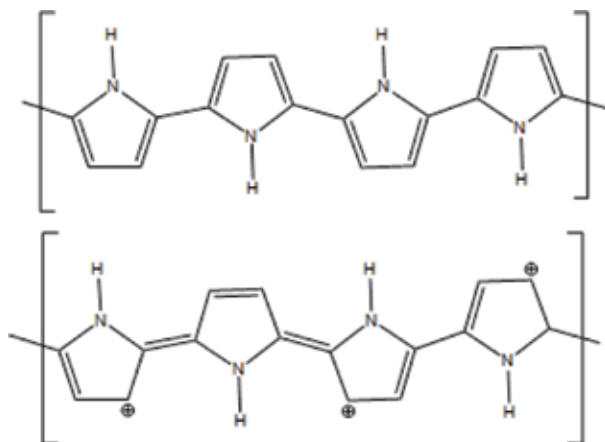


Figure 8. Polypyrrole in the ideal reduced form (above) is normally obtained as partially oxidized (p-doped) form (below). Charges are compensated by anions trapped in the polymeric material.

This way and controlling current and cycle number the layer thickness can be determined. Anyhow the polymer obtained this way has some disadvantages that limit its use in photovoltaic devices. First of all doping is only reversible in very thin layers. This limits the available charges as well as the mechanical stability of the polymer film. Second polypyrroles have shown to be very sensitive to excessive oxidation as it leads to chain degradation especially by reactions through positions 3 and 4 of the pyrrole system [30]. Blocking these positions with substituents or forming copolymers with aniline this type of degradation can be prevented leading to electrochemical more stable polymers.

These substituents according to their electron donor or acceptor characteristics will also alter the color of the polymer as they influence the HOMO and LUMO energy levels. There is also an influence due to steric hindrance as this will force the rings to present torsion angles and interrupt the perconjugated π -system. Less conjugation on the other hand will lead to decreased electron mobility and increased electrical resistance. So these effects have to be taken into account when designing a polymer more resistant to oxidative degradation.

3.2.2 Polythiophenes

Polythiophenes (**Figure 9**) are among the best studied and most promising conducting polymers [31]. Similar to polypyrroles polythiophenes can be obtained by electropolymerization from acetonitrile solutions at potentials between 0 and +1 V. The polymerization process starts with the generation of a cation radical. Due to the high reactivity of this species anhydrous conditions are crucial. The larger attention received by polythiophenes compared to polypyrroles is due to its higher chemical stability. Additionally it can be more easily processed and it is easy to obtain derivatives of the monomer. This allows tuning optical and mechanical properties of the polymeric materials and converts thiophenes in one of the most valuable starting materials for tailor made organic semiconductors.

The influences of the substituents on the properties of the polymer chain depend largely on their positions in the chain. For example, the reduced form of poly-3-methyl-thiophene shows a large variety of colors as small changes in conjugation will lead to large effects on optical- and redox properties and morphologies.

Introducing an electron withdrawing group instead of the methyl moiety will help to stabilize the radical anion when n-doping the polymer material.

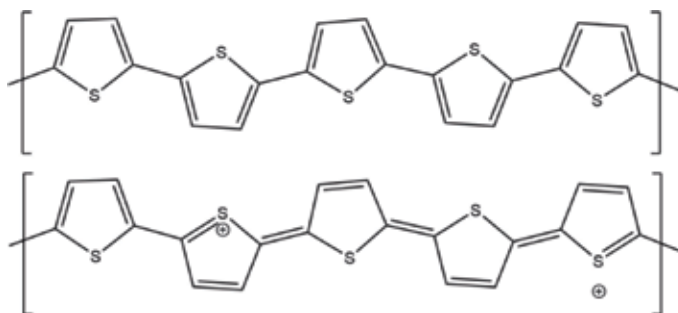


Figure 9. Polythiophene in the "normal" reduced form (above) and in the partially oxidized p-doped form presenting two charges in form of a bipolaron (below).

With copolymers obtained from nitrothiophenes and linked to carbon nanotubes yields of about 2% have been obtained [32]. They have an open circuit potential superior to polythiophenes without nitro group [33]. Other devices from polythiophenes with electron attracting groups equally have shown yields of up to 3% with an open circuit voltage of close to 1 V [34]. This shows that the groups help to stabilize the electron in the LUMO and the band match with the electron acceptor entity increases the yield [35].

Alkoxy groups as donor substituents will increase the electron density in the polymer chain and help to decrease the HOMO-LUMO-band gap leading to a red shift of the corresponding absorption band in the UV-Vis spectrum. Variations in the length of the alkyl chains however have little or no influence on the properties and no changes in conjugation or band gap values have taken place. When formed the alkoxy modified polymers are colorless and do not show absorption in the visible spectrum but turn dark blue on electrochemical reduction.

As an example 3,4-ethylenedioxythiophene (see **Figure 10**) and its polymers have a low oxidation potential, high chemical stability even at elevated temperatures and high conductivity. The copolymer with polystyrenesulfonate is one of the best organic candidates to substitute ITO as electrode material as it is at the same time highly transparent and has a very high ductility. It is already used as antistatic coating [36].

3.2.3 Polyanilines

Like polythiophenes, polyanilines (PANI) can be obtained by electrochemical oxidation via cationic radicals in a complex oxidation and reduction process as it goes along with protonation and deprotonation reactions. In acid media a typical voltamperogram of PANI shows two redox processes that correspond to the conversion of two oxidation stages present in this polymer that go along with electrochromatism. The completely reduced form is colorless and therefore known as leucoemeraldine, from Greek “leucos” = white. In this form only phenylic systems are present that are linked by secondary amino groups.

A partially oxidized form, known as emeraldine due to its green color, is formed by alternating quinoid and phenylic structures with one quinoid structure every four ring systems. The end product of oxidation known as pernigranile, presents only quinoid structures and can be distinguished by its dark blue to black color (see **Figure 11**).

Chemically all polyanilines are basic due to the presence of trivalent nitrogen. Hydrogen of secondary amino groups can also become slightly acidic, especially when the polymer is p-doped and thus positive charges are introduced to the chain.

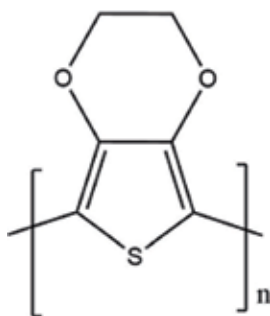


Figure 10.
Motive of poly-3,4-ethylenedioxythiophene.

Deprotonation will reduce charge density in the polymer and limits its conductivity. Otherwise it is of the same magnitude as that of other polymeric aromatic systems.

3.2.4 Aniline copolymers

In previous works we have synthesized aniline-thiophene and aniline-pyrrole copolymers to improve conductivity, conductivity and optical properties. The obtained materials show—as expected—optical and electrical properties in between the pure polymers obtained from aniline and thiophene respectively. Anyhow solubility in all cases is higher for the copolymers than for the simple separated substrates.

In the UV-Vis spectrum of the aniline-thiophene-copolymer various absorption maxima could be observed: benzenic π - π^* transitions at around 350 nm; π - π^* transitions of the thiophene systems at 450 nm and quinoid transitions at about 700 nm. Additionally in the 650–800 nm range n- π^* transitions could be detected that correspond to the transitions of non-bonding sp^2 nitrogen electrons present on quinoid ring systems [37].

When photovoltaic devices were built from this copolymer the ABL material did not have any influence on the light absorption of the polymer neither in presence of MO_3 nor CuI with no change in absorption rates and position of the peaks in the UV-Vis spectra. As consequence the band gap also remains unaltered. On the other hand the copolymer had a higher red shift than any of the pure substrates. This means that conjugation rate had increased and the band gap diminished when compared to polyaniline and polythiophene. Herewith the copolymer is a better candidate for photovoltaic devices. Effectively unlike polyaniline it shows photovoltaic yield as electron donor when used with MO_3 , CuI or mixtures of both as ABL layers with a modest yield of 0.2–0.5%. A possible explication could be the interaction of the polymer with the copper metal centers that only leads to crystallinity close to the

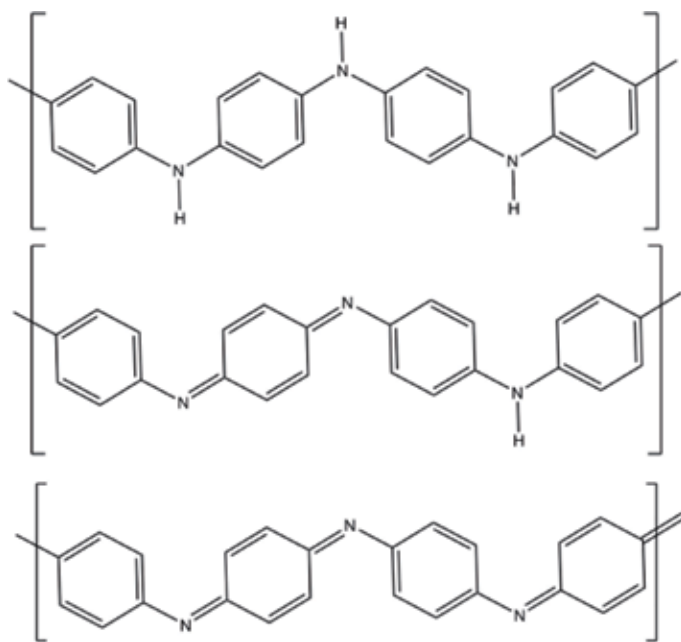


Figure 11. Polyaniline in the completely reduced (leuco) form (above), the partially oxidized (emeraldine) form and the completely oxidized (pernigraniline) form (below).

polymer-buffer layer interface while the rest of the polymer has low crystallinity. The polymer has also only a modest conductivity and a medium light absorption coefficient at about 700 nm. Thus the few polarons generated by light absorption have little mobility and most of them recombine before reaching the next layer [18, 38].

Bernède et al. have shown that MO_3 helps to increase extraction work achieving a match for the band gap between ABL and polymer. When poly-aniline-pyrrole is deposited over MO_3/CuI as ABL a small red-shift of the absorption maxima in the UV-Vis spectrum is observed compared to other ABL substrates. As in other cases the red-shift in absorption corresponds to a smaller band gap in the electronic characteristics. The photovoltaic behavior is similar to that of aniline-thiophene copolymer on any MO_3/CuI combination as ABL substrate.

3.2.5 Non polymeric organic and organometalic substrates

As already mentioned the use of different tampon layers changes the photovoltaic yield and in the right combination it helps to improve it. The effect has been studied by us and Bernède et al. not only with polymers but also with monomeric species. Copper-phthalocyanines behave similar to polymers when deposited on different buffer layers.

To find out if these or other molecules could be used in organic photovoltaic devices their electrochemical properties play a crucial role and herewith the energy of the frontier orbitals. When these molecules are deposited on an electrode by cyclic voltametry the potentials of oxidation and reduction starts can be determined. These values are related to the energies of the frontier orbitals as in oxidation an electron is withdrawn from the HOMO while during reduction an electron is deposited in the LUMO. Orbital energies are proportional to the corresponding redox potentials. Due to the experimental ease these values can be obtained the technique is used by an increasing number of workgroups.

3.3 Functional groups modifying electron density

3.3.1 Electron withdrawing groups

Electron withdrawing groups lower the energy of the antibonding LUMOs and herewith stabilize charges present in this orbital. For this reason they are used often in the design of material for electron accepting layers. They can also help to improve the electron transition between accepting and donating molecules. This is not only due to the stabilization effect on the LUMO but they also increase the interaction between both molecules. In some cases they can directly bind acceptor and donor units. The most commonly used electron attracting groups are carboxylic acids and their derivatives.

Lately investigations turned to other functional moieties as sulfonates, salicylates pyridine, catechol, etc. that help to fix both parts together [39–41] even so their electron attraction capacity is only moderate. All of these groups have proven useful in the development of devices with higher overall yield. Another new target group is the nitro moiety. It does not only withdraw more electron density, shifts the absorption maximum of the modified substrates to farther red but also has higher stability than the carboxy-derivatives. Its anchoring abilities could be attributed to the formation of π -complexes as these interactions are well known for electron rich aromatic systems and others bearing nitro groups. All these effects even increase when several nitro groups are present. As mentioned earlier this is caused by the fact that the nitro group helps to link to the electron donor and it increases the band gap and with it the open circuit voltage [42, 43].

3.3.2 Electron donating groups

While electron withdrawing groups stabilize electrons in the LUMO or the corresponding conduction band electron donor groups have the opposite effect and achieve a relative stabilization of holes in the HOMO increasing the energy of this orbital. The observed increase is even higher on the LUMO and as a consequence the gap between conduction and valence band becomes larger. When charges are present in both bands the larger energy difference leads electrically to a higher measurable open circuit cell voltage.

Donor groups also diminish the translation energy for holes making positive charge transport more effective. Unfortunately at the same time electron transport is hindered and slows down. For this reason one has to take care to equilibrate the number of electron donor and electron withdrawing groups to guarantee that both speeds are comparable and holes and electrons reach their respective electrodes at about the same time [44–46].

3.4 Buffer layers

Buffer layers also known as interface layers are crucial in organic photovoltaic devices to improve the overall yield. The correct selection and deposition of the materials that form this layer are therefore important decisions that could decide if a new approach has success or not. Changing the construction of the buffer layers up to 10-fold increase in the overall electrical yield has been observed in an extreme case [47] due to rise of the open circuit potential, the short circuit current and the form factor.

Many materials that could be used in buffer layers are permeable as well for electrons as for holes. This lowers the yield as it leads to electron-hole recombination on the electrodes. MoO₃/CuI-layers however let pass selectively positive charges and improve their pass to the anode. As during this step they are separated from the electrons this prevents recombination and herewith keeps the yield high.

The buffer layer material has also influence on the morphology of the material deposited in the next layer. In chemistry the affinity between copper and nitrogen, sulfur or other heteroatoms with free electron pairs is well known. When these elements are present in the substrate used in the next layer the intermolecular interactions will force the molecules in a defined shape and herewith provoke a determined morphology. Generally it increases the degree of order and crystallinity at least close to the interphase. This helps to increase the charge transport to the anode [47–49]. The effect of incorporation of other elements with modified affinities has still to be studied.

4. Conclusions

Photovoltaic devices nowadays represent a fast growing multi-million dollar market that has the potential to provide energy to humanity without contributing to CO₂ emissions. The largest part of it belongs to classical cells based on silicon as inorganic semiconductor. These devices however require a large amount of prime matter that are themselves highly energy consuming in their fabrication. Additionally they are not flexible, a fact that reduces the possible application fields.

A solution can be organic photovoltaic solar cells based on conducting polymers. These devices can be built as thin multi-layer constructions on flexible substrates as plastics or thin glass plates consuming just a little portion of the resources used for silicon devices. Anyhow organic cells still provide much lower conversion yields than the inorganic counterparts.

Organic bulk heterojunction cells are large constructs with various stacked layer. In the stack every layer has a dedicated function and the overall yield depends on the combination and cooperation of all parts. Strategies to improve the device will have to include necessarily not only fine tuning of each of the parts but also take into account the interaction of the layers. We present some viable and proven strategies to ameliorate the properties and interactions of several of the involved materials. These strategies include co-polymerization, the selection of appropriate functional groups understanding the influence they have on the polymer and the construction and interaction of the layers in direct contact with the semiconducting polymer.

Acknowledgements


We thank the faculty of Natural Sciences and the Department of Chemistry and Biology of the University of Atacama for financial support of the publication.

Author details

Pedro Pablo Zamora* and Klaus Bieger
University of Atacama, Copiapó, Chile

*Address all correspondence to: pedro.zamora@uda.cl

IntechOpen

© 2020 The Author(s). Licensee IntechOpen. This chapter is distributed under the terms of the Creative Commons Attribution License (<http://creativecommons.org/licenses/by/3.0>), which permits unrestricted use, distribution, and reproduction in any medium, provided the original work is properly cited. 

References

- [1] Liang Y, Xu Z, Xia J, Tsai S-T, Wu Y, Li G, et al. For the bright future—Bulk heterojunction polymer solar cells with power conversion efficiency of 7.4%. *Advances Energy Materials*. 2010;**22**:E135-E138. DOI: 10.1002/adma.200903528
- [2] Dennler G, Scharber MC, Brabec CJ. Polymer-fullerene bulk-heterojunction solar cells. *Advanced Materials*. 2009;**21**:1323-1338. DOI: 10.1002/adma.200801283
- [3] Hendsbee AD, Yuning L. Performance comparisons of polymer semiconductors synthesized by direct (hetero)arylation polymerization (DHAP) and conventional methods for organic thin film transistors and organic photovoltaics. *Molecules*. 2018;**23**:1255-1273. DOI: 10.3390/molecules23061255
- [4] Youqin Z, Jingli L, Yang L, Bo Q, Dandan S, Zheng X. Improving the charge carrier transport and suppressing recombination of soluble squaraine-based solar cells via parallel-like structure. *Materials*. 2018;**5**:759-769. DOI: 10.3390/ma11050759
- [5] Hu L, Qiao W, Zhou X, Zhang X, Ma D, Li Y, et al. Effect of compositions of acceptor polymers on dark current and photocurrent of all-polymer bulk-heterojunction photodetectors. *Polymer*. 2017;**114**:173-179. DOI: 10.1021/acs.macromol.5b00859
- [6] Li S, Ye L, Zhao W, Zhang S, Mukherjee S, Ade H, et al. Energy-level modulation of small-molecule electron acceptors to achieve over 12% efficiency in polymer solar cells. *Advanced Materials*. 2016;**28**:9423-9429. DOI: 10.1002/adma.201602776
- [7] Yoo D, Kim Y, Min M, Ahn GH, Lien D-H, Jang J, et al. Highly reliable superhydrophobic protection for organic field-effect transistors by fluoroalkylsilane-coated TiO₂ nanoparticles. *American Chemical Society Nano*. 2018;**12**:11062-11069. DOI: 10.1021/acsnano.8b05224
- [8] Qi X, Lo Y-C, Zhao Y, Xuan L, Ting H-C, Wong K-T, et al. Two novel small molecule donors and the applications in bulk-heterojunction solar cells. *Frontiers in Chemistry*. 2018;**6**:1-8. DOI: 10.3389/fchem.2018.00260
- [9] Nam PH, Dinh N, Thu L, Ngo TT. Light absorption and luminescence quenching properties of hybrid bulk heterojunction materials based on the blend conducting polymers. *Journal of Nanoscience and Nanotechnology*. 2017;**17**:450-453. DOI: 10.1166/jnn.2017.12423
- [10] Kislyuk V, Dimitriev OP, Pud A, Ledoux-Rak I. In-situ conductivity and UV-Vis absorption monitoring of iodine doping-dedoping processes in poly(3-hexylthiophene) (P3HT). *Journal of Physics Conference Series*. 2011;**286**:012009. DOI: 10.1088/1742-6596/286/1/012009
- [11] Singh AK, Prakash R. Conduction mechanism in electronic polymers: Effect of morphology. *Advanced Optoelectronic Materials and Devices*. 2008;**33**:65-74. DOI: 10.1016/j.progpolymsci.2008.08.001
- [12] Stafström S, Brédas JL, Epstein AJ, Woo HS, Tanner DB, Huang WS, et al. Polaron lattice in highly conducting polyaniline: Theoretical and optical studies. *Physical Review Letters*. 1987;**59**:1464-1467. DOI: 10.1103/PhysRevLett.59.1464
- [13] Brédas JL, Scott JC, Yakushi K, Street GB. Polarons and bipolarons in polypyrrole: Evolution of the band structure and optical spectrum upon doping. *Physical Review B*. 1984;**30**:1023-1025. DOI: 10.1103/PhysRevB.30.1023

- [14] Kaneto K, Kohno Y, Yoshino K. Absorption spectra induced by photoexcitation and electrochemical doping in polythiophene. *Solid State Communications*. 1984;**51**:267-269. DOI: 10.1016/0038-1098(84)90684-7
- [15] Zheng S et al. Isolation and crystal structures of two singlet bis(triarylamine) dications with nonquinoidal geometries. *Journal of the American Chemical Society*. 2006;**128**:1812-1817. DOI: 10.1021/ja0541534
- [16] Virkar A, Mannsfeld S, Bao Z, Stingelin N. Organic semiconductor growth and morphology—considerations for organic thin-film transistors. *Advanced Materials*. 2010;**22**:3857-3875. DOI: 10.1002/adma.200903193
- [17] Cattin L, Bernède JC, Lare Y, Dabos-Seignon S, Stephant N, Morsli M, et al. Improved performance of organic solar cells by growth optimization of MoO₃/CuI double anode buffer. *Physica Status Solidi A*. 2013;**4**:802-808. DOI: 10.1002/pssa.201228665
- [18] Bailey-Salzman RF, Rand BP. Semitransparent organic photovoltaic cells. *Applied Physics Letters*. 2006;**88**:233502. DOI: 10.1063/1.2209176
- [19] Samiullah M, Moghe D, Scherf U, Guha S. Diffusion length of triplet excitons in organic semiconductors. *Physical Review B*. 2010;**82**:205211. DOI: 10.1103/PhysRevB.82.205211
- [20] Mikhnenko O, Blom PWM, Nguyen T-Q T. Exciton diffusion in organic semiconductors. *Energy & Environmental Science*. 2015;**8**:1867-1888. DOI: 10.1039/C5EE00925A
- [21] Bernède JC, Cattin L, Morsli M, Kanth SRB, Patil S, Stephant N. Improvement of the efficiency of organic solar cells using the terthiophene-pyran-malononitrile (T3PM) as electron donor, through the use of a MoO₃/CuI anode buffer layer. *Energy Procedia*. 2012;**31**:81-88. DOI: 10.1016/j.egypro.2012.11.168
- [22] Stasyuk A, Stasyuk O, Sola M, Voityuk A. Peculiar photoinduced electron transfer in porphyrin-fullerene akamptisomers. *Chemistry A European Journal*. 2019;**25**:1-18. DOI: 10.1002/chem.201804999
- [23] Suryana R. Variation of MEH-PPV layers with/without PEDOT:PSS layer in organic solar cells. *IOP Conf Series. Materials Science and Engineering*. 2018;**333**:012022. DOI: 10.1088/1757-899X/333/1/012022
- [24] Sun J, Ma X, Zhang Z, Yu J, Zhou J, Yin X, et al. Dithieno[3,2-b:2',3'-d]pyrrol fused nonfullerene acceptors enabling over 13% efficiency for organic solar cells. *Advanced Materials*. 2018;**30**:1-8. DOI: 10.1002/adma.201707150
- [25] O'Regan B, Schwartz DT. Efficient photo-hole injection from adsorbed cyanine dyes into electrodeposited copper(I) thiocyanate thin films. *Chemistry of Materials*. 1995;**7**:1349-1354. DOI: 10.1021/cm00055a012
- [26] Gregg BA. Excitonic solar cells. *The Journal of Physical Chemistry B*. 2003;**107**:4688-4698. DOI: 10.1021/jp022507x
- [27] Miettunen K, Vapaavuori J, Poskela A, Tiihonen A, Lund PD. Recent progress in flexible dye solar cells. *Energy & Environment*. 2018;**7**:1-11. DOI: 10.1002/wene.302
- [28] Cova T, Pais A, de Melo J. Reconstructing the historical synthesis of mauveine from Perkin and Caro: Procedure and details. *Scientific Reports*. 2017;**7**:1-8. DOI: 10.1038/s41598-017-07239-z

- [29] Neoh KG, Tan TC, Kang ET. Chemical synthesis and characterization of polypyrrole-chlorine complex. *Polymer*. 1988;**29**:553-558. DOI: 10.1016/0032-3861(88)90377-1
- [30] Otero TF, Garcia de Otazo JM. Polypyrrole oxidation: Kinetic coefficients, activation energy and conformational energy. *Synthetic Metals*. 2009;**59**:681-688. DOI: 10.1016/j.synthmet.2008.12.017
- [31] Osaka I, Abe T, Shinamura S, Miyazaki E, Takimiya K. High-mobility semiconducting naphthodithiophene copolymers. *Journal of the American Chemical Society*. 2010;**132**:5000-5001. DOI: 10.1021/ja101125p
- [32] Minas M, Mikroyannidis JA, Kymakis E. A facile covalent modification of a single wall carbon nanotubes by thiophene for use in organic photovoltaic cells. *Solar Energy Materials & Solar Cells*. 2010;**94**:267-274. DOI: 10.1016/j.solmat.2009.09.013
- [33] Wu J, Ma Y, Wu N, Lin Y, Lin J, Wang L, et al. 2,2-Dicyanovinyl-ended capped oligothiophenes as electron acceptor in solution processed bulk heterojunction organic solar cells. *Organic Electronics*. 2015;**23**:28-38. DOI: 10.1016/j.orgel.2015.04.003
- [34] Kim J, Cho N, Min H, Kim C, Kwan J, Ko J. Push pull organic semiconductors comprising of bis dimethylfluorenyl amino benzothiophene donor and various acceptors of solution processed small molecule organic solar cells. *Solar Energy Materials and Solar Cells*. 2012;**102**:159-166. DOI: 10.1016/j.solmat.2012.03.007
- [35] Li Z, Liu C, Guo J, Zhang X, Zhou Y, Shen L, et al. Reducing charge recombination of polymer solar cells by introducing composite anode buffer layer. *Solar Energy*. 2018;**171**:8-15. DOI: 10.1016/j.solener.2018.06.056
- [36] Groenendaal L, Jonas F, Freitag D, Pielartzik H, Reynolds JR. Poly(3,4-ethylenedioxythiophene) and its derivatives: Past, present, and future. *Advanced Materials*. 2000;**7**:481-494. DOI: 10.1002/(SICI)1521-4095(200004)12:7<481::AID-ADMA481>3.0.CO;2-C
- [37] Yang C, Fang Z, Zhang P. UV-Vis spectra of polyaniline doped with camphor sulfonic acid in organic solvent. *Central South University of Technology*. 1999;**16**:76-78. DOI: 10.1007/s11771-999-0014-6
- [38] Cattin L, Dahou F, Lare Y, Morsli M, Tricot R, Jondo K, et al. The influence of the HOMO energy level of the organic electron donor on the effectiveness of the anode buffer layer in photovoltaic solar cells. *Energy Procedia*. 2012;**31**:89-95. DOI: 10.1016/j.egypro.2012.11.169
- [39] Lan T, Lu X, Zhang L, Chen Y, Zhou G, Wang Z. Enhanced performance of quasi-solid-state solar cells by tuning the building blocks in D-(π)-A'- π -A. *Journal of Materials Chemistry A*. 2014;**2**:1-11. DOI: 10.1039/C5TA01025J
- [40] Leandri V, Ruffo R, Trifiletti V, Abbotto A. Asymmetric tribranched dyes: An intramolecular cosensitization approach for dye-sensitized solar cells. *European Journal of Organic Chemistry*. 2013;**30**:6793-6801. DOI: 10.1002/ejoc.201300962
- [41] Cong J, Yang X, Liu J, Zhao J, Hao Y, Wang Y, et al. Nitro group as a new anchoring group for organic dyes in dye sensitized solar cells. *Chemical Communications*. 2012;**53**:6663-6665. DOI: 10.1039/C2CC31516E
- [42] Khanmohammadi K, Sohrabi B, Zamanib MR. Effect of electron-donating and -withdrawing substitutions in naphthoquinone sensitizers: The structure engineering of dyes for DSSCs. *Journal of Molecular*

Structure. 2018;**1167**:274-279. DOI: 10.11648/j.jenr.20140303.13

[43] Lin K, Xie B, Wang Z, Xie R, Huang Y, Duan C, et al. Star-shaped electron acceptors containing a truxene core for non-fullerene solar cells. *Organic Electronics*. 2018;**52**:42-50. DOI: 10.1016/j.orgel.2017.10.009

[44] Wen SH, Li A, Song J, Deng WQ, Han KL, Goddard WA. First principles investigation of anisotropic hole mobilities in organic semiconductors. *Journal of Physical Chemistry B*. 2009;**113**:8813-8819. DOI: 10.1021/jp900512s

[45] Chi W-J, Zheng D-Y, Chen X-F, Li Z-S. Optimizing thienothiophene chain lengths of D- π -D hole transport materials in perovskite solar cells for improving energy levels and hole mobility. *Journal of Materials Chemistry C*. 2017;**5**:10055-10060. DOI: 10.1039/C7TC03232C

[46] Brédas J-L, Beljonne D, Coropceanu V, Cornil J. Charge-transfer and energy transfer processes in π -conjugated oligomers and polymers: A molecular picture. *Chemical Reviews*. 2004;**104**:4971-5004. DOI: 10.1021/cr040084k

[47] Zamora PP, Diaz FR, del Valle MA, Cattin L, Louarn GJ, Bernède JC. Effect of CuI anode buffer layer on the growth of polymers thin films and on the performances of organic solar cells. *Natural Resources*. 2013;**4**:123-133. DOI: 10.4236/nr.2013.41A016

[48] Han S, Shin SW, Seo M, Gupta D. Improving performance of organic solar cells using amorphous tungsten oxides as an interfacial buffer layer on transparent anodes. *Organic Electronics*. 2009;**10**:791-797. DOI: 10.1016/j.orgel.2009.03.016

[49] Bernède JC, Cattin L, Morsli M, Berredjem Y. Ultra-thin metal

layer passivation of the transparent conductive anode in organic solar cells. *Solar Energy Materials & Solar Cells*. 2008;**92**:1508-1520. DOI: 10.1016/j.solmat.2008.06.016

Impact of Active Layer Morphology, Density of States, Charge Carrier Concentration, and Local Charge Density Fluctuations on Bimolecular Recombination of Bulk Heterojunction Solar Cells: A Theoretical Perspective

Daniel Christiansen and Shafiq Mehraeen

Abstract

We study the merits of a reaction-diffusion model to unravel the effects of active layer morphology and donor-acceptor interfacial roughness, density of states, charge carrier concentration, and local charge density fluctuations on the bimolecular recombination kinetics in bulk heterojunction organic semiconductors. We consider the cases of a single and composite electronic density of states (DoS) that consists of a superposition of a Gaussian and an exponential DoS. Using kinetic Monte Carlo (KMC) simulations, we apply the reaction-diffusion model in order to investigate the factors impacting bimolecular recombination (BMR) kinetics and rates at short and long time scales. We find that morphology, donor-acceptor interfacial roughness, and charge carrier concentration only affect BMR time, whereas DoS characteristics as well as local charge density fluctuations can significantly impact BMR kinetics and rates.

Keywords: organic photovoltaics, bimolecular recombination, Langevin dynamics, bulk heterojunction, reaction-diffusion, kinetic Monte Carlo

1. Introduction

Early organic photovoltaic (OPV) devices based on bilayer architectures suffered from limited interfacial area between the donor (D) and acceptor (A) components, which resulted in low charge separation efficiency. To overcome this issue, the bulk heterojunction (BHJ) architecture was introduced in the mid-1990s and consists of a D/A blend. Compared to the bilayer architecture, the blend structure provides a much larger D/A interfacial area that is distributed throughout the active layer, facilitating exciton dissociation and thereby charge separation. Recent data [1–5] using high-resolution temporal techniques underlie that exciton in

high-performance devices can readily dissociate within less than 100 fs. In such cases, exciton formation, diffusion, and dissociation are efficient. However, it is the competition between charge migration toward the electrodes and bimolecular charge recombination [6], which appears to play the leading role in decreasing the performance of OPV devices. Thus, a detailed understanding of the loss mechanism emerging from BMR is critical.

While the dominant loss mechanism is still a matter of debate [7], there is increasing evidence [1, 8, 9] that in BHJ-based solar cells, non-geminate (bimolecular) recombination represents the primary factor limiting device performance [10–13]. However, establishing the most relevant physical model of BMR remains a challenge. Previously, a number of experimental data show that, depending on the mobility of charge carriers [14], recombination evolves from trap-assisted first-order (monomolecular) dynamics under short-circuit current conditions to second-order (bimolecular) Langevin dynamics under open-circuit voltage conditions [1, 15–19]. Though, many recent studies [20–29] indicate that BMR in organic solar cells significantly deviates from a traditional Langevin description.

In the case of polymer-fullerene-based devices, the charge decay dynamics at open-circuit voltage exhibit approximately a third-order dependence on charge density [24, 25]. Thus, in order to be consistent with experimental data, the proportionality constant of the Langevin model must depend on charge density. This third-order dependence of the BMR rate on charge density has been suggested to arise as a result of either a carrier lifetime dependence on charge density [30], recombination via an exponential tail of states [31, 32], or carrier trapping in an inhomogeneous distribution of localized states [20, 21, 26]. Also, it was suggested that although traps can sometimes enhance the dissociation of geminate pairs into free carriers [33], they also act as recombination centers leading to a Shockley-Read-Hall (SRH) recombination dynamics [34–38].

While experimental efforts have been extensive, there are few theoretical studies to date [26, 39–41] that have been conducted to understand the charge carrier loss mechanisms in organic solar cells. As a result, the mechanisms underlying BMR in OPV devices remain poorly understood. Thus, it is desirable to develop a thorough understanding of the BMR loss mechanisms that currently limit the enhancement of the efficiency of organic solar cells.

The purpose of the present work is to investigate how the kinetics of non-geminate recombination is affected by (i) the detail of the morphology of the active layer; (ii) energetic disorder and various distributions of densities of electronic states, (iii) charge carrier density, and (iv) local charge density fluctuations. Utilizing KMC simulations, we develop a reaction-diffusion model to explain the role that abovementioned factors play in BMR of BHJ OPV solar cells.

2. Theoretical model

To study the impact of interfacial roughness, DoS, and charge carrier density on BMR in a BHJ device at open-circuit voltage, we develop a theoretical three-dimensional reaction-diffusion lattice model. In this model, we only look at electron-hole recombination after exciton dissociation.

We represent electrons and holes as particles and antiparticles that can randomly diffuse through the space, restricted to a cubic lattice, and react (recombine) once they collide (occupy same lattice site). In our model, we restrict holes and electrons to move exclusively within the D/A domains of a randomly generated morphology, which are discussed next in this section. Based on the reaction-diffusion model,

we perform KMC simulations on a cubic lattice of $100 \times 100 \times 100$ sites with lattice spacing equivalent to 1 nm, unless otherwise mentioned. We ignore additional charge generation or charge extraction processes at the electrodes. Since we are mainly interested in BMR kinetics at low charge carrier concentrations, we also neglect the effect of electrostatic interactions.

To evaluate the kinetics of BMR at the device scale, unless otherwise mentioned, we apply a reflective boundary condition on all sides such that charge carriers cannot exit from the simulation box until they entirely recombine. We perform KMC simulations on disordered morphologies. In creating bulk heterojunction OPV using solution processing, a disordered morphology, also called random morphology, is formed. This random morphology is comprised of two organic semiconductors, intermixed randomly within the active (light-absorbing) layer. We computationally generate the random morphologies utilizing the potential model [42–45] in which random morphologies of D/A domains in space are represented by means of a random potential $\psi(x, y, z)$. ψ is a random scalar function represented as a sum of several propagating plane waves in random directions given by

$$\psi(x, y, z) = \sum_{i=1}^M \sin \left(\frac{2\pi}{\lambda} [k_{i1}x + k_{i2}y + k_{i3}z] + \theta_i \right), \quad (1)$$

where $k_{i1} = \cos(\alpha_i) \sin(\varphi_i)$, $k_{i2} = \sin(\alpha_i) \sin(\varphi_i)$, $k_{i3} = \cos(\varphi_i)$, $M = 25$, α_i and θ_i are uniformly distributed random numbers between $[0, 2\pi]$, and φ_i is another uniformly distributed random number between $[0, \pi]$. λ in Eq. (1) is directly proportional to the average size of D and A domains. ψ , whose value fluctuates between $-M$ and M , randomly splits the space into D domains wherever $\psi \geq 0$ and A domains wherever $\psi < 0$. In this way, ψ allows the representation of a random morphology within the simulation box.

The diffusion and recombination of charge carriers are simulated using the KMC technique where the charge carrier transfer rate ν_{ij} from any site i to one of the six nearest neighboring sites, j , is described by the Miller-Abrahams model [46]:

$$\nu_{ij} = \nu_0 \exp(-2\gamma r_{ij}) \exp[-\beta(\Delta E_{ij} + |\Delta E_{ij}|)/2], \quad (2)$$

where $\vec{r}_{ij} = \vec{r}_j - \vec{r}_i$, $r_{ij} = |\vec{r}_{ij}|$, and \vec{r}_i are the position vectors of site i , in our simulations $r_{ij} = a = 1$ nm represents the lattice site spacing, $\nu_0 = 7 \times 10^{12} \text{ s}^{-1}$ denotes the intrinsic attempt frequency, $\gamma = 3 \times 10^7 \text{ cm}^{-1}$ indicates the inverse of localization radius, $\beta = (k_B T)^{-1}$ is the Boltzmann constant, and $\Delta E_{ij} = E_j - E_i$ is the energy level difference between adjacent sites i and j .

We make use of the first reaction method [47, 48] in the KMC simulations. At each step of the KMC simulations, we compute the hopping rates of all possible hops of all charge carriers and make a hopping list. The next hop is randomly selected from the hopping list. We find the hopping time, τ_k , for the k th step in the KMC simulation from

$$\tau_k = \frac{-\ln(X)}{\sum_{i,j, i \neq j}^N \nu_{ij} L_i}, \quad (3)$$

where N represents the total number of sites, L_i is equal to unity if site i is occupied by a charge carrier and zero otherwise, and X is a random number uniformly distributed between 0 and 1 (note that the ν_{ij} values are the rates of possible hops updated at each time step). We run each simulation until all charge carriers recombine.

To study the effect of DoS on the kinetics of BMR, we consider the diffusion of electrons and holes in energetically disordered systems, where we separately describe the energetic spectrum of the system by (i) a Gaussian distribution of states, centered at $E = 0$, with a total DoS concentration N_G and a distribution width δ_G :

$$\rho_G(E) = \frac{N_G}{\sqrt{2\pi\delta_G^2}} \exp\left(\frac{-E^2}{2\delta_G^2}\right), \quad (4)$$

and (ii) an exponential distribution of states:

$$\rho_E(E) = \frac{N_E}{\delta_E} \exp\left(\frac{E}{\delta_E}\right), E \leq 0, \quad (5)$$

where the DoS concentration and distribution width are given by N_E and δ_E , respectively. We also study the BMR kinetics in the presence of a composite DoS for which we superpose a Gaussian and an exponential distribution. To generate an energetic disorder in the KMC simulations, a random Gaussian or exponentially distributed value taken from Eq. (4) or (5), respectively, is assigned to each lattice site in the beginning of each simulation. We start each simulation with a random distribution of equal numbers of electrons and holes, whose initial densities are given by ρ_0 , within the A and D domains. We allow single occupancy on each lattice site only.

3. Results and discussions

It has been shown experimentally that morphology of the active layer is indeed one of the primary factors affecting bimolecular recombination and so the device efficiency [49–51]. To demonstrate the role of morphology in BMR kinetics, we apply our reaction-diffusion model to four different morphologies. Random morphologies are obtained using the potential model according to Eq. (1). These morphologies are depicted in **Figure 1A–D** where hollow and red regions represent D and A domains, respectively. **Figure 1A** and **B** represents a bilayer solar cell with flat and rough interfaces, correspondingly. The structures in **Figure 1C** and **D** are representative of BHJs with large and small domain sizes of D and A, generated using Eq. (1) with $\lambda = 100$ nm and 20 nm (with domains of size 50 and 10 nm), respectively. **Figure 1E** illustrates an initial distribution of 600 electrons and holes illustrated by red and blue dots, respectively, in the simulation box of $100 \times 100 \times 100$ lattice sites representing a charge density of $6 \times 10^{17} \text{ cm}^{-3}$ in a BHJ device. In **Figure 1E** the domain size of D and A is smaller than the lattice size (1 nm); thus, for this structure, charge carriers are allowed to occupy any lattice sites during diffusion.

Figure 1F compares the KMC simulation results (solid lines) with analytical results (color dashed lines) for the decay of the charge density, ρ , with time, t , using morphologies in **Figure 1A–E**. Details of the analytical form of charge carrier density decay are given in Appendix B. In these simulations, we assume an isoenergetic energy spectrum, where DoS is theoretically a delta function peaked at $E = 0$, to consider solely the effect of morphology and the interfacial roughness on BMR kinetics. According to **Figure 1F**, density decay is only delayed as the D/A interfacial area increases from **Figure 1A–E**. The quantities of interest are the impact of morphology and interfacial roughness on BMR exponent, α , which is defined by

$$\rho(t) \sim t^{-\alpha}, \text{ as } t \rightarrow \infty, \quad (6)$$

and charge carrier lifetime. **Figure 1F** suggests that any variation in D/A interfacial area via morphological change does not influence BMR exponent. This is clearly seen from the charge density decay curves in **Figure 1F** at long time, exhibiting Langevin dynamics ($\rho \sim t^{-1}$) regardless of the morphology.

Details of how to obtain charge carrier lifetime from density decay are given in Appendix B (Eq. (B7)). As shown in **Figure 1F**, the time it takes to reach a certain density decreases from morphology 1A–E, suggesting that charge carrier lifetime decreases with the D/A interfacial area from **Figure 1A–E**. Time shifts in the density decay illustrated in **Figure 1F** indicate that each sequential increase in the D/A interfacial area from the morphology in **Figure 1A–E**, which corresponds to a decrease in D and A average domain sizes, enhances the charge carrier lifetime.

Figure 2 illustrates the effect of morphology shown in **Figure 1A–E** on charge carrier lifetime, τ (see Appendix B for details). **Figure 2A** illustrates that morphology only affects charge carrier lifetime at short time, whereas at long time, charge carrier lifetime linearly increases with time, independent of the morphology. This long-time behavior demonstrates the charge carrier diffusion-limited recombination, which does not depend on the morphology. **Figure 2B** demonstrates that for a fixed charge carrier density, charge carrier lifetime always decreases with D/A interfacial area. This decrease can be as large as two orders of magnitude between morphologies in **Figure 1A** and **E**. **Figure 2B** also shows that in isoenergetic DoS, charge carrier lifetime decreases with carrier density, proportional to $\rho^{-1/\alpha}$, independent of the morphology.

We now look at how BMR rate is affected by morphology and D/A interfacial area. Utilizing the analytical form (see Appendix B) which approximates KMC simulation results for charge density decay shown in **Figure 1F**, we find that BMR rate at short time is intimately correlated with the D/A domain size. As shown in

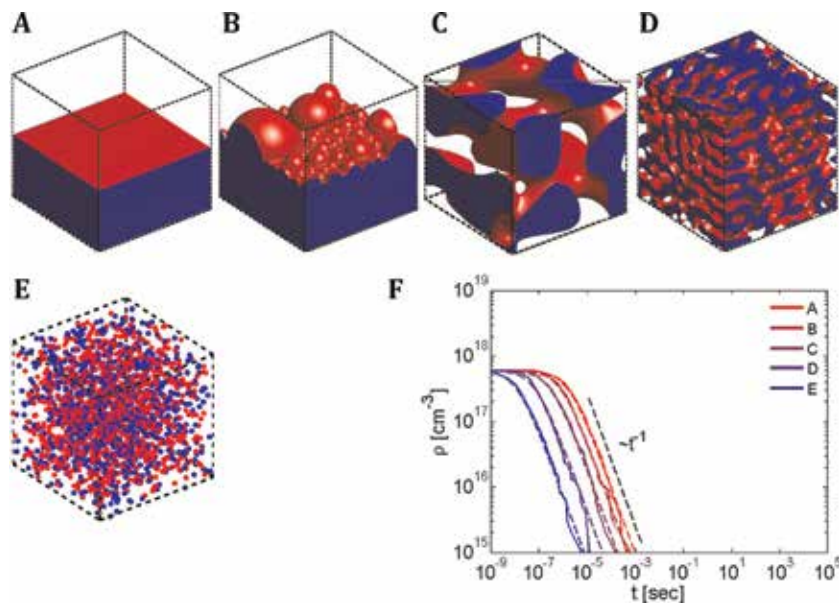


Figure 1. Regardless of morphology, in a bilayer with (A) flat interface and (B) rough interface, a BHJ with (C) coarse and (D) fine donor (hollow regions)-acceptor (red regions) network, and a BHJ with D/A cluster size of less than 1 nm (E) long-time behavior of charge carriers during BMR follows Langevin dynamics ($\rho \sim t^{-1}$), i.e., variation in D/A interfacial area does not change BMR exponent. Solid lines are from KMC simulations, and color dashed lines are analytical form (F).

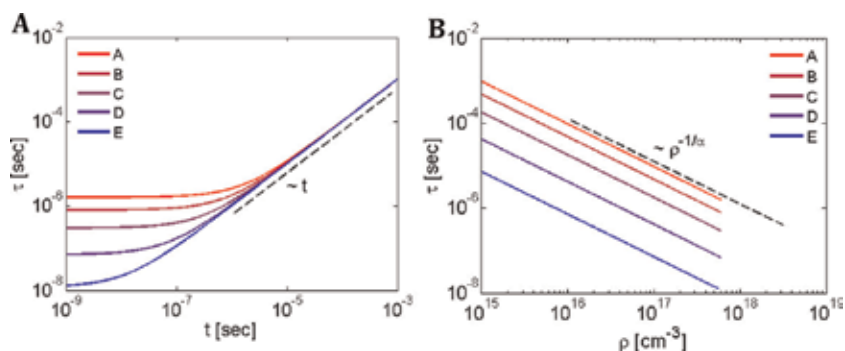


Figure 2. Variation of charge carrier lifetime with (A) time and (B) charge carrier density for different morphologies shown in **Figure 1A–E**.

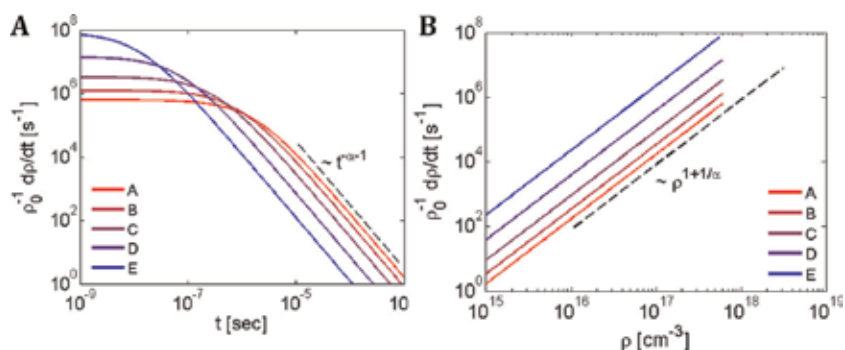


Figure 3. Variation of BMR rate with (A) time and (B) charge carrier density for different morphologies shown in **Figure 1A–E**.

Figure 3A, at short time, BMR rate is inversely proportional to the D/A interfacial area and domain size, i.e., BMR rate is the highest for morphology in **Figure 1E** and the lowest for the morphology in **Figure 1A**. However, at long time, BMR rate becomes proportional to the D/A interfacial area and domain size, meaning that BMR rate is the highest for morphology in **Figure 1A** and the lowest for the morphology in **Figure 1E**. Results shown in **Figure 3A** suggest that BMR rate at long time in **Figure 1A** can be two orders of magnitude larger than that in **Figure 1E**. Such a difference in BMR rate will be explained in the following paragraphs.

Initially, due to very close proximity of counter charge carriers at short time when charge carrier density is high, BMR rate is large for morphologies with small domain size. However, at longer time, when charge carrier density decreases, morphologies with small domain size restrict the motion of charge carriers (holes within D and electrons within A domains) more than those with large domain size. This restriction lowers BMR rate in morphologies with smaller domain size, and so diffusion-limited recombination will be the dominant effect at low charge carrier density.

The abovementioned BMR kinetics is only observed when we look at the effect of BMR on BMR rate in time. However, if we express BMR rate in terms of charge carrier density, as shown in **Figure 3B**, for a given carrier density, morphologies with small domain size (large D/A interfacial area shown in **Figure 1E**) always exhibit larger BMR rate than those with large domain size (small D/A interfacial

area depicted in **Figure 1A**). This trend in BMR rate is consistently observed regardless of charge carrier density shown in **Figure 3B**.

To justify that variation in morphology and D/A interfacial area of an organic solar cell does not affect BMR rate at long time, we look at charge density decay using the morphologies in **Figure 1A–E** but now in the presence of two different DoS, Gaussian and exponential distributions. **Figure 4** compares KMC simulation results of charge density decay due to BMR in the presence of DoS with energies of all lattice sites taken from a Gaussian distribution with $\delta_G = 3 k_B T$ (**Figure 4A**) and an exponential distribution with $\delta_E = 3 k_B T$ (**Figure 4B**). From KMC simulation results in **Figure 4**, we observe that for a given DoS distribution and different morphologies, charge density decay curves stay parallel at long time. Our observation suggests that morphology impacts the delay in BMR kinetics by shifting the density decay curves in time as the D/A interfacial area increases, whereas DoS affects the BMR rate ($\rho_0^{-1} d\rho(t)/dt$) and BMR exponent in particular.

Figure 5 compares the effect of DoS distribution at low DoS concentration on the charge carrier density decay during BMR. **Figure 5A and B** illustrates charge density decay in the presence of Gaussian DoS distribution with $N_G = 10^{19} \text{ cm}^{-3}$ and exponential distribution with $N_E = 10^{19} \text{ cm}^{-3}$, respectively. For these simula-

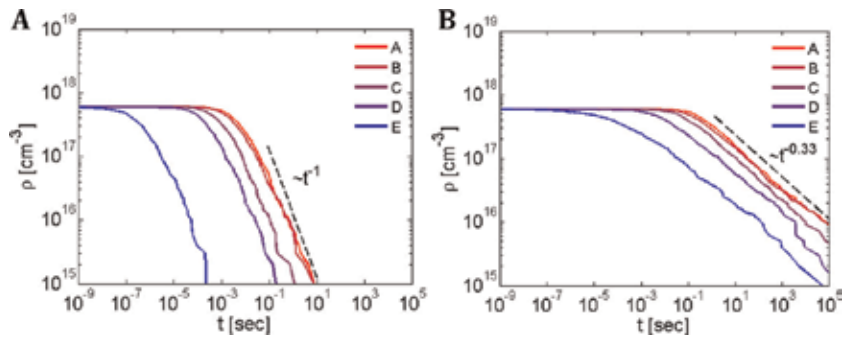


Figure 4. Impact of DoS, with (A) Gaussian distribution using $N_G = 10^{21} \text{ cm}^{-3}$ and $\delta_G = 3 k_B T$ and (B) exponential distribution using $N_E = 10^{21} \text{ cm}^{-3}$ and $\delta_E = 3 k_B T$, on BMR kinetics. Different morphologies in **Figure 1A–E**, corresponding to red to blue, only shift the density decay in time, whereas DoS impacts the BMR exponent and thus rate at long time.

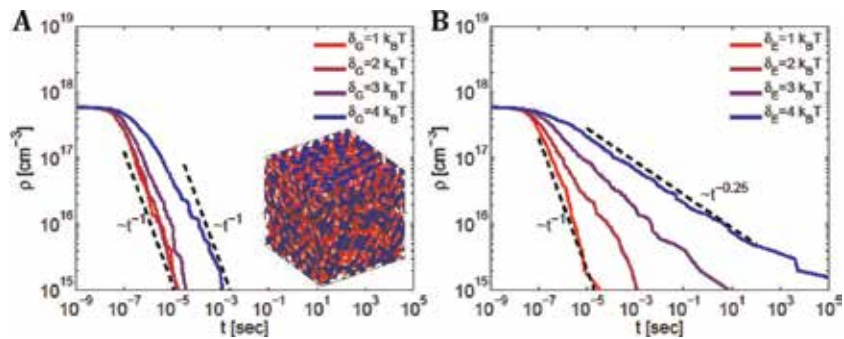


Figure 5. KMC simulations of density decay due to BMR in 1% DoS ($N_G = N_E = 10^{19} \text{ cm}^{-3}$) in an otherwise isoenergetic spectrum with a random morphology generated by potential model ($\lambda = 10 \text{ nm}$, see inset in panel A) using (A) Gaussian and (B) exponential DoS. For Gaussian DoS, the results manifest a constant BMR exponent (-1) and thus decay rate at long time regardless of distribution width. However, exponential DoS exhibits BMR exponent (varying from -1 to -0.25) and decay rates depending on the width of the distribution.

tions, 1% of lattice site energies are taken from Gaussian or exponential distributions with different distribution widths ranging from $1 k_B T$ to $4 k_B T$. The energies for the rest of lattice sites are set to $E = 0$ (isoenergetic spectrum). Our KMC simulation results of BMR illustrated in **Figure 5A** in the presence of Gaussian DoS demonstrate that increasing the distribution width, from $\delta_G = 1 k_B T$ to $4 k_B T$, only delays BMR, while it does not affect BMR exponent. These results suggest that the behavior of charge carriers at long time within a Gaussian DoS follows Langevin dynamics, $\rho \sim t^{-1}$, as shown by long-time asymptotes in dashed lines.

In contrast to Gaussian DoS, 1% exponential DoS (low concentration) in an otherwise isoenergetic spectrum not only delays BMR but also decreases BMR exponent. This is clearly demonstrated in **Figure 5B**, where KMC simulation results (solid lines) agree with the theoretical long-time asymptotic predictions, $\rho \sim t^{-(T/T_0)}$ [52, 53], $T_0 = \delta_E/k_B$, illustrated by dashed lines for the same range of distribution width, δ_E , and DoS concentration, $N_E = 10^{19} \text{ cm}^{-3}$. Comparing **Figure 5A** and **B** suggests that BMR kinetics is highly influenced by exponential DoS compared to Gaussian DoS. Specifically, $3 k_B T$ variation in distribution width slows BMR by 10 orders of magnitude to reduce carrier density to 0.001 of initial carrier concentration if exponential DoS is present (compare abscissa in **Figure 5B** for $\delta_E = 1 k_B T$ and $4 k_B T$). This is comparable to the Gaussian DoS in which BMR is only slowed to about two orders of magnitude by the same variation in the distribution width (compare abscissa in **Figure 5A** for $\delta_G = 1 k_B T$ and $4 k_B T$). It is noteworthy that results in **Figure 5** are rendered when DoS concentration is low. Next, we will consider cases where DoS concentration is high.

Looking at high DoS concentrations (100% of energies of lattice sites taken from a DoS distribution) shown in **Figure 6** reveals that Gaussian DoS ($N_G = 10^{21} \text{ cm}^{-3}$) does not change BMR exponent, leading to Langevin behavior of charge carriers at long time ($\rho \sim t^{-1}$). However, when exponential DoS with high concentration ($N_E = 10^{21} \text{ cm}^{-3}$) is employed, BMR exponent, BMR rate, and the long-time kinetics of charge carriers during BMR are highly influenced by the width of the distribution. Particularly, there is a significant change in the BMR exponent and thus the rate for $\delta_E > 1 k_B T$ as shown in **Figure 6B**. Comparing **Figures 5** and **6** suggest that DoS concentration only delays the BMR, whereas DoS distribution (Gaussian or exponential) affects the BMR exponent and rate at long time.

To further study the effect of DoS concentration on the BMR kinetics, we now look at different DoS concentrations for two cases: a Gaussian and an exponential

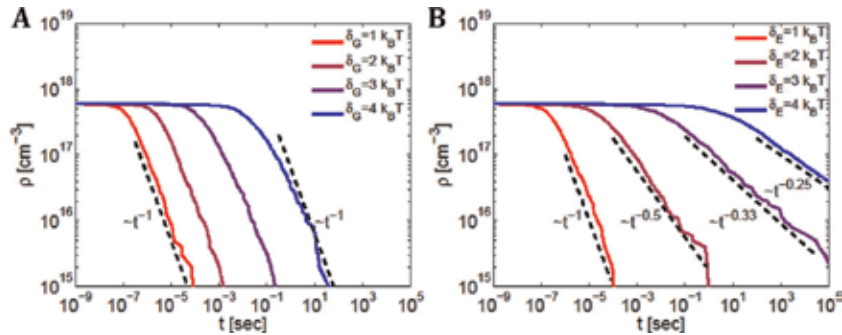


Figure 6.

KMC simulation results (solid lines) of density decay of charge carriers in a BHJ with a random morphology generated by potential model (see **Figure 5A** inset) using (A) Gaussian and (B) exponential DoS with high concentration ($N_G = N_E = 10^{21} \text{ cm}^{-3}$) and different distribution widths varying from $1 k_B T$ to $4 k_B T$. Dashed lines indicate asymptotes at long time.

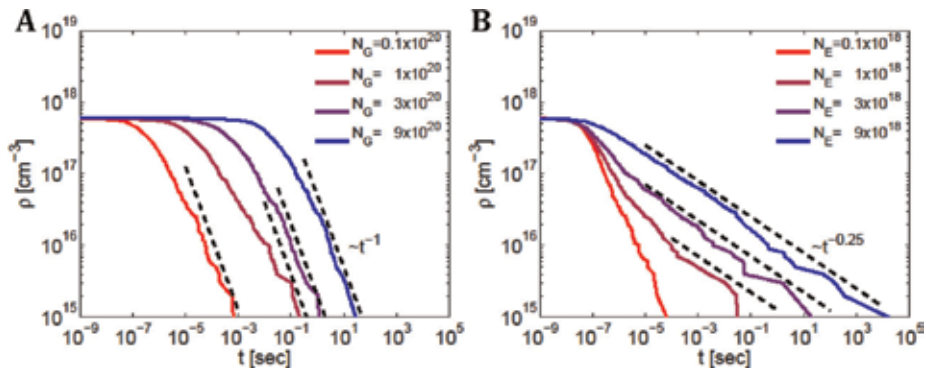


Figure 7. KMC simulations of charge density decay (solid lines) due to BMR for different DoS concentrations with (A) Gaussian DoS, $N_G = 0.1 \times 10^{20}$, 1×10^{20} , 3×10^{20} , and $9 \times 10^{20} \text{ cm}^{-3}$ and (B) exponential DoS, $N_E = 0.1 \times 10^{18}$, 1×10^{18} , 3×10^{18} , and $9 \times 10^{18} \text{ cm}^{-3}$, in an otherwise isoenergetic spectrum. Dashed lines illustrate long-time asymptotes to the density curves.

DoS distribution with fixed distribution width $\delta_G = \delta_E = 3 k_B T$. **Figure 7** compares the impact of DoS concentration on BMR kinetics. For a Gaussian DoS, increasing the DoS concentration, N_G , from 0.1×10^{20} to $9 \times 10^{20} \text{ cm}^{-3}$ only delays BMR (shift the density decay curve in time) without any impact on the BMR exponent and rate as shown in **Figure 7A**. A similar trend is observed when an exponential DoS is utilized as shown in **Figure 7B**. Note that in our KMC simulations, BMR exponent, which is constant as shown in **Figure 7A** and **B**, at long time only depends on the width of the DoS distribution for exponential DoS but is independent of the width for Gaussian DoS. The BMR exponent and thus the rate can be readily obtained from asymptotic dashed lines shown in **Figure 7A** and **B**. These results indicate that DoS concentration only delays BMR and does not affect BMR exponent and rate at long time.

We now turn to the effect of initial charge carrier density on the kinetics of BMR. **Figure 8** illustrates the KMC simulation results of charge density decay due to BMR for different initial charge carrier concentrations, ranging from $\rho_0 = 10^{17} \text{ cm}^{-3}$ to $27 \times 10^{17} \text{ cm}^{-3}$, from red to blue, respectively, for isoenergetic DoS with $E = 0$ (**Figure 8A**), Gaussian DoS (**Figure 8B**), and exponential DoS (**Figure 8C**) with DoS concentration of 10^{21} cm^{-3} with $3k_B T$ distribution width. Results in **Figure 8** reveal that charge carrier density at long-time approaches a unique asymptote regardless of the initial charge concentration. We observe that the only influence of initial charge carrier concentration is to delay the transition time at which BMR exponent and rate transition from nearly zero at very short time to the asymptotic value at long time. We find that this shift strongly correlates with the DoS distribution, which is larger in exponential (**Figure 8C**) than Gaussian (**Figure 8B**) DoS. Overall, the results illustrated in **Figure 8** suggest that initial charge carrier density does not affect BMR exponent and rate. It also does not render a delay in BMR, as all charge density decay curves with different initial charge densities merge at long time.

Thus far, we have looked at the kinetics of BMR in a BHJ device in the presence of single DoS distribution. In reality, however, DoS distributions may better be explained by a composite DoS, representing two distributions for band (conducting) and band-tail (trap) states. To account for the effect of a composite DoS, we now consider a DoS consisting of Gaussian band states and exponential band-tail states, illustrated in **Figure 9**.

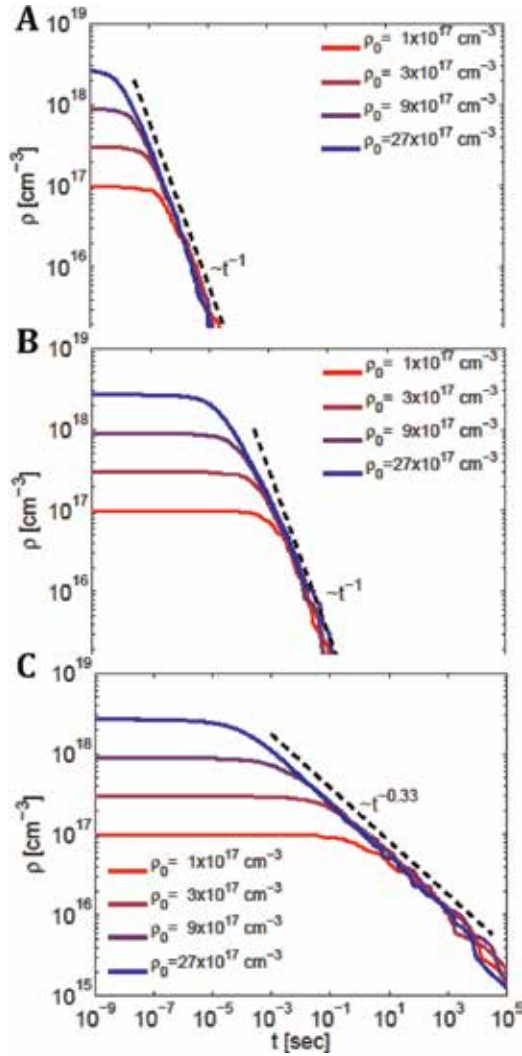


Figure 8.

KMC simulation results of charge carrier density decay (solid lines) during BMR for different initial charge carrier densities ranging from $\rho_0 = 10^{17}$ to $27 \times 10^{17} \text{ cm}^{-3}$ with (A) isoenergetic DoS, (B) a Gaussian DoS with concentration $N_G = 10^{21} \text{ cm}^{-3}$, and (C) an exponential DoS with concentration $N_E = 10^{21} \text{ cm}^{-3}$ and fixed $3k_B T$ distribution width. Dashed lines are the long-time asymptotes. These results indicate that initial charge carrier concentration neither changes BMR exponent or rate nor delays BMR.

KMC simulation results for BMR and charge density decay in the presence of a composite DoS shown in **Figure 9** are presented in **Figure 10**. **Figure 10A** illustrates the density decay (solid lines) during BMR using Gaussian band states with DoS concentration of $N_G = 0.99 \times 10^{21} \text{ cm}^{-3}$, for different distribution width of $\delta_G = 1, 2, 3,$ and $4 k_B T$, corresponding to red to blue, respectively, and exponential band-tail states with DoS concentration of $N_E = 0.01 \times 10^{21} \text{ cm}^{-3}$ and distribution width of $\delta_E = 3k_B T$. Results in **Figure 10** demonstrate that as the Gaussian distribution of band states broadens, BMR kinetics is delayed, exhibiting the dominance of Langevin dynamics ($\rho \sim t^{-1}$) at intermediate time with BMR exponent of 1. However, the long-time BMR exponent is always governed by the width of band-tail state distribution ($\rho \sim t^{-0.33}$), which is 0.33, depicted by dashed line in **Figure 10A**.

The dependence of long-time BMR density decay on the band-tail state distribution width can be further justified by **Figure 10B**, depicting the impact of

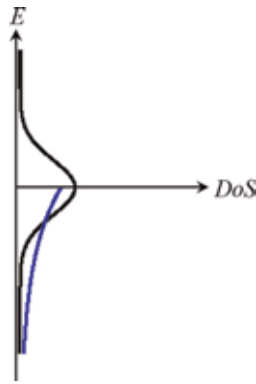


Figure 9. Energetic disorder described by superimposing two distributions, a Gaussian DoS (black), $\rho_G(E)$, centered at $E = 0$, and an exponential DoS (blue), $\rho_E(E)$, positioned below $E = 0$.

exponential band-tail state distribution width on the BMR density decay. The width of distribution ranges from $\delta_E = 1$ to $4 k_B T$, and its DoS concentration is the same as that utilized in **Figure 10A**. Results in **Figure 10B** suggest that BMR decay rate is directly correlated with the width of band-tail state distribution. As the band-tail state distribution broadens (the band-tail state distribution width increases), BMR exponent and rate decrease. In this case, the charge density decay approaches that of analytical form for exponential DoS shown by dashed lines ($\rho \sim t^{-(T_0/T)}$, $T_0 = \delta_E/k_B$). Elevating the DoS concentration of band-tail state distribution (increasing DoS concentration of exponential distribution in the composite DoS shown in **Figure 9**), from $N_E = 0.05 \times 10^{19}$ to $4 \times 10^{19} \text{ cm}^{-3}$, with the total DoS concentration being constant, $N_G + N_E = 10^{21} \text{ cm}^{-3}$, only delays the BMR (shifts charge density decay in time) without changing long-time BMR rate as shown in **Figure 10C**.

Overall, **Figure 10** indicates that (i) Gaussian band states only widen the intermediate time window at which charge carrier behavior can be described by Langevin dynamics ($\rho \sim t^{-1}$), (ii) long-time behavior of charge carriers is governed by the distribution of band-tail states, and (iii) the ratio of band to band-tail state DoS concentrations only induces a time delay to the instant at which initial BMR regime with small BMR rate transitions to the long-time BMR regime with large BMR rate. Charge carriers' behavior during this transition state is governed by band state DoS distribution.

Thus far, our theoretical treatment provides a detailed prediction of the physical behavior underlying BMR in bilayer and BHJ solar cells. Specifically, our theoretical model predicts the effect of morphology, DOS, trap (i.e., band-tail states) concentration on the BMR, and its rate in such devices. We now demonstrate that our theoretical model reproduces experimental data [25] taken from 170 nm thick 1:1 blend film of P3HT and PCBM at various light-pulse intensities at open-circuit voltage. Using the potential model in Eq. (1) with $\lambda = 50 \text{ nm}$, we generate random morphologies reminiscent of BHJs, as shown in the inset of **Figure 11**. To simulate various light-pulse intensities as shown in **Figure 11**, from top to bottom corresponding to 60, 24, 6, and $3.6 \mu \text{ J cm}^{-2}$, respectively, we perform simulations with various initial charge densities. We utilize our theoretical model with initial charge densities of $n = 6.3 \times 10^{17}$, 4×10^{17} , 1.3×10^{17} , and $0.58 \times 10^{17} \text{ cm}^{-3}$, respectively. To match the experimental data, we apply the model to an energetically disordered D/A network with Gaussian ($\delta_G = 2k_B T$) and exponential ($\delta_E = 2.2k_B T$) DOS for band and band-tail states, respectively. We set the density of

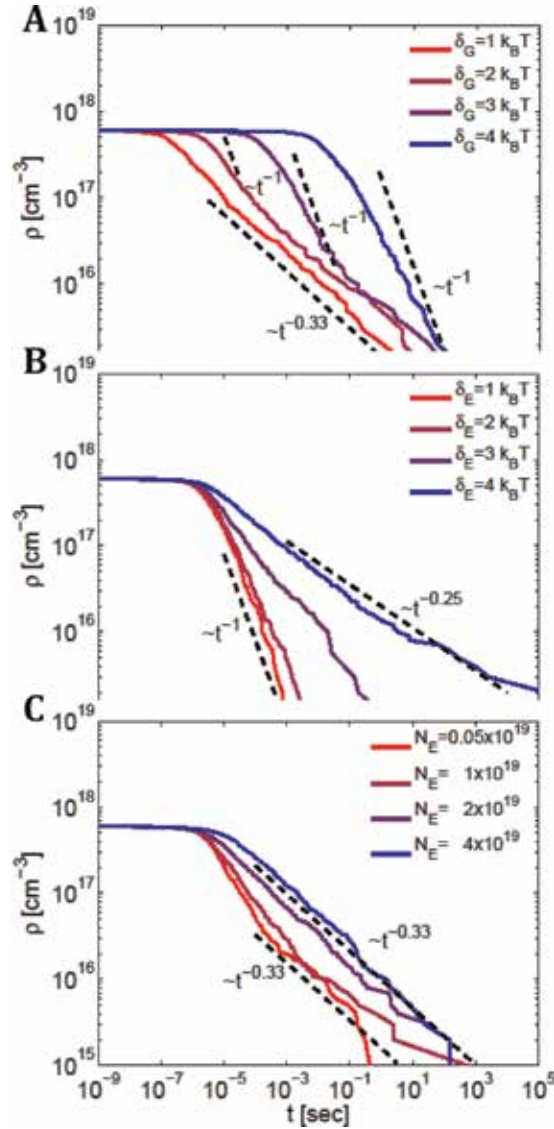


Figure 10.

KMC simulation results of density decay due to BMR for a composite DoS shown in **Figure 9**, with (A) different δ_G varying from $1 k_B T$ to $4 k_B T$, $\delta_E = 3 k_B T$, $N_G = 0.99 \times 10^{21} \text{ cm}^{-3}$, $N_E = 0.01 \times 10^{21} \text{ cm}^{-3}$; (B) different δ_E varying from $1 k_B T$ to $4 k_B T$, $\delta_G = 2 k_B T$, with the same DoS concentration described in **Figure 10A**; and (C) band-tail state DoS concentration varying from $N_E = 0.05 \times 10^{19}$ to $4 \times 10^{19} \text{ cm}^{-3}$, subject to $N_G + N_E = 10^{21} \text{ cm}^{-3}$, $\delta_G = 2 k_B T$, and $\delta_E = 3 k_B T$.

“conducting” (band) and “trapping” (band-tail) states, N_G and N_E to $0.97 \times 10^{21} \text{ cm}^{-3}$ and $2.6 \times 10^{19} \text{ cm}^{-3}$, respectively.

Figure 11 demonstrates that simulation results (solid lines) for decay of charge density, ρ , at open-circuit voltage are in reasonably good agreement with experimental data [25] (black dots) taken at various light-pulse intensities. The question that arises is whether the superposition of two DOS distributions for band and band-tail states is necessary to reproduce experimental data shown in **Figure 11**. We attempted to fit experimental data using only exponential distribution for band-tail states with parameters $\nu_0 = 5.9 \times 10^{11} \text{ s}^{-1}$, $N_E = 2.3 \times 10^{19} \text{ cm}^{-3}$, and $\delta_E = 2.2 k_B T$. Our simulation results (not shown) suggest that using only exponentially

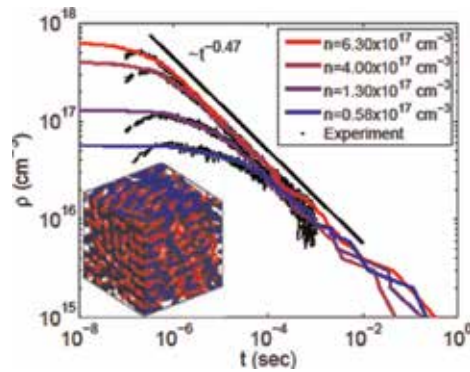


Figure 11.

Comparison of charge density decay with time from experimental data (black dots) at open-circuit voltage and various light-pulse intensities and from simulation results (solid lines) at various initial charge densities utilizing Gaussian band states and exponential band-tail states.

distributed band-tail states requires initial charge concentration $n = 10^{18}$, 6×10^{17} , 1.4×10^{17} , and $0.65 \times 10^{17} \text{ cm}^{-3}$, from high to low light intensities, respectively, which seems to be systematically higher than those with two DOS distributions. For instance, given the simulation results, we suspect that charge concentration at the highest light-pulse intensity, 10^{18} cm^{-3} , is beyond the physical values; thus, making it difficult to justify that only exponential distribution for band-tail states without the need for band states is enough.

Altogether, our results, illustrating the impact of DoS on BMR exponent and rate, demonstrate that for narrow exponential distribution of DoS ($\delta_E \leq k_B T$), charges move diffusively; therefore, recombination exhibits a Langevin-type dynamics. As distribution becomes broader, electrons and holes transition from a diffusive to sub-diffusive motion, leading to a sub-diffusion-limited reaction process.

Sub-diffusive motion of polarons comes from anomalous diffusion in disordered media. This is due to long waiting times occurring during diffusion through traps. There are physical mechanisms of sub-diffusion including random walks in dynamically disordered medium. Essentially, sub-diffusive motions and thus sub-diffusive limited reactions (electron-hole collision) arise when the waiting time between hops follows a power-law distribution with finite variance at long time [54–57]. This is true provided that reactants are distributed homogeneously throughout the medium. Given this condition, utilizing thermally activated or Miller-Abrahams hopping mechanisms, one will find (see Appendix A) that reacting random walkers, such as electrons and holes, in quench disordered exponentially distributed DoS sampled from a power-law hopping time distribution, exhibit a sub-diffusive motion. Consequently, if electrons and holes move sub-diffusively in a medium and are allowed to recombine, they manifest a sub-diffusive limited reaction. This is reminiscent to what is observed in transient absorption spectroscopy and transient photovoltage experimental data [25] taken from P3HT/PCBM BHJ device.

Another mechanism by which sub-diffusive limited reactions can occur is where reactants are inhomogeneously dispersed; thus there will be local relative density fluctuations (density difference) in the medium. The role of local relative density fluctuations on the charge density decay can be better understood by invoking of binary reactions with two species. In Langevin dynamics, the relative density is zero due to the uniform density assumption. However, because of initial fluctuations in the relative density of the reactants, experimental observations [58–61], theoretical

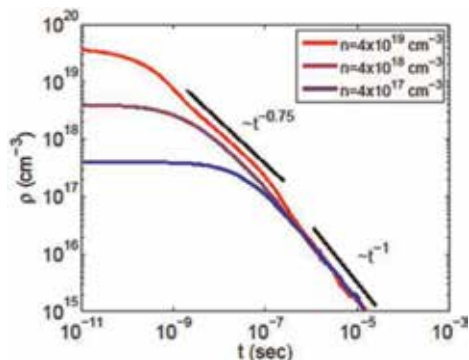


Figure 12.

KMC simulation results (solid lines) illustrating the effect of local relative density fluctuation on the dynamics of bimolecular recombination applied to BHJ morphology shown in **Figure 1D**. At high density ($\geq 4 \times 10^{18} \text{ cm}^{-3}$), deviation from Langevin dynamics is apparent with charge density decay $\sim t^{-3/4}$. Effect of local relative density fluctuations is not present in low initial densities ($< 4 \times 10^{18} \text{ cm}^{-3}$).

predictions, numerical simulations [62–68] of reaction-diffusion of two species with periodic boundary conditions in one and two dimensions [63, 69], and reflective boundary conditions in three dimensions [65] demonstrate deviation from Langevin dynamics. These relative density fluctuations lead to the density decay of species with a power law given by Ref. [69]

$$\rho \sim t^{-\frac{d_f}{2d_w}}, \quad (7)$$

where d_f is the fractal dimension of the medium and d_w is the fractal dimension of the random walk. Here, it is assumed that charges diffuse in the medium similar to a random walk.

Similar to binary reactions, in random distribution of electrons and holes in BHJs, the uniform charge density assumption may not be valid, especially in a D/A network, where initial charge separation is indicative of non-zero local relative density fluctuations. To find the extent of influence of relative density fluctuations in BHJs on BMR, we perform KMC simulations. We employ our theoretical model in a cubic cell of size $200 \times 200 \times 200$ with morphology given in **Figure 1D**. Our simulation results (solid lines) shown in **Figure 12** indicate deviation from Langevin dynamics at charge concentration greater than $4 \times 10^{18} \text{ cm}^{-3}$. Transition to Langevin-type behavior occurs at about 10^{-6} s at which point the density starts to decay as t^{-1} . Such deviation is not observed for lower initial charge densities. We also find that our observation is consistent with previous calculations for binary reactions [64].

4. Conclusions

Developing a reaction-diffusion model, we have studied the effect of morphology, DoS, charge carrier density, and local charge density fluctuations on BMR kinetics in OPV cells at short and long time scales. We have looked at single as well as composite DoS that consists of a superposition of Gaussian and exponential distributions. In all of our KMC simulations, we always find two regimes during BMR: a slow charge density decay (small BMR rate) followed by a fast electron-hole

annihilation (large BMR rate). Our KMC simulation results obtained from bilayer as well as BHJs with random morphology indicate that D/A interfacial roughness and morphology in organic solar cells only affect the total BMR time and do not influence BMR exponent and rate at short or long time scales. Our simulation results also illustrate that charge carrier concentrations in BHJ devices neither change BMR rate nor time. It only shifts the time at which transition from slow to fast BMR occurs.

Furthermore, we find that the effect of morphology, interfacial roughness, and charge carrier density is in contrast to the effect of DoS, whose characteristics can completely modify BMR kinetics and rate. We find that kinetics of charge carriers due to BMR in a Gaussian DoS can be explained by Langevin dynamics, demonstrating a density decay inversely proportional to time. However, dynamics of charge carriers in the presence of exponential DoS deviates from Langevin dynamics, illustrating a slower dynamics for distribution width higher than the thermal energy. Particularly, our KMC simulations show that the BMR rate at long time is controlled by the width of DoS distribution and that the DoS concentration changes BMR time without changing the BMR rates at short or long time. Extending our findings from single to composite DoS indicates that the BMR rate is controlled by the characteristics of trap state distribution and that the ratio of band to tail state concentration dictates the BMR time, specifically the transition time from slow to fast BMR regime.

We also demonstrate that decrease in recombination rate can be due to local fluctuation in the electron and hole density difference and sub-diffusive motion of polarons. Sub-diffusivity arises from a power-law distribution of jump time. Utilizing Miller-Abrahams charge transfer relation, we find that such power-law distribution is present in the hopping mechanism provided by our theoretical model. The power-law distribution necessitates an exponentially distributed dynamically disordered system, to which Miller-Abrahams or thermally activated hopping is applied. We also find that existence of a quenched material is not necessary for a sub-diffusive motion of charges. Altogether, we find a very rich predicted behavior on which bimolecular loss mechanisms can depend.

Future work will address the effect of positional disorder and its coupling effect with energetic disorder on charge transfer rate and transport properties of OPV cells using hopping mechanisms and lattice model.

Acknowledgements

This work has been supported by the seed funding from the College of Engineering at University of Illinois, Chicago.

Appendix A. Bimolecular recombination kinetics at long-time limit

The long-time behavior of charge carriers in bulk heterojunction OPVs is approximated by the behavior of reacting continuous time random walk (CTRW) in Euclidean medium, representing a sequence of jump-trap-release events. For reacting CTRW, $\rho(t) \sim R(t)$, where $\rho(t)$ and $R(t)$ are the carrier density and survival probability at time t , respectively. It turns out that for a reacting CTRW, $R(t) \sim 1/S(t)$ for three dimensions [70], where $S(t)$ is the number of distinct sites visited by a CTRW. $S(t)$ can be visualized as the volume that a carrier sweeps during

diffusion. One may also note that in regular lattices, $S(t) \sim \langle \vec{r}^2(t) \rangle$ [67], where $\langle \vec{r}^2(t) \rangle$ is the mean square displacement (MSD) of CTRW at time t . From the above argument, one concludes that

$$\rho(t) \sim \frac{1}{\langle \vec{r}^2(t) \rangle}. \quad (\text{A1})$$

Without loss of generality, in the one-dimensional analogue of CTRW model, we describe the transport in terms of succession of jumps of length x , which is drawn from a probability distribution function (PDF), $\lambda(x)$, followed by a trapping event at the same position x for time interval t drawn from the PDF, $w(x)$. In this model, the probability that a carrier is found at position x in space at time t is given by propagator $W(x, t)$, whose Fourier-Laplace transform obeys the relation [54]

$$W(k, u) = \frac{1 - w(u)}{u} \frac{W_0(k)}{1 - w(u)\lambda(k)}, \quad (\text{A2})$$

where k and u represent Fourier and Laplace variables, respectively, $W_0(k)$ indicates the Fourier transform of the initial condition $W_0(x)$, and $w(u)$ and $\lambda(k)$ are the Laplace and Fourier transform of $w(t)$ and $\lambda(x)$, respectively.

In our KMC simulations, jump length is equal to the lattice spacing; thus for small k values.

$$\lambda(x) = \delta(x - a) \text{ and } \lambda(k) = \exp(-ika) = 1 - a^2k^2 + O(k^4), \quad (\text{A3})$$

where $\delta(x)$ is the delta function. Note that in our reaction-diffusion model, waiting time PDF is governed by the DoS distribution. Here, we consider Gaussian, uniform, and exponential DoS as follows.

Gaussian DoS. Using Eq. (4), a thermally activated process [53] with hopping frequency from a site with energy E to any other site is expressed by

$$\nu = \nu_0 \exp\left(\frac{E}{k_B T}\right), E \leq 0, \quad (\text{A4})$$

where ν_0 is the intrinsic attempt frequency. Since the jump time, τ , is inversely proportional to the hopping frequency; thus,

$$\tau = \frac{1}{\nu_0} \exp\left(-\frac{E}{k_B T}\right) \quad (\text{A5})$$

The randomness in jump time comes from the randomness in energies sampled from DoS distribution. Thus, finding E from Eq. (A5) and its derivative with respect to τ , one arrives at the PDF of the jump time

$$w(\tau)d\tau = -\rho_G(E)dE \quad (\text{A6})$$

with a finite mean jump time $\bar{\tau}$ equal to

$$\begin{aligned}
 \bar{\tau} &= \int_0^{\infty} \tau w(\tau) d\tau = \int_{-\infty}^0 \rho_G(E) \tau dE \\
 &= \frac{1}{\sqrt{2\pi}\delta_G\nu_0} \int_{-\infty}^0 \exp\left(\frac{-E^2}{2\delta_G^2} - \frac{E}{k_B T}\right) dE \\
 &= \frac{1}{\sqrt{2\pi}\delta_G\nu_0} \exp\left[\frac{2\delta_G^2}{(k_B T)^2}\right] \int_{-\infty}^0 \exp\left[-\left(\frac{E}{\sqrt{2}\delta_G} + \frac{\sqrt{2}\delta_G}{k_B T}\right)^2\right] dE \\
 &= \frac{1}{2\nu_0} \left[1 + \operatorname{erf}\left(\frac{\sqrt{2}\delta_G}{k_B T}\right)\right].
 \end{aligned} \tag{A7}$$

where $w(t) = \gamma \exp\left\{-\gamma^2[\log(\nu_0\tau)]^2/2\right\}/(\sqrt{2\pi}\tau)$ and $\gamma = k_B T/\delta_G$. For any DoS with finite mean jump time, using Taylor series for small u , one can write

$$w(u) = 1 - u\bar{\tau} + O(\bar{\tau}^2) \tag{A8}$$

With initial condition $W_0(x) = \delta(x)$, Eqs. (A2), (A3), (A7), and (A8) imply

$$W(k, u) = \frac{1}{u + Dk^2} \tag{A9}$$

where $D = a^2/\bar{\tau}$ is the diffusion constant. Taking the inverse Fourier-Laplace transform from Eq. (A9), we arrive at the diffusion equation

$$\frac{\partial W(x, t)}{\partial t} = D \frac{\partial^2 W(x, t)}{\partial x^2} \tag{A10}$$

with initial condition $W(x, 0) = W_0(x)$. Solution to Eq. (A10) is the well-known Gaussian propagator

$$W(x, t) = \frac{1}{\sqrt{4\pi Dt}} \exp\left(-\frac{x^2}{4Dt}\right) \tag{A11}$$

Note that the long-time form of the propagator was considered through the assumption of k being very small. Recall that for a Gaussian propagator, MSD is given by

$$\langle \vec{r}^2(t) \rangle \sim t. \tag{A12}$$

Using Eqs. (A1) and (A12), one finds that for a Gaussian DoS in a thermally activated process, charge carrier density decays as

$$\rho(t) \sim t^{-1}, \tag{A13}$$

which is indicative of Langevin dynamics. This relation holds true for any DoS distribution, whose jump time distribution has a finite mean value.

Uniform DoS. Plugging the uniform distribution

$$\rho_U(E) = \frac{N_U}{\delta_U}, \quad -E_U \leq E \leq 0, \quad (\text{A14})$$

into Eq. (A7) renders

$$\bar{\tau} = \frac{1}{E_U \nu_0} \int_{-E_U}^0 \exp\left(-\frac{E}{k_B T}\right) dE = \frac{k_B T}{E_U \nu_0} \left[\exp\left(\frac{N_U}{k_B T}\right) - 1 \right], \quad (\text{A15})$$

where $w(t) = k_B T (E_U t)^{-1}$. Note that $\bar{\tau}$ is a finite value. Thus, following the same procedure performed for Gaussian DoS, we conclude that $\rho(t) \sim t^{-1}$.

Exponential DoS. For an exponential DoS given in Eq. (5), one can rewrite Eq. (A7)

$$\bar{\tau} = \alpha \nu_0 \int_{\nu_0^{-1}}^{\infty} (\nu_0 \tau)^{-\alpha} d\tau \quad (\text{A16})$$

to yield $w(t) = \alpha \nu_0 (\nu_0 t)^{-(\alpha+1)}$, where $\alpha = k_B T / \delta_E$ and $0 < \alpha < 1$. Note that $\bar{\tau}$ diverges which is indicative of a dispersive process. The Laplace transform of $w(t)$ for small u is [71]

$$w(u) \approx 1 - \left(\frac{u}{\nu_0}\right)^\alpha + O(u). \quad (\text{A17})$$

Substitution of Eqs. (A3) and (A17) into Eq. (A2) leads to the propagator

$$W(k, u) = \frac{1}{u(1 + D_\alpha u^{-\alpha} k^2)} \quad (\text{A18})$$

where $D_\alpha = a^2 / \nu_0^\alpha$. From Eq. (A18), MSD is found by inverse Laplace transform of $\langle x^2(u) \rangle = \lim_{k \rightarrow 0} \{-d^2 W(k, u) / dk^2\}$, which leads to

$$\langle x^2(t) \rangle = \frac{2D_\alpha}{\Gamma(\alpha + 1)} t^\alpha, \quad (\text{A19})$$

where the condition of u being small has been applied. Eq. (A19) can be generalized to three dimensions, illustrating that $\langle \vec{r}^2(t) \rangle \sim t^\alpha$. Using this relation and Eq. (A1), we conclude that $\rho(t) \sim t^{-\alpha}$.

Appendix B. Charge carrier lifetime in bimolecular recombination

Assuming the general form for non-Langevin dynamics in BMR, we express the time variation of charge carrier density by

$$\frac{d\rho(t)}{dt} = -\beta(t) \rho(t)^2 \quad (\text{B1})$$

where $\rho(t)$ is the charge carrier density and $\beta(t)$ is the time-dependent rate coefficient [72]. Considering boundary condition $\rho = \rho_0$ at $t = 0$, one finds that

$$\frac{\rho(t)}{\rho_0} = \left[1 + \rho_0 \int_0^t \beta(t) dt \right]^{-1}. \quad (\text{B2})$$

The choice of $\beta(t)$ is semiempirical. Note that the charge density decay follows a power law at long time ($\rho(t) \sim t^{-\alpha}$), so it has been suggested [72] that $\beta(t) = \beta_0 t^{\alpha-1}$, $0 < \alpha < 1$, where β_0 is some constant. For this particular choice of $\beta(t)$, solving BMR Eq. (B1) leads to

$$\frac{\rho(t)}{\rho_0} = \left[1 + \left(\frac{t}{\tau_0} \right)^\alpha \right]^{-1}, \quad (\text{B3})$$

where $\tau_0 = [\alpha/(\rho_0\beta_0)]^{1/\alpha}$ is called the effective bimolecular lifetime [72].

Although charge carrier lifetime can be seen as the mean survival time, which is directly related to the survival probability $S(t)$ [73, 74] via $\tau = \int_0^\infty S(t) dt$, calculating carrier lifetime using the concept of survival probability seems to be impractical as the abovementioned integral is diverging due to long-lived charge carriers trapped in the band-tail states. However, neglecting those long-lived carriers, we can intuitively find carrier lifetime using [75]

$$\tau = \frac{\rho(t)}{-\frac{d\rho(t)}{dt}}, \quad (\text{B4})$$

for which substituting Eq. (B3) into Eq. (B4) leads to $\tau = (\rho_0\beta_0)^{-1} [1 + (t/\tau_0)^\alpha] t^{1-\alpha}$. However, in this equation, as t tends to zero, $d\rho/dt$ diverges; thus, carrier lifetime diminishes, meaning that charge carriers annihilate immediately after charge separation. Such a fast recombination mechanism can also be seen for the other choice of time-dependent rate coefficient, $\beta(t)$, mentioned before.

To resolve this instantaneous recombination at short time, we modify the above time-dependent rate coefficient to $\beta(t) = \beta_0 (1 + t/\eta)^{\alpha-1}$ where $\eta = \alpha/(\rho_0\beta_0)$ is a time scaling constant. Experimental data [72] shows that η is on the order of μs at room temperature for MDMO-PPV and PCBM blend. For this choice of $\beta(t)$, from Eq. B1, one finds

$$\frac{\rho(t)}{\rho_0} = \left(1 + \frac{t}{\eta} \right)^{-\alpha}, \quad (\text{B5})$$

for which BMR rate can be defined as

$$\frac{1}{\rho_0} \frac{d\rho(t)}{dt} = -\frac{\alpha}{\eta} \left(1 + \frac{t}{\eta} \right)^{-\alpha-1} = -\frac{\alpha}{\eta} \left(\frac{\rho}{\rho_0} \right)^{1+\frac{1}{\alpha}}. \quad (\text{B6})$$

Using Eqs. (B5) and (B6), one can express carrier lifetime in Eq. (B4) in terms of the carrier density

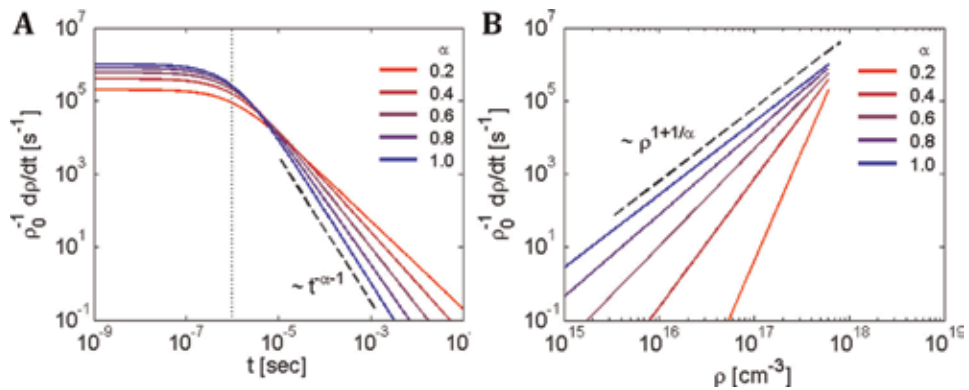


Figure B1.

Impact of BMR exponent, α , on BMR rate with (A) time and (B) charge carrier density utilizing Eq. (B6). In panel A, vertical dotted line corresponds to $t = \eta = 10^{-6} \text{ s}^{-1}$ using which these results were obtained.

$$\tau = \frac{\eta}{\alpha} \left(1 + \frac{t}{\eta} \right) = \frac{\eta}{\alpha} \left(\frac{\rho(t)}{\rho_0} \right)^{-\frac{1}{\alpha}}, \quad (\text{B7})$$

which can very well be approximated by $\tau \approx t/\alpha$ at long time. In contrast to the density decay in Eq. (B3), Eq. (B5) leads to a finite value for $d\rho/dt$ in Eq. (B6) as t tends to zero, giving rise to a non-zero initial carrier lifetime $\tau = \eta/\alpha$. Eq. (B7) also demonstrates that carrier lifetime decreases with carrier density (see **Figure 2**) which suggests that ultimately, long-lived carriers in the deep band-tail states dominate the carrier lifetime.


Figure B1 illustrates the results taken from analytical form in Eq. (B6), indicating the impact of BMR exponent on BMR rate for a fixed $\eta = 10^{-6} \text{ s}^{-1}$. **Figure B1A** indicates that there is a transition at $t = \eta$ where BMR rate transitions from a constant to a rate decreasing with time. Furthermore, the effect of BMR exponent on the BMR rate is reversed at this point, suggesting that BMR rate increases with BMR exponent at short time but decreases at long time. **Figure B1B** demonstrates that at a given charge carrier density, as BMR exponent decreases (e.g., band-tail state distribution becomes deeper), BMR rate also decreases.

Author details

Daniel Christiansen and Shafiq Mehraeen*
Department of Chemical Engineering, University of Illinois, Chicago, IL, USA

*Address all correspondence to: tranzabi@uic.edu

IntechOpen

© 2019 The Author(s). Licensee IntechOpen. This chapter is distributed under the terms of the Creative Commons Attribution License (<http://creativecommons.org/licenses/by/3.0>), which permits unrestricted use, distribution, and reproduction in any medium, provided the original work is properly cited. 

References

- [1] Cowan SR, Banerji N, Leong WL, Heeger AJ. Charge formation, recombination, and sweep-out dynamics in organic solar cells. *Advanced Functional Materials*. 2012; **22**:1116-1128. DOI: 10.1002/adfm.201101632
- [2] Etzold F, Howard IA, Mauer R, Meister M, Kim TD, Lee KS, et al. Ultrafast exciton dissociation followed by nongeminate charge recombination in Pcdtbt:Pcbm photovoltaic blends. *Journal of the American Chemical Society*. 2011; **133**:9469-9479. DOI: 10.1021/Ja201837e
- [3] Bakulin AA, Rao A, Pavelyev VG, van Loosdrecht PHM, Pshenichnikov MS, Niedzialek D, et al. The role of driving energy and delocalized states for charge separation in organic semiconductors. *Science*. 2012; **335**: 1340-1344. DOI: 10.1126/science.1217745
- [4] Grancini G, Maiuri M, Fazzi D, Petrozza A, Egelhaaf HJ, Brida D, et al. Hot exciton dissociation in polymer solar cells. *Nature Materials*. 2013; **12**:29-33. DOI: 10.1038/nmat3502
- [5] Jailaubekov AE, Willard AP, Tritsch JR, Chan W-L, Sai N, Gearba R, et al. Hot charge-transfer excitons set the time limit for charge separation at donor/acceptor interfaces in organic photovoltaics. *Nature Materials*. 2013; **12**:66-73. DOI: 10.1038/nmat3500
- [6] Heiber MC, Okubo T, Ko SJ, Luginbuhl BR, Ran NA, Wang M, et al. Measuring the competition between bimolecular charge recombination and charge transport in organic solar cells under operating conditions. *Energy & Environmental Science*. 2018; **11**: 3019-3032. DOI: 10.1039/c8ee01559g
- [7] Hahn T, Tscheuschner S, Kahle FJ, Reichenberger M, Athanasopoulos S, Saller C, et al. Monomolecular and bimolecular recombination of electron-hole pairs at the interface of a bilayer organic solar cell. *Advanced Functional Materials*. 2017; **27**:1-11. Article ID: 1604906. DOI: 10.1002/adfm.201604906
- [8] Credgington D, Kim Y, Labram J, Anthopoulos TD, Durrant JR. Analysis of recombination losses in a pentacene/C60 organic bilayer solar cell. *Journal of Physical Chemistry Letters*. 2011; **2**: 2759-2763. DOI: 10.1021/Jz201338d
- [9] Kopelman R. Fractal-like exciton kinetics in membranes, glasses and films. *Journal de Physique*. 1985; **46**:9-13
- [10] Garcia-Belmonte G, Bisquert J. Open-circuit voltage limit caused by recombination through tail states in bulk heterojunction polymer-fullerene solar cells. *Applied Physics Letters*. 2010; **96**:113301. DOI: 10.1063/1.3358121
- [11] Tachiya M, Seki K. Theory of bulk electron-hole recombination in a medium with energetic disorder. *Physical Review B*. 2010; **82**:085201. DOI: 10.1103/Physrevb.82.085201
- [12] Hilczer M, Tachiya M. Unified theory of geminate and bulk electron-hole recombination in organic solar cells. *Journal of Physical Chemistry C*. 2010; **114**:6808-6813. DOI: 10.1021/Jp912262h
- [13] Fukuhara T, Tamai Y, Osaka I, Ohkita H. Bimolecular recombination and fill factor in crystalline polymer solar cells. *Japanese Journal of Applied Physics*. 2018; **57**:1-5. Article ID: 08RE01. DOI: 10.7567/Jjap.57.08re01
- [14] Kuik M, Koster LJA, Wetzelaer GAH, Blom PWM. Trap-assisted

- recombination in disordered organic semiconductors. *Physical Review Letters*. 2011;**107**:256805. DOI: 10.1103/PhysRevLett.107.256805
- [15] Leong WL, Cowan SR, Heeger AJ. Differential resistance analysis of charge carrier losses in organic bulk heterojunction solar cells: Observing the transition from bimolecular to trap-assisted recombination and quantifying the order of recombination. *Advanced Energy Materials*. 2011;**1**:517-522. DOI: 10.1002/aenm.201100196
- [16] Cowan SR, Roy A, Heeger AJ. Recombination in polymer-fullerene bulk heterojunction solar cells. *Physical Review B*. 2010;**82**:245207. DOI: 10.1103/PhysRevB.82.245207
- [17] Soci C, Moses D, Heeger AJ. Effects of bimolecular recombination and charge-trapping on the transient photoconductivity of poly(P-phenylene vinylene). *Synthetic Metals*. 2005;**153**: 145-148. DOI: 10.1016/j.synthmet.2005.07.153
- [18] Soci C, Moses D, Xu QH, Heeger AJ. Charge-carrier relaxation dynamics in highly ordered poly(p-phenylene vinylene): Effects of carrier bimolecular recombination and trapping. *Physical Review B*. 2005;**72**:245204. DOI: 10.1103/PhysRevB.72.245204
- [19] Oosterhout SD, Ferguson AJ, Larson BW, Olson DC, Kopidakis N. Modeling the free carrier recombination kinetics in Ptb7:Pcbm organic photovoltaics. *Journal of Physical Chemistry C*. 2016; **120**:24597-24604. DOI: 10.1021/acs.jpcc.6b07614
- [20] Montanari I, Nogueira AF, Nelson J, Durrant JR, Winder C, Loi MA, et al. Transient optical studies of charge recombination dynamics in a polymer/fullerene composite at room temperature. *Applied Physics Letters*. 2002;**81**:3001-3003. DOI: 10.1063/1.1512943
- [21] Nogueira AF, Montanari I, Nelson J, Durrant JR, Winder C, Sariciftci NS. Charge recombination in conjugated polymer/fullerene blended films studied by transient absorption spectroscopy. *Journal of Physical Chemistry B*. 2003;**107**:1567-1573. DOI: 10.1021/Jp027101z
- [22] Shuttle CG, Hamilton R, O'Regan BC, Nelson J, Durrant JR. Charge-density-based analysis of the current-voltage response of polythiophene/fullerene photovoltaic devices. *Proceedings of the National Academy of Sciences of the United States of America*. 2010;**107**:16448-16452. DOI: 10.1073/pnas.1004363107
- [23] Shuttle CG, Maurano A, Hamilton R, O'Regan B, de Mello JC, Durrant JR. Charge extraction analysis of charge carrier densities in a polythiophene/fullerene solar cell: Analysis of the origin of the device dark current. *Applied Physics Letters*. 2008;**93**:183501. DOI: 10.1063/1.3006316
- [24] Shuttle CG, O'Regan B, Ballantyne AM, Nelson J, Bradley DDC, de Mello J, et al. Experimental determination of the rate law for charge carrier decay in a polythiophene: Fullerene solar cell. *Applied Physics Letters*. 2008;**92**: 093311. DOI: 10.1063/1.2891871
- [25] Shuttle CG, O'Regan B, Ballantyne AM, Nelson J, Bradley DDC, Durrant JR. Bimolecular recombination losses in polythiophene: Fullerene solar cells. *Physical Review B*. 2008;**78**: 113201. DOI: 10.1103/PhysRevB.78.113201
- [26] Nelson J. Diffusion-limited recombination in polymer-fullerene blends and its influence on photocurrent collection. *Physical Review B*. 2003;**67**: 155209. DOI: 10.1103/PhysRevB.67.155209
- [27] Novikov S, Bimolecular V. Recombination of charge carriers in polar amorphous organic

- semiconductors: Effect of spatial correlation of the random energy landscape. *Journal of Physical Chemistry C*. 2018;**122**: 22856-22863. DOI: 10.1021/acs.jpcc.8b06768
- [28] Pivrikas A, Juska G, Mozer AJ, Scharber M, Arlauskas K, Sariciftci NS, et al. Bimolecular recombination coefficient as a sensitive testing parameter for low-mobility solar-cell materials. *Physical Review Letters*. 2005;**94**:1-4. Article ID: 176806. DOI: 10.1103/PhysRevLett.94.176806
- [29] Heiber MC, Nguyen TQ, Deibel C. Charge carrier concentration dependence of encounter-limited bimolecular recombination in phase-separated organic semiconductor blends. *Physical Review B*. 2016;**93**:1-8. Article ID: 205204. DOI: 10.1103/PhysRevB.93.205204
- [30] Credgington D, Durrant JR. Insights from transient optoelectronic analyses on the open-circuit voltage of organic solar cells. *Journal of Physical Chemistry Letters*. 2012;**3**:1465-1478. DOI: 10.1021/Jz300293q
- [31] Kirchartz T, Pieters BE, Kirkpatrick J, Rau U, Nelson J. Recombination via tail states in polythiophene: Fullerene solar cells. *Physical Review B*. 2011;**83**: 115209. DOI: 10.1103/PhysRevB.83.115209
- [32] Wetzelaer GJAH, Kuik M, Blom PWM. Identifying the nature of charge recombination in organic solar cells from charge-transfer state electroluminescence. *Advanced Energy Materials*. 2012;**2**:1232-1237. DOI: 10.1002/aenm.201200009
- [33] Street RA. Localized state distribution and its effect on recombination in organic solar cells. *Physical Review B*. 2011;**84**: 075208. DOI: 10.1103/PhysRevB.84.075208
- [34] Street RA, Schoendorf M. Determination of recombination mechanisms in organic solar cells. *IEEE Photovoltaic Specialists Conference*. 2010;**35**:79-84
- [35] Cowan SR, Street RA, Cho SN, Heeger AJ. Transient photoconductivity in polymer bulk heterojunction solar cells: Competition between sweep-out and recombination. *Physical Review B*. 2011;**83**:035205. DOI: 10.1103/PhysRevB.83.035205
- [36] Street RA, Schoendorf M. Interface state recombination in organic solar cells. *Physical Review B*. 2010;**81**: 205307. DOI: 10.1103/PhysRevB.81.205307
- [37] Lenes M, Morana M, Brabec CJ, Blom PWM. Recombination-limited photocurrents in low bandgap polymer/fullerene solar cells. *Advanced Functional Materials*. 2009;**19**: 1106-1111. DOI: 10.1002/adfm.200801514
- [38] Street RA, Northrup JE, Krusor BS. Radiation induced recombination centers in organic solar cells. *Physical Review B*. 2012;**85**:205211. DOI: 10.1103/PhysRevB.85.205211
- [39] Bar D. Diffusion-limited reaction for the one-dimensional trap system. *Physical Review E*. 2003;**67**: 056123. DOI: 10.1103/PhysRevE.67.056123
- [40] Yan HP, Swaraj S, Wang C, Hwang I, Greenham NC, Groves C, et al. Influence of annealing and interfacial roughness on the performance of bilayer donor/acceptor polymer photovoltaic devices. *Advanced Functional Materials*. 2010;**20**:4329-4337. DOI: 10.1002/adfm.201001292
- [41] Deibel C, Wagenpfahl A, Dyakonov V. Origin of reduced polaron recombination in organic semiconductor devices. *Physical Review*

- B. 2009;**80**:075203. DOI: 10.1103/PhysRevB.80.075203
- [42] Isichenko M, Percolation B. Statistical topography, and transport in random-media. *Reviews of Modern Physics*. 1992;**64**:961-1043
- [43] Ziman JM. Localization of electrons in ordered and disordered systems. 2. Bound bands. *Journal of Physics C: Solid State Physics*. 1969;**2**:1230-1247. DOI: 10.1088/0022-3719/2/7/316
- [44] Ziman JM. Localization of electrons in ordered and disordered systems. 3. Quantum-mechanical particles in free bands. *Journal of Physics C: Solid State Physics*. 1969;**2**:1704-1716. DOI: 10.1088/0022-3719/2/10/302
- [45] Zallen R, Scher H. Percolation on a continuum and localization-delocalization transition in amorphous semiconductors. *Physical Review B*. 1971;**4**:4471-4479. DOI: 10.1103/PhysRevB.4.4471
- [46] Miller A, Abrahams E. Impurity conduction at low concentrations. *Physical Review*. 1960;**120**:745-755. DOI: 10.1103/PhysRev.120.745
- [47] Gillespie DT. Exact stochastic simulation of coupled chemical-reactions. *Journal of Physical Chemistry*. 1977;**81**:2340-2361
- [48] Gillespie D, General T. Method for numerically simulating stochastic time evolution of coupled chemical-reactions. *Journal of Computational Physics*. 1976;**22**:403-434
- [49] Aytun T, Barreda L, Ruiz-Carretero A, Lehrman JA, Stupp SI. Improving solar cell efficiency through hydrogen bonding: A method for tuning active layer morphology. *Chemistry of Materials*. 2015;**27**:1201-1209. DOI: 10.1021/cm503915t
- [50] Benanti TL, Venkataraman D. Organic solar cells: An overview focusing on active layer morphology. *Photosynthesis Research*. 2006;**87**:73-81. DOI: 10.1007/s11120-005-6397-9
- [51] Kim J-H, Schaefer C, Ma T, Zhao J, Turner J, Ghasemi M, et al. The critical impact of material and process compatibility on the active layer morphology and performance of organic ternary solar cells. *Advanced Energy Materials*. 2018;**9**:1-14. Article ID: 1802293
- [52] Nelson J. Continuous-time random-walk model of electron transport in nanocrystalline TiO₂ electrodes. *Physical Review B*. 1999;**59**:15374-15380. DOI: 10.1103/PhysRevB.59.15374
- [53] Scher H, Montroll EW. Anomalous transit-time dispersion in amorphous solids. *Physical Review B*. 1975;**12**:2455-2477
- [54] Metzler R, Klafter J. The random walk's guide to anomalous diffusion: A fractional dynamics approach. *Physics Reports*. 2000;**339**:1-77
- [55] Montroll EW, Lebowitz JL. *Fluctuation Phenomena*. Pbk. edn. North-Holland; Sole distributors for the U.S.A. and Canada: Elsevier Science Pub. Co.; 1987
- [56] Montroll EW, Weiss GH. Random walks on lattices. 2. *Journal of Mathematical Physics*. 1965;**6**:167
- [57] Weiss GH. *Aspects and Applications of the Random Walk*. Amsterdam: North-Holland; 1994
- [58] Monson E, Kopelman R. Nonclassical kinetics of an elementary A + B → C reaction-diffusion system showing effects of a speckled initial reactant distribution and eventual self-segregation: Experiments. *Physical*

- Review E. 2004;**69**:1-12. DOI: 10.1103/PhysRevE.69.021103
- [59] Yen A, Koo YEL, Kopelman R. Experimental study of a crossover from nonclassical to classical chemical kinetics: An elementary and reversible $A+B \rightarrow C$ reaction-diffusion process in a capillary. *Physical Review E*. 1996;**54**: 2447-2450
- [60] Taitelbaum H, Vilensky B, Lin AA, Yen AD, Koo YEL, Kopelman R. Competing reactions with initially separated components. *Physical Review Letters*. 1996;**77**:1640-1643
- [61] Galfi L, Racz Z. Properties of the reaction front in an $A+B-C$ type reaction-diffusion process. *Physical Review A*. 1988;**38**:3151-3154
- [62] Ovchinnikov AA, Zeldovich YB. Role of density fluctuations in bimolecular reaction-kinetics. *Chemical Physics*. 1978;**28**:215-218
- [63] Toussaint D, Wilczek F. Particle antiparticle annihilation in diffusive motion. *The Journal of Chemical Physics*. 1983;**78**:2642-2647
- [64] Lin A, Kopelman R, Argyrakis P. Nonclassical kinetics in three dimensions: Simulations of elementary $A+B$ and $A+A$ reactions. *Physical Review E*. 1996;**53**:1502-1509
- [65] Leyvraz F. 2-species annihilation in 3 dimensions—A numerical study. *Journal of Physics A: Mathematical and General*. 1992;**25**:3205-3212
- [66] Ben-Avraham D, Havlin S. *Diffusion and Reactions in Fractals and Disordered Systems*. Cambridge, UK: Cambridge University Press; 2000
- [67] Zschokke I. *Optical Spectroscopy of Glasses*. D. Dordrecht, Holland: Reidel Pub. Co.; Sold and distributed in the U.S.A. and Canada by Kluwer Academic Publishers; 1986
- [68] Kang K, Redner S. Fluctuation-dominated kinetics in diffusion-controlled reactions. *Physical Review A*. 1985;**32**:435-447
- [69] Meakin P, Stanley HE. Novel dimension-independent behavior for diffusive annihilation on percolation fractals. *Journal of Physics A: Mathematical and General*. 1984;**17**: L173-L177
- [70] Scher H. Recombination in disordered solids. *Journal de Physique*. 1981;**42**:547-550. DOI: 10.1051/jphyscol:19814118
- [71] Klafter J, Blumen A, Shlesinger MF. Stochastic pathway to anomalous diffusion. *Physical Review A*. 1987;**35**: 3081-3085. DOI: 10.1103/PhysRevA.35.3081
- [72] Mozer AJ, Dennler G, Sariciftci NS, Westerling M, Pivrikas A, Osterbacka R, et al. Time-dependent mobility and recombination of the photoinduced charge carriers in conjugated polymer/fullerene bulk heterojunction solar cells. *Physical Review B*. 2005;**72**:035217. DOI: 10.1103/PhysRevB.72.035217
- [73] Torquato S, Kim IC. Cross-property relations for momentum and diffusional transport in porous-media. *Journal of Applied Physics*. 1992;**72**:2612-2619. DOI: 10.1063/1.351561
- [74] Tomadakis MM, Rupani D. Diffusion controlled reaction rate, survival probability, and molecular trajectory characteristics in the bulk, transition and Knudsen regime. *Chemical Engineering Journal*. 2007; **128**:1-10. DOI: 10.1016/j.cej.2006.10.005
- [75] Zaban A, Greenshtein M, Bisquert J. Determination of the Electron Lifetime in Nanocrystalline Dye Solar Cells by Open-Circuit Voltage Decay Measurements. *Chemphyschem*. 2003;**4**: 859-864. DOI: 10.1002/cphc.200200615

Nanoplasmonic for Solar Energy Conversion Devices

*Samy K.K. Shaat, Hussam Musleh, Jihad Asad,
Nabil Shurrab, Ahmed Issa, Amal AlKahlout and
Naji Al Dahoudi*

Abstract

The effect of nanoplasmonic (Ag) on the performance of DSSCs has been studied in doped and undoped ZnO (DZ and UZ) NPs, which were prepared by the urea-assisted combustion route. Different techniques were conducted to characterize DZ and UZ NPs. XRD patterns were indexed to the hexagonal wurtzite structure of ZnO NPs (ICSD-52362). The values of average crystalline size of UZ and DZ (1.0 mol% Ag) NPs were 20.45 and 22.30 nm, respectively. HR-TEM micrograph revealed good crystallization with an intermediate or poor agglomeration with distribution of semispherical morphologies of ZnO NPs. The energy bandgap of UZ and DZ NPs was changed from 3.21 to 3.31 eV. The deconvolution of the PL spectra recognized eight peaks into near ultraviolet (NUV) and visible regions. The PL emission of visible region overshadowed NUV transition. The photovoltaic cell with the doped photoanode DZ:1.0 mol% Ag exhibited the best performance parameters: $V_{oc} = 0.46$ V, $J_{sc} = 7.81$ mA.cm⁻², $P_m = 1.91$, FF = 51%, and $\eta = 1.91\%$. A double exponential function was used as a powerful fitting function for the TOCVD data. The results revealed that τ_n in the UZ NPs photoanode was longer than that in the DZ:1.0 mol% Ag NPs photoanode.

Keywords: combustion synthesis, eosin Y, nanoplasmonic, solar energy conversion device, renewable energy, defects, lifetime, electron recombination

1. Introduction

The exacerbation of energy worldwide crisis in addition to two bottlenecks: (i) the inevitable exhaustion of fossil fuel in the coming fifty years and (ii) the global environmental damage caused by the combustion of large amounts of fossil fuels [1], spurs us to find a new pollution-free, eco-friendly, renewable, clean and sustainable energy source [2]. There are many types of renewable energy resources—such as wind, biomass, and tidal, geothermal, and solar energy [3]. Accordingly, solar energy has been increasingly exploited, which is the most promising one to meet the future demands as it is in limitless supply [2]. Consequently, it is imperative to develop solutions to broaden light absorption and suppress charge recombination toward efficient solar energy conversion (SEC) [2]. Hence, SEC into a most usable form, i.e., electrical energy, is highly important to fulfill the ever-increasing demand for energy [1]. Photoelectrical conversion (PEC) is a promising

and environmentally friendly technology to solve the energy crisis faced because sunlight gives a power of 106 TW/year continuously [4]. Photovoltaic cells (PVs) are an essential component in smart grids and mobile commerce or in the development of integrated photovoltaics (BIPVs) and vehicles [5]. Dye-sensitized solar cells (DSSCs) are a class of mesoporous solar device which have evolved as credible alternative to conventional solid-state p-n junction photovoltaics [6, 7]. The DSSCs have several advantages, showing higher performance with relatively lower cost, lower handling expenses, lower strength of optical and incidence angles, higher mechanical durability, lighter weight, and more aesthetically pleasing and transparent design [1, 5]. With the advantages of being easily manufactured, colored, and flexible, this type of solar cells has become available and considerable for reducing the cost of electricity generation [8]. Nevertheless, their low efficiencies remain a major roadblock to commercialization in DSSCs [5]. In addition, light absorption, charge recombination, and dye pickup are still a challenge in the field of DSSC technology [9]. Numerous strategies have been investigated to enhance PCE of DSSC by improvement of light harvesting, carrier collection and noble metal NPs, using semiconductor quantum dots, developing new dyes and designing new morphology [10]. Moreover, different approaches were designed such as large surface area mesoporous photoanode; hierarchically Nano-structured and scattering top-layer photoanode; new panchromatic absorbing dyes; photonic crystal photoanode and plasmonic photoanode [5, 6]. In PEC, semiconductors play an important role in capturing light to generate electron-hole pairs for subsequent electricity and chemical fuel production. Also, they generate photocurrent and produce H₂ under visible light illumination [4]. Recent researches on pure and alloyed metal NPs demonstrated high potential in this field to improve light absorption/scattering properties of semiconductor network. This is due to their unique response under particular wavelengths known as plasmonic effect [9]. Newly, ZnO has been used as an alternative n-type semiconducting photoanode material for DSSCs. This is because ZnO has high electron dynamics, and a versatile nanostructure morphology relative to others [11]. ZnO plays an important role in the optoelectronic devices. This is because of its excellent properties of piezoelectric, electron conductivity, and a large exciton binding energy of 60 meV [12]. One general advantage of incorporating NPs into DSSCs is that they provide far-field scattering and concomitant enhancement. This is due to longer effective optical path lengths [13]. Their outstanding light trapping and electromagnetic field concentrating properties proved very effective [9]. Further modifications have been performed by mixing with other nanostructured metal oxides or with metallic NPs. These metallic NPs include noble metals (NMs) Au, Ag, and Cu, i.e., nanoplasmonic (NPL) metals), for improving their charge carrier and absorption properties [11]. NMs in nanoscale have widely been applied in various research fields, including optical sensors, catalysts, and surface-enhanced Raman scattering. This is due to their characteristic optical and electrical properties, which are not available with bulk analogues [14]. NPL has unique optical characteristics that can be harnessed for several technological applications from spectroscopy to nanomedicine to photovoltaics [7]. NPL is a rapidly growing research field that exploits enhancement of concentrated optical energy on the nanoscale in nanostructured metal [11]. Also, NPL enhanced photocatalytic including water splitting, artificial photosynthesis, and photodegradation of organic pollutant and photovoltaic systems [2, 4, 13]. On the other hand, NPL introduction in photoactive layers of DSSC, to trap or confine light inside the active layer and enhance the absorption in the semiconductor film could provide superior performances presumably due to their unique electronic, optical and magnetic properties [15]. Moreover, NPL enhancement in solar cells is achieved by four possible mechanisms. They are far-field coupling of scattered

light, which can be trapped in the mesoporous semiconductor, near-field coupling of electromagnetic fields, plasmon resonance energy transfer from nanostructures to semiconductor, and hot-electron transfer [4, 7, 14]. As sun light possesses less energetic photons, the hot electrons cannot be produced just by the solar spectrum. In DSSC technology, this problem can be solved by the use of exothermic chemical processes [9]. In another study, quantum capacitance-like effect has been observed in the device, which accelerates the carrier transport via additional electric field [9]. The enhanced electromagnetic field is highly dependent upon the wavelength of incident light, also, the shape, size, and aggregation state of the NPs [10]. The increasing of the light-harvesting efficiency was done by introducing NPL structures into various types of PVs such as silicon, thin-film, organic solar, and polymer solar cell [10, 11, 13, 14]. Among the NMs silver, which have the critical advantages and is considered as one of the most suitable candidates for practical applications due to its facile easy preparation and lower cost than others [10]. As to the electrical aspect, Ag NPs could play a role as the electron transport separation center, which accelerated the electron to move through the photoanode network and reduced the charge recombination [8]. However, the exact mechanism for the plasmon-induced charge separation process in plasmonic photovoltaic devices is not clarified yet [14]. In conclusion, the possibility of photosensitization of MOs using plasmonic metal NPs is tantalizing [7]. While there is increasing evidence for hot-electron injection, there is no consensus to date. Further research is necessary to establish more firmly the possibility [4]. More work is also needed to better understand what factors determine the mechanism of operation. The strength of interaction between the metal NP and MOs is likely a critical factor, which may in turn depends on the detailed structures of both constituents down to the molecular or atomic level [4]. The merits designate the implementation of plasmonic nanostructures into photocatalysis and photovoltaics as a promising strategy for solar energy conversion [2]. Several methods have been reported to deposit Ag NPs onto DSSC photoanode. However, none is able to prevent the aggregation of Ag NPs and keep structures uniform during the deposition process [10]. Until now, there has been strong controversy regarding the role of plasmonic NPs in DSSCs. In addition, more in-depth investigation for the enhancement mechanism is still required [14]. Guided by this principle, in this study, we designed a kind of unique Ag-doped ZnO NPs as a photoanode in DSSCs, to investigate the plasmonic effects and elucidate the working principle more systematically. Nevertheless, this method has never been used for doping metallic particles for plasmon effect in DSSCs. The present work is the first effort to employ solution combustion method for enhancing plasmon effect in DSSCs. The plasmonic effect of Ag on the performance of DSSCs has been studied. A dramatic increase in efficiency is achieved in the device of Ag NPs/ZnO NPs compared with that of ZnO NPs.

2. Practical and experimental techniques

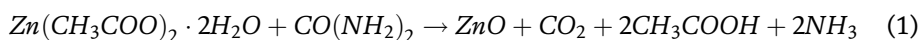
2.1 Synthesis of ZnO nanoparticles

Doped and undoped (i.e., pristine sample which was used as a control specimen) ZnO (DZ and UZ) NPs were prepared by the urea-assisted combustion route. The detailed synthetization of DZ and UZ NPs has been reported elsewhere [16]. Zinc acetate (ZA) dihydrate, $(\text{Zn}(\text{CH}_3\text{COO})_2 \cdot 2(\text{H}_2\text{O}))$ assay $\geq 98.9\%$, Merck Co.), urea (U), $(\text{CO}(\text{NH}_2)_2)$, assay $\geq 99.9\%$, Merck Co.), and silver nitrate AgNO_3 (SN) were used as starting materials (precursors). They were utilized as purchased without further purification. The distilled water (DW) was employed to dissolve



Figure 1.
A schematic illustration of the synthesis procedure of UZ and DZ NPs.

stoichiometric amounts of ZA (solutions A) and U (solutions B). Solutions A and B were stirred vigorously for 15 min at room temperature. After that, the two solutions A and B were mixed to produce solution C. A transparent homogeneous solution C was stirred vigorously for 15 min at 60°C in a beaker and was sonicated for 30 min. Solution C was transferred to a muffle furnace maintained at a temperature of 500 ± 10°C. Solution C started to boil and undergo dehydration. Due to the exothermic nature of this process, a large amount of heat escaped with a huge flame. In meantime, further decomposition of the reagents and liberating more gases during the evaporation of liquid were happened. After 1 min, the flame damped, and the combustion reaction was accomplished within 5 min. White foamy and voluminous ash was achieved after spontaneous ignition occurred and underwent smoldering combustion with enormous swelling. The product ash was left to cool down to room temperature. Then, white ash was grounded gently into fine powders using a pestle and mortar:



The same producers were repeated to prepare the UZ and DZ NPs with different molar concentration of Ag (0.5, 1.0, 1.5, and 5.0%). The obtained powders were characterized without any further post-preparation treatment. The scheme for the synthesis techniques of the DZ and UZ NPs is illustrated schematically in **Figure 1**. The chemical reaction to derive ZnO NPs from solution combustion-assisted urea is written in Eq. (1).

2.2 Fabrication and assembly of the DSSCs devices

The as-synthesized DZ and UZ NPs (which was designed as a reference photoanode) were consumed to fabricate the working electrode (WE) for DSSCs. Two slurry pastes were prepared by mixing a small quantity of the as-synthesized DZ and UZ NPs with polyethylene glycol 400 (PEG 400) and absolute ethanol using a mortar and pestle for 12 min. The obtained homogenous pastes were layered on fluorine-doped tin oxide (FTO) substrates (Sigma-Aldrich, sheet resistance

7 Ω/cm^2) by doctor blade technique. FTO substrates were washed using ethanol and DW several times followed by ultra-sonication using acetone for 15 min. The coated FTO substrates were heated at 450°C for 45 min. The estimation thickness of the heated layers was 1215 μm with an active covered area 0.25 cm^2 . In this stage, the derived photoanodes from DZ and UZ NPs were fabricated. The fabricated photoanodes were, separately, immersed in eosin Y (EY) dyes. After 24 h, the dyed photoanodes were rinsed in absolute ethanol and were dried in air at room temperature. Finally, the different DSSC devices were assembled by fixing the WE (A Pt-coated FTO substrate) and the counter electrode by paper clips with a spacer between the two electrodes. After that, the redox electrolyte solution was injected between the two electrodes to filling the space. The filling redox electrolyte solution (I-/I-3) was composed of 32 mL p-carbonate, 8 mL acetonitrile, 0.253 g iodine (I_2), and 2.672 g lithium iodide. At last, the fabricated DSSC devices were used to measurements.

2.3 Characterization technique

Different techniques were conducted to characterize the as-synthesized DZ and UZ NPs. Crystal identification and crystal size analysis were tested by X-ray diffractometer (XRD), Philips Expert, where Cu-K α radiation ($\lambda = 1.5418 \text{ \AA}$) monochromatic by a nickel filter. The values of diffraction angle (2θ) range from 15° to 80° and scan rate about 0.02 s⁻¹. The nanostructures and their lattice images were possessed with a 200 kV high-resolution transmission electron microscopy (HR-TEM) (JEM-2100), 200 kV. Samples for HR-TEM studies were prepared by placing a drop of nanosuspension on a carbon-coated Cu grid, and the solvent was evaporated at room temperature. Double-beam UV-Vis spectrophotometer (Shimadzu UV-1601 PC) was used to carry out the absorption spectra of synthesized UZ and DZ NPs and the absorption of sensitizing dye in the range from 300 to 800 nm in ethanolic solution. Photoluminescence (PL) emission measurements were performed at room temperature in absolute ethanol over the range from 300 to 800 nm with excitation wavelength 320 nm using (SPF-200, Biotech Engineering Management Co., UK) spectrofluorometer with 150 W xenon lamp with a high-sensitivity photomultiplier tube.

2.4 Measurement techniques

The photovoltaic characteristics of the fabricated DSSCs were executed under focusing irradiation using white light (40 W Xenon arc lamp) in ambient atmosphere. In addition, they were simulated with AM 1.5 sunlight illumination with an output power of 100 mWcm^{-2} . The characteristic curves of the current and the voltage (I-V) of the fabricated cells were carried out by applying an external reverse bias voltage in the range of -1 to 1 V of the solar cell. A personal computer (PC) was connected to Elvis National Instruments (ENI) in combination with a LabVIEW program to collect the data of I-V characteristic curves. The transient open-circuit photovoltage (TOCPV) decay experiment was conducted by monitoring the subsequent decay. This was due to the light source being turned off after illuminating the DSSC devices based on the of 0.32 mM EY dye for 5 min. UV-Vis spectrophotometer double-beam Shimadzu UV-1601 PC with a diffraction grating with a self-aligning was equipped to measure the dye concentration of the desorbed-dye solution as described in the previous work [2]. A deuterium lamp covered the UV where a halogen lamp was the source of the visible region. The colored photoanode was immersed in a 0.1 M NaOH solution of water and ethanol (1:1, v/v).

3. Analysis and result discussion

3.1 X-ray diffraction pattern study

XRD technique was used to investigate the crystallography structure phase and lattice parameters of the as-synthesized samples UZ and DZ (1.0 mol % Ag) NPs. **Figure 2** depicts the intense and crystalline XRD patterns of the as-synthesized samples UZ and DZ (1.0 mol% Ag) NPs, which were registered at room temperature. All the diffraction peaks are indexed to the standard hexagonal wurtzite structure of ZnO NPs (inorganic crystal structure database number ICSD-52362). The sharpness of the broadened XRD diffraction peaks is an indication of the small size and the good crystallinity of the NPs, whereas the crystallinity of DZ (1.0 mol % Ag) NPs is better than UZ NPs. In addition, no peak corresponding to any impurity could be seen, and this confirms the formation of single phase of ZnO NPs. Moreover, no peak indicates the existence of other phase of Ag NPs. It was reported that no Ag peaks could be observed for 1% and 3% Ag concentrations; however, Ag peaks can still be detected in the XRD pattern of ZnO:5% Ag NPs [17]. Furthermore, XRD peaks related to Ag were presented in the samples calcined at 500, 700, and 900°C but disappear at 1100°C calcination temperature. This reveals that Ag atoms may have diffused in ZnO matrix. It can be noted that the preferred orientation corresponding to the plane (101), which overwhelms the other peaks, is the most prominent peak, which agrees with the results of Kumar et al. [18]. The XRD diffraction peaks are significantly broadened due to the small size of the NPs [19]. The calculated lattice parameters (a , c , and c/a) of samples UZ and DZ (1.0 mol% Ag) NPs are listed in **Table 1**. The calculated parameters match with the results of Xiaofeng Zhou et al. [20] and H. Zayed et al. [21]. Based on the Scherrer equation, the estimated average crystallite size (D) of the samples DZ and UZ NPs has been calculated from the highest diffraction peak along the (101) plane [22]:

$$D = \frac{k \lambda}{\beta \cos(\theta)} \quad (2)$$

where k is the particle shape factor ($k = 0.9$ for spherical particle), λ is the Cu-K α X-ray wavelength (0.15418 nm), β is the full width at half maximum (FWHM) of XRD peaks, and θ is the Bragg angle corresponding to the same plane which obtained from the diffraction angle (2θ). The calculated values of D of the

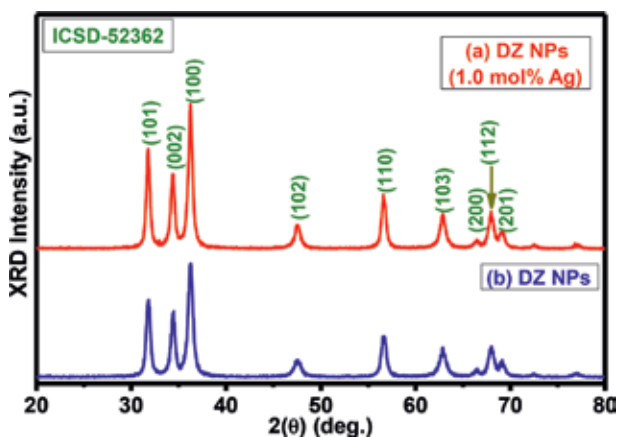


Figure 2. X-ray diffraction patterns the samples UZ and DZ (1.0 Mol% Ag) NPs.

Sample	(hkl)	(2 θ)	FWHM	c (nm)	a (nm)	c/a	d _{hkl} (nm)	D (nm)	
								XRD	HR-TEM
UZ	100	31.804	0.592	0.325	0.562	1.731	0.126	20.55	22
	002	34.419	0.667				0.147		
	101	36.261	0.707				0.203		
DZ 1.0 mol% Ag	100	31.804	0.523	0.325	0.563	1.731	0.281	23.02	24
	002	34.419	0.614				0.260		
	101	36.261	0.621				0.247		

Table 1.
 Geometric parameters of the samples UZ and DZ (1.0 mol% Ag) NPs.

samples UZ and DZ (1.0 mol% Ag) NPs are given in **Table 1**, which are 20.45 and 22.30 nm, respectively.

3.2 HR-TEM analysis

HR-TEM bright-field photomicrographs were used to determine the actual shape and size distribution of the as-synthesized samples UZ and DZ (1.0 mol% Ag) NPs. Therefore, it is important to know that the differences in the NP size and the dense distribution were used to explain these phenomena. Indeed, the larger size and highly dense distribution of Ag NPs mean that they could not preferentially attach to specific sites on the photoanode surface, resulting in a decrease of the catalytic activity [23]. **Figures 3** and **4** depict the HR-TEM micrograph of the samples UZ and DZ (1.0 mol% Ag) NPs, respectively. As revealed in **Figure 3A** and **4A**, the HR-TEM micrograph suggests that ZnO NPs are, well, crystallized with an intermediate or poor agglomeration. Moreover, as presented in **Figure 3A** and **4A**, the HR-TEM images show the distribution of semispherical morphologies of ZnO NPs. The selected area electron diffraction (SAED) patterns of samples UZ and DZ (1.0 mol% Ag) NPs are illustrated in **Figure 3B** and **4B**. This confirms the crystalline nature of the ZnO NPs. Five bright concentric diffraction rings in the SAED can be indexed as the (100), (002), (101), (102), and (110) planes of the wurtzite ZnO. The quantitative analysis of the size distribution for the ZnO NPs was achieved by plotting the histogram in **Figure 3C** and **4C**. The size distribution of UZ and DZ (1.0 mol% Ag) NPs is given by mean standard deviation (SD), which can be produced from fitting the histogram using the normal function [solid brown line in **Figures 3C** and **4C**]. The estimated values of D of the samples UZ and DZ (1.0 mol% Ag) NPs are 22 and 24 nm, respectively (**Table 1**). It is evident that the estimated D from HR-TEM images is in good agreement with the D estimated from the XRD patterns. The lattice fringe (**Figures 3D** and **4D**) gives interlayer spacing of 0.22 and 0.24 nm, which corresponds to the d-spacing of (101) plane ($d_{101} = 0.203$ and 0.247 nm from XRD calculation for UZ and DZ (1.0 mol% Ag) NPs, respectively). Some small black dots are shown in **Figure 4A**, which can be indicated to the Ag NPs. The size distribution of Ag NPs was obtained from fitting the histogram using the normal function [solid red line in **Figure 5**]. The estimated value of Ag NPs size is 3.55 nm (quantum dots). The size and the agglomeration of Ag NPs can produce shift in the Fermi level, and therefore, the recombination of the accumulated electrons with the oxidized redox electrolyte and/or dye species will change [13]. LSPR is barely dependent on the NPL; near-field plasmonic enhancement increases significantly with decreasing particle size [13]. Metal plasmon must be 16 nm in size to escape recombination and produce enhanced photovoltaic parameters [15]. Another

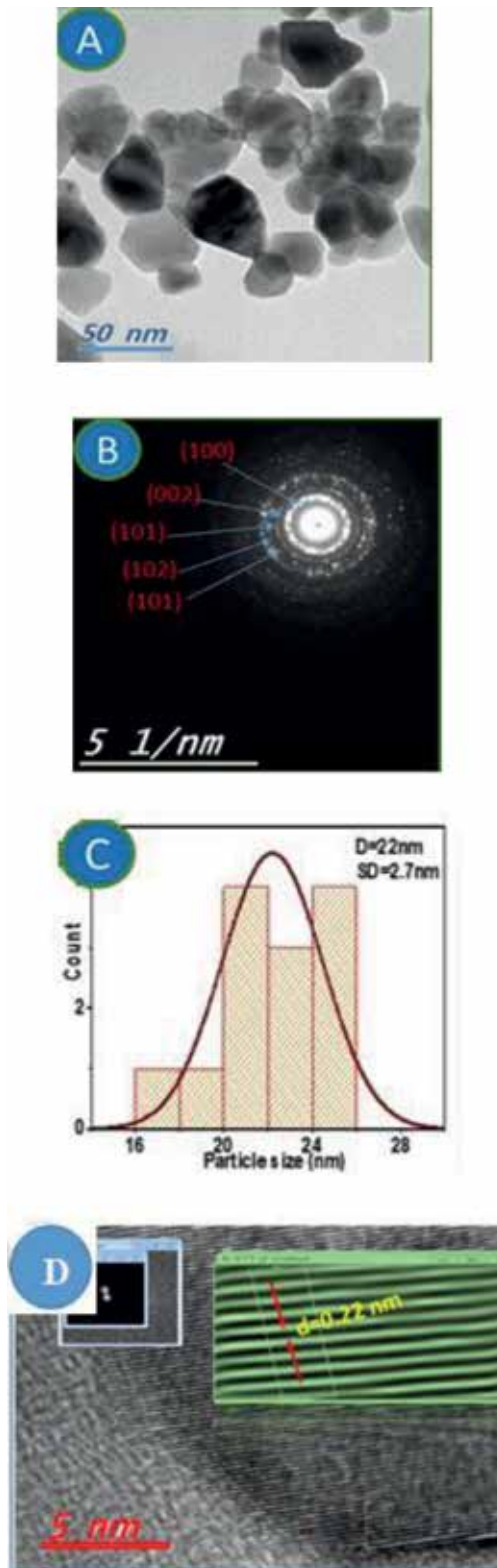


Figure 3. HR-TEM micrograph of sample UZ NPs (A) micrograph image, (B) diffraction patterns, (C) histograms, and (D) selected electron diffraction area.

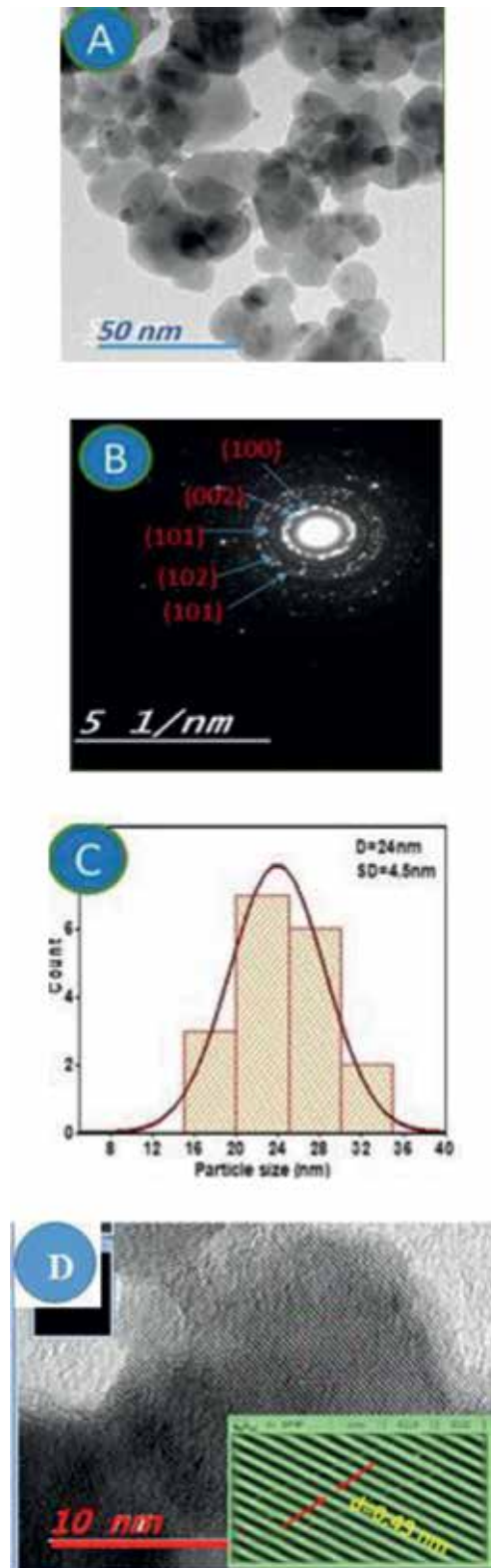


Figure 4. HR-TEM micrograph of sample DZ (1.0 Mol% Ag) NP (A) micrograph image, (B) diffraction patterns, (C) histograms, and (D) selected electron diffraction area.

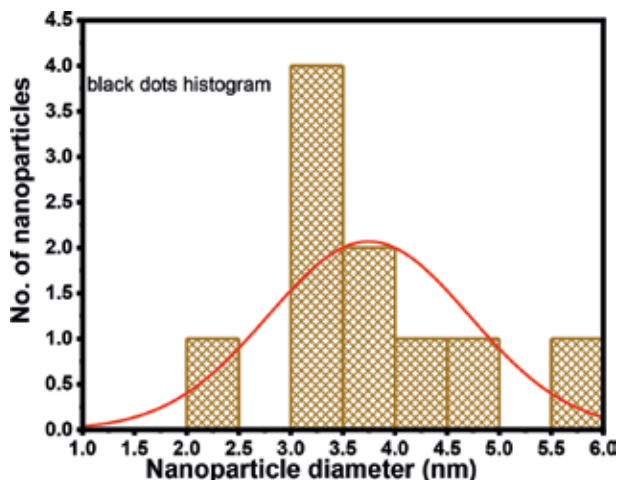


Figure 5.
Histogram of black dot sample DZ (1.0 Mol% Ag) NPs.

study has shown that smaller plasmonic Ag NPs, with an average diameter less than 25 nm in the intrinsic size regime, would exhibit an increased plasmon bandwidth [11]. Conversely, as the Ag NPs size became larger (32 nm), Ag NPs easily aggregated and formed islands. This could not preferentially attach to specific sites on the MO surface, resulting in the decrease of catalytic activity, thereby reducing the reaction rate between MO/dye [15]. In addition, as the thickness of the film is around 32 nm, the mixed films might result in blockage of sunlight which would prevent the incident light from reaching the MO NPs effectively, resulting in the decrease in the photocurrent density.

3.3 Optical absorbance and bandgap

Figure 6 displays typical optical absorption spectra for the as-synthesized samples UZ and DZ NPs. It is clear that the samples have a very high absorbance in the UV region. They decrease exponentially with increasing of the wavelength in the visible region. An enhance photon absorption can be noted in the visible region in

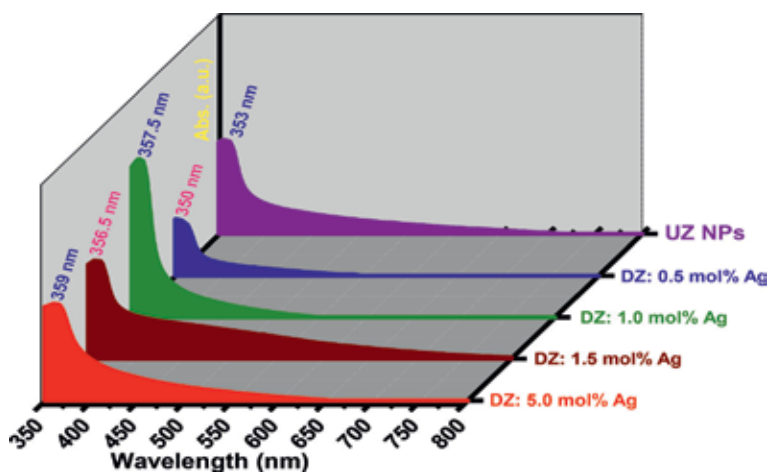


Figure 6.
UV-Vis spectra of UZ and DZ NPs.

the presence of Ag NPs. Furthermore, the highest absorption band can be observed over the range of 350–359 nm, which is ascribed to the band-to-band transition of the ZnO NPs [24]. This exciton absorption peak is being less than of the bulk ZnO (388 nm) which indicates the monodispersing of ZnO NPs as suggested by Brintha et al. [25]. The edge of allowed direct optical bandgap energy (E_g) of UZ and DZ NPs was determined using the Tauc Davis and Mott Equation [26]:

$$(h\nu)^2 = S(h\nu - E_g) \quad (3)$$

where S is constant, α is the absorption coefficient of the material, and $h\nu$ (eV) = $1239.7/\lambda$ (nm) is the photon energy. E_g was estimated by plotting $(\alpha h\nu)^2$ versus $h\nu$ as shown in **Figure 7**. E_g of UZ and DZ NPs were estimated by extrapolating the linear region to the abscissa, i.e., $(\alpha h\nu)^2 = 0$, yielding $E_g = 3.21$ to 3.31 eV. The estimated energy bandgaps agreed well with the obtained results in Türkyılmaz et al. [27]. It can be seen that the addition of Ag NPs decreased the E_g of ZnO (the inset of **Figure 7**). This implies that the presence of Ag NPs has downshifted the Fermi level of ZnO toward the valence band [1]. As a result, the driving force for electron injection from dye-excited state to ZnO conduction band is increased [1].

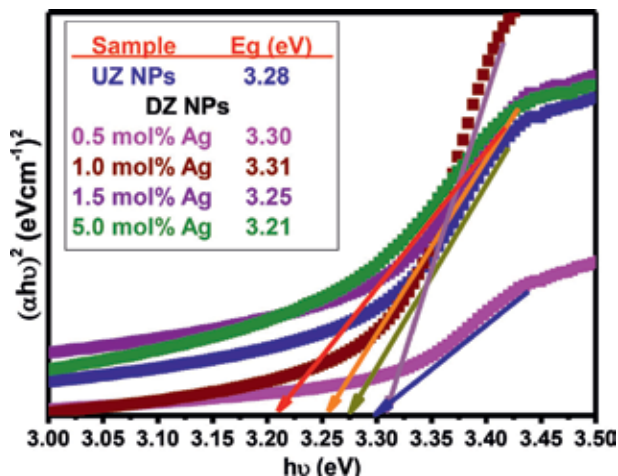


Figure 7. $(\alpha h\nu)^2$ versus photon energy ($h\nu$), the inset is the estimated values of E_g .

3.4 Photoluminescence study

It is well-known that the PL technique is one of the best optical methods for probing electron transitions between high- and low-energy levels as well as for finding electron densities of states [28]. On one hand, it can harness in the material science to identify defects and traps in materials, as well as to estimate the bandgaps of materials. Typically, the PL emission (PLE) spectrum of ZnO NPs exhibits a linear emission in the near ultraviolet (NUV) range (originating from exciton mechanism) and in the visible region (nonradioactive recombination) that is frequently originated from several, intrinsic, and extrinsic defects of ZnO NPs [29]. Different defects or interior energy traps (IETs) can be found within the bandgap of the ZnO NPs, such as vacancies, impurities, imperfections, interstitials, Zn residues, and antisites, mainly from various oxygen vacancies [30, 31]. It is worthy to mention that these IETs play a crucial role in various applications such as the performance of the DSSCs. Therefore, it is hard to recognize the IETs that may be produced, simultaneously, during the synthesization method [29]. **Figure 8**

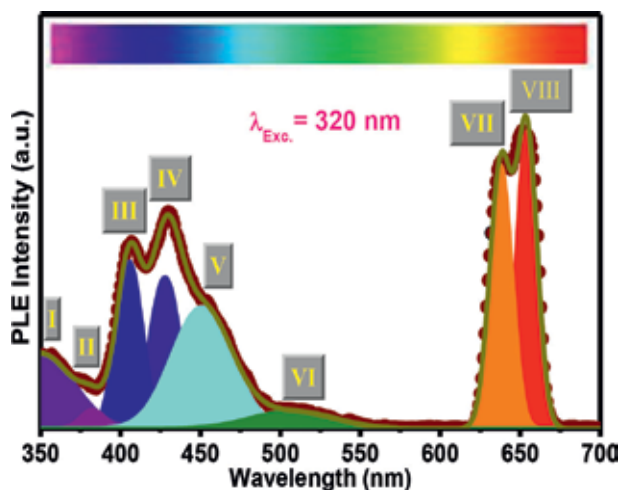


Figure 8.
PLE spectrum and deconvoluted peaks of UZ NPs was excited at 320 nm.

demonstrates the room temperature PLE spectrum of the as-synthesized UZ, which was registered at excitation wavelength of 320 nm at room temperature. The deconvolution of the PLE spectrum recognizes eight peaks (I to VII) as shown in **Figure 8**. The main features of the PLE spectrum of UZ NPs can be resolved into two divisions: NUV and visible. For the PLE spectrum (peak I) of NUV region or the near band edge (NBE) transition, it is designated to the radiative recombination of free excitons through an exciton-exciton collision process [32]. The intensity of such NBE excitonic emission depends on the size of the exciton binding energy of ZnO [33]. Different kinds of IETs are supposed to elucidate the observed transition in the visible range. The transition at peak II is allocated to the movement of the excited electrons from the donor (bottom) of conduction band to the acceptor energy level of Zn vacancy (VZn), which concludes that the ZnO NPs are n-type semiconductors [34], whereas peak III is produced by the transition of electrons from conduction band edge to the IETs complex (VZnO) [28], while peak IV is created by the transition of electrons from interstitial of (Zni) to the IETs complex (VZnO). However, the peak V is originated from transition of electrons from conduction band edge to the IETs complex OZn. The transition at peak VI is ascribed to deep IETs (a shallow surface defect level) of electrons from conduction band edge to the IETs complex vacancies of oxygen (VO). Ultimately, peak VII is attributed to the transition of electrons from interstitial of (Zni) to the IET complex (VO). The center, width, and area of the fitted peaks for the PLE spectrum and the corresponding energy for each peak are tabulated in **Table 2**. As shown in this table, the emission of the visible region is overshadowing NBE transition. The percentage areas of the NBE and the IETs transitions are an indicator of the quality of ZnO (i.e., the ratio of the defects in the ZnO). This is very imperative to facilitate the usage of the ZnO such as DSSCs; a high ratio of defects (IETs transition) is required. This indicates that the defects in ZnO NPs are large, which is deduced from the XRD analysis. Generally, FWHM of intrinsic emission in PL spectrum is related to the crystal quality. A small FWHM indicates that the crystal is of high quality, and its large value suggests that the crystal is imperfect, showing it may have point defects. Meanwhile, at FWHM, the values for both samples are nearly close to each other [35]. The schematic energy band diagram of the PLE spectrum constructed from the data is illustrated in **Figure 9**. The comparative room temperature PLE spectra (excitation at 320 nm) of DZ:1.0 mol% Ag NPs are shown in **Figure 10**. PLE spectrum of DZ:1.0 mol% Ag NPs is used to verify the quality crystal and possible

Peak #	Center (nm)	Energy (eV) =1239.7/Center	Width (nm)	Height (a.u.)	Area	Normalized area%
I	350.223	3.540	40.938	45.426	9395.400	14.194
II	382.585	3.240	14.725	183.117	838.326	01.267
III	405.491	3.057	6.116	403.887	8157.638	12.324
IV	427.827	2.898	18.833	365.869	8635.687	13.046
V	450.922	2.749	37.306	293.802	13736.875	20.753
VI	508.012	2.044	52.285	42.542	2787.723	04.212
VII	637.758	1.944	13.689	637.142	10931.550	16.515
VIII	654.309	1.895	13.001	718.651	11709.966	17.691

Table 2. Center, energy, width, height, and area of the measured PLE spectrum of UZ NPs.

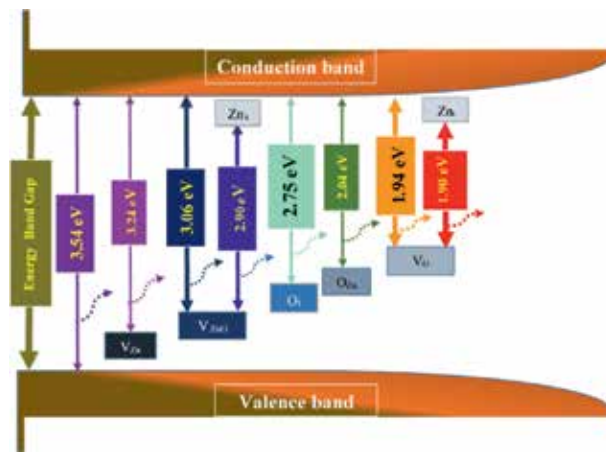


Figure 9. Schematic energy band diagram from PLES spectra.

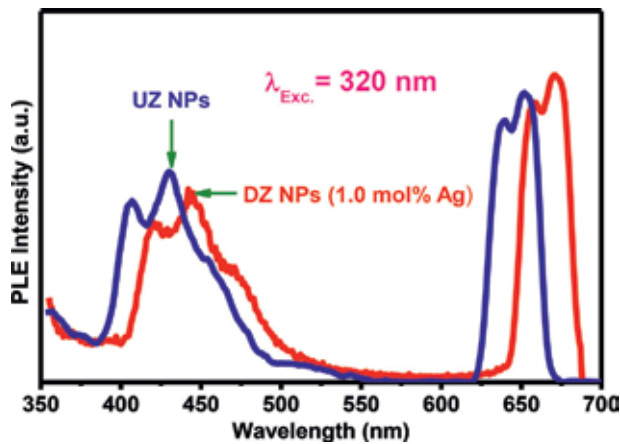


Figure 10. PLE spectrum for UZ and DZ:1.0 Mol% Ag NPs was excited at 320 nm.

effects of DZ:1.0 mol% Ag NPs [36]. It is worthy to mention that the intensity and the position of the PLE spectrum DZ:1.0 mol% Ag NPs are dependent on different factors such as the concentration of the noble metal dopants, temperature,

compressive strain, tensile strain, and shape of the particle. It is reported that the decrease in UV intensity was due to the interactions between the excited ZnO NPs and Ag NPs in the grain boundaries, which created a large amount of defects, as confirmed [37]. These kinds of interactions via the Schottky contact, metal–semiconductor diode effect decrease the recombination of electrons and holes generated from UV light irradiation and improved the photocatalytic activities [37]. It could be seen from the PLE spectra that the UV emission in DZ:1.0 mol% Ag NPs decreases which indicates the decrease in electron–hole recombination. This decrease in emission intensity is in accordance with the Stern–Volmer quenching, and similar results were previously reported [35]. The intensity of visible emission initially decreases for 0.5% nominal silver doping and then increases for higher Ag concentrations. Such anomalous intensity variation in Ag-doped ZnO NPs can be understood considering the Ag incorporation process in the NPs. The Ag⁺ ions can be incorporated into the ZnO NPs in two different ways: substituting Zn²⁺ ions creating doubly ionized oxygen vacancies VO[•] or incorporating as interstitials (Ag_i) [36]. In addition, PL intensity decreases with increasing amount of Ag doping, indicating that the core of Ag NPs captures the excited electrons before they recombine, causing the so-called electron-sink effect. This causes the accumulation of electrons on the Ag NPs, which improves electron life time and can thus reduce charge recombination, ultimately, improving electron transport [6]. While for low doping concentrations, e.g., 0.5%, most of the incorporated Ag⁺ ions might occupy ZnO lattice through Zn²⁺ ion substitution; for higher concentrations, the excess amount of Ag⁺ ions is incorporated into the NPs interstitially, creating larger amount of lattice defects [36]. By increasing Ag concentration, the intensity of defect decreased. The reduction of defects with Ag doping represented a decline in the defects and improved crystallization [37], which agreed well with XRD results. Compared to the PLE spectra of UZ NPs and DZ:1.0 mol% Ag NPs, it reveals a red-shift (longer wavelength) which is consistent with previous observations [38, 39]. This shift was due to the variation of the energy bandgap of UZ NPs [40], which agree with the UV–Vis results. The dopant Ag has a great effect on the separation and recombination process of photo-induced charge carriers of ZnO, which can further effect on PL performance [41]. It indicates that the PLE mechanism of Ag-doped/ZnO is very complex, and further research is needed.

3.5 Photovoltaic performance

The radiant light can be enhanced after being effectively coupled with plasmon absorption due to the increase of the optical density around Ag NPs. According to that, there were more photons, which were usually absorbed by the dye molecules placed in the vicinity of Ag NPs, resulting in the improvement of the device performance [23]. The system so constructed therefore provides a more efficient charge-transfer process with enhanced light absorption, thus leading to a better overall performance of Ag NPs photoanode [11]. The performance of the UZ and DZ NPs photoanodes that were sensitized by EY dye was scanned from 0 to 0.6 V. The characteristic photocurrent density-voltage (J-V) curves of different fabricated DSSCs devices are plotted in **Figure 11**. The calculated values of the photovoltaic performance parameters (efficiency (η), fill factor (FF), maximum power (P_m), maximum voltage (V_m), maximum current density (J_m), open-circuit voltage (V_{OC}), and short circuit photocurrent density (J_{SC})) for all fabricated DSSC devices are plotted in **Figure 12**. The cell with the doped photoanode DZ:1.0 mol% Ag exhibited the highest η and best performance, which has the following performance parameters: V_{oc} = 0.46 V, J_{sc} = 7.81 mA.cm⁻², P_m = 1.91, FF = 51%, and η = 1.91% (**Figure 12**). Through small additions of metal nanostructures (<2 wt %), the active

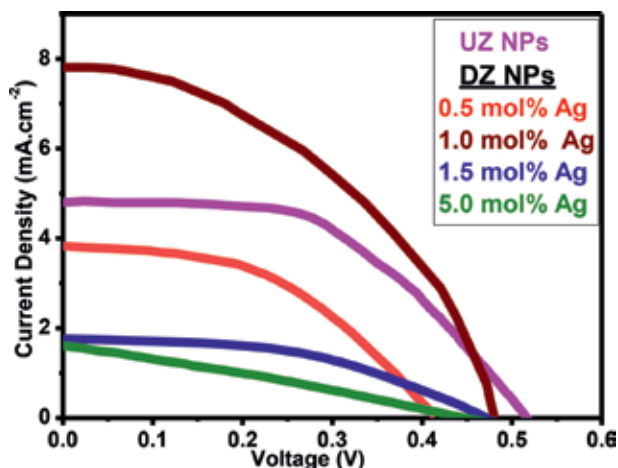


Figure 11.
J-V behavior for DSSCs based on UZ and DZ NPs photoanode sensitized with EY.

material required to achieve high efficiency solar conversion can be drastically reduced [5]. However, when the concentration was increased further, the photocurrent decreased, presumably because the Ag NPs act as recombination sites of excited electrons [14]. Consequently, to maximize the plasmonic effect in DSSCs, the optimal concentration of the plasmonic structure was decided to be 0.5 wt% [14]. Previously, it is reported that plasmon-enhanced dye excitation by an electromagnetic field decreased as the distance between dye molecules and plasmonic nanoparticles increased [14]. The enhanced J_{sc} is related to the light-harvesting capability of dye molecules by plasmon-enhanced excitation [14]. Decrease in J_{sc} and photon-to-current efficiency beyond 1.0 mol% Ag NPs can also result in a loss of absorbing dye volume due to the large volume of Ag NPs.

In addition, aggregation of Ag NPs may also occur resulting in electron trapping [1]. This process would diminish the electron density, thus decreasing J_{sc} [1]. This is probably due to plasmonic-induced photocurrents, in that the hot electrons driven from the plasmon-induced charge separation of Ag NPs can be injected into the conduction band of ZnO, resulting in plasmon-assisted photocurrent generation [14]. The improved J_{sc} is resulted from higher plasmon resonance effect caused by coverage of Ag NPs on the ZnO NPs, which increases the number of photoelectrons generated and improves the effective separation of electron-hole pairs. Therefore, the loaded Ag nanoparticles can improve J_{sc} rather than the V_{oc} in these DSSCs. Interestingly, the efficiency of DSSC based on Ag-modified ZnO NPs array decreases again. Such agglomeration of Ag NPs on ZnO NPs results in less surface area for dye loading as well as ineffective light absorption and charge separation [10]. It can be concluded that the improved J_{sc} may be attributed to not only the increase in the dye excitation by the effects of NPL associated with near-field enhancement and scattering but also to the generation of additional photocurrent owing to the NPL-induced direct hot-electron transfer from plasmonic structures to MO conduction bands [1]. For the higher concentrations of Ag NPs, it may cluster to form larger Ag NPs groups with lower electron storage capability, reducing V_{oc} [15]. Consequently, the probability of electrons and holes to recombine may increase, so J_{sc} and V_{oc} would decrease. Therefore, some of the Ag NPs in the AgZnO network structure may be corroded by electrolyte and oxidized to Ag + ions [1, 15]. This can also increase the recombination rate that could lead to a reduction in electron density in the conduction band of ZnO [1]. This diminishes the number of charge carriers, thereby acting as recombination centers that could lead to a

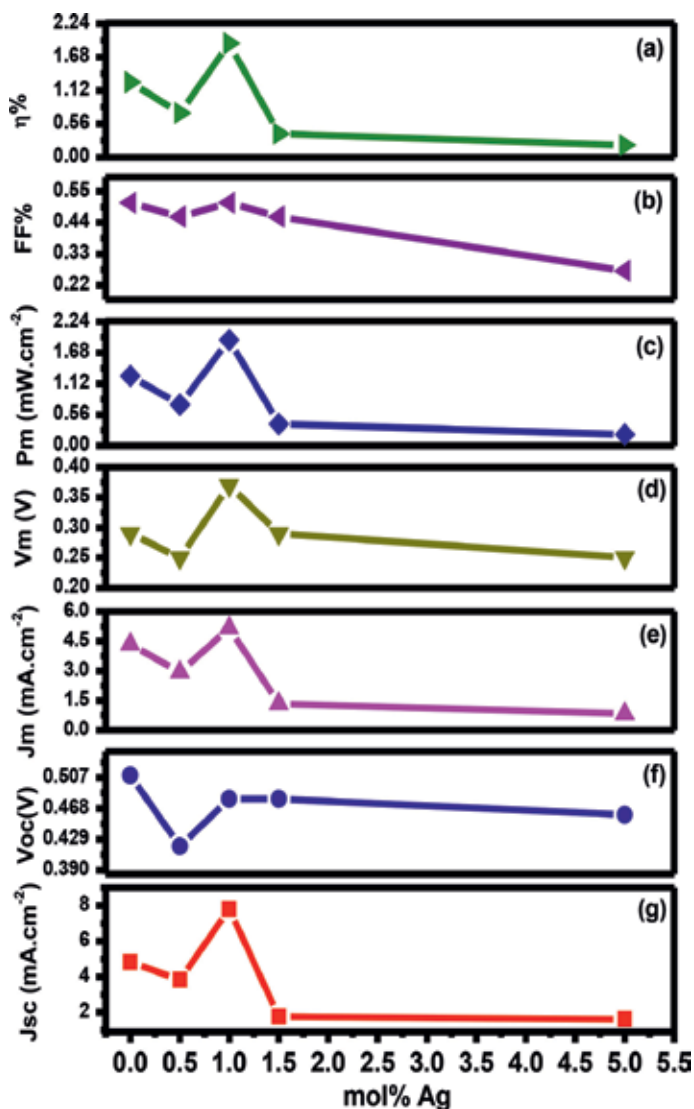


Figure 12.

Photovoltaic parameters of UZ and DZ NPs for the DSSCs sensitized with EY dye (a) $\eta\%$, (b) FF%, (c) P_m , (d) V_m , (e) J_m , (f) V_{oc} , and (g) J_{sc} .

reduction in electron concentration in the conduction band of ZnO, thus resulting in a decrease in J_{sc} and V_{oc} [1, 15]. There are contradictory reports on the increase or decrease in the V_{oc} value induced by the presence of metal NPs in the photoanode [14]. Furthermore, in the case of a further decrease in V_{oc} as well as FF was observed, it may imply that exposed Ag NPs can act as recombination centers [14]. V_{oc} is typically in proportion to the difference between the quasi-Fermi level and the Nernst potential of the redox couple. Thus, the slight decrease in V_{oc} can be explained by the downshifted Fermi level due to the incorporation of plasmonic particles [6, 13, 14]. The FF of the fabricated cells changes from 27 to 51% for 5% Ag and 1% Ag, respectively. Generally, the low values of the current density may be attributed to the anchoring group missing in the chemical structure of EY dye. These groups make a strong link between ZnO semiconductor surface and the dye molecule, in order to enhance electron injection from the LUMO energy level of the dye molecule to the conduction band of the semiconductor layer [42]. Nevertheless,

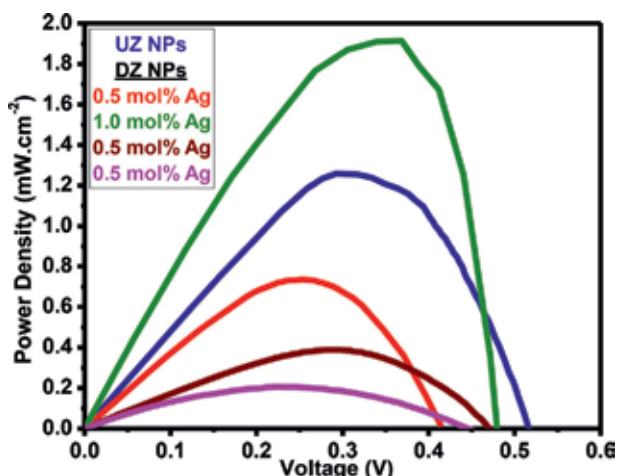


Figure 13.
Power density for DSSCs based on UZ and DZ NPs photoanode sensitized with EY.

metallic NPs have been reported to exhibit electron-sink (or photo charging) effect [6]. It was predicted that due to the electron-sink effect of the Ag NPs, a reduction in charge recombination and improved charge transport are evidenced in improving FF value with increasing plasmonic NP doping. Thus, this would account for the slight increase in J_{sc} . **Figure 13** presents the power density for DSSCs based on UZ and DZ NPs photoanode sensitized with EY.

3.6 Transient open-circuit voltage decay measurement

Agreeing to the proposed simple model of the DSSCs by Ref. [43] at short circuit, different charge-transition processes can be found in the DSSCs devices, in which the slower recombination process is preferable. In addition, the charge can present more than one kind of motion status at different voltage-dependent regions. Among them, the exponential increase region relates to internal trapping of the photoanode material, which reveals the apparent electron lifetime or response time (τ_n) or the electron recombination rate (k_{rec}) in the photoanode material. The transient open-circuit photovoltage decay (TOCVD) is a suitable method to study τ_n and k_{rec} in DSSC, which can provide some quantitative information on the electron recombination velocity in DSSC [44]. In order to conduct the TOCVD measurement, the DSSCs devices, based on UZ and DZ 1.0 mol% Ag NPs, were illuminated for 2 min to be equilibrium.

Between electron injection and electron recombination at the FTO surface, i.e., a steady-state voltage was obtained and V_{oc} was recorded after that, the subsequent decay of photovoltage during the light source was turned off. The decay of the photovoltage reflects the decrease of the electron concentration at the FTO surface, which is primarily produced by the charge recombination. In other words, the recombination velocity of photoelectron is proportional to the response of the TOCVD [44]. **Figure 14** depicts TOCVD experiment for the DSSCs devices, which follow a pseudoexponential (semilog) form. Two decayed components are distinguished, fast and slow decays, which may be ascribed to their intrinsic material properties [45]. This, also, may be attributed to the different defects of the ZnO NPs that were proved in the PL results earlier. A double exponential function was used as a powerful fitting function for the TOCVD data as depicted in Eq. (4) to extract the decay parameters [24]:

$$V_{OC} = V_0 + V_1 e^{-\frac{(t-t_0)}{\tau_1}} + V_2 e^{-\frac{(t-t_0)}{\tau_2}} \quad (4)$$

where V_0 is the offset of the V_{OC} . The amplitudes of VOC for fast and slow decay are V_1 and V_2 , respectively; it is the decay time and is the center of the fitting curve. The decay time constant (lifetime) for fast curve and slow curve is τ_1 and τ_2 , respectively. For the right-hand side of Eq. (4), it describes the fast and slow decays, respectively, the second term for the fast decay and the third term for the slow decay [24]. All extracted decay parameters of the TOCPV are listed in **Table 3**. As it was reported in Ref. [24], the k_{rec} is determined by

$$k_{rec} = \left[\frac{V_1}{\tau_1} e^{-\frac{(t-t_0)}{\tau_1}} + \frac{V_2}{\tau_2} e^{-\frac{(t-t_0)}{\tau_2}} \right] (V_T)^{-1} \quad (5)$$

where the thermal voltage ($V_T = K_B T/q$), with K_B , is Boltzmann constant, T is the absolute temperature, and q is the elementary charge, using the following Equation [36]

$$\tau_n = -V_T \left(\frac{dV_{os}}{dt} \right)^{-1} \quad (6)$$

Meanwhile, the recombination rate of the device based on DZ:1.0 mol% Ag NPs photoanode is slower than that of UZ NPs photoanode. The results revealed that the τ_n in the UZ NPs photoanode-based DSSC was longer than that in the DZ:1.0 mol% Ag NPs photoanode-based DSSCs, demonstrating that the latter possessed a higher

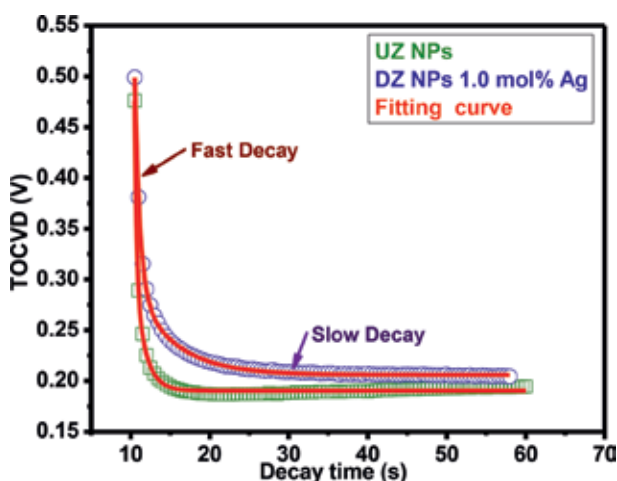


Figure 14. TOCPVD of the DSSCs cells is the sensitized EY based on UZ and DZ 1.0 Mol% Ag NPs, and the red line is the double exponential decay fitted curve.

Decay parameters	V_o (V)	t_o (s)	Fast decay		Slow decay		τ_n (s)	k_{rec} (s) ⁻¹	R^2
			V_1 (V)	τ_1 (s)	V_2 (V)	τ_2 (s)			
UZ	0.190	10.471	0.194	0.244	0.115	1.294	1.538	0.650	0.993
1.0 mol% Ag	0.206	10.448	0.227	0.651	0.085	5.096	5.747	0.174	0.991

Table 3. The parameters of the TOCPVD.

surface trap density [45] that might result from the larger surface area. The higher recombination rate and shorter electron lifetime within ZnO NPs photoanode were the reason why the FF of the corresponding DSSCs decreased.

3.7 Dye absorption spectrum

A major problem, however, is the attachment of less dye, reducing the J . One approach to solve this problem is based on a plasmonic structure, such as silver (Ag NPs), gold (Au NPs), or gold nanorods [10]. **Figure 15** displays the UV–Vis absorption spectra of one derivative of EY dye, which was dissolved in absolute ethanol. It is clear that the maximum absorption peak of EY is positioned at 526 nm; also, other small peak is located at 309 nm. EY exhibits a powerful absorption peak in the visible region, and its spectrum covers broader window than the others. The intensity of the observed absorption peaks in testing rang represents a part of energy losses in the transition in the UV region. In the DSSC application, it is much of interests to concentrate in the visible solar spectrum. In addition to that, the molar extinction coefficient of EY equals $112,000 \text{ (cmM)}^{-1}$, corresponding to $\pi \rightarrow \pi^*$ transitions of conjugated molecules [46, 47]. To investigate the effect on the light absorption enhancement of dye molecules of the DSSCs photoanode, the optical absorbance was measured of dye-sensitized plasmonic NP composite-embedded photoanode and compared them to that of the reference UZ photoanode. The results are shown in **Figure 16**. The relatively broad and strong enhancement is observed in the range of 250–550 nm with a maximum enhancement around 307 nm, which coincides with the absorption band position of decorated Ag NPs. These features suggest that dye molecules in the vicinity of Ag NPs can absorb more photons, presumably due to the intensified near-field effect of the surface plasmon and spectral overlap between the dye and plasmon, which may eventually lead to an increase in the number of charge carriers and J_{sc} values [14]. The plasmonic photoanode recorded higher absorbance than the pristine photoanode. This is a typical result in many reported works on plasmonic DSSCs [6]. The absorption in the visible region is shifted from 526 to 518.06 nm, as revealed in **Figure 16**. This can be explained by a change in the energy levels of highest occupied molecular orbital (HOMO) and lowest unoccupied molecular orbital (LUMO) of EY compared to those in solution, due to the interaction between EY molecules and the ZnO film

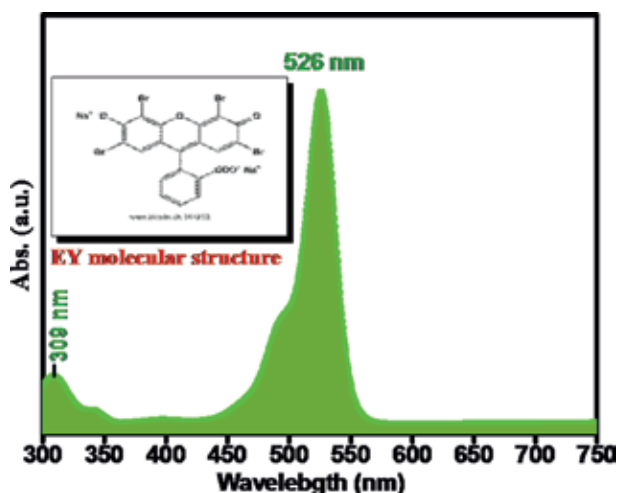


Figure 15.
UV–Vis absorption spectra of EY dyes dissolved in absolute ethanol.

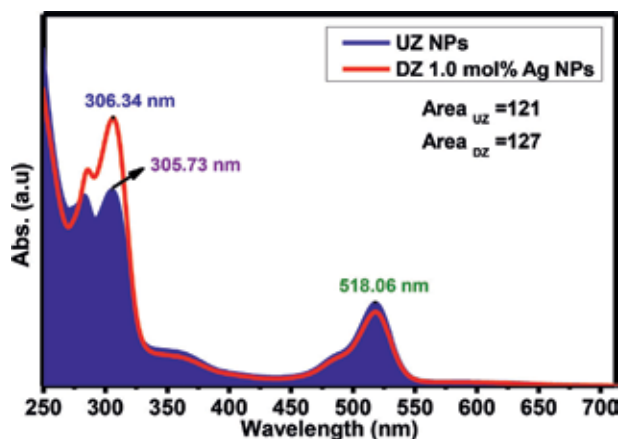


Figure 16. UV-Vis adsorption spectra of EY dyes absorbed by UZ and DZ 1.0 Mol % Ag NPs.

[48, 49]. These results show a synergistic effect between the dye and plasmonic NPs, on the light absorption enhancement effect [6].

4. Conclusion

Undoped and doped (Ag) ZnO NPs photoanodes were successfully synthesized and mediated by the combustion method. XRD results indicated that a single phase of hexagonal wurtzite structure was formed. The XRD confirmed that no Ag peaks could be observed for 1%. The HR-TEM micrograph showed that semispherical particles (20.45 and 22.30 nm) for ZnO NPs were well crystallized with an intermediate or poor agglomeration. The average ZnO NPs size was confirmed by XRD and HR-TEM inspections. The calculated bandgap of the ZnO NPs was found to be changed with the addition of the Ag⁺ ions. The PLE spectrum of the undoped ZnO NPs was examined and decomposed into two divisions: NUV and visible (violet-blue, blue-green, and orange-red). The PLE spectrum changed with the dopant Ag. The DZ:Ag 1.0 mol% dye-sensitized cells presented the best DSSCs performance among others. The results showed an enhancement of efficiency of both the J_{sc}, J_m, V_m, P_m, and FF% efficiency and the V_{oc} for the (Ag 1.0 mol%) dye-sensitized cells compared to others, which is attributed to the light-harvesting capability of dye molecules by plasmon-enhanced excitation. In addition, the recombination rate of the device based on DZ:1.0 mol% Ag NPs photoanode was slower than that of UZ NP photoanode. The lower recombination rate and shorter electron lifetime within the ZnO NP photoanode were the reason why the FF of the corresponding DSSCs increased.

Acknowledgements

The authors would like to thank the Palestinian German Joint Research Project PALGER2015-34-012 and the PHC Al Maqdisi grant No. 37038WF for their partially financial support of this research. The authors would, also, like to thank Mr. Ahmad Ashour for his technical assistant.

Conflict of interest

Authors confirm that there are no conflicts of interest.

Author details

Samy K.K. Shaat^{1*}, Hussam Musleh², Jihad Asad², Nabil Shurrah³, Ahmed Issa⁴, Amal AlKahlout² and Naji Al Dahoudi²

1 Department of Physics, Islamic University of Gaza, Gaza, Palestine

2 Department of Physics, Al Azhar University-Gaza, Gaza, Palestine

3 Department of Chemistry, Al Azhar University-Gaza, Gaza, Palestine

4 Department of Engineering, Al Azhar University-Gaza, Gaza, Palestine

*Address all correspondence to: samyshaat@yahoo.com

IntechOpen

© 2019 The Author(s). Licensee IntechOpen. This chapter is distributed under the terms of the Creative Commons Attribution License (<http://creativecommons.org/licenses/by/3.0>), which permits unrestricted use, distribution, and reproduction in any medium, provided the original work is properly cited. 

References

- [1] Shah S, Noor IM, Pitawala J, Albinson I, Bandara TMWJ, Mellander B-E, et al. Plasmonic effects of quantum size metal nanoparticles on dye-sensitized solar cell. *Optical Materials Express*. 2017;7(6):2069-2083
- [2] Wei Y, Ran L, Hao H, Yujie X. Plasmonic nanostructures in solar energy conversion. *Journal of Materials Chemistry C*. 2017;5:1008
- [3] Nada A. Renewable energy types. *Journal of Clean Energy Technologies*. 2014;2(1):61-64
- [4] Ying-Chih P, Jin Z. Mechanisms behind plasmonic enhancement of photocurrent in metal oxides. *Austin Journal of Nanomedicine & Nanotechnology*. 2014;2(5):1030
- [5] Song DH, Kim HS, Suh JS, Jun BH, Rho WY. Multi-shaped Ag nanoparticles in the plasmonic layer of dye-sensitized solar cells for increased power conversion efficiency. *Nanomaterials*. 2017;7(6):136. DOI: 10.3390/nano7060136
- [6] Pascal N, Go K, Wai T, Hiroyuki M, Atsunori M. Systematic characterization of the effect of Ag@TiO₂ nanoparticles on the performance of plasmonic dye-sensitized solar cells. *Scientific Reports*. 2017;7(1-12):15690. DOI: 10.1038/s41598-017-15541-z.
- [7] Holly Z, William E, Abdelaziz B, Olivia H, Joseph W, Alexander P, et al. Improving light harvesting in dye-sensitized solar cells using hybrid bimetallic nanostructures. *ACS Photonics*. 2016;3(3):385-394. DOI: 10.1021/acsp Photonics.5b00552
- [8] Hua D, Zhaoxin W, Yucui G, Ahmed E, ShuYa N, Jun X, et al. Silver-loaded anatase nanotubes dispersed plasmonic composite photoanode for dye-sensitized solar cells. *Organic Electronics*. 2014;15:2847-2854
- [9] Ahmad M, Pandey A, Rahim N. Towards the plasmonic effect of Zn nanoparticles on TiO₂ monolayer photoanode for dye sensitized solar cell applications. *Materials Letters*. 2017;195:62-65
- [10] Xinning L, Ying W. Plasmon-enhanced performance of dye-sensitized solar cells based on electrodeposited Ag nanoparticles. *Journal of Materials Science and Technology*. 2014;30(1):1-7
- [11] Marwa A, Nafiseh M, Lei Z, Joseph T, Donald M, Saurabh S, et al. Plasmonic gold nanoparticles for ZnO-nanotube photoanodes in dye-sensitized solar cell application. *Nanoscale*. 2016;8:1658
- [12] Vinod K, Swart H, Som S, Vijay K, Yousif A, Anurag P, et al. The role of growth atmosphere on the structural and optical quality of defect free ZnO films for strong ultraviolet emission. *Laser Physics*. 2014;24:105704
- [13] Stafford S, Heeso N, Gary B, Hui C, Charles S. Plasmonic Enhancement Of Dye-sensitized solar cells using core-shell nanostructures. *The Journal of Physical Chemistry C*. 2013;117(2):927-934. DOI: 10.1021/jp311881k
- [14] Yoon J, Yu J, Saji K, Myunghwan B, Zhiqun L, Dong K. Plasmonic dye-sensitized solar cells incorporated with Au-TiO₂ nanostructures with tailored configurations. *Nanoscale*. 2014;6:1823
- [15] Danladi E, Joshua O, Gabriel O, Ezeoke J. Plasmon-enhanced efficiency in dye sensitized solar cells decorated with size-controlled silver nanoparticles based on anthocyanins as light harvesting pigment. *Journal of Photonic*

- Materials and Technology. 2016;2(1): 6-13. DOI: 10.11648/j.jmpt.20160201.12
- [16] Kumar V, Prakash J, Singh J, Chae K, Swart C, Ntwaeaborwa O, et al. Role of silver doping on the defects related photoluminescence and antibacterial behaviour of zinc oxide nanoparticles. *Colloids and Surfaces B: Biointerfaces*. 2017;1(159):191-199. DOI: 10.1016/j.colsurfb.2017.07.071.
- [17] Rad M, Kompany A, Zak A, Abrishami E. The effect of silver concentration and calcination temperature on structural and optical properties of ZnO:Ag nanoparticle. *Modern Physics Letters B*. 2015;29(1): 1450254. DOI: 10.1142/S0217984914502546
- [18] Vinod K, Swart H, Ntwaeaborwa O, Kroon R, Terblans J, Shaat SKK, et al. Origin of the red emission in zinc oxide nanophosphors. *Materials Letters*. 2013; **101**:57-60
- [19] Talaat JKS, Hammad M, Roger H. The influence of annealing temperature on the structure, morphologies and optical properties of ZnO nanoparticles. *Superlattices and Microstructures*. 2010; **47**:335-340
- [20] Zhou X, Xie Y, Mi H, Ma J, Yang J, Cheng J. Comparative study of two methods for the synthesis of CuBi₂O₄ particles and their application in ZnO-based dye-sensitized solar cells. *Journal of Materials Science: Materials in Electronics*. 2017;28:13437-13444
- [21] Zayed H, Musleh H, Shaat SKK, Shurrah N, Asaad J, AlDahoudi N. Synthesis of zinc oxide nanoparticles at different aging time for low cost dye sensitized solar cells. *Journal of Scientific Research in Science*. 2018;34: 275-286
- [22] Salem J, Hammad T, Kuhn S, Draaz M, Hejazy N, Hempelmann R. Structural and optical properties of Co-doped ZnS nanoparticles synthesized by a capping agent. *Journal of Materials Science: Materials in Electronics*. 2014; **25**:2177-2182
- [23] Van-Duong D, Ho-Suk C. Highly-efficient plasmon-enhanced dye-sensitized solar cells created by means of dry plasma reduction. *Nanomaterials*. 2016;6(4):70. DOI: 10.3390/nano6040070
- [24] Shaat SKK, Zayed H, Musleh H, Shurrah N, Issa A, Asad J, et al. Inexpensive organic dyes-sensitized zinc oxide nanoparticles photoanode for solar cells devices. *Journal of Photonics for Energy*. 2017;7:025504-025504
- [25] Brintha S, Ajitha M. Synthesis and characterization of ZnO nanoparticles via aqueous solution, sol-gel and hydrothermal methods. *IOSR Journal of Applied Chemistry*. 2015;8(11):66-72
- [26] Shaat SKK, Swart H, Ntwaeaborwa O. Investigation of luminescent properties of Ca_{0.3}Sr_{0.7}Al₂O₄:Tb³⁺,Eu³⁺ excited using different excitation sources. *Journal of Electron Spectroscopy and Related Phenomena*. 2014;197:72-79
- [27] Türkyılmaz ŞŞ, Güy N, Özacar M. Photocatalytic efficiencies of Ni, Mn, Fe and Ag doped ZnO nanostructures synthesized by hydrothermal method: The synergistic/antagonistic effect between ZnO and metals. *Journal of Photochemistry and Photobiology A: Chemistry*. 2017;341:39-50
- [28] Jin-Han L, Ranjit P, Rupesh D, Zhe-An L, Yi-Ping W, Ching-Hwa H, et al. Photoluminescence mechanisms of metallic Zn nanospheres, semiconducting ZnO nanoballoons, and metal-semiconductor Zn/ZnO nanospheres. *Scientific Reports*. 2014; **4**(6967):1-8

- [29] Manoranjan G, Raychaudhuri A. Shape transition in ZnO nanostructures and its effect on blue-green photoluminescence. *Nanotechnology*. 2008;**19**(44):445704
- [30] Nanda S, Asit P, Tapendu M, Monica K. Processing temperature dependent morphological and optical properties of ZnO nanorods. *Materials Science in Semiconductor Processing*. 2014;**20**:55-60
- [31] Karkeng L, Muhammad H, Roslinda S, Al-Hardan NH, Ishak M, Weesiong C. Temperature-driven structural and morphological evolution of zinc oxide nano-coalesced microstructures and its defect-related photoluminescence properties. *Materials*. 2016;**9**(4):300-315
- [32] Irimpan L, Nampoorei VPN, Radhakrishnan P. Size dependent fluorescence spectroscopy of nanocolloids of ZnO. *Journal of Applied Physics*. 2007;**102**:063524
- [33] Chang K, Pyung M, Sungyeon K, Jae M, Hyeon J, Jungsik B, et al. Effect of carrier concentration on optical bandgap shift in ZnO:Ga thin films. *Thin Solid Films*. 2010;**518**(22): 6304-6307
- [34] Aneesh PM, Vanaja KA, Jayaraj MK. Synthesis of ZnO nanoparticles by hydrothermal method. *Proceedings of SPIE*. 2007;**6639**:66390J
- [35] Shah AH, Manikandan E, Ahmed M, Ganesan V. Enhanced bioactivity of Ag/ZnO Nanorods-a comparative antibacterial study. *Journal of Nanomedicine & Nanotechnology*. 2013;**4**:3
- [36] Zeferino R, Flores M, Pal U. Photoluminescence and Raman scattering in Ag-doped ZnO nanoparticles. *Journal of Applied Physics*. 2011;**109**:014308. DOI: 10.1063/1.3530631
- [37] Hosseini SM, Sarsari I, Kameli P, Salamati H. Effect of Ag doping on structural, optical, and photocatalytic properties of ZnO nanoparticles. *Cond-mat.mtrl-sci*. 2015:1-13. rXiv: 1508.00382v1. DOI: 10.1016/j.jallcom. 2015.03.136
- [38] Kuznetsov AS, Lu Y-G, Turner S, Shestakov V, Tikhomirov VK, Kirilenko D, et al. Preparation, structural and optical characterization of nanocrystalline ZnO doped with luminescent Ag-nanoclusters. *Optical Materials Express*. 2012;**2**(6):723
- [39] Oleg L, Vasilii C, Vasile P, Mahdi ABRC, Lee C, Ion T, et al. Silver-doped zinc oxide single nanowire multifunctional nanosensor with a significant enhancement in response. *Sensors and Actuators B*. 2016;**223**: 893-903
- [40] Gem T, Rhituraj S. A review on the optical properties of ZnO nanostructures for optoelectronic device application. *International Journal of Management, Technology and Engineering*. 2546;**8**(XI):2018
- [41] Nguyen N, Tran T, Nguyen T, Doan T. Preparation and characterization of silver doped ZnO nanostructures. *Open Journal of Synthesis Theory and Applications*. 2012;**1**:18-22
- [42] Calogero G, Bartolotta A, Marco G, Carlo A, Bonaccorso F. Vegetable-based dye-sensitized solar cells. *Chemical Society Reviews*. 2015;**44**:3244-3294
- [43] Zhang Z. École polytechnique fédérale de lausanne [PhD thesis]. Switzerland; 2008
- [44] Fabregat-Santiago F, García-Cañadas J, Palomares E, Clifford JN, Haque SA, Durrant JR, et al. The origin of slow electron recombination processes in dye-sensitized solar cells with a

lumina barrier coatings. *Journal of Applied Physics*. 2004;**96**:6903-6907

[45] Chengkun X, Paul S, Liangliang C, Jiamin W, Di G. Ordered TiO₂ nanotube arrays on transparent conductive oxide for dye-sensitized solar cells. *Chemistry of Materials*. 2010;**22**(1):143-148. DOI: 10.1021/cm9027513.

[46] Musleh H, AlDahoudi N, Zayed H, Shaat SKK, Tamous HM, Shurrab N, et al. Synthesis and characterization of ZnO nanoparticles using hydrothermal and sol-gel techniques for dye-sensitized solar. *Journal of University of Babylon for Engineering Sciences*. 2018; **26**(9):256-267

[47] Shaat SKK, Musleh H, Zayed H, Tamous H, Issa A, Shurrab N, et al. Solution combustion-derived ZnO nanoparticles for photoanode of solar cells. *Materials Science and Engineering B*. 2019;**241**:75-81

[48] Hara K, Horiguchi T, Kinoshita T, Sayama K, Sugihara H, Arakawa H. Highly efficient photon-to-electron conversion with mercurochrome-sensitized nanoporous oxide semiconductor solar cells. *Solar Energy Materials and Solar Cells*. 2000;**64**: 115-134

[49] Rohatgi K, Singhal G. Nature of bonding in dye aggregates. *The Journal of Physical Chemistry*. 1966;**70**: 1695-1701

Heterojunction-Based Hybrid Silicon Nanowires Solar Cell

Riam Abu Much, Prakash Natarajan, Awad Shalabny, Sumesh Sadhujan, Sherina Harilal and Muhammad Y. Bashouti

Abstract

It is known that defect-free, i.e., oxide-free, Si nanowires (Si NWs) exhibit lower defect density emissions than unmodified Si NWs. This is successfully established by grafting organic molecules on the surface. Here we show that by using a two-step chlorination/alkylation process, we are able to graft organic molecules on Si NWs for solar cell applications. Afterward, we show the electronic properties of the molecular surface (such as work function and band bending). Finally, we correlate these properties to the solar cell performance.

Keywords: silicon nanowire, defect-free surface, oxide-free silicon, chlorination/alkylation process, hybrid solar cell, oxidation resistance, photoemission, heterojunction

1. Introduction

Recently, many one-dimensional (1D) nanostructures have been realized by different methods [1, 2]. One-dimensional nanostructures such as nanowires (NWs) are considered a promising material for various applications in electronics [3], optoelectronics [4], photovoltaics [2, 5–15], and sensing [16–18].

Specifically, silicon nanowires (Si NWs) received a considerable attention since it can be integrated in the microelectronic industry. Therefore, Si NWs revealed their potential to become the mainstream building blocks of future nanodevices such as field effect transistors (FETs) [19–21] and solar cells [21–26], thus reducing process redesign costs. However, before such applications, we need at first to control the growth of the Si NWs and to understand its electronic properties. Here, we show a promising growth method and robust characterization method, i.e., the vapor-liquid-solid (VLS) method and the X-ray photoelectron spectroscopy (XPS), respectively.

Moreover, studies show that the electronic properties of Si NWs can be tuned through attachment of molecules at the surface. The high ratio between the surface and the volume of NWs makes the electronic properties highly sensitive to surface properties. To this end, grafting the surface (through dangling bonds) with organic molecules is expected to have a significant impact on the final physical and chemical properties of Si NWs. The resulting surface is known as “hybrid Si NWs” [27, 28].

However, for many applications the presence of oxide (mainly native oxide) at the Si surfaces introduces defects and decreases the device performance. Native oxide grows at the Si surface after exposure to air or/and to humidity. The defects form an undesirable layer of oxide with high impurity levels, which can result in uncontrolled

oxide/silicon interfaces. Thus, to obtain efficient Si NWs, we need to protect the surface against oxidation. For example, hydrogenated Si NWs, i.e., Si—H bonds, exhibit low surface recombination velocities [29]. However, the Si—H bonds tend to oxidize within a few minutes. Another method to functionalize the Si NW is through different bonds such as Si—C bonds, which may increase the oxidation resistance from several minutes to a few hundred hours or even months [27, 28]. Another advantage of the Si—C bonds (rather than stability and tuning the electronic properties) is their being selectively sensitive to the environment. For instance, gas sensors based on Si NWs can tune their functionality by adding special molecules at the surface with specific reactivity with the target gas [30–32]. In this article, we, first, explain how to grow the Si NWs, then how we functionalize their surface through chlorination/alkylation process, electronic properties, and finally, their application in solar cells.

2. Experimental procedure

2.1 Growth of Si NW

Si NWs were prepared by vapor-liquid-solid (VLS) method by using chemical vapor deposition (CVD) with a silane gas. The obtained Si NWs is shown in **Figure 1**. The main steps of the VLS growth can be summarized as follows:

- i. Evaporation of growth species and their diffusion and dissolution into liquid droplets
- ii. Diffusion and precipitation of saturated species at the liquid—substrate interface
- iii. Nucleation and growth of desired material on the interface
- iv. Separation of droplets from the substrate by further precipitation and the growth of NWs

Before starting the growth, the Si substrate [the (111)] is immersed in a dilute HF solution (2%) to remove the native oxide. Subsequently, we evaporate 2 nm thick Au film or drop cast a gold nanoparticle on the Si surface. The gold nanoparticles can control the diameter of the Si NWs. The substrate is annealed

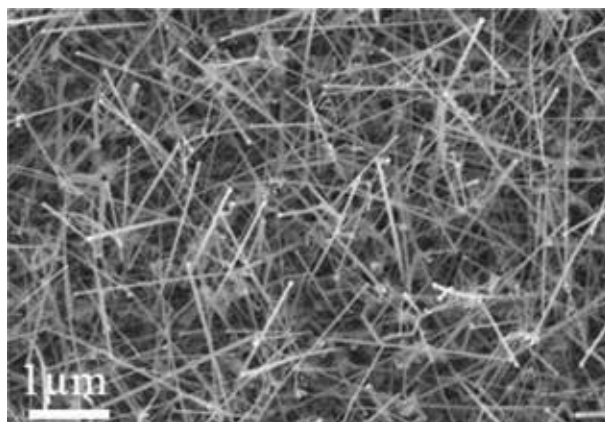


Figure 1. SEM image of VLS-grown Si NWs with lengths of $3 \pm 1 \mu\text{m}$ and diameters of $60 \pm 10 \text{ nm}$.



Figure 2.
The chlorination/alkylation system. In Figure 4, different reactions are carried in the same time.

under vacuum at the CVD chamber to 580°C for 10 min. The temperature was then reduced to 520°C, and a mixture of 10:5 sccm (standard cm³ min⁻¹) of Ar:SiH₄ was introduced for 20 min at a pressure of 0.5–2 mbar. The growth time can basically control the final length of the Si NWs (see **Figure 1**).

The VLS-grown Si NW can be with lengths from 1 to 20 μm and diameters of 10–100 nm [33]. As shown in the SEM image, the Si NWs were grown in random orientations.

2.2 Organic grafting via chlorination/alkylation

Among those methods developed for planar silicon, the chlorination/alkylation process is considered a promising method for molecular grafting. In this method, we cover the Si surface with Cl atoms and then convert them to R molecules. The conversion process should maintain an inert atmosphere such as reflux system or glove box (**Figure 2**).

2.3 X-ray photoelectron spectroscopy

X-ray photoelectron spectroscopy (XPS) can be used to investigate the chemical and electronic surface properties of the Si NWs. The final output of XPS measurements is the function of kinetic energy (or binding energy) versus the intensity. A schematic layout of the XPS system is depicted in **Figure 3** which shows the main components. A monochromatic Al K radiation (1487 eV) is irradiated to the sample to extract the core-level and valence band photoelectron spectra (0–1000 eV). They are collected at a take-off angle of 35° by a hemispherical analyzer with an adjustable overall resolution between 0.8 and 1.2 eV. In our case, it is very important to get high resolution for the following individual spectra:

- i. Si 2p from 95.0 to 110.0 eV: to follow the properties of Si
- ii. C 1s from 282.0 to 287.0 eV: to figure out the grafting profile either physical or chemical grafting, molecular coverage, and functional group in the molecules
- iii. 1s from 520 to 550 eV: to follow the oxidation of the surface

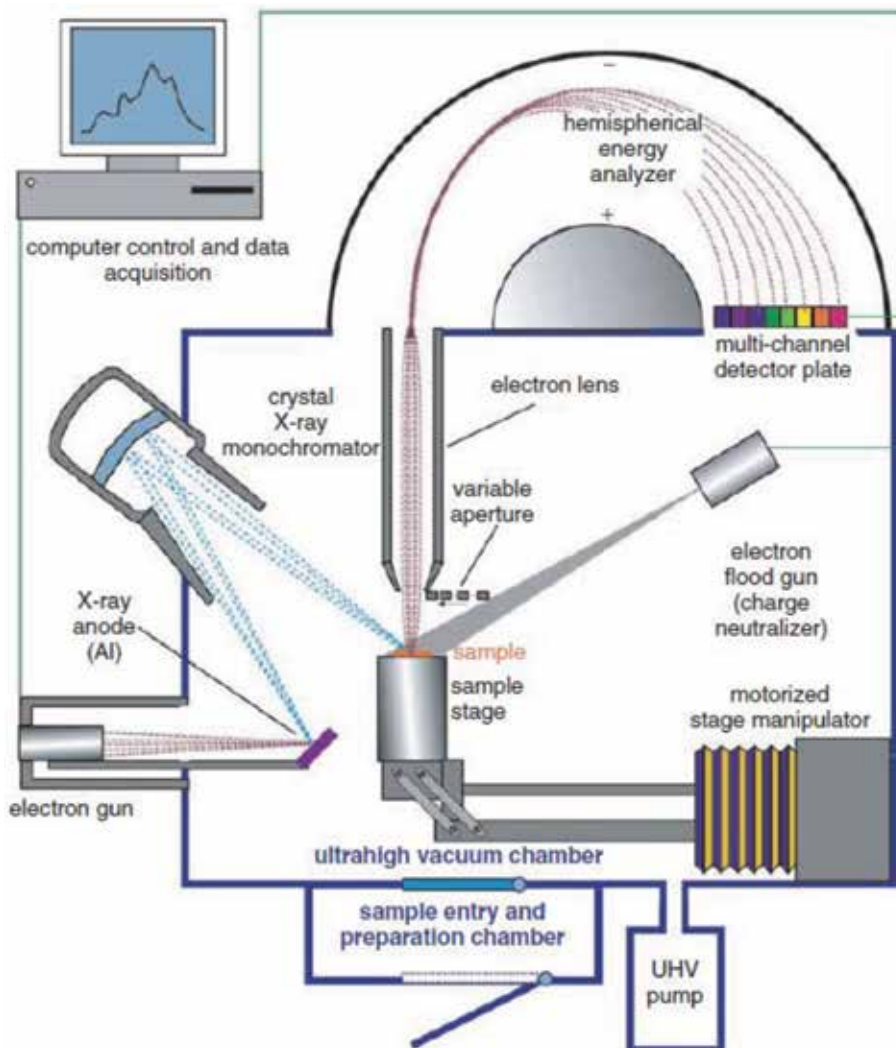


Figure 3. Schematic layout of an X-ray photoelectron spectroscopy (XPS) system including the analyzer, sample stage, X-ray anode, X-ray monochromator, and electron gun.

The resulting XPS spectra were analyzed, and oxide levels were determined by spectral decomposition using the XPS peak software.

3. Results and discussion

Usually “hybrid materials” are used to describe two conjugated components that are chemically different. Here, we use it to define the molecular junction that are obtained after grafting an organic molecule to Si. An example for this is illustrated in **Figure 4**, where alkyl molecules are chemically attached to Si NW via Si—C bonds [27].

3.1 Organic functionalization via chlorination/alkylation

The method provides oxide-free Si and is consistent By chlorination/alkylation as shown in **Figure 5**. After hydrogenation and for the first step, we get Cl bonds by immersing the Si NWs sample in a saturated PCl_5 solution. In the second step, we

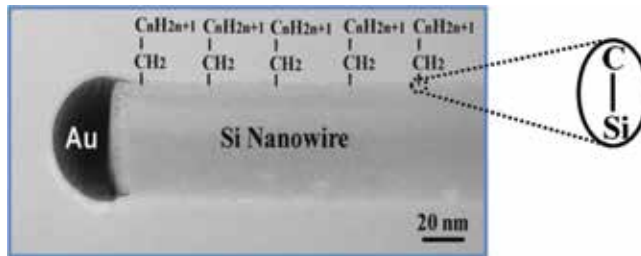


Figure 4.
 Hybrid Si NW: the organic molecules (alkyl as example) are chemically connected to Si NW by covalent bonds Si—C.

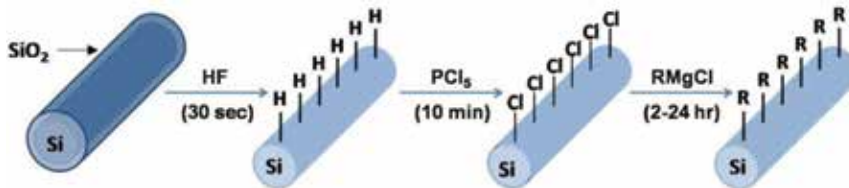


Figure 5.
 Scheme illustrating the functionalization of Si NWs through the two-step chlorination/alkylation process.

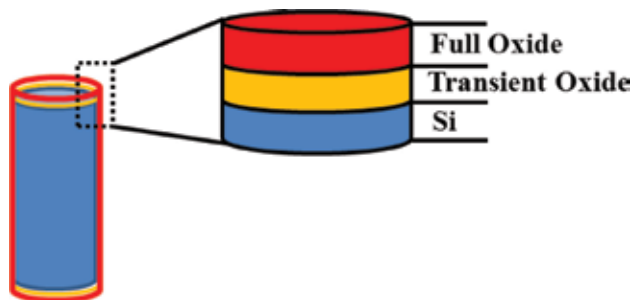


Figure 6.
 Schematic diagram of SiOx/Si interface.

convert the chlorine atoms by Grignard reaction to organic molecules. The organic molecule (alkyl as an example) will be attached normally to the surface by silicon-alkyl surface bonds, i.e., Si—C bonds [30, 34].

3.2 Native oxide

The Si NWs tends to form a native oxide at the surface. The chemical stoichiometric can be explored by XPS. It was found that there are two types of Si oxide: (i) interfacial sub-stoichiometric oxides, termed as *transient oxides* including Si₂O (n = 1), SiO (n = 2), and Si₂O₃ (n = 3), and (ii) stoichiometric or full oxide SiO₂ (n = 4) as schematically shown in **Figure 6** [33–36].

3.3 Prior termination

Before any surface treatment, we removed the oxides by immersing the Si NWs in HF solution, and Si—H can be formed. Obtaining Si—H bonds has three main advantages: (i) it helps us explore oxidation mechanism since Si—H bonds are stable for a few minutes (less than 5 min), (ii) it gives full monolayer, and (iii) H-terminated is the starting step for molecular grafting [33–36].

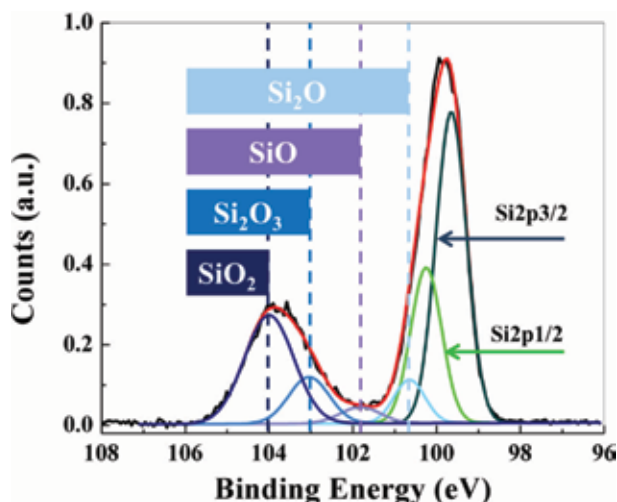


Figure 7. XPS spectrum of Si2p core-level emission showing two silicon and four oxide peaks.

To follow the stability of the Si—H bonds or in other words to follow the oxidation of the Si NWs, we followed the Si2p emission spectra. As you can see in **Figure 7**, the Si2p emission includes two silicon spin-splitting peaks: (i) Si $2p_{1/2}$ and (ii) Si $2p_{3/2}$.

We can follow the amount of each oxide state (I_{SiO_x}) by the relative integrated area under each peak. For example, we divide the integrated area under the oxide state (A_{SiO_x}) by the sum of the integrated area under the Si2p, i.e., the Si $2p_{1/2}$ and Si $2p_{3/2}$ peaks ($A_{Si\ 2p_{1/2}} + A_{Si\ 2p_{3/2}}$). Therefore, the total oxidation (I_{ox}) can be calculated by the sum of the all the oxide states, i.e., ($I_{ox} = I_{SiO} + I_{SiO_2} + I_{SiO_3} + I_{SiO_4}$). It is worth to mention that the oxidation rate is different at low or high temperature (**Figure 8**). For example, Bashouti and co-authors observed different mechanisms at low temperatures (from 25 to 150°C), in which the suboxide states are the main share of the total oxide state, while at high temperatures (200–400°C), the full oxide state (i.e., SiO₂) is the main contributor to the total oxide [37, 38].

Each oxide state shows different shift and intensity relative to the Si2p. Therefore, each state has its own oxidation rate. To this end, we can calculate the respective activation energies (E_A^{ox}) of each state. Roughly speaking, since all the

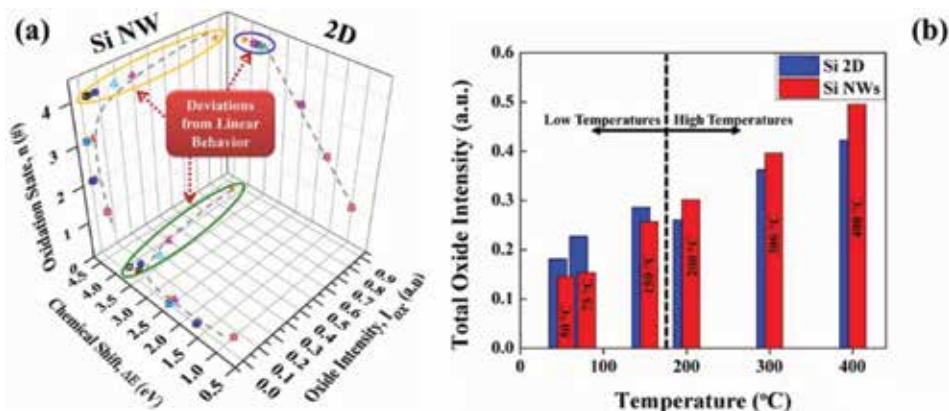


Figure 8. (a) The sub- and full oxide distribution as function of binding energy shift and intensity per suboxide and (b) total oxide intensity of all oxide states in low and high temperature in Si NWs and 2D surfaces.

suboxides show similar rate, the E_A^{ox} was 46.35 and 23.31 meV in high and low temperature, respectively [39, 40]. The differences in the activation energies of Si NW in the high and low temperatures reveal different oxidation kinetic mechanisms:

- i. **Low-temperature mechanism:** below the Si—H bonds, the back bond starts to be oxidized and turns to be suboxides. Therefore, oxidation of the backbonds (Si—O—Si) can be considered as the primary mechanism. For longer oxidation times, more backbonds are oxidized backbond form and isolated Si—OH bonds [41]. The schematic diagram of the mechanism is illustrated in **Figure 9** [42].
- ii. **High-temperature mechanism:** the oxidation of the Si NWs can be attributed to the self-limited oxidation caused by the function of the initially formed oxide layer as a diffusion barrier (see **Figure 10**).

Understanding the oxidation mechanism will help us get high stable molecules on the Si NWs surface. In addition, since most of the electronic devices are operated in low temperature (below 200°C), the understanding of the low-temperature mechanism is very valuable [42].

3.4 Si2p emission

As explained above, the Si NWs show native oxide on the surface. The emission of the native oxide (without charging effect) appears in the 101–104 eV. By removing the native oxide and obtaining Si—H bonds, we can start the chlorination/alkylation process. Removing the native oxide is confirmed by the absence of the emission in 101–104 eV as seen **Figure 11** [46].

3.5 Carbon 1S emission

The emission of the C1 s confirms that the attachment via the chlorination/alkylation gives either chemical or physical bonds. Before grafting, or in the case of physical bonding, no Si—C should be available. However, in the case of chemical bond, the Si—C should be observed in the C1 s emission. For example, **Figure 12** depicts the C1 s emission of the CH₃-terminated Si NWs. Before termination, no Si—C bond was found. In this case only two emissions observed: C—C at 285.20 ± 0.02 eV and C—O at



Figure 9.
Scheme of the suggested mechanism for low-temperature oxidation of the H-terminated Si NW.

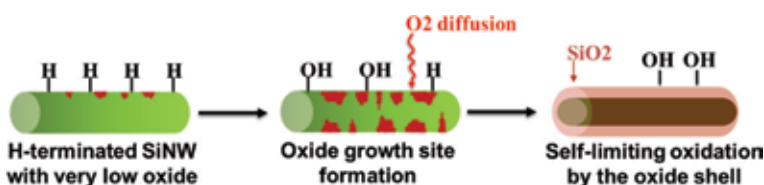


Figure 10.
Scheme of the suggested mechanism for high-temperature oxidation of the H-terminated Si NW.

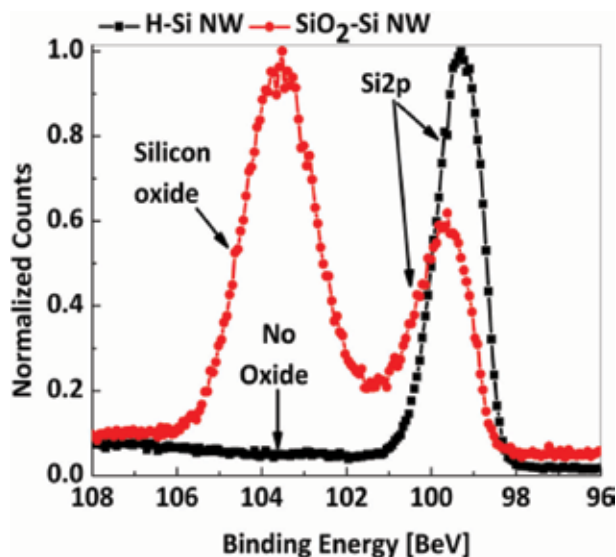


Figure 11.

Si_{2p} emission of SiO₂-Si NW and H-Si NW.

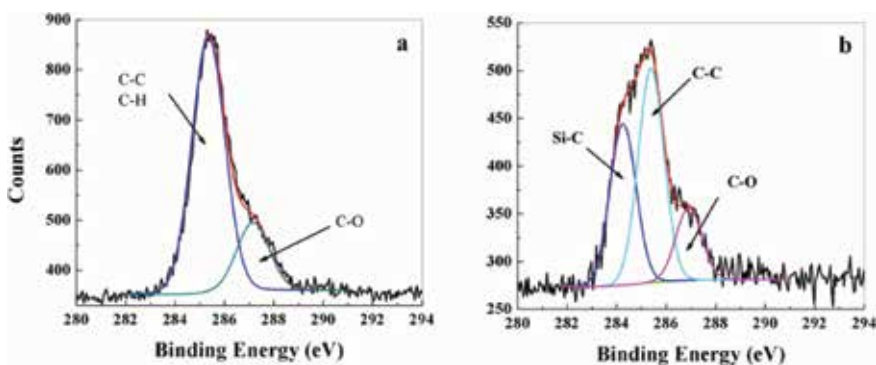


Figure 12.

XPS data from the C_{1s} emission region before and after alkyl-terminated Si NWs. (a) H-Si NWs show two peaks: C—C at 285.20 ± 0.02 eV and C—O at 286.69 ± 0.02 eV. (b) Methyl-Si NWs show three peaks: C—Si at 284.11 ± 0.02 eV, C—C at 285.20 ± 0.02 eV, and C—O at 286.69 ± 0.02 eV.

286.69 ± 0.02 eV which may belong to adventitious hydrocarbons. After termination, the CH₃ is chemically bonded to the Si and the Si—C is observed. Therefore, the emission of the C_{1s} fitted to three peaks: C—Si at 284.11 ± 0.02 eV, C—C at 285.20 ± 0.02 eV, and C—O at 286.69 ± 0.02 eV. The deconvolution method is described in [27].

3.6 Calculating the molecular density on the Si NW surface

In order to address this issue, we used a “model” molecule. In our case we chose the methyl (i.e., CH₃) since it is the smallest organic alkyl molecule with a van der Waals diameter (VDW) of 2.5 Å lower than the internuclear distance between adjacent Si atoms (3.8 Å). To this end, theoretically, the molecule should give nearly full surface density (100%), i.e., coverage (see Figure 13). The molecular coverage can be obtained by dividing the area under the C—Si peak to the area under the Si_{2p} peak (sum of Si_{2p_{1/2}} and Si_{2p_{3/2}}). Subsequently, we ratioed all the molecular coverage to the methyl, i.e., “(C—Si/Si_{2p})_{alkyl}/(C—Si/Si_{2p})_{max.methyl}” [27].

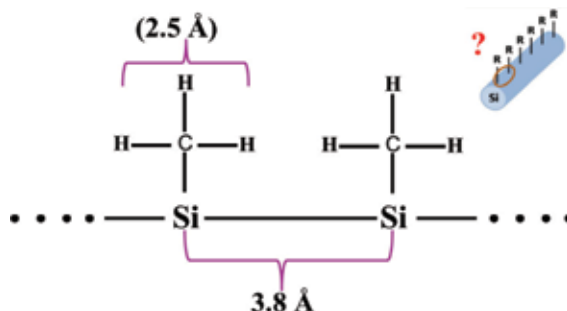


Figure 13.
 Schematic diagram of methyl connected to adjacent Si atoms.

3.7 Termination of the Si NW with different molecules

Here we use alkyl molecules since they have the same structure as in methyl. The molecular coverage was found to be dependent on the steric effects which caused by the lateral interactions between the molecules. Steric effects decrease the coverage level for any molecule longer than methyl. This is due to the fact that longer molecules have higher VDW diameter (4.5–5.0 Å) than the diameter of the Si atoms. In our case, we used molecule with the form of C_nH_{2n+1} (where $n = 1-10$) and represented by C_n . For example, methyl and decyl are represented by C_1 and C_{10} , respectively. As the VDW diameter increases, low coverage decreases as shown in **Figure 14**.

We compare the coverage between the Si NWs and the 2D silicon. We found a similar decay but lower coverage of 10% in average than the 1Si NWs. This is maybe due to the couverture effect, which causes the molecule to be normal to the surface, and therefore, the steric effect can be lower in the case of the Si NWs. However, after $> C_6$, an inconsistency is observed. Based on this we can consider two main factors for grafting:

- i. Molecule-substrate vertical interaction
- ii. Molecule-molecule lateral interaction

The first factor can play a role in the short molecules (C_1-C_5), since they exhibit liquid-like behavior and thermal fluctuations; the determining factor is the vertical

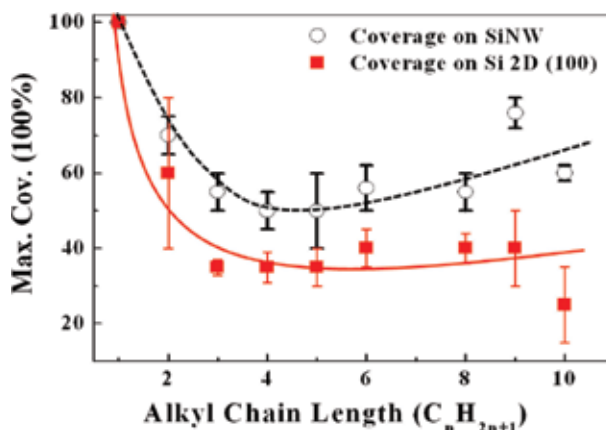


Figure 14.
 $\Gamma_{max-alkyl}$ versus alkyl chain length on Si NWs and, for comparison, on 2D Si(100) surfaces. Note: $(\Gamma_{max-alkyl}) (C-Si/Si2p)_{max-alkyl}/(C-Si/Si2p)_{max-C_1}$. Reproduced with permission from [28].

interaction [43]. The second factor may play a role in the longer molecule, i.e., (C_6 – C_{10}) that forms a solid-like phase, and therefore, the lateral interactions become dominant in this regime [44].

3.8 Stability of functionalized Si NW

It was found that the stability of grafted molecules on the Si NWs is the function of several factors mainly the (i) molecular chain length, (ii) coverage level, and (iii) surface energy and diameter.

3.9 Effect of coverage and chain length

The molecular surfaces (C_1 – C_{10}) were exposed to ambient air for 100 hours at room temperature, as shown in **Figure 15**. In the first days, all the alkylated Si NW show high oxide resistivity. However, after 8 days the oxide intensity became considerable and found to be dependent on the chain length and the coverage level. For example, in the case of C_3 – C_6 , the oxide level rose to ~ 0.13 . However, at the same time, C_1 shows only 0.03, which is twofold higher oxidation resistance than that of C_3 – C_6 –Si NWs. This implies that stability of the Si NWs is dependent on the molecule coverage [28].

3.10 Effect of surface energy and diameter

Different diameters of Si NW have been used to explore the impact of the diameter: 2D (100), 2D (111), Si NW 50 nm in diameter (Si NW_{50nm}), and Si NW 25 nm in diameter (Si NW_{25nm}). To make a proper comparison, we used the same molecule (CH_3) in all the different samples. Then we exposed them to ambient air for same periods (see **Figure 16**).

Interestingly, the stability of methyl groups on Si NW is dependent on the surface. For example, the CH_3 molecule on 2D (111) was more stable than 2D (100). For example, they show the same oxidation level, but after 40 and 20 days, the Si (111) and (100), respectively, i.e., (111), show double stability than (100). The higher stability of the 2D (111) relative to the 2D (100) structure is understandable since it naturally has a 15–20% higher coverage than the 2D (100) case [45, 46].

Compering to the NWs, the NWs show almost threefold *lower* oxidation than the Si (111) and (100). These observations can be attributed to the stronger Si—C

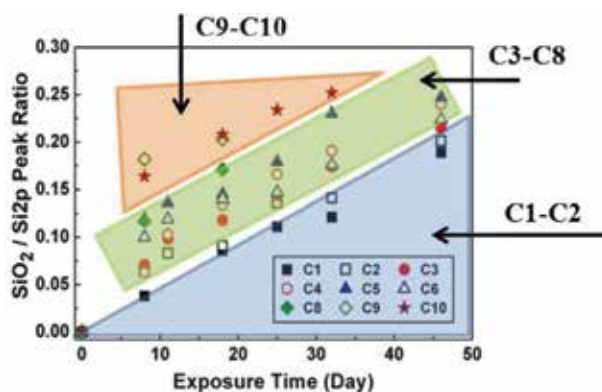


Figure 15. Observed oxidation intensity ($SiO_2/Si2p$ peak ratio) of alkyl-terminated Si NWs at different exposure times to ambient air. Reproduced with permission from [28].

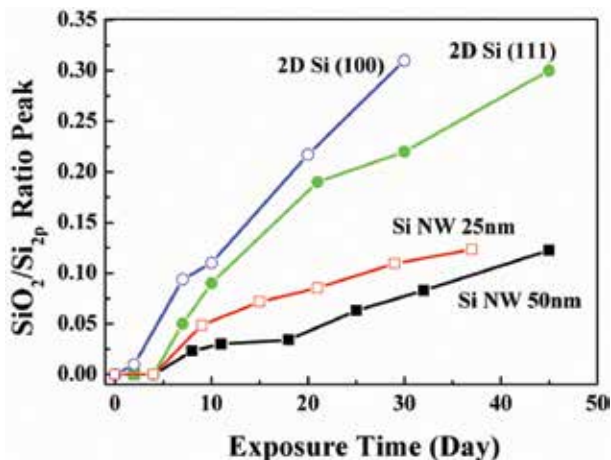


Figure 16. Ratio of the oxidized to bulk Si_{2p} peak areas for the methyl modification of NW_{25nm} and NW_{50nm} and 2D Si (111), exposed to air over extended time periods.

bonds on Si NW surfaces. This is supported by the shift in the Si—C bond in the NWs from 284.33 ± 0.02 eV (Si NW_{25nm}) and 284.22 ± 0.02 eV (Si NW_{50nm}) to 284.11 ± 0.02 eV for planar 2D Si. The $\sim 0.11 \pm 0.02$ eV to higher binding energy ascribed to the higher reactivity of atop sites.

3.11 Effect of bonds type: π - π vs. σ - σ interactions

Not only the coverage degree and surface may affect the stability of the molecules on the Si surface. It was found that bond type interactions (π - π vs. σ - σ) can tune the stability. To check this, Si NW were embedded with methyl CH₃ and propenyl (CH₃—CH=CH—Si NWs). **Figure 17** shows the oxidation of CH₃—CH=CH—Si and CH₃—Si NWs. The oxidation began for the two molecules after only ~ 100 hours of exposure. However, after 100 hours, the propenyl shows higher stability, i.e., less oxidation. This became more clear after 180 hours; the propenyl

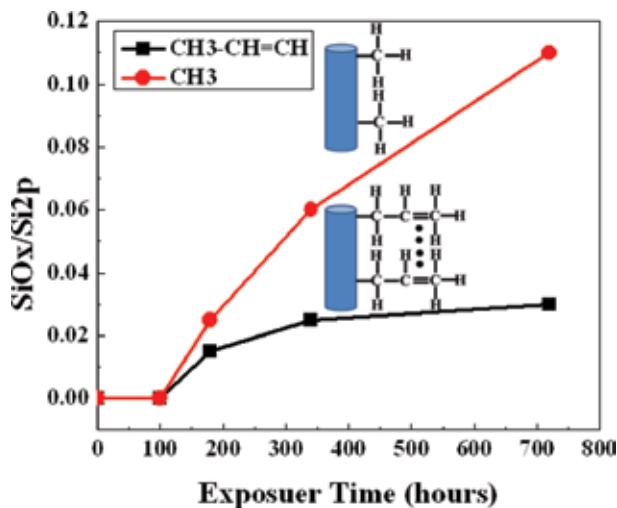


Figure 17. Ratio of the SiO₂ to Si_{2p} peak areas for the different surface modifications of Si NWs, exposed to air over extended time periods. Reproduced with permission from [47].

shows much lower intensity of 0.015 ± 0.005 , that is, almost 8 times less than the methyl 0.11 ± 0.017 . The high stability of the $\text{CH}_3\text{—CH}=\text{CH—Si}$ NW can be attributed to the $\pi\text{-}\pi$ interactions between the adjacent molecules [47–49].

3.12 Integration of hybrid Si NWs into solar cells

The performance of the Si solar cell can be improved by grafting molecules on the surface. Here, we present three different surface terminations: (i) H—Si NWs, (ii) $\text{SiO}_2\text{—Si}$ NWs, and (iii) $\text{CH}_3\text{—Si}$ NW. The surface Fermi level was calculated from the emission of the Si2p emission and the work function measured by the KP and summarized in the following table:

	H—Si NW	$\text{SiO}_2\text{—Si}$ NW	$\text{CH}_3\text{—Si}$ NWs
Surface Fermi level	1.05 eV	0.98 eV	0.83 eV
Work function	4.26 eV	4.32 eV	4.22 eV
Electron affinity	4.12 eV	4.29 eV	3.93 eV
Surface dipoles δ_{ss}	+0.07 eV	+0.24 eV	-0.12 eV

The electron affinity is calculated according to $\chi = \Phi - E_{\text{g}} + (E_{\text{F}} - E_{\text{V}})$, while the surface dipole is calculated by $\chi - \chi_{\text{B}}$, when χ_{B} is the affinity of the bulk (4.05 eV) [50].

3.13 Photoelectron yield spectroscopy of the solar cell heterojunction

The photoemission yield (PYS) of electrons is a function of the electronic properties of the interface. As shown in **Figure 18**, each PYS shows two thresholds near 5.0 ± 0.2 and 4.2 ± 0.2 eV. The higher energy band, i.e., near the 5.0 ± 0.2 , corresponds to the valence band, while the lower band 4.2 ± 0.2 eV corresponds to the defects in the band gap [50].

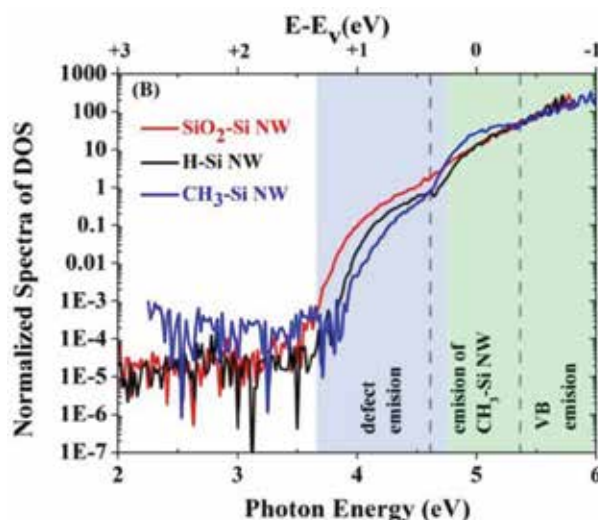


Figure 18.

Photoelectron yield $Y(h\nu)$ spectral and spectral density of states of $\text{SiO}_2\text{—Si}$ NW, H—Si NW, and $\text{CH}_3\text{—Si}$ NW.

To compare the quality of the surface, we normalized the valence emission at 0.76 eV below the valence band maximum where they should be strongly dominated by the valence band emission only. Therefore, all the three samples show identical PYS. To this end, we can clearly see that the SiO₂—Si NWs show the highest defect density in the bandgap, while the CH₃—Si NWs show the lowest defect density.

3.14 I-V curves of solar cells

The three samples were assembled as photovoltaic cells together with polymer (PEDOT:PSS). The polymer is considered as a hole conductor, while the Si NW plays the role of light absorber and electron conductor [9]. In this cell configuration, the photo-generated electron-hole pairs are separated at a heterojunction as shown in **Figure 19**.

Four main advantages for this configuration [51, 52]:

- i. Efficient light absorption
- ii. Short diffusion distance of carriers
- iii. Air-stable and robust polymer, PEDOT:PSS, as an efficient hole conductor [9]
- iv. Utilizing only 1% of the Si used in other thin-film cells

Figure 20 shows the current-voltage (*I-V*) characteristics of CH₃—Si NW/PEDOT:PSS and SiO₂—Si NW/PEDOT:PSS solar cells under AM1.5 illumination. The SiO₂—Si NW/PEDOT:PSS shows low performance: short circuit current (J_{sc}) of 1.6 mA/cm², an open circuit voltage (V_{oc}) of 320 mV, a fill factor (FF) of 0.53, and a conversion efficiency (μ) of 0.28%. However, in the CH₃—Si NW/PEDOT:PSS, the devices show superior performance relative to the CH₃—Si NW/PEDOT:PSS and exhibit improved performance with J_{sc} , V_{oc} , FF , and μ magnitudes of 7.0 mA/cm², 399 mV, 0.44, and 1.2%, respectively.

Both samples show low values due to the high contact resistances (R_s 300 Ω). However, the comparative increase in efficiency (by about a factor of four) upon methylation proves that this kind of surface functionalization has very promising prospective.

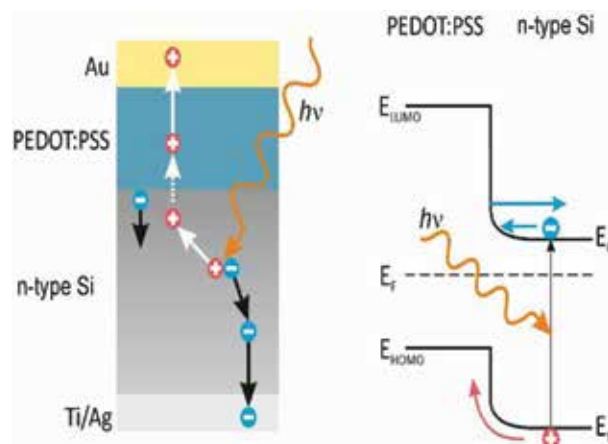


Figure 19. Schematic diagram shows the charge separation near the Si/polymer interface.

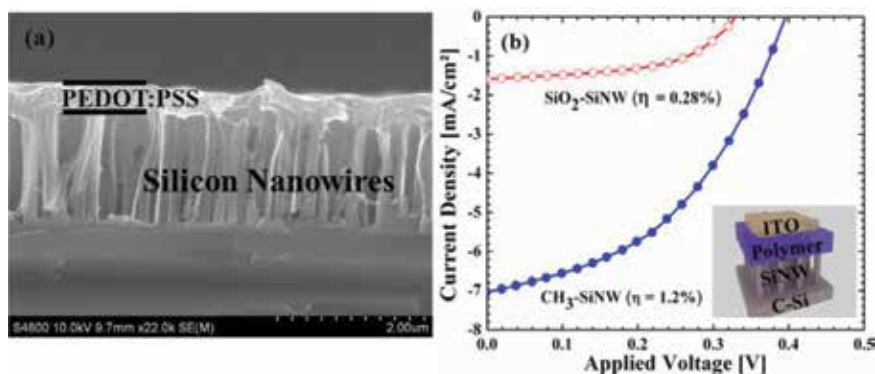


Figure 20.

(a) Tilted view of the heterojunction Si NW/PEDOT:PSS. (b) J - V characteristic under AM1.5 illuminations of the radial heterojunction solar cells from CH_3 -NWs to SiO_2 -NWs. Inset: schematic view of solar cell device structure.

The improved performance of the CH_3 -Si NWs is attributed to the removal of the defects on the surface; therefore, the charges can transfer with low recombination rate: hole to the polymer and electron to Si. In addition, efficient charge coupling can improve the performance which will improve the charge transfer causing to an increase in V_{oc} . According to the Shockley diode equation, $V_{oc} = k_B T/q \ln(J_{sc}/J_0)$, where J_0 is the saturation current. It should be mentioned that observed gain in the V_{oc} gain cannot be explained by the increase of the current alone. Assuming a similar J_0 , the increase of J_{sc} would lead to a V_{oc} gain of 0.037 V. However, we observed a gain of $\Delta V_{oc} = 0.079$ V. This can be attributed to the grafting effect which reduces the surface recombinations (as measured by PY) and/or a favorable barrier formation (surface dipole) [50–58].

4. Conclusions

Chlorination/alkylation process was used to graft different molecules on the Si NWs. The methyl provided the highest coverage (100%) among all of the alkyl molecules (50–70%). We show different parameters that affect the stability of the molecules on the surface: molecular coverage, chain length, types of bond interactions, surface energy, and Si NW diameter. However, the propenyl (CH_3 -CH=CH-Si NWs) showed excellent surface oxidation resistance: very small amount of oxides forming after more than 2 months of exposure to ambient air. Studies on the H-terminated Si NW oxidation kinetics revealed that their thermal stability relies strongly on the temperature. At lower temperatures, initially Si-Si backbond oxidation. At higher temperatures, oxygen diffusion is considered to be the initial rate-determining step, as it controls the growth site concentration.

We show that the molecules affect the solar cell performance, and a proper molecular may lead to superior solar cell performance. For instance, Si NW attached to CH_3 shows higher performance than oxide surface (by factor of four). This is attributed to the low surface recombination, low defects, and efficient charge transfer at the heterojunction. All these can be achieved by grafting a molecule of the surface. This type of heterojunction is used in advanced solar cell configurations and still under review.

Acknowledgements

This work was supported by a MAOF Grant from the Council for Higher Education in Israel for new faculty members. Dr. P. Natarajan is thankful for

the SEEDER scholarship for postdoctoral students. Awad Shalabny and Sumesh Sadhujan are appreciative of the institutional scholarships for PhD students they received from Ben-Gurion University of the Negev.

Author details

Riam Abu Much¹, Prakash Natarajan², Awad Shalabny², Sumesh Sadhujan², Sherina Harilal² and Muhammad Y. Bashouti^{2,3*}


1 The Academic Arab College for Education, Haifa, Israel

2 Jacob Blaustein Institutes for Desert Research, Environmental Physics and Solar Energy, Ben-Gurion University of the Negev, Sede-Boqer, Israel

3 The IISe-Katz Institute for Nanoscale Science and Technology, Ben-Gurion University of the Negev, Beer-Sheva, Israel

*Address all correspondence to: bashouti@bgu.ac.il

IntechOpen

© 2019 The Author(s). Licensee IntechOpen. This chapter is distributed under the terms of the Creative Commons Attribution License (<http://creativecommons.org/licenses/by/3.0>), which permits unrestricted use, distribution, and reproduction in any medium, provided the original work is properly cited. 

References

- [1] Lifshitz E, Bashouti M, Kloper V, Kigel A, Eisen MS, Berger S. Synthesis and characterization of PbSe quantum wires, multipods, quantum rods, and cubes. *Nano Letters*. 2003;**3**:857-862
- [2] Leschkies KS, Divakar R, Basu J, Enache-Pommer E, Boercker JE, Carter CB, et al. Photosensitization of ZnO nanowires with CdSe quantum dots for photovoltaic devices. *Nano Letters*. 2007;**7**:1793-1798
- [3] Bashouti MY, Tung RT, Haick H. Tuning the electrical properties of Si nanowire field-effect transistors by molecular engineering. *Small*. 2009;**5**:2761-2769
- [4] Schmitt SW, Schechtel F, Amkreutz D, Bashouti M, Srivastava SK, Hoffmann B, et al. Nanowire arrays in multicrystalline silicon thin films on glass: A promising material for research and applications in nanotechnology. *Nano Letters*. 2012;**12**:4050-4054
- [5] Sivakov V, Andra G, Gawlik A, Berger A, Plentz J, Falk F, et al. Silicon nanowire-based solar cells on glass: Synthesis, optical properties, and cell parameters. *Nano Letters*. 2009;**9**:1549-1554
- [6] Kelzenberg MD, Turner-Evans DB, Kayes BM, Filler MA, Putnam MC, Lewis NS, et al. Photovoltaic measurements in single-nanowire silicon solar cells. *Nano Letters*. 2008;**8**:710-714
- [7] Kelzenberg MD, Turner-Evans DB, Putnam MC, Boettcher SW, Briggs RM, Baek JY, et al. High-performance Si microwire photovoltaics. *Energy & Environmental Science*. 2011;**4**:866-871
- [8] Kim SK, Day RW, Cahoon JF, Kempa TJ, Song KD, Park HG, et al. Tuning light absorption in core/shell silicon nanowire photovoltaic devices through morphological design. *Nano Letters*. 2012;**12**:4971-4976
- [9] Kirchmeyer S, Reuter K. Scientific importance, properties and growing applications of poly(3,4-ethylenedioxythiophene). *Journal of Materials Chemistry*. 2005;**15**:2077-2088
- [10] Kuo CY, Gau C, Dai BT. Photovoltaic characteristics of silicon nanowire arrays synthesized by vapor-liquid-solid process. *Sol Energ Mat Sol C*. 2011;**95**:154-157
- [11] Lee HC, Wu SC, Yang TC, Yen TJ. Efficiently harvesting sun light for silicon solar cells through advanced optical couplers and a radial p-n junction structure. *Energies*. 2010;**3**:784-U215
- [12] Li QL, Zhu XX, Yang Y, Ioannou DE, Xiong HD, Kwon DW, et al. The large-scale integration of high-performance silicon nanowire field effect transistors. *Nanotechnology*. 2009;**20**:415202
- [13] Lin CX, Povinelli ML. Optical absorption enhancement in silicon nanowire arrays with a large lattice constant for photovoltaic applications. *Optics Express*. 2009;**17**:19371-19381
- [14] Liu CW, Cheng CL, Dai BT, Yang CH, Wang JY. Fabrication and photovoltaic characteristics of coaxial silicon nanowire solar cells prepared by wet chemical etching. *International Journal of Photoenergy*. 2012;**2012**:701809
- [15] Chen C, Jia R, Yue HH, Li HF, Liu XY, Wu DQ, et al. Silicon nanowire-array-textured solar cells for photovoltaic application. *Journal of Applied Physics*. 2010;**108**:094318
- [16] Paska Y, Haick H. Interactive effect of hysteresis and surface chemistry on gated silicon nanowire gas sensors. *ACS Appl Mater Inter*. 2012;**4**:2604-2617
- [17] Paska Y, Stelzner T, Assad O, Tisch U, Christiansen S, Haick H. Molecular

- gating of silicon nanowire field-effect transistors with nonpolar analytes. *ACS Nano*. 2012;**6**:335-345
- [18] Paska Y, Stelzner T, Christiansen S, Haick H. Enhanced sensing of nonpolar volatile organic compounds by silicon nanowire field effect transistors. *ACS Nano*. 2011;**5**:5620-5626
- [19] Cui Y, Zhong ZH, Wang DL, Wang WU, Lieber CM. High performance silicon nanowire field effect transistors. *Nano Letters*. 2003;**3**:149-152
- [20] Peng KQ, Jie JS, Zhang WJ, Lee ST. Silicon nanowires for rechargeable lithium-ion battery anodes. *Applied Physics Letters*. 2008;**93**:033105
- [21] Ruruli R. Colloquium: Structural, electronic, and transport properties of silicon nanowires. *Reviews of Modern Physics*. 2010;**82**:427-449
- [22] Haick H, Hurley PT, Hochbaum AI, Yang PD, Lewis NS. Electrical characteristics and chemical stability of non-oxidized, methyl-terminated silicon nanowires. *Journal of the American Chemical Society*. 2006;**128**:8990-8991
- [23] Shirak O, Shtempluck O, Kotchtakov V, Bahir G, Yaish YE. High performance horizontal gate-all-around silicon nanowire field-effect transistors. *Nanotechnology*. 2012;**23**:395202
- [24] Shu QK, Wei JQ, Wang KL, Song SA, Guo N, Jia Y, et al. Efficient energy conversion of nanotube/nanowire-based solar cells. *Chemical Communications*. 2010;**46**:5533-5535
- [25] Eisenhawer B, Sensfuss S, Sivakov V, Pietsch M, Andra G, Falk F. Increasing the efficiency of polymer solar cells by silicon nanowires. *Nanotechnology*. 2011;**22**:315401
- [26] Garnett EC, Yang PD. Silicon nanowire radial p-n junction solar cells. *Journal of the American Chemical Society*. 2008;**130**:9224
- [27] Bashouti MY, Stelzner T, Berger A, Christiansen S, Haick H. Chemical passivation of silicon nanowires with C(1)-C(6) alkyl chains through covalent Si-C bonds. *Journal of Physical Chemistry C*. 2008;**112**:19168-19172
- [28] Bashouti MY, Stelzner T, Christiansen S, Haick H. Covalent attachment of alkyl functionality to 50 nm silicon nanowires through a chlorination/alkylation process. *Journal of Physical Chemistry C*. 2009;**113**:14823-14828
- [29] Jie JS, Zhang WJ, Peng KQ, Yuan GD, Lee CS, Lee ST. Surface-dominated transport properties of silicon nanowires. *Advanced Functional Materials*. 2008;**18**:3251-3257
- [30] Terry J, Linford MR, Wigren C, Cao RY, Pianetta P, Chidsey CED. Determination of the bonding of alkyl monolayers to the Si(111) surface using chemical-shift, scanned-energy photoelectron diffraction. *Applied Physics Letters*. 1997;**71**:1056-1058
- [31] Effenberger F, Gotz G, Bidlingmaier B, Wezstein M. Photoactivated preparation and patterning of self-assembled monolayers with 1-alkenes and aldehydes on silicon hydride surfaces. *Angew Chem Int Edit*. 1998;**37**:2462-2464
- [32] Sieval AB, Linke R, Heij G, Meijer G, Zuilhof H, Sudholter EJR. Amino-terminated organic monolayers on hydrogen-terminated silicon surfaces. *Langmuir*. 2001;**17**:7554-7559
- [33] Wagner RS, Ellis WC. Vapor-liquid-solid mechanism of single crystal growth (new method growth catalysis from impurity whisker epitaxial + large crystals Si E). *Applied Physics Letters*. 1964;**4**:89

- [34] Bansal A, Li XL, Yi SI, Weinberg WH, Lewis NS. Spectroscopic studies of the modification of crystalline Si(111) surfaces with covalently-attached alkyl chains using a chlorination/alkylation method. *The Journal of Physical Chemistry. B.* 2001;**105**:10266-10277
- [35] Himpfel FJ, Mcfeely FR, Talebibrabimi A, Yarmoff JA, Hollinger G. Microscopic structure of the SiO₂/Si interface. *Physical Review B.* 1988;**38**:6084-6096
- [36] Himpfel FJ, Talebibrabimi A, Yarmoff JA, Hollinger G. Microscopic structure of the SiO₂/Si interface. *Journal of the Electrochemical Society.* 1988;**135**:C136-C136
- [37] Bashouti MY, Sardashti K, Ristein J, Christiansen SH. Early stages of oxide growth in H-terminated silicon nanowires: Determination of kinetic behavior and activation energy. *Physical Chemistry Chemical Physics.* 2012;**14**:11877-11881
- [38] Bashouti M, Sardashti K, Ristein J, Christiansen S. Kinetic study of H-terminated silicon nanowires oxidation in very first stages. *Nanoscale Research Letters.* 2013;**8**(1):41
- [39] Whidden TK, Thanikasalam P, Rack MJ, Ferry DK. Initial oxidation of silicon(100)—a unified chemical-model for thin and thick oxide-growth rates and interfacial structure. *Journal of Vacuum Science and Technology B.* 1995;**13**:1618-1625
- [40] Ma DDD, Lee CS, Au FCK, Tong SY, Lee ST. Small-diameter silicon nanowire surfaces. *Science.* 2003;**299**:1874-1877
- [41] Mawhinney DB, Glass JA, Yates JT. FTIR study of the oxidation of porous silicon. *The Journal of Physical Chemistry. B.* 1997;**101**:1202-1206
- [42] Tian RH, Seitz O, Li M, Hu WC, Chabal YJ, Gao JM. Infrared characterization of interfacial Si–O bond formation on silanized flat SiO₂/Si surfaces. *Langmuir.* 2010;**26**:4563-4566
- [43] Schwartz DK. Mechanisms and kinetics of self-assembled monolayer formation. *Annual Review of Physical Chemistry.* 2001;**52**:107-137
- [44] Nuzzo RG, Zegarski BR, Dubois LH. Fundamental-studies of the chemisorption of organosulfur compounds on Au(111)—implications for molecular self-assembly on gold surfaces. *Journal of the American Chemical Society.* 1987;**109**:733-740
- [45] Sivakov VA, Scholz R, Syrowatka F, Falk F, Gosele U, Christiansen SH. Silicon nanowire oxidation: The influence of sidewall structure and gold distribution. *Nanotechnology.* 2009;**20**:405607
- [46] Bashouti MY, Paska Y, Puniredd SR, Stelzner T, Christiansen S, Haick H. Silicon nanowires terminated with methyl functionalities exhibit stronger Si–C bonds than equivalent 2D surfaces. *Physical Chemistry Chemical Physics.* 2009;**11**:3845-3848
- [47] Assad O, Puniredd SR, Stelzner T, Christiansen S, Haick H. Stable Scaffolds for reacting Si nanowires with further organic functionalities while preserving Si–C passivation of surface sites. *Journal of the American Chemical Society.* 2008;**130**:17670
- [48] Puniredd SR, Assad O, Haick H. Highly stable organic monolayers for reacting silicon with further functionalities: The effect of the C–C bond nearest the silicon surface. *Journal of the American Chemical Society.* 2008;**130**:13727-13734
- [49] Puniredd SR, Assad O, Stelzner T, Christiansen S, Haick H. Catalyst-free functionalization for versatile modification of nonoxidized silicon structures. *Langmuir.* 2011;**27**:4764-4771

[50] Bashouti MY, Pietsch M, Brönstrup G, Sivakov V, Ristein J, Christiansen S. Hybrid polymer/silicon nanowire solar cell with high efficiency through covalent Si–C terminated surface passivation. *Prog. Photovolt: Res. Appl.* 2014;**2**:1050-1061

[51] Putnam MC, Boettcher SW, Kelzenberg MD, Turner-Evans DB, Spurgeon JM, Warren EL, et al. Si microwire-array solar cells. *Energy & Environmental Science.* 2010;**3**:1037-1041

[52] Tian BZ, Zheng XL, Kempa TJ, Fang Y, Yu NF, Yu GH, et al. Coaxial silicon nanowires as solar cells and nanoelectronic power sources. *Nature.* 2007;**449**:885-U888

[53] Maldonado S, Knapp D, Lewis NS. Near-ideal photodiodes from sintered gold nanoparticle films on methyl-terminated Si(111) surfaces. *Journal of the American Chemical Society.* 2008;**130**:3300

[54] Ambrico M, Ambrico PF, di Mundo R. Electrical transport Features of SiNWs random network on Si support after covalent attachment of new organic functionalities. *Nanomater. Nanotechnol.* 2012;**2**:1-8

[55] Zhong Y, Xiao Y, Chen Q, Zhu H. Heterojunction solar cells based on graphene woven fabrics and silicon. *Materiomics.* 2018;**4**:135-138

[56] Yu L, Tune D, Shearer C, Grace T, Shapter J. Heterojunction solar cells based on silicon and composite films of polyaniline and carbon nanotubes. *IEEE J. Photo Volt.* 2016;**6**

[57] Silicon Based Heterojunction Solar Cells and Photodetectors. Ph.D. thesis Zhen Gao

[58] Ghosh BK, Weoi CNJ, Islam A, Ghoshb SK. Recent progress in Si hetero-junction solar cell: A comprehensive review. *Renewable and Sustainable Energy Reviews.* 2018;**82**:1990-2004

Aqueous-Mediated Synthesis of Group IIB-VIA Semiconductor Quantum Dots: Challenges and Developments

Jejiron Maheswari Baruah and Jyoti Narayan

Abstract

Quantum dots (QDs) of group IIB-VIA are one of the most promising materials for various advanced technological applications in the field of optoelectronics, photovoltaic solar cells and biomedicine. Recent developments have suggested the incorporation of aqueous-mediated synthesis for the QDs, as it is greener, environment friendly, cost-effective and reproducible. However, the process involves several challenges, which ought to be met in order to produce stable, consistent and sustainable product formation. The present review discusses the significance of semiconducting QDs, their synthesis through various processes, their pros and cons, and above all the advantage of aqueous-mediated, atom economic and energy-saving methodologies.

Keywords: quantum dots, group IIB-VIA semiconductors, aqueous synthesis, luminescence properties, surface passivation, optoelectronics

1. Introduction

Nanoscience and nanotechnology is one of the highest potential applicative research fields in today's world. The current scenario of world depicts the valuation of nano sized materials (1–100 nm) [1] quite high in various areas of scientific applications, such as, photovoltaic solar cells [2–5], optoelectronics [6–10], biomedical [11–13], food and agriculture, industrial, textiles, etc. [14]. It has been observed that larger ratio of surface to volume of a catalyst would facilitate a better catalytic activity; therefore the size controlled synthesis of QDs to produce a larger ratio of surface to volume is of great importance. The enhanced surface to volume ratio would cause increase of surface states, which will change the activity of electrons and holes, thereby, affecting the chemical reaction dynamics as a whole. Studies reveal that the size quantization increases the band gap of photo catalysts to enhance the redox potential of conduction band electrons and valence band holes [15–17]. The resulting dominance of these tiny sized artificial atoms/molecules/materials reveals a prediction of market value of \$16.8 billion in upcoming future [18].

2. Classification of nanostructure materials

The nanomaterials can broadly be classified in four categories. They are (a) zero dimensional (0D), (b) one dimensional (1D), (c) two dimensional (2D) and (d) three dimensional (3D). (a) Zero dimensional nanostructures (e.g., quantum dots and nanoparticles) have all the dimensions within the nanoscale region. They are also addressed as artificial atoms as their size restriction, particularly quantum dots, can be found within a few nanometer ranges like atoms/molecules. They have grown themselves up in recent years as suitable applicant in the field of optoelectronics, biomedical, energy, textile industries, etc. (b) One dimensional nanostructure (e.g., nanowires, nanotubes, nanorods, etc.) have diameter/thickness in nanometer range, however its length to width ratio may be more than 1000 nm, i.e., several micrometers. It means that in this kind of material, one dimension of the nanostructure is not in the nanometer range. This specific class of nanomaterial has immense applications in electronics, in addition to other domains of applications like energy and environment [19]. (c) Two dimensional nano structures (e.g., nanofilms, nanosheets, nanowires, graphene, etc.) have two dimensions outside the nanometer range. It indicates that although the area (length and breadth) of these kinds of materials is more than nanometer scale, but the thickness is always within the nanoscale region. They are very useful in the applications of sensors, templates, photocatalysis, nanoreactors and nanocontainers. (d) Three dimensional nanostructures (e.g., bulk powders, nanocomposites, bundle of nanotubes/nanowires, multilayer films, nanotextured surfaces, etc.) are the nanomaterials in which, all the three dimensions of a material are not within nanoscale region. This class of materials has applications in all such fields where introduction of other dimensional nanomaterials is required in high scale, including the fields where electronics, optical, mechanical and magnetic properties are necessary.

2.1 Defining QDs: physical and quantum mechanical concept

QDs are having quite resemblance with the atomic confinements. Basically, they are the nanoparticles of bulk semiconductors and their average size range lies within 1–10 nm. The physics behind the size of a QD is the exciton Bohr radius. It states that if the size of a particle is less than twice the size of the exciton Bohr radius of a specific material, then, the particle behaves as a quantum confined matter. At this point, the particle acts as a particle within a box of quantum mechanics. Brus et al. were the first to use the term ‘Quantum Dot’ [20]. They defined these artificial atoms’ behavior as molecule like. They realized that this particular class of particle has discrete and quantized energy states, due to which their electronic properties possess resemblance with atoms/molecules. Although, nanoparticles of the semiconductor materials are found to be within the quantum confined region, it is quite obvious to achieve bigger particles during the process of synthesis within the same solution of nanoparticles, than, the Bohr exciton radius. But, people are focusing on the production of smaller size, i.e., within quantum region. The idea behind targeting quantum confinement is their dramatic change in electronic properties within the quantum dimension, which cannot be achieved beyond that size. Hence, nanoparticles of semiconductors are synthesized within that confinement precisely. One of the primary reasons behind occasional achievement of bigger particles is the aggregation of individual particles. This can be overcome by effective encapsulation with suitable capping agents during the course of various physical and chemical synthesis processes.

2.2 Semiconductors: introduction and utility

Semiconductors are well known class of compounds, whose properties are considered to be between metals and insulators. The fundamental expression of this idea is the band gap energy, generated due to the presence of distinct valence band, VB (HOMO) and conduction band, CB (LUMO). The overlapping of both VB and CB is very much absent in semiconductors; instead they are differing by 'specific amount' of energy. However, there is a provision for the electrons in the VB to jump into CB by absorbing that particular 'specific amount' of energy. The required threshold energy to overcome the VB-CB difference is termed as 'Band Gap Energy'. Since the QDs are the diminutive form of the bulk semiconductors, hence they also follow the band gap theory. In QDs, the transition of electrons from the HOMO to LUMO, primarily, depends on the size of the individual particles. Smaller the size of the particle, higher energy is required for an electron to jump to conduction band and vice versa. Therefore, smaller particles show more blue shift from the bulk in both absorption and luminescence spectra than the bigger particles (**Figure 1**). Interestingly, in a solution, the particle size of QDs of a particular material is never homogeneous, i.e., the size of each dot cannot be exactly the same. Therefore, when absorption spectrum of QDs in a solution is recorded, due to the merging of peaks for each and every particle (responsible for individual electronic transition of individual particle), the absorption maximum is always broad, sometime edge only [21]. That is why, these QDs can cover a wide range of light spectrum to excite its electrons as per the requirement of energy. The broader excitation spectra of the QDs also help them in the illumination of multicolored QDs through the excitation of single light. The high stoke shift finds the QDs resistant toward the auto fluorescence, hence their sensitivity is enhanced drastically. These metamaterials are synthesized in laboratories according to their requirement in a specific application. A very interesting and important factor behind the utility of these nano materials is their tunability in size and shape. Different sized particles of different materials within the same

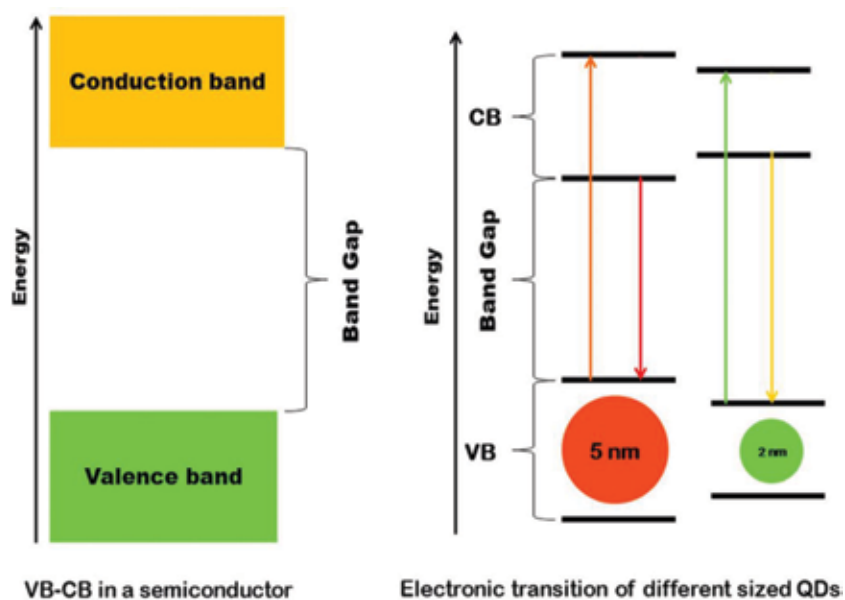


Figure 1.
Effect of size of QDs on electronic properties.

Materials	ZnS	ZnSe	ZnTe	CdS	CdSe	CdTe
Band gap (eV)	3.61	2.69	2.39	2.49	1.74	1.44
Wavelength (nm)	343.2	460.5	518.4	497.5	712.1	860.3

Table 1.

Band gap and excitonic wavelength of group IIB-VIA semiconductors revealing the capacity of accessing the visible light spectrum, thereby exhibiting their potential applications in optical and electronic devices.

application are essential for providing improved efficacy of the device, e.g., quantum dot sensitized solar cells. Researchers around the world have reported various shapes of nanoparticles, viz., spherical, cubic, hexagonal, triangular, wire, ball, necklace, etc. They deliver different properties and can be utilized for different applications.

Among various semiconductors, the QDs of group IIB-VIA [zinc sulfide (ZnS), cadmium sulfide (CdS), zinc selenide (ZnSe), cadmium selenide (CdSe), zinc telluride (ZnTe) and cadmium telluride (CdTe)] are potential candidates in various applications, primarily in optoelectronics due to their wide and direct band gap (**Table 1**).

Chemistry of these semiconductors suggests that the formation of variable strong bonding between these molecules is responsible for their differences in band gap and absorption maxima. The covalency of the molecules from Sulfur to Tellurium is different in these hybrid molecules, so as their electronic transition properties are varied and hence the band gap.

3. Synthesis of QDs: aqueous route and mechanism

The effective synthesis of QDs is a challenging task. Research is warranted in the mechanism of synthesis, leading to the reproducibility of size and shape of QDs, so that the growth of QDs at the time of nucleation can be controlled effectively [22–26]. There are several methods of synthesis of QDs: molecular beam epitaxy (MBE), vapor phase epitaxy (VPE), metal organic chemical vapor deposition (MOCVD), radio frequency sputtering (RFS), electron beam lithography (EBL), optical ablation, Ball milling, quenching methods, reduction with microorganisms or plants [14] and chemical method [27–34]. Among all, chemical method is the most widely used method for the synthesis of QDs due to its better accuracy and large scale production [35–56]. Various reducing agents such as sodium borohydride, hydrazine hydrate, etc. are used during the chemical reduction synthesis. These methods are broadly divided into non-aqueous and aqueous-mediated reactions. Non-aqueous method have received first remarkable development from Bawendi, Alivisatos and Peng [57–62], popularly known as TOP-TOPO (trioctylphosphine for TOP and TOP oxide) or hot injection method in 1990s. Although the reaction developed by Murray et al. [57] for the synthesis of cadmium chalcogenides is probably the first ever controlled synthesis of semiconducting CdE (E = S, Se, Te) QDs. However, due to the highly toxic, pyrophoric and unstable nature of main precursor dimethyl cadmium [(CH₃)₂Cd] at room temperature, the method was not preferred [63–67]. Peng et al. [68, 69] contributed a comparatively greener method for the synthesis of CdE, as the first most efficient process of synthesizing highly fluorescent QDs with excellent morphological uniformity. The formed QDs in this high temperature method involved long chain organic solvents with high value of boiling point. Resultant QDs were found to be less defective due to effective surface passivation by TOP/TOPO. Both, the choice of ligand as well

as the growth temperature, allowed the lattice morphology to be modified in a better way toward the synthesis of QDs. Hot injection method processes through two steps, i.e., rapid nucleation, while the reaction is heated up to the utmost temperature, followed by slow growth of colloidal nano crystals (CNCs) due to the addition of another precursor, with much lowered temperature. Though this method was observed to be suitable for the synthesis of the CNCs/QDs, there are some unexpected drawbacks, which lead the scientists to rethink about this particular process, before they could propose this method for the up gradation of the end products at the industrial level. The primary issues with this method are (a) use of non-ecofriendly organic solvents, (b) cannot be scaled up for mass production, which require several and repetitive reactions to achieve the desired amount of product, (c) non-biocompatibility, as water is not a suitable solvent for them to get solubilized, (d) difficult purification and extraction methods of the QDs from its mother liquor, (e) high cost of solvents as well as the process and (f) non-cooperation of green chemistry principles, which leads the whole process of synthesis into an environmentally challenging problem. Adoption of non-water soluble surface passivators (i.e., TOP/TOPO) confirms the non-biocompatibility mode for these high temperature synthesis methods; therefore the concept of biocompatible aqueous phase QDs synthesis is warranted. Aqueous route of synthesis have all the positive aspects and most importantly, they are easy to carry out and are environmentally benign. Additionally, one can use high fluorescent nature of QDs in various bio-medications due to their water solubility. One can modify the surface of the QDs as required, with the help of water soluble chiral capping molecules to make the dots size dependent chiral optical property enhancer [70, 71]. Moreover, utilization of short water soluble ligands boost the optoelectronic applications (including photodetectors, solar cells and photocatalysis) too, by reducing dielectric barrier and inter dot separation distances in a solid QD film. Hence the objective of preparation of QDs reach to another domain of methodology, i.e., water-mediated or water soluble routes of synthesis. In early 1980s, Brus [72] and Henglein [3] and their co-workers first pioneered the aqueous synthesis route. They reported the change of band gap of QDs with their size. Vossmeier et al. presented their work on CdS QDs. They reported the variation of UV-vis absorption spectrum with the change of size of CdS QDs. However, none of them discussed the photoluminescence property. First aqueous based synthesis with fluorescence properties of QDs was introduced by Weller et al. [73]. They have reported the water based synthesis of CdTe QDs under reflux condition at 96°C for prolonged hours, to obtain photoluminescence emission. After that, several approaches have been made toward the aqueous synthesis of CdSe and CdTe QDs. Although, they have achieved a mile stone, but as the research progressed, researchers tried to find the best route of synthesis in which they were able to synthesize the same or better quality CNCs. In the way of harvesting betterment and refinement of the existing methodologies, present day world scientists are trying to reach to a mile stone, in which the QDs are prepared as multiuse molecules. Hence, the aqueous synthesis method is still under investigation and modification. Therefore warrants systematic studies under variable conditions. Presently, global scenario speaks about the understanding of the reaction mechanisms and the suitable greener conditions involved during the synthesis of better quality QDs with easy, cost effective and most importantly greener technological way. However, achievement is still under the margin.

4. Factors responsible in aqueous synthesis of QDs

There are four major parameters which are primarily responsible for precision of the end product during aqueous synthesis route. They are (a) the solubility product

of the semiconductor compounds in water, (b) binding affinity of the capping agent molecules toward the metal atom, (c) binding affinity of water and hydroxyl atom for the metal atoms and (d) pH of the reaction medium [74–81]. These enlisted thermodynamic parameters can be understood with the help of HSAB (hard and soft acids and bases) theory. HSAB states that hard-hard or soft-soft interactions are expected to have lower water solubility [82, 83]. Since chalcogenides ions (S^{-2} , Se^{-2} and Te^{-2}) are soft bases and (Cd^{+2} and Zn^{+2}) are borderline soft acids, it is expected that they readily form insoluble compounds. Soft-soft interaction leading to the low solubility of these compounds is the basis of their semiconducting nature. Their covalent nature increases in comparison to the hard-hard interactions. The pH of the medium also effects the formation of the desired compounds in a dramatic way. Since we know that $-OH$ (hydroxyl) ion is a hard base, therefore its binding affinity toward hard metal cations is more and hence $-OH$ can easily form bonds with Zn^{+2} than Cd^{+2} in basic conditions, thus effecting their solubility product constant (K_{sp}). Therefore, careful pH management is very necessary for Zn chalcogenide than Cd chalcogenide compounds to prevent formation of metal hydroxide compounds. Because Cd can tolerate more basic condition than Zn due to its comparative more softness. Thus, one can understand that acidic condition may be more suitable for Zn chalcogenide compounds than Cd compounds, which can accommodate basicity up to $pH = 12.5$. Beyond this, Cd metal atoms will form $Cd(OH)_2$ compounds. Hence, the conclusion can be drawn that, acidic condition is more suitable for the synthesis of these compounds. Another very important positive concept of utilization of acidic condition is that, it enhances the formation of smaller QDs than basic condition. The presence of $-OH$ radical in the medium is found to be responsible for this, due to the bigger size of the hydroxyl group than H^+ in acidic medium. The chemistry of the group IIB-VIA compounds overall reveals that aqueous medium is very easy and effective way of production of the QDs of those bulk compounds due to their solubility factor in water. We can easily extract them from the medium as after formation they show poor solubility in water. The band gap energy of these compounds can also be understood from the covalent nature of the bonding between the metal atom and the chalcogenide. It is observed that the pattern of band gap energy of metal (M) chalcogenides (S, Se and Te) is $MS > MSe > MTe$. The fact behind this order is the electronegativity of the anions. Since, the bigger sized anion (lower electronegative chalcogenides) does not hold their outermost electrons as strongly as the anions of their group possessing higher electronegativity, therefore covalent character is enhanced in these compounds. As a result, their bulk band gap (BG) gets decreased in a group with the same metal atom ($CdS_{BG} > CdSe_{BG} > CdTe_{BG}$).

5. Surface chemistry of QDs: role of capping agent in aqueous synthesis

The surface chemistry of the CNCs is very interesting, as well as challenging one to achieve. Due to the presence of high surface to volume ratio, the surface of the QDs generates dangling bonds of both cationic and anionic substituents. Noteworthy, the dangling bonds in a QD are generated due to the unsaturated surface level atoms of the QD, which may alter the electronic transition by introducing new electronic states. The primary strategy to satisfy these surface defects is by using more cationic precursor to satisfy the anionic part, while the stabilizing agent, has to satisfy the dangling bonds formed from the cationic part. In most of the reactions, the presence of a stabilizing agent is very necessary to overcome the instability factor in the colloidal solution. In colloidal synthesis method, it is almost

mandatory to use a capping agent [2, 37, 84] as a capping agent does not allow the QDs to grow, after reaching a certain size depending upon the capacity of the agent. On the other hand, in an appropriate solvent, a stabilizing agent, not only caps the QD, but also offers stability to it to retain its size in the solution. The terminology of stabilizing agents is slightly different from surface capping agents. But efforts have been made by researchers to put both the surface modifying agents within a single umbrella by trying to use the same molecule for both the purposes. These molecules attach with the surface of the NCs by dative, covalent or ionic bond and provide them electrostatic stabilization as well as surface passivation. These agents are often called as surface ligands, due to their capacity to act as ligands in a coordination complex, which attach to the metal ion by exchanging electrons. The molecular structure of a stabilizing agent/surface capping agent is very much different in aqueous medium than non-aqueous medium. In non-aqueous solvents, these molecules are normally water insoluble long chain hydrocarbons, whereas in aqueous media the capping agents have short hydrocarbon chain and a polar group at one end. The polar group can provide stabilization to the QD as well as passivation to the surface. But, importantly the ratio of capping agent with the precursor also plays an important role in the nature of the solubility and formation of the QDs. It is because, higher concentration of these molecules may not allow the metal atom to form the semiconducting NCs and lower concentration may lead to the instability of the QD in the medium due to weak interaction between the capping molecule and the metal ion. In this context, till date thiol or carboxyl or phosphate group holding polymers and macromolecules have been tried to achieve better surface stability. However, at the same time, ligands capable of binding with more than one binding site are also drawing tremendous attention of the researchers due to the probability of fetching aspired product. Selecting effective surface modifying agents and optimization of the added amount of them are at utmost importance to develop better synthesis route to achieve desired QDs. Another aspect of choosing an effective surface capping agent is the biocompatibility and thus, their application in biomedical sectors [85–87]. The advantageous positions of these inorganic artificial atoms as fluorophores over organic dyes is due to their bright (10–20 times more than organic dyes) and narrow fluorescent and less photo bleaching (up to 30–40 ns) nature than the traditional dyes. The primary issues regarding the use of these QDs in biological application are non-biocompatibility, ineffective coating and the use of hazardous capping agent. It is well understood that although the synthesis of QDs are performed in water medium, it may not offer the biocompatible nature to the dots and hence they can undergo oxidative degradation inside the cell and harm the same. Moreover, non-functionalization may lead to unspecified exit route of these drugs from the treated organism, hence the treated organism may become intoxicated. Therefore, surface functionalization of these dots is the most important part if we want to cast them inside the body of an organism. Secondly, capping agent has to be a perfect surface passivator, which will act as inhibitor to the surface trap states in the QDs. Thirdly, it is also observed that many a times the capping agent/stabilizer/surface passivating agent itself act as a harmful material toward to treated organism. Hence, selection has to be made on this scenario too. Overall, the research of biologically active and applicative QDs demands the production of such engineered QDs, which can answer all the three major problems. At the same time, the role of capping agent/stabilizer/surface passivator has to be restricted to only one molecule, which can act as capping agent, stabilizer and surface passivator in parallel. Therefore, the quest of potential multiuse QDs with multiuse surface modifying agents is still going on around the globe and warrants a thorough investigation.

6. Challenges of aqueous synthesis of group IIB-VIA QDs

The process of synthesizing all the QDs of the mentioned semiconductors in aqueous media is a challenging task. Literature [88, 89] to some extent reveals that the anionic/chalcogenide portion of the semiconductors plays the key role in the synthesis. It is because the reduction of sulfur (S), selenium (Se) and tellurium (Te) is very much different from each other due to the difference in their reduction potential, i.e., -0.467 , -0.924 and -1.143 respectively. Reduction of S is relatively easier in comparison to Se and Te in water, because it easily dissociates into S^{-2} from its available metallic salt. But strong reducing reagents are required to reduce Se and Te in room temperature. Moreover, they are not stable in the solution and can readily form Se^0 and Te^0 once the effect of reducing agent is finished. Proper precaution has to be taken. In case of Te, reduction has to be carried out under inert atmosphere (nitrogen/argon atmosphere) as it readily converts to Te^0 in non-inert condition [90]. During the addition to the metal precursor, one has to be delicate and calculated enough, or else, Te^{-2} will be readily converted to Te^0 . Hence, performing the synthesis in the aqueous medium at room temperature is a challenging task; however, the successful completion of this challenge may lead the world into different class of environmentally benign, easy and cost effective synthesis route for QDs.

7. Application of group IIB-VIA semiconductor QDs

Most essential part of these QDs is their application in optoelectronics such as light emitting diodes [91–99], photodetectors [100] and photovoltaic solar cells or quantum dot sensitized solar cells (QDSSC) [101–105]. Colvin and his associates had first designed QD-LED (1994) [91] and this invention was a milestone in optoelectronics. The quantum efficiency of first CdSe QDs was 0.01%, which was a better result in that time, although much lesser than today's QD-LEDs. The reason behind fast development of efficiency of the QDs in LEDs is the report of newer developments in synthesis methodologies and their quality along with that. Recently, impressive development has been made by Samsung electronics in the form of quantum dot televisions. The manufacturing authority claims that the color intensity is much more intense than an ordinary TV and it happens due to the incorporation of QDs. The greatest potential of colloidal QDs in optoelectronics lies in their humongous flexibility of semiconducting and optical nature over wide range of light spectrum, which allows the tailoring of QDs according to their desired applications. In addition to that, the low cost production and effective charge transfer capability also offers these dots the suitability in optoelectronic appliances. The utility of the QDs in LEDs or QDSSCs can be consolidated by fabricating the thin films of them. Thin films are the easiest but effective support as well as cost effective solution to incorporate the highly luminescent QDs in a device. In thin film science, a thickness range of nanometers to a few micrometers of the synthesized QDs is spread over suitable templates (commonly used glass, ITO, FTO, mica, etc.) by various methods (e.g., chemical vapor deposition, electron beam deposition, spin coating, dipping, etc.). First generation silicon solar cells were the first thin film solar cells, however, slowly 3rd generation thin film solar cell has been replacing them. In the preparation of a thin film, the suitable roughness according to their thickness has to be maintained to receive desired optical luminescence. In the fabrication of thin films, the methodology to prepare them is very important. It is because during the process of fabrication, the characteristics of the synthesized QDs must not change, as making of thin films may undergo different rigorous

treatment including heating too. Therefore, to find a valid and effective method of thin film fabrication is very important. Simultaneously, the cost of production of the thin films also has to be minimal so that the product will be a cheaper one. Hence, research is undergoing intense investigation to find a low cost and effective way of production of QD thin films, which can necessarily, fulfill the demand of industry as well as global market. Although having tremendous potential utility of these QDs in various application fields of science and technology, their high production cost (~\$10,000 per gram of QDs) makes it difficult to raise them as a part of our day to day life [106, 107]. Unless scientists develop some sort of easier and cost effective way to produce and fabricate specific shape and sized QDs in mass scale, we cannot understand their broad application [108]. Therefore, chemical engineering of QDs has begun to solve these two major following issues: (a) use of eco-friendly inexpensive starting material for synthesis of QDs and (b) development of green synthesis routes with the optimization of all the reaction parameters [62]. Therefore, it is become mandatory for the research community to design newer and greener optimized synthesis processes, so that in near future these QDs can become leader in every aspects of mankind.

8. Future work

Semiconductor QDs are advanced materials for various applications which have been discussed elaborately. Their unique physico-chemical properties make them suitable for applications in energy conservation, imaging devices, non-linear optics, nano electronics, nano photonics, solar cells, miniaturized sensors, photography and bio-medical domains. Material preparation and physico-chemical characterization of group IIB-VIA QDs should be further modified in order to fabricate smart devices. The future work toward the greener synthesis of binary and multicomponent nanocomposites is warranted as doping with suitable metal and metal alloys enhances the optoelectronic and optoelectrical properties of these QDs.

Conflict of interest


The authors declare that there is no conflict of interest.

Author details

Jejiron Maheswari Baruah and Jyoti Narayan*
Synthetic Nanochemistry Laboratory, Department of Basic Sciences and Social
Sciences, School of Technology, North Eastern Hill University, Shillong, India

*Address all correspondence to: jnarayan.nehu@gmail.com

IntechOpen

© 2020 The Author(s). Licensee IntechOpen. This chapter is distributed under the terms of the Creative Commons Attribution License (<http://creativecommons.org/licenses/by/3.0>), which permits unrestricted use, distribution, and reproduction in any medium, provided the original work is properly cited. 

References

- [1] Buzea C, Pacheco I, Robbie K. Nanomaterials and nanoparticles: Sources and toxicity. *Biointerphases*. 2007;**2**:MR17-MR71. DOI: 10.1116/1.2815690
- [2] Rogach AL, Katsikas L, Kornowski A, Su D, Eychmüller A, Weller H. Synthesis and characterization of thiol-stabilized CdTe nanocrystals. *Berichte der Bunsengesellschaft für Physikalische Chemie*. 1996;**100**:1772-1778. DOI: 10.1002/bbpc.19961001104
- [3] Rogach AL, Franzl T, Klar TA, Feldmann J, Gaponik N, Lesnyak V, et al. Aqueous synthesis of thiol-capped CdTe nanocrystals: State-of-the-art. *The Journal of Physical Chemistry C*. 2007;**111**:14628-14637. DOI: 10.1021/jp072463y
- [4] Takagahara T, Takeda K. Theory of the quantum confinement effect on excitons in quantum dots of indirect-gap materials. *Physical Review B*. 1992;**46**:15578-15581. DOI: 10.1103/PhysRevB.46.15578
- [5] Kan S, Mokari T, Rothenberg E, Banin U. Synthesis and size-dependent properties of zinc-blende semiconductor quantum rods. *Nature Materials*. 2003;**2**:155-158. DOI: 10.1038/nmat830
- [6] Remacle F, Collier CP, Markovich G, Heath JR, Banin U, Levine RD. Networks of quantum nanodots: The role of disorder in modifying electronic and optical properties. *The Journal of Physical Chemistry B*. 1998;**102**:7727-7734. DOI: 10.1021/jp9813948
- [7] Soloviev VN, Eichhöfer A, Fenske D, Banin U. Size-dependent optical spectroscopy of a homologous series of cdse cluster molecules. *Journal of the American Chemical Society*. 2001;**123**:2354-2364. DOI: 10.1021/ja003598j
- [8] Tessler N. Efficient near-infrared polymer nanocrystal light-emitting diodes. *Science*. 2002;**295**:1506-1508. DOI: 10.1126/science.1068153
- [9] Anikeeva PO, Halpert JE, Bawendi MG, Bulović V. Quantum dot light-emitting devices with electroluminescence tunable over the entire visible spectrum. *Nano Letters*. 2009;**9**:2532-2536. DOI: 10.1021/nl9002969
- [10] Shevchenko EV, Ringler M, Schwemer A, Talapin DV, Klar TA, Rogach AL, et al. Self-assembled binary superlattices of CdSe and Au nanocrystals and their fluorescence properties. *Journal of the American Chemical Society*. 2008;**130**:3274-3275. DOI: 10.1021/ja0564261
- [11] Prasad PN. *Nanophotonics*. Hoboken, New Jersey: John Wiley & Sons, Inc., Published simultaneously in Canada. 2004. DOI: 10.1002/0471670251.ch9
- [12] Prasad PN. *Introduction to Biophotonics*. Hoboken, New Jersey: John Wiley & Sons, Inc., Published simultaneously in Canada. 2004. DOI: 10.1002/0471670251
- [13] Prasad PN. *Introduction to Nanomedicine and Nanobioengineering*. Hoboken, New Jersey: John Wiley & Sons, Inc.; 2012
- [14] Farkhani SM, Valizadeh A. Review: Three synthesis methods of CdX (X = Se, S or Te) quantum dots. *IET Nanobiotechnology*. 2014;**8**:59-76. DOI: 10.1049/iet-nbt.2012.0028
- [15] Li Y, He X, Cao M. Micro-emulsion-assisted synthesis of ZnS nanospheres and their photocatalytic activity. *Materials Research Bulletin*. 2008;**43**:3100-3110. DOI: 10.1016/j.materresbull.2007.11.016

- [16] Shi H, Li X, Wang D, Yuan Y, Zou Z, Ye J. NaNbO₃ nanostructures: Facile synthesis, characterization, and their photocatalytic properties. *Catalysis Letters*. 2009;**132**:205-212. DOI: 10.1007/s10562-009-0087-8
- [17] Hoffman AJ, Mills G, Yee H, Hoffmann MR. Q-sized cadmium sulfide: Synthesis, characterization, and efficiency of photoinitiation of polymerization of several vinylic monomers. *The Journal of Physical Chemistry*. 1992;**96**:5546-5552. DOI: 10.1021/j100192a067
- [18] Available from: <https://globenewswire.com/news-release/2017/08/02/1070735/0/en/Global-Nanomaterials-Market-Will-Reach-USD-16-8-Billion-by-2022-Zion-Market-Research.html>
- [19] Available from: <http://www.understandingnano.com/nanowires-applications.html>
- [20] Brus LE. A simple model for the ionization potential, electron affinity, and aqueous redox potentials of small semiconductor crystallites. *The Journal of Chemical Physics*. 1983;**79**:5566-5571. DOI: 10.1063/1.445676
- [21] Baruah JM, Narayan J. Development of greener methodology for the synthesis of CdSe quantum dots and characterization of their thin films. *Journal of Optics*. 2017;**47**:202-207. DOI: 10.1007/s12596-017-0417-y
- [22] Lamer VK, Dinegar RH. Theory, production and mechanism of formation of monodispersed hydrosols. *Journal of the American Chemical Society*. 1950;**72**:4847-4854. DOI: 10.1021/ja01167a001
- [23] Lamer VK. Nucleation in phase transitions. *Industrial & Engineering Chemistry*. 1952;**44**:1270-1277. DOI: 10.1021/ie50510a027
- [24] Mullin JW. *Crystallization*. Oxford: Butterworth-Heinemann; 2001. DOI: 10.1021/op0101005
- [25] Puentes VF, Zanchet D, Erdonmez CK, Alivisatos AP. Synthesis of Hcp-Co nanodisks. *Journal of the American Chemical Society*. 2002;**124**:12874-12880. DOI: 10.1021/ja027262g
- [26] Robinson I, Zacchini S, Tung LD, Maenosono S, Thanh NTK. Synthesis and characterization of magnetic nanoalloys from bimetallic carbonyl clusters. *Chemistry of Materials*. 2009;**21**:3021-3026. DOI: 10.1021/cm9008442
- [27] Yuan J, Kajiyoshi K, Yanagisawa K, Sasaoka H, Nishimura K. Fabrication of silica nanocoatings on ZnS-type phosphors via a sol-gel route using cetyltrimethylammonium chloride dispersant. *Materials Letters*. 2006;**60**:1284-1286. DOI: 10.1016/j.matlet.2005.11.015
- [28] Cheng X, Zhao Q, Yang Y, Tjong SC, Li RKY. A facile method for the synthesis of ZnS/polystyrene composite particles and ZnS hollow micro-spheres. *Journal of Materials Science*. 2010;**45**:777-782. DOI: 10.1007/s10853-009-4000-z
- [29] Maity R, Maiti U, Mitra M, Chattopadhyay K. Synthesis and optical characterization of polymer-capped nanocrystalline ZnS thin films by chemical process. *Physica E: Low-dimensional Systems and Nanostructures*. 2006;**33**:104-109. DOI: 10.1016/j.physe.2005.11.015
- [30] Liao XH, Zhu JJ, Chen HY. Microwave synthesis of nanocrystalline metal sulfides in formaldehyde solution. *Material Science Engineering B*. 2001;**85**:85-89. DOI: 10.1016/S0921-5107(01)00647-X
- [31] Shafiq I, Sharif A, Sing LC. ZnS_xSe_{1-x} nanowire arrays with

- tunable optical properties grown on ZnS nanoribbon substrates. *Physica E: Low-dimensional Systems and Nanostructures*. 2009;**41**:739-745. DOI: 10.1016/j.physe.2008.12.003
- [32] Zhu J, Zhou M, Xu J, Liao X. Preparation of CdS and ZnS nanoparticles using microwave irradiation. *Materials Letters*. 2001;**47**:25-29. DOI: 10.1016/S0167-577X(00)00206-8
- [33] Zhao Q, Hou L, Huang R. Synthesis of ZnS nanorods by a surfactant-assisted soft chemistry method. *Inorganic Chemical Communication*. 2003;**6**:971-973. DOI: 10.1016/S1387-7003(03)00146-1
- [34] Samokhvalov P, Artemyev M, Nabiev I. Basic principles and current trends in colloidal synthesis of highly luminescent semiconductor nanocrystals. *Chemistry—A European Journal*. 2013;**19**:1534-1546. DOI: 10.1002/chem.201202860
- [35] Tessier MD, Dupont D, Nolf KD, Roo JD, Hens Z. Economic and size-tunable synthesis of InP/ZnE (E = S, Se) colloidal quantum dots. *Chemistry of Materials*. 2015;**27**:4893-4898. DOI: 10.1021/acs.chemmater.5b02138
- [36] Zhuang Z, Peng Q, Li Y. Controlled synthesis of semiconductor nanostructures in the liquid phase. *Chemical Society Reviews*. 2011;**40**:5492. DOI: 10.1039/C1CS15095B
- [37] Fu T, Qin HY, Hu HJ, Hong Z, He S. Aqueous synthesis and fluorescence-imaging application of CdTe/ZnSe core/shell quantum dots with high stability and low cytotoxicity. *Journal of Nanoscience and Nanotechnology*. 2010;**10**:1741-1746. DOI: 10.1166/jnn.2010.2049
- [38] Tan J, Liang Y, Wang J, Chen J, Sun B, Shao L. Facile synthesis of CdTe-based quantum dots promoted by mercaptosuccinic acid and hydrazine. *New Journal of Chemistry*. 2015;**39**:4488-4493. DOI: 10.1039/C5NJ00075K
- [39] Rogach AL, Kornowski A, Gao M, Eychmüller A, Weller H. Synthesis and characterization of a size series of extremely small thiol-stabilized CdSe nanocrystals. *The Journal of Physical Chemistry B*. 1999;**103**:3065-3069. DOI: 10.1021/jp984833b
- [40] Rogach A, Kershaw SV, Burt M, Harrison MT, Kornowski A, Eychmüller A, et al. Colloidally prepared HgTe nanocrystals with strong room-temperature infrared luminescence. *Advanced Materials*. 1999;**11**:552-555. DOI: 10.1002/(SICI)1521-4095(199905)11:7<552::AID-ADMA552>3.0.CO;2-Q
- [41] Tsay JM, Pflughoeft M, Bentolila LA, Weiss S. Hybrid approach to the synthesis of highly luminescent CdTe/ZnS and CdHgTe/ZnS nanocrystals. *Journal of the American Chemical Society*. 2004;**126**:1926-1927. DOI: 10.1021/ja039227v
- [42] Tang B, Yang F, Lin Y, Zhuo L, Ge J, Cao L. Synthesis and characterization of wavelength-tunable, water-soluble, and near-infrared-emitting CdHgTe nanorods. *Chemistry of Materials*. 2007;**19**:1212-1214. DOI: 10.1021/cm062805x
- [43] Nakane Y, Tsukasaki Y, Sakata T, Yasuda H, Jin T. Aqueous synthesis of glutathione-coated PbS quantum dots with tunable emission for non-invasive fluorescence imaging in the second near-infrared biological window (1000-1400 nm). *Chemical Communications*. 2013;**49**:7584. DOI: 10.1039/C3CC44000A
- [44] Pradhan N, Efrima S. Single-precursor, one-pot versatile synthesis

under near ambient conditions of tunable, single and dual band fluorescing metal sulfide nanoparticles. *Journal of the American Chemical Society*. 2003;**125**:2050-2051. DOI: 10.1021/ja028887h

[45] Cao YC, Wang J. One-pot synthesis of high-quality zinc-blende CdS nanocrystals. *Journal of the American Chemical Society*. 2004;**126**: 14336-14337. DOI: 10.1021/ja0459678

[46] Zhang LJ, Shen X, Liang H, Guo S, Liang ZH. Hot-injection synthesis of highly luminescent and monodisperse CdS nanocrystals using thioacetamide and cadmium source with proper reactivity. *Journal of Colloid and Interface Science*. 2010;**342**:236-242. DOI: 10.1016/j.jcis.2009.10.030

[47] Ouyang J, Zaman MB, Yan FJ, Johnston D, Li G, Wu X, et al. Multiple families of magic-sized CdSe nanocrystals with strong bandgap photoluminescence via noninjection one-pot syntheses. *The Journal of Physical Chemistry C*. 2008;**112**: 13805-13811. DOI: 10.1021/jp803845n

[48] Mekis I, Talapin DV, Kornowski A, Haase M, Weller H. One-pot synthesis of highly luminescent CdSe/CdS core-shell nanocrystals via organometallic and “greener” chemical approaches. *The Journal of Physical Chemistry C*. 2003;**107**:7454-7462. DOI: 10.1021/jp0278364

[49] Wang J, Zhai J, Han S. Non-injection one-pot preparation strategy for multiple families of magic-sized CdTe quantum dots with bright bandgap photoemission. *Chemical Engineering Journal*. 2013;**23**:215-216. DOI: 10.1016/j.cej.2012.10.092

[50] Kanehara M, Arakawa H, Honda T, Saruyama M, Teranishi T. Large-scale synthesis of high-quality metal sulfide semiconductor quantum dots with tunable surface-plasmon resonance

frequencies. *Chemistry—A European Journal*. 2012;**18**:9230-9238. DOI: 10.1002/chem.201201159

[51] Liu TY, Li M, Ouyang J, Zaman MB, Wang R, Wu X, et al. Non-injection and low-temperature approach to colloidal photoluminescent PbS nanocrystals with narrow bandwidth. *The Journal of Physical Chemistry C*. 2009;**113**:2301-2308. DOI: 10.1021/jp809171f

[52] Wang D, Qian J, Cai F, He S, Han S, Mu Y. Green²-synthesized near-infrared PbS quantum dots with silica-peg dual-layer coating: Ultrastable and biocompatible optical probes for in vivo animal imaging. *Nanotechnology*. 2012;**23**:245701. DOI: 10.1088/0957-4484/23/24/245701

[53] Jiang P, Wang R, Chen Z. Thiol-based non-injection synthesis of near-infrared Ag₂S/ZnS core/shell quantum dots. *RSC Advances*. 2015;**5**:56789-56793. DOI: 10.1039/C5RA08008H

[54] Du Y, Xu B, Fu T, Cai M, Li F, Zhang Y, et al. Near-infrared photoluminescent Ag₂S quantum dots from a single source precursor. *Journal of the American Chemical Society*. 2010;**132**:1470-1471. DOI: 10.1021/ja909490r

[55] Anastas PT, Zimmerman JB. Peer reviewed: Design through the 12 principles of green engineering. *Environmental Science & Technology*. 2003;**37**:94A-101A. DOI: 10.1021/es032373g

[56] Murray CB, Norris DJ, Bawendi MG. Synthesis and characterization of nearly monodisperse CdE (E = sulfur, selenium, tellurium) semiconductor nanocrystallites. *Journal of the American Chemical Society*. 1993;**115**:8706-8715. DOI: 10.1021/ja00072a025

[57] Murray CB, Kagan CR, Bawendi MG. Synthesis and characterization

- of monodisperse nanocrystals and close-packed nanocrystal assemblies. *Annual Review of Materials Science*. 2000;**30**:545-610. DOI: 10.1146/annurev.matsci.30.1.545
- [58] Dabbousi BO, Rodriguez-Viejo J, Mikulec FV, Heine JR, Mattoussi H, Ober R, et al. (CdSe)ZnS core-shell quantum dots: Synthesis and characterization of a size series of highly luminescent nanocrystallites. *The Journal of Physical Chemistry B*. 1997;**101**:9463-9475. DOI: 10.1021/jp971091y
- [59] Peng X, Schlamp MC, Kadavanich AV, Alivisatos AP. Epitaxial growth of highly luminescent CdSe/CdS core/shell nanocrystals with photostability and electronic accessibility. *Journal of the American Chemical Society*. 1997;**119**:7019-7029. DOI: 10.1021/ja970754m
- [60] Peng X, Wickham J, Alivisatos AP. Kinetics of II-VI and III-V colloidal semiconductor nanocrystal growth: "Focusing" of size distributions. *Journal of the American Chemical Society*. 1998;**120**:5343-5344. DOI: 10.1021/ja9805425
- [61] Peng X, Manna L, Yang W, Wickham J, Scher E, Kadavanich A, et al. Shape control of CdSe nanocrystals. *Nature*. 2000;**404**:59-61. DOI: 10.1038/35003535
- [62] Pu Y, Cai F, Wang D, Wang JX, Chen JF. Colloidal synthesis of semiconductor quantum dots toward large-scale production: A review. *Industrial & Engineering Chemistry Research*. 2018;**57**:1790-1802. DOI: 10.1021/acs.iecr.7b04836
- [63] Peng X. Green chemical approaches toward high-quality semiconductor nanocrystals. *Chemistry—A European Journal*. 2002;**8**:334-339. DOI: 10.1002/1521-3765(20020118)8:2<334::AID-CHEM334>3.0.CO;2-T
- [64] Jin S, Hu Y, Gu Z, Liu L, Wu HC. Application of quantum dots in biological imaging. *Journal of Nanomaterials*. 2011;**2011**:1-13. DOI: 10.1155/2011/834139
- [65] Dahl JA, Maddux BLS, Hutchison JE. Toward greener nanosynthesis. *Chemical Reviews*. 2007;**107**:2228-2269. DOI: 10.1021/cr050943k
- [66] Peng ZA, Peng X. Formation of high-quality CdTe, CdSe, and CdS nanocrystals using CdO as precursor. *Journal of the American Chemical Society*. 2001;**123**:183-184. DOI: 10.1021/ja003633m
- [67] Qu L, Peng ZA, Peng X. Alternative routes toward high quality CdSe nanocrystals. *Nano Letters*. 2001;**1**:333-337. DOI: 10.1021/nl0155532
- [68] Zhou Y, Zhu Z, Huang W, Liu W, Wu S, Liu X, et al. Optical coupling between chiral biomolecules and semiconductor nanoparticles: Size-dependent circular dichroism absorption. *Angewandte Chemie International Edition*. 2011;**50**:11456-11459. DOI: 10.1002/ange.201103762
- [69] Zhou Y, Yang M, Sun K, Tang Z, Kotov NA. Similar topological origin of chiral centers in organic and nanoscale inorganic structures: Effect of stabilizer chirality on optical isomerism and growth of CdTe nanocrystals. *Journal of the American Chemical Society*. 2010;**132**:6006-6013. DOI: 10.1021/ja906894r
- [70] Rossetti R, Nakahara S, Brus LE. Quantum size effects in the redox potentials, resonance raman spectra, and electronic spectra of CdS crystallites in aqueous solution. *The Journal of Chemical Physics*. 1983;**79**:1086-1088. DOI: 10.1063/1.445834
- [71] Henglein A. Photochemistry of colloidal cadmium sulfide. 2. Effects of adsorbed methyl viologen and of

- colloidal platinum. *The Journal of Physical Chemistry*. 1982;**86**:2291-2293. DOI: 10.1021/j100210a010
- [72] Vossmeier T, Katsikas L, Giersig M, Popovic IG, Diesner K, Chemseddine A, et al. CdS nanoclusters: Synthesis, characterization, size dependent oscillator strength, temperature shift of the excitonic transition energy, and reversible absorbance shift. *The Journal of Physical Chemistry*. 1994;**98**:7665-7673. DOI: 10.1021/j100082a044
- [73] Gao M, Kirstein S, Möhwald H, Rogach AL, Kornowski A, Eychmüller A, et al. Strongly photoluminescent CdTe nanocrystals by proper surface modification. *The Journal of Physical Chemistry B*. 1998;**102**:8360-8363. DOI: 10.1021/jp9823603
- [74] Zhang H, Zhou Z, Yang B, Gao M. The influence of carboxyl groups on the photoluminescence of mercaptocarboxylic acid-stabilized CdTe nanoparticles. *The Journal of Physical Chemistry B*. 2003;**107**:8-13. DOI: 10.1021/jp025910c
- [75] Kwon BH, Lee KG, Park TJ, Kim H, Lee TJ, Lee SJ, et al. Continuous in situ synthesis of ZnSe/ZnS core/shell quantum dots in a microfluidic reaction system and its application for light-emitting diodes. *Small*. 2012;**8**:3257-3262. DOI: 10.1002/smll.201200773
- [76] Kikkeri R, Laurino P, Odedra A, Seeberger PH. Synthesis of carbohydrate-functionalized quantum dots in microreactors. *Angewandte Chemie International Edition*. 2010;**49**:2054-2057. DOI: 10.1002/anie.200905053
- [77] Marre S, Park J, Rempel J, Guan J, Bawendi MG, Jensen KF. Supercritical continuous-microflow synthesis of narrow size distribution quantum dots. *Advanced Materials*. 2008;**20**:4830-4834. DOI: 10.1002/adma.200801579
- [78] Lignos I, Protesescu L, Stavrakis S, Piveteau L, Speirs MJ, Loi MA, et al. Facile droplet-based microfluidic synthesis of monodisperse IV-VI semiconductor nanocrystals with coupled in-line NIR fluorescence detection. *Chemistry of Materials*. 2014;**26**:2975-2982. DOI: 10.1021/cm500774p
- [79] Pearson RG. Hard and soft acids and bases. *Journal of the American Chemical Society*. 1963;**85**:3533-3539. DOI: 10.1021/ja00905a001
- [80] Parr RG, Pearson RG. Absolute hardness: Companion parameter to absolute electronegativity. *Journal of the American Chemical Society*. 1983;**105**:7512-7516. DOI: 10.1021/ja00364a005
- [81] Eychmüller A, Rogach AL. Chemistry and photophysics of thiol-stabilized II-VI semiconductor nanocrystals. *Pure and Applied Chemistry*. 2000;**72**:179-188. DOI: 10.1351/pac200072010179
- [82] Boles MA, Ling D, Hyeon T, Talapin DV. The surface science of nanocrystals. *Nature Materials*. 2016;**15**:141-153. DOI: 10.1038/nmat4526
- [83] Jing L, Kershaw SV, Li Y, Huang X, Li Y, Rogach AL, et al. Aqueous based semiconductor nanocrystals. *Chemical Reviews*. 2016;**116**:10623-10730. DOI: 10.1021/acs.chemrev.6b00041
- [84] Kilina SV, Tamukong PK, Kilin DS. Surface chemistry of semiconducting quantum dots: Theoretical perspectives. *Accounts of Chemical Research*. 2016;**49**:2127-2135. DOI: 10.1021/acs.accounts.6b00196
- [85] Tsoi KM, Dai Q, Alman BA, Chan WCW. Are quantum dots toxic? Exploring the discrepancy between cell culture and animal studies. *Accounts of Chemical Research*. 2012;**46**:662-671. DOI: 10.1021/ar300040z

- [86] Derfus AM, Chan WCW, Bhatia SN. Probing the cytotoxicity of semiconductor quantum dots. *Nano Letters*. 2004;**4**:11-18. DOI: 10.1021/nl0347334
- [87] Yao J, Yang M, Duan Y. Chemistry, biology, and medicine of fluorescent nanomaterials and related systems: New insights into biosensing, bioimaging, genomics, diagnostics, and therapy. *Chemical Reviews*. 2014;**114**:6130-6178. DOI: 10.1021/cr200359p
- [88] Milazzo G. Tables of standard electrode potentials. *Journal of the Electrochemical Society*. 1978;**125**:261C. DOI: 10.1149/1.2131790
- [89] Bratsch SG. Standard electrode potentials and temperature coefficients in water at 298.15 K. *The Journal of Physical and Chemical Reference Data*. 1989;**18**:1-21. DOI: 10.1063/1.555839
- [90] Liu Y, Chen W, Joly AG, Wang Y, Pope C, Zhang Y, et al. Comparison of water-soluble CdTe nanoparticles synthesized in air and in nitrogen. *The Journal of Physical Chemistry B*. 2006;**110**:16992-17000. DOI: 10.1021/jp063085k
- [91] Colvin VL, Schlamp MC, Alivisatos AP. Light-emitting diodes made from cadmium selenide nanocrystals and a semiconducting polymer. *Nature*. 1994;**370**:354-357. DOI: 10.1038/370354a0
- [92] Schlamp MC, Peng X, Alivisatos AP. Improved efficiencies in light emitting diodes made with CdSe(CdS) core/shell type nanocrystals and a semiconducting polymer. *Journal of Applied Physics*. 1997;**82**:5837-5842. DOI: 10.1063/1.366452
- [93] Mattoussi H, Radzilowski LH, Dabbousi BO, Thomas EL, Bawendi MG, Rubner MF. Electroluminescence from heterostructures of poly(phenylene vinylene) and inorganic CdSe nanocrystals. *Journal of Applied Physics*. 1998;**83**:7965-7974. DOI: 10.1063/1.367978
- [94] Chaudhary S, Ozkan M, Chan WCW. Trilayer hybrid polymer-quantum dot light-emitting diodes. *Applied Physics Letters*. 2004;**84**:2925-2927. DOI: 10.1063/1.1699476
- [95] Coe-Sullivan S, Steckel JS, Woo WK, Bawendi MG, Bulović V. Large-area ordered quantum-dot monolayers via phase separation during spin-casting. *Advanced Functional Materials*. 2005;**15**:1117-1124. DOI: 10.1002/adfm.200400468
- [96] Steckel JS, Snee P, Coe-Sullivan S, Zimmer JP, Halpert JE, Anikeeva P, et al. Color-saturated green-emitting qd-leds. *Angewandte Chemie International Edition*. 2006;**45**:5796-5799. DOI: 10.1002/anie.200600317
- [97] Caruge JM, Halpert JE, Bulović V, Bawendi MG. NiO as an inorganic hole-transporting layer in quantum-dot light-emitting devices. *Nano Letters*. 2006;**6**:2991-2994. DOI: 10.1021/nl0623208
- [98] Sun Q, Wang YA, Li LS, Wang D, Zhu T, Xu J, et al. Bright, multicoloured light-emitting diodes based on quantum dots. *Nature Photonics*. 2007;**1**:717-722. DOI: 10.1038/nphoton.2007.226
- [99] Mueller AH, Petruska MA, Achermann M, Werder DJ, Akhadov EA, Koleske DD, et al. Multicolor light-emitting diodes based on semiconductor nanocrystals encapsulated in GaN charge injection layers. *Nano Letters*. 2005;**5**:1039-1044. DOI: 10.1021/nl050384x
- [100] Kim JY, Voznyy O, Zhitomirsky D, Sargent EH. 25th anniversary article: Colloidal quantum dot materials and devices: A quarter-century of advances. *Advanced Materials*. 2013;**25**:4986-5010. DOI: 10.1002/adma.201301947

[101] Chuang CHM, Brown PR, Bulović V, Bawendi MG. Improved performance and stability in quantum dot solar cells through band alignment engineering. *Nature Materials*. 2014;**13**:796-801. DOI: 10.1038/nmat3984

[102] Lan X, Voznyy O, Arquer FPGD, Liu M, Xu J, Proppe AH, et al. 10.6% certified colloidal quantum dot solar cells via solvent-polarity-engineered halide passivation. *Nano Letters*. 2016;**16**:4630-4634. DOI: 10.1021/acs.nanolett.6b01957

[103] Mcdaniel H, Fuke N, Makarov NS, Pietryga JM, Klimov VI. An integrated approach to realizing high-performance liquid-junction quantum dot sensitized solar cells. *Nature Communications*. 2013;**4**:2887. DOI: 10.1038/ncomms3887

[104] Semonin OE, Luther JM, Choi S, Chen HY, Gao J, Nozik AJ, et al. Peak external photocurrent quantum efficiency exceeding 100% via meg in a quantum dot solar cell. *Science*. 2011;**334**:1530-1533. DOI: 10.1126/science.1209845

[105] Luther JM, Gao J, Lloyd MT, Semonin OE, Beard MC, Nozik AJ. Stability assessment on a 3% bilayer PbS/ZnO quantum dot heterojunction solar cell. *Advanced Materials*. 2010;**22**:3704-3707. DOI: 10.1002/adma.201001148

[106] Sanderson K. Quantum dots go large. *Nature*. 2009;**459**:760-761. DOI: 10.1038/459760a

[107] Bourzac K. Quantum dots go on display. *Nature*. 2013;**493**:283-283. DOI: 10.1038/493283a

[108] Howes PD, Chandrawati R, Stevens MM. Colloidal nanoparticles as advanced biological sensors. *Science*. 2014;**346**:1247390-1247390. DOI: 10.1126/science.1247390



*Edited by Majid Nayeripour,
Mahdi Mansouri and Eberhard Waffenschmidt*

This edited volume *Solar Cells* is a collection of reviewed and relevant research chapters offering a comprehensive overview of recent developments in the field of renewable energy. The book comprises single chapters authored by various researchers and is edited by a group of experts active in the physical sciences, engineering, and technology research areas. All chapters are complete in themselves but united under a common research study topic. This publication aims at providing a thorough overview of the latest research efforts by international authors on physical sciences, engineering, and technology, and opens new possible research paths for further novel developments.

Published in London, UK

© 2020 IntechOpen
© schulzie / iStock

IntechOpen

